Lehrstuhl für Technische Elektrophysik

# Modeling and Simulation of Wide Bandgap Semiconductor Devices: 4H/6H-SiC

**Martin Lades**

Vollständiger Abdruck der von der Fakultät für Elektrotechnik und Informationstechnik
der Technischen Universität München zur Erlangung des akademischen Grades eines
Doktors-Ingenieur (Dr.-Ing.)
genehmigten Dissertation.

Vorsitzende: Univ.-Prof. Dr. rer. nat. D. Schmitt-Landsiedel

Prüfer der Dissertation:

1. Univ.-Prof. Dr. rer. nat. G. Wachutka
2. Univ.-Prof. Dr.-Ing., Dr.-Ing. habil. M. Claassen

Die Dissertation wurde am 15.05.2000 bei der Technischen Universität München
eingereicht und durch die Fakultät für Elektrotechnik und Informationstechnik
am 01.08.2000 angenommen.

*to Simone, Yannic, Luisa, and our family*

# Contents

**Zusammenfassung** 1

**Abstract** 3

**1 Introduction** 5

1.1 Wide bandgap semiconductor materials . . . . . 5

1.2 Numerical simulation of SiC devices . . . . . 7

1.3 Scope of this work . . . . . 8

**2 Electrothermal transport model** 10

2.1 Electrothermal Transport theory . . . . . 11

2.1.1 Local thermal equilibrium and fundamental Gibbs relations . . . . . 11

2.1.2 Gibbs-, Fermi-, and Boltzmann distributions . . . . . 13

2.1.2.1 Free carrier densities . . . . . 14

2.1.2.2 Impurities . . . . . 15

2.1.3 Balance equations and constitutive current relations . . . . . 16

2.2 Carrier emission and capture kinetics . . . . . 17

2.2.1 Quasi-static approximation . . . . . 18

2.2.2 Carrier emission and capture coefficients . . . . . 19

2.2.3 Classification of impurities . . . . . 20

2.2.3.1 Generation-recombination centers . . . . . 20

2.2.3.2 Dopants and deep traps . . . . . 21

2.3 Generic model for anisotropic material properties . . . . . 22

2.4 Extended electrothermal drift-diffusion model . . . . . 24

2.5 Boundary conditions . . . . . 26

**3 Modeling of 4H/6H-SiC material properties** 28
3.1 General material characteristics and process technology . . . 28
3.2 Effective density of states and intrinsic carrier density . . . 30
3.3 Dielectric constant . . . 34
3.4 Free carrier mobilities . . . 34
3.4.1 Acoustic-phonon and ionized-impurity scattering . . . 35
3.4.2 Carrier-carrier and surface scattering . . . 36
3.4.3 High-field drift velocity saturation . . . 37
3.5 Thermal properties . . . 38
3.6 Carrier generation and recombination . . . 40
3.6.1 Generalized field-dependent Shockley-Read-Hall statistics . . . 40
3.6.2 Auger recombination . . . 42
3.6.3 Impact ionization . . . 42

**4 Incomplete ionization of dopants** 44
4.1 Electrothermal equilibrium . . . 45
4.2 Measurement of ionization time constants . . . 49
4.2.1 Thermal admittance spectroscopy (TAS) . . . 51
4.2.2 Simulation of TAS: Serial resistances and doping profiles . . . 52
4.2.2.1 Simulation of TAS spectra . . . 54
4.2.2.2 Evaluation of “freeze-out signal” . . . 56
4.2.2.3 Concept of TAS applied to the highly-doped part of a pn-junction . . 57
4.2.2.4 Evaluation of TAS signals arising from the highly-doped part of a pn-junction . . . 59
4.2.2.5 Influence of doping profile . . . 62
4.2.3 Deep level transient spectroscopy (DLTS) . . . 63
4.2.3.1 Basic theory . . . 64
4.2.3.2 Influence of serial resistance . . . 66
4.2.3.3 DLTS at the highly-doped part of a pn-junction . . . 68
4.3 Ionization energy and capture cross sections of N, Al, and B in 4H/6H-SiC . . . 68

**5 Simulation of 4H/6H-SiC devices 70**

5.1 The PN-junction - Evaluation of material parameters and models . . . . . . . . . . . . 70

5.1.1 Basic considerations . . . . . . . . . . . . . . . . . . . . . . . . . . . . . . 72

5.1.1.1 Statistical limit . . . . . . . . . . . . . . . . . . . . . . . . . . . . 73

5.1.1.2 Validity of the quasi-static approximation . . . . . . . . . . . . . . . . 74

5.1.1.3 Numerical instabilities . . . . . . . . . . . . . . . . . . . . . . . . . 75

5.1.2 Forward characteristics . . . . . . . . . . . . . . . . . . . . . . . . . . . . 76

5.1.2.1 Influence of surface recombination . . . . . . . . . . . . . . . . . . . 76

5.1.2.2 Temperature dependence of SRH lifetimes . . . . . . . . . . . . . . . 77

5.1.2.3 Field-dependent SRH lifetimes . . . . . . . . . . . . . . . . . . . . . 79

5.1.2.4 IV characteristics at high current ratings . . . . . . . . . . . . . . . . 80

5.1.2.5 Discussion of material parameters . . . . . . . . . . . . . . . . . . . 80

5.1.2.6 Summary . . . . . . . . . . . . . . . . . . . . . . . . . . . . . . . . 82

5.1.3 Reverse characteristics . . . . . . . . . . . . . . . . . . . . . . . . . . . . 82

5.1.3.1 Temperature activation of reverse current . . . . . . . . . . . . . . . 83

5.1.3.2 Coupled defect-level generation current . . . . . . . . . . . . . . . . 84

5.2 The JFET - Concept of inverse modeling . . . . . . . . . . . . . . . . . . . . . . . . 86

5.2.1 Characterization of implanted-gate 6H-SiC JFET . . . . . . . . . . . . . . . 86

5.2.1.1 Basic characteristics . . . . . . . . . . . . . . . . . . . . . . . . . . 87

5.2.1.2 Inhomogeneous channel properties . . . . . . . . . . . . . . . . . . . 90

5.2.1.3 Temperature dependence of channel properties . . . . . . . . . . . . 93

5.2.2 Extraction of channel length of buried-gate 6H-SiC JFET . . . . . . . . . . . 94

5.3 Impact of anisotropic material properties on device characteristics . . . . . . . . . . . 96

5.3.1 Planar 6H-SiC pn-diode characteristics . . . . . . . . . . . . . . . . . . . . 97

5.3.2 UMOS and lateral JFET characteristics . . . . . . . . . . . . . . . . . . . . 99

5.3.3 DIMOS characteristics . . . . . . . . . . . . . . . . . . . . . . . . . . . . . 100

5.3.4 Vertical high-power JFET characteristics . . . . . . . . . . . . . . . . . . . 103

5.3.5 Summary . . . . . . . . . . . . . . . . . . . . . . . . . . . . . . . . . . . . 103

5.4 Dynamics of incomplete ionization of dopants . . . . . . . . . . . . . . . . . . . . . 105

5.4.1 PN-junction characteristics . . . . . . . . . . . . . . . . . . . . . . . . . . . 106

5.4.2 Dynamic punch-through . . . . . . . . . . . . . . . . . . . . . . . . . . . . 108

5.4.3 Impact ionization and dynamic ionization . . . . . . . . . . . . . . . . . . . 113

5.4.3.1 Non-punch-through diode design . . . . . . . . . . . . . . . . . . . . 114

5.4.3.2 Punch-through diode design . . . 115
5.4.3.3 Inhomogeneous compensation profile . . . 117
5.4.3.4 Summary . . . 118

**6 Conclusions** **121**
6.1 Incomplete ionization of dopants . . . 121
6.2 Ionization time constants measured by DLTS and thermal admittance spectroscopy . . 122
6.3 Anisotropic material properties . . . 123
6.4 Investigations on PN-diode and JFET characteristics . . . 123
6.5 Summary and outlook . . . 124

**A Material parameters for 4H- and 6H-SiC** **126**

**B Numerical methods** **128**
B.1 Discretization . . . 128
B.2 Calculation of junction admittance . . . 129

**C Generation-Recombination models** **132**

**D Analytical model of dual-gate JFET characteristics** **134**

**E Maximum dynamic depletion region width** **137**

**F List of symbols** **139**

**Bibliography** **142**

# Acknowledgements

I am greatly indepted to Prof. Gerhard Wachutka for giving me the opportunity to work on many challenging projects, his encouragement and his support at any time. I would also like to extend my graditude to Prof. Manfred Claassen for accepting to co-examine this thesis.

Many people helped me during my work. First of all, I am greatly indebted to my former diplomants Florian Pschenitzka, Michael Wendler, Daniel Berz, and Winfried Kaindl for there contributions to this work. In particular, I want to thank Winfried Kaindl for the valuable measurement results, many ideas, and support at any time.

I want to thank the staff of the chair for Physics of Electrotechnology for the friendly and cooperative working atmosphere including any support whenever needed. Among all of them, let me particularly thank Robert Thalhammer, Gabriele Schrag, Peter Scheubert, Peter Awakowicz, Yvonne Müller, Günter Speckhofer, and Stefan Schaub.

I wish to express my sincere appreciation to Prof. Wolfgang Fichtner who made it possible to be with the Integrated Systems Laboratory at the Swiss Federal Institut of Technology for a period of four months and provided access to the source code of DESSIS$_{-ISE}$. Among the many members of the IIS and the ISE who helped me during this time and also later I am especially grateful to Ulrich Krumbein, Andreas Schenk, Thomas Feudel, Christoph Wicki, Hartmut Dettmer, and Concetta Riccobene.

Many thanks to my "partner" Nando Kaminski at Daimler-Benz for his support and the many valuable discussions and contributions to this work. I will never forget his mental support by phone from Switzerland at 2am right before the deadline of a publication. I am very grateful to Ulrich Schmid for many valuable measurement results. Furthermore, I want to thank Dr. F. Wischmeyer, Christian Schröder, Raban Held, Dr. Wolfgang Wondrak, Dr. Scott Sheppard, Ekkehard Niemann and Dr. Rainer Constapel.

Among all the people who have given technically support I want particularly thank Nudjarin Ramungul for measurement results, Norbert Achtziger for several valuable discussions about DLTS and Eckhardt Böttger for the good cooperation during the diamond project.

Let me further thank Paul Womelsdorf and Florian Pschenitzka for reading and correcting this thesis. My very special thanks to my wife Simone for their patience and support during all the time.

I acknowledge the financial support of the Daimler-Benz AG (now DaimlerChrysler), Research & Technology, and the BMBF project FKZ03N1001.

# Zusammenfassung

Siliziumkarbid (SiC) besitzt als Ausgangsmaterial für Halbleiterbauelemente vielversprechende Eigenschaften für Anwendungen in der Hochleistungs-, Hochtemperatur- und Hochfrequenzelektronik. Intensive Forschungsanstrengungen auf diesem Gebiet in den vergangenen Jahren haben eine gute technologische Ausgangsbasis für die Weiterentwicklung der bisher realisierten Prototypen aller wichtigen Bauelemente bis hin zur Produktreife geschaffen. Neben der Weiterentwicklung der Prozesstechnologie gewinnt daher die numerische Simulation von SiC eine zunehmende Bedeutung für die Entwicklung und Optimierung von Bauelementen.

In dieser Arbeit wird ein im Rahmen der phänomenologischen Transporttheorie entwickeltes erweitertes elektrothermisches Drift-Diffusionsmodell beschrieben. Dabei wurde insbesondere auf die Unterschiede gegenüber konventionellen Halbleiter-Transport-Modellen eingegangen. Mehrere physikalische Modelle, die insbesondere für SiC relevant sind, wurden auf Source-Code-Ebene in ein kommerziell verfügbares mehrdimensionales Programm für die Halbleiter-Simulation implementiert: Der Poole-Frenkel Effekt, ein Model zur Beschreibung anisotroper Materialeigenschaften und die allgemeine Störstellenkinetik.

Die Auswirkung dieser Modelle auf das stationäre und transiente Bauelementeverhalten wurden anhand numerischer Simulation und experimenteller Charakterisierung realer Bauelemente aus 4H- und 6H-SiC untersucht. Dies ermöglichte eine Kalibrierung aller Modelparameter welche systematisch erörtert und zu einem Parametersatz für die Bauelementesimulation von 4H/6H-SiC zusammengefasst wurden.

Der PN-Übergang als Grundbaustein für Halbleiter-Bauelemente wurde basierend auf dieser Parameterzusammenstellung, einschliesslich der neu implementierten Modelle, analysiert. Hierbei ergibt sich, dass die Shockley-Read-Hall Statistik hervorragend die Eigenschaften des vorwärtsgepolten PN-Übergangs beschreibt. Andererseits zeigt sich ebenso, dass die Eigenschaften des PN-Übergangs in Rückwärtspolung nur unzureichend durch die in dieser Arbeit untersuchten Modelle beschrieben werden können. Weitergehende experimentelle und theoretische Arbeiten sind hierzu erforderlich.

Das Konzept der quasi-stationären Näherung der Störstellenkinetik in SiC wurde überarbeitet und die Grenzen für dessen Anwendung ermittelt. Jenseits dieser Grenzen ermöglicht die konsistente Einbindung der Störstellenkinetik in das elektrothermische Transportmodell die Untersuchung wichtiger physikalischer Effekte durch die transiente Ionisation von Dotierung und tiefen Störstellen. Diese sind bestimmt durch entsprechende Ionisationszeitkonstanten welche durch "deep level transient spectroscopy" (DLTS) und thermischer Admittanzspektroskopie über einen weiten Temperaturbereich gemessen wurden. Die Auswirkungen auf die Bauelementeigenschaften werden grundsätzlich durch eine transiente Erweiterung der Raumladungszone an einem PN-Übergangs bestimmt wenn die Zeitkonstante der äusseren Anregung kleiner als die charakteristische Ionisationszeitkonstante ist.

Die gemessenen Ergebnisse zeigen, dass die transiente unvollständige Ionisation von Stickstoff und Aluminium im Rahmen der gegenwärtig vorkommenden Anforderungen der Leistungselektronik vernachlässigbar ist. Dagegen beeinflusst Bor die dynamischen Eigenschaften von Bauelementen auch bei höheren Temperaturen. Damit verbundene mögliche Ausfallmechanismen wie der dynamische "punch-through" in NPN-Übergängen oder eine dynamisch reduzierte Durchbruchsspannung von PN-Übergängen werden diskutiert.

Darüberhinaus ergibt eine detaillierte numerische Analyse von DLTS und Admittanzspektroskopie neue Erkenntnisse betreffend der Interpretation der gemessenen Daten, welche sich der konventionellen Auswertung entziehen. Desweiteren wird der Einfluss von Serienwiderständen auf die Auswertung der gemessenen Signale eingehend erörtert.

Die grundsätzlichen Aspekte anisotroper Materialeigenschaften, insbesondere bezüglich der Ladungsträgerbeweglichkeit und der Dielektrizitätskonstanten, und ihr Einfluss auf das Bauelementeverhalten werden aufgezeigt. Die Untersuchungen zeigen, abhängig von Polytyp und Struktur des Bauelements, dass eine genaue Berücksichtigung dieser Eigenschaften für eine Beschreibung des Bauelements erforderlich ist.

Schliesslich wird durch eine eingehende Untersuchung der Bauelementeigenschaften bei verschiedensten Betriebsbedingungen aufgezeigt, dass das Konzept der inversen Modellierung auf heutige SiC Sperrschichtfeldeffekttransistoren (JFET) angewendet werden kann.

# Abstract

State-of-the-art silicon carbide (SiC) devices have matured to powerful prototypes demonstrating the promising properties of SiC as basic material for high-power, high-temperature, and high-frequency applications. Apart from further technological progress in this field, numerical simulations based on accurate device models are more and more required for design and optimization of SiC devices.

In this work, an extended electrothermal drift-diffusion model formulated within the framework of phenomenological transport theory is described with emphasis on pointing out the differences and extensions compared to conventional semiconductor transport models. Based on a commercially available general-purpose multi-dimensional device simulation tool originally developed for simulation of Si devices, various physical models particularly relevant to SiC are implemented on the source code level. They include the Poole-Frenkel generation-recombination mechanism, a generic model describing anisotropic material properties, and general impurity kinetics of shallow and deep traps.

The implications of these models on quasi-stationary and transient device behavior are investigated by numerical simulation of "real" state-of-the-art 4H- and 6H-SiC devices as well as by experimental characterization, thus allowing for immediate comparison and calibration of the model parameters. All required model parameters are systematically discussed and summarized to a template parameter set for 4H- and 6H-SiC device simulation.

The pn-junction, being the basic building block for semiconductor devices, is analyzed based on this set of parameters including the implemented new models. It is found that Shockley-Read-Hall statistics excellently model the characteristics of forward biased pn-junctions. The physical mechanisms leading to excess reverse leakage currents, on the other hand, are still unclear and further theoretical work based on detailed experimental investigations is required for a progress in explaining the measured data.

The concept and the limits of the quasi-static approximation of impurity kinetics are revisited. For device operation beyond these limits, the consistent coupling of impurity kinetics to the electrothermal transport model reveals various effects arising from the dynamic ionization of dopants and traps. These are governed by corresponding ionization time constants which have been measured using deep level transient spectroscopy (DLTS) and thermal admittance spectroscopy. The basic impact on device characteristics results from a dynamically enlarged extension of depletion regions if the rise time of a reverse bias pulse is equal or smaller than the characteristic ionization time constant. The measurement results prove that transient incomplete ionization is negligible for dopants like nitrogen and aluminum, at least within today's high-power device operation areas, whereas boron significantly influences the dynamic device characteristics even above room temperature. Related possible device failure mechanisms are discussed including dynamic punch-through which may occur in back-to-back junction configurations and a dynamically reduced blocking capability of pn-junctions.

Additionally, a detailed numerical analysis of the DLTS and thermal admittance spectroscopy measurement methods provides new insights concerning the interpretation of the measured data which can not be obtained by applying the conventional analytical theory of these methods. Furthermore, the influence of serial resistances on the evaluation of the measured signal is discussed in detail.

The basic aspects of anisotropic material properties, in particular the free carrier mobility, are discussed and their impact on the device performance are demonstrated. The studies show that, depending on polytype and device structure, it can become indispensable to accurately model the anisotropic effects, because they may significantly alter the internal device behavior and the terminal characteristics.

Finally, it is shown that the concept of inverse modeling is applicable to state-of-the-art SiC junction field effect transistors (JFET) by carefully analyzing several device characteristics at various bias conditions and temperatures.

# Chapter 1

# Introduction

The enormous technical progress in the 20th century has been mainly supported by the emergence and continuous development of semiconductor electronics. Silicon (Si) - although only one of a large variety of semiconductor materials - can be taken today as a synonym for this evolution. Its properties and the control of the underlying process technology have finally lead to the integration of complex functionality in electronic chips on microscopic dimensions, resulting in the emergence of today's omnipresent computer and information technology.

Semiconductor electronics is widely dominated by Si at present. The choice of a semiconductor material for a specific application is driven by issues like choosing a material with optimal properties, the complexity of the required process technology, and reliability, all of them eventually determining the costs of a new technology. One approach to respond to the first of these arguments - optimal material properties - is considering the logical sequence of Ge, Si, SiC, and C [1]. However, especially the remaining requirements have prevented any alternative semiconductor materials from entering the commercial market for decades except for high-frequency (GaAs) and optical applications. It turned out that the fabrication of electronic devices using such materials is associated with considerably larger technological difficulties compared to Si. Furthermore, each new semiconductor material has now to compete with a well established Si technology, thus leading only to niche applications of such materials at present. However, any breakthrough in this field would significantly shift the limitations for electronic device specification even far beyond those of the most advanced Si device concepts such as the CoolMOS [2]. Therefore, large efforts in research of wide bandgap materials have been undertaken during the recent decades.

## 1.1 Wide bandgap semiconductor materials

Given a matrix of all semiconductor materials and their properties, the highest and the lowest of these property values will almost always be associated with wide bandgap materials [3]. Generally, a wide bandgap semiconductor is defined as any material exhibiting a bandgap substantially in excess of the bandgaps of materials in general use at present. In Tab. 1.1, some basic mean properties of wide bandgap materials proven to be most relevant are compiled together with those of Si. Based on their generally larger thermal conductivity, dielectric strength, electron saturation velocity, and the bandgap

itself compared to conventional semiconductor materials, they offer great potential especially in the field of high-temperature, high-power, high-frequency, and optical applications.

| | $E_g$ [eV] | $n_i(300\,\mathrm{K})$ [$cm^{-3}$] | $\varepsilon_r$ | $\mu_n$ [$cm^2/Vs$] | $\mu_p$ [$cm^2/Vs$] | $v_{sat}$ $10^7$[cm/s] | $E_{crit}$ [MV/cm] | $\kappa$ [W/cm°C] |
|---|---|---|---|---|---|---|---|---|
| Si | 1.12 | $1.45\cdot10^{10}$ | 11.7 | 1400 | 471 | 1.0 | 0.3 | 1.5 |
| 3C-SiC | 2.20 | 6.9 | 9.72 | 900 | 40 | 2.0 | 1.20 | 4.5 |
| 6H-SiC | 3.00 | $2.3\cdot10^{-6}$ | $9.66^a$ | $400^a$ | $101^a$ | 2.0 | 2.4 | 4.5 |
| 4H-SiC | 3.26 | $8.2\cdot10^{-9}$ | $9.66^a$ | $1000^a$ | $115^a$ | 2.0 | 2.0 | 4.5 |
| GaN | 3.39 | $1.6\cdot10^{-10}$ | 9.00 | 900 | 850 | 2.5 | 3.3 | 1.3 |
| C | 5.45 | $1.6\cdot10^{-27}$ | 5.50 | 1900 | 1600 | 2.7 | 5.6 | 20 |

Table 1.1: Average properties of wide bandgap semiconductors compared to Si at 300 K. Data is adapted from [3,6,10] ($^a$ values perpendicular to the ĉ-axis).

Wide bandgap semiconductors are indispensable for optical emission and detection throughout the visible and into the ultra-violet spectrum. Furthermore, low thermal leakage currents due to the wide bandgap and the corresponding extremely low intrinsic concentration of free carriers can be expected provided that parasitic effects related to non-optimal material quality are not predominant. The maximum device operation temperature is therefore shifted towards much higher values and it is practically no longer limited by the semiconductor material itself but by external influences related to, for instance, contacts and packaging issues. High-temperature applications are primarily driven by the automotive and aerospace industry (mechatronics, smart sensors and actuators), but are also needed for satellites, space exploration, and geothermal wells [4]. The most important material property for high-power applications is the high electric breakdown field as power losses can be reduced or higher breakdown voltages can be achieved [5]. In addition, self-heating due to higher power densities is less critical because of the large thermal conductivity. These findings together with a large electron saturation velocity render wide bandgap materials also well suited for the high-frequency domain.

The benefits of such promising properties can be quantified with respect to high-power and high-frequency applications by figure-of-merits (FOM) which relate the limiting parameters of a certain class of devices to the basic material properties [6, 7, 8, 9, 10, 11]. From Tab. 1.1 and the corresponding FOM [10, 11] it can be concluded that diamond (C) theoretically represents the ideal semiconductor material [12]. However, in addition to such basic properties, many other aspects such as crystal quality, availability of appropriate substrates, good ohmic contacts, and oxide quality have to be considered. Additionally, a release of commercial applications requires low cost process technology facing yield and reliability issues. Grain-boundary free single crystalline diamond films have been grown only on expensive natural diamond and cubic boron nitrides [3] preventing any commercial application. However, remarkable prototypes of electronic applications have been demonstrated including Schottky-diodes [13, 14], MESFETS [15, 16], pn-diodes [17], and bipolar junction transistors [28].

C devices grown on Si substrates usually results in polycrystalline material because of the lattice mismatch which significantly degrades the material properties [29]. Although electronic device operation has been demonstrated with polycrystalline C, any commercial applications seem to be far from real-

ization at present and only some special sensor applications are projected for realization in the near future [30].

GaN within the group of III-nitrides semiconductor materials, despite owing fundamentally superior electronic properties than SiC polytypes, must overcome the lack of a native substrate excluding any vertical high-power devices. The most promising field for applications is therefore the high-frequency and optical domain using lateral GaN device configurations on SiC substrates. Due to its direct band-to-band transition it is superior to SiC for optical applications, and therefore GaN on SiC substrates took over the place of the SiC blue LED. It has been the first commercial mass application currently used as background light in the automobile models "Passat" and "Golf" of the Volkswagen AG [25].

Apart from 4H- and 6H-SiC, there are no other native substrates available for homoepitaxial growth of wide bandgap materials at present [18]. The first commercial application of SiC shortly after its first synthesis in 1891 has been the use as grinding paste because of its excellent hardness [19]. However, it took nearly a century up to the first semiconductor application of SiC: Blue light emitting diodes on 6H-SiC in 1983 [20]. SiC is the only wide bandgap semiconductor owing a native oxide ($SiO_2$) and it is benefiting from the fact that the process technology is rather closely related to Si. The progress of SiC process technology since the first commercial availability of SiC substrates in the early 90s has been excellently expressed by D. Stephani, leader of the Siemens SiC research activities, while presenting a packaged high-power module combining a 4H-SiC pin-diode and a Si IGBT [21] with the words: "*Just five years ago, the wafer had more holes than a sponge and got so drenched with photoresist that it stuck to the spinner chuck.*"

Today, the density of micropipes has been reduced to below $1\,\mathrm{cm}^{-2}$ and a large variety of powerful prototypes of all device categories has been realized confirming the promising properties of SiC [10, 11, 26, 27]. Among those, the focus is currently on 4H-SiC unipolar rectifiers (Schottky-diode [31, 32, 33, 34]) and field effect transistors (JFET [35], MOSFET [36, 180], MESFET [37, 38, 39]). The first bipolar application is expected to be a high-power 4H-SiC PN-diode [41, 42] whereas thyristors [40, 199, 200] and other bipolar device concepts (IGBT, BJT [195]) still suffer from a number of material-related insufficiencies [195]. Although being a normally-on device, the first active device application will probably be a 4H-SiC JFET as the MOS interface is still far away from being technologically controlled [43, 44, 45, 46, 78, 79, 80, 180]. Hence, the major interest of industrial SiC research now moves over to cost, yield, packaging, and reliability issues, and the first release of SiC commercial applications is expected in the very near future [21, 22, 23, 24]. Beside that, a large variety of technological and theoretical aspects are still remaining to be solved for qualifying SiC as alternative to Si on a large scale.

## 1.2 Numerical simulation of SiC devices

A semiconductor device can be modeled on different levels of physical description ranging from microscopic carrier transport including quantum-mechanical effects up to the system level where compact models with a given number of terminals are defined using basic analytical relations and experimental results. "Device simulation" is the commonly used term for a continuous-field description in space and time, where the internal physical quantities - e.g., the carrier densities or the electric potential distribu-

tion - are considered as basic variables from which the static or transient terminal currents and voltages are derived. Device simulation has gained increasing relevance for the design and optimization of electronic semiconductor applications due to the rising design complexity and the cost reduction achieved by reducing the number of experimental batch cycles. Today, multi-dimensional general purpose device simulators are available developed for modeling Si and GaAs devices. State-of-the-art simulation tools provide a coupled electrothermal description of arbitrary device structures ranging from "large" high-power devices down to sub-micron VLSI structures including various physical effects and external influences [47].

As the same general concepts used for modeling conventional semiconductors can be applied to wide bandgap electronic devices, it is possible to adapt such available simulation tools to reflect wide bandgap material properties. First systematic work on material models and parameters for numerical simulation has been published in 1994 [49] and 1997 [113] for 6H- and 4H-SiC, respectively. Quantitative predictions of 4H/6H-SiC device performance have been based on that work reflecting mainly the ideal material properties and neglecting findings such as poor MOS interface properties and excess leakage currents.

An accurate modeling of all relevant physical mechanisms is indispensable for identifying the impact of material properties on basic device characteristics and for device design and optimization. Furthermore, the interpretation of measurement results supported by numerical simulation is presently of particular interest in order to separate characteristics resulting from non-optimal material quality from those resulting from material properties inherent to SiC[1].

## 1.3 Scope of this work

A quantitative comparison of simulated and measured device characteristics requires sufficient material quality with small standard deviations between the data of several samples originating from the same wafer. 4H- and 6H-SiC with such quality have become available since only the recent three years. Therefore, systematic quantitative numerical investigations of various device types are needed in order to evaluate the available physical models and parameters. In contrast to analyzing only some characteristics of general device behavior at a given temperature, such work must include a maximum of information about the device such as, e.g., the temperature-dependent transfer- and output-characteristics of many samples of a JFET with different channel lengths including the subthreshold region, or the forward characteristics of pn-diodes at low, medium, and high injection levels within a wide range of temperature.

Furthermore, severe convergence problems and various numerical artifacts have to be addressed resulting from very low intrinsic carrier densities. For instance, the density of majority and minority carriers in 6H-SiC at room temperature differ by about 30 orders of magnitude and corresponding gradients have to be numerically handled.

Based on the complete source code distribution of a commercial multi-dimensional general purpose device simulator [47] and in cooperation with the SiC research group of the Daimler-Benz AG (now

[1] e.g. identifying the physical mechanism governing a dynamic reduction of the breakdown voltage [52].

DaimlerChrysler AG), Research and Technology, Frankfurt, basic steps towards the aforementioned requirements are the

- review of the theoretical background of electrothermal device simulation with respect to wide bandgap materials (chapter 2) including material property modeling (chapter 3)
- systematic work on material property models and parameters based on previous work [49, 113], the large amount of new data published since that, and own measurements (chapter 3 and 4)
- quantitative evaluation of the resulting model and parameter set with respect to realized devices (chapter 3 - 5)
- identification of additional physical mechanisms not yet covered by the simulation tool (chapter 3 - 5)
- modeling, implementation, and validation of such physical mechanisms (chapter 3 - 5)
- investigation of principal physical mechanisms inherent to SiC (e.g. anisotropy, incomplete ionization) and their impact on device characteristics (chapter 4 and 5)
- quantitative investigation of realized devices (chapter 5)
- predictive simulations based on the validated material models and parameters as basis for device design and optimization (chapter 5).

The organization of this work addresses its possible use as reference for the numerical investigation of SiC devices. Therefore, after presenting the theoretical background in chapter 2, the material models and parameters are collected in chapter 3. The underlying simulation results for validating this data are presented in the following chapters with cross-references included. Additionally, a detailed numerical analysis of thermal admittance spectroscopy and DLTS is given in chapter 4. Finally, the impact of specific material properties on device characteristics based on the implemented extensions of the simulation tool is investigated in chapter 5.

Many of the applied concepts and results with respect to theory and modeling will be closely related to other wide bandgap semiconductor materials as well. They may therefore also serve as reference for the numerical simulation of other wide bandgap materials.

# Chapter 2

# Electrothermal transport model

The choice for an adequate physically-based model level for investigations on electronic devices is driven by the need for a realistic, but yet numerically tractable description of the internal device behavior. Basically, a semiconductor constitutes a many-body problem of quantum-mechanics. A rigorous treatment of such a problem is still not available. However, for pure semiconductors, considerable progress has been made to reduce the many-body interactions to an effective one-particle potential. Using the quantum-mechanical information obtained by such calculations, e.g. the electronic band structure, a semiconductor can be conceived as a many-particle system composed of free carriers, impurities, and the host lattice.

On the microscopic model level, transport processes in such a many-particle system are described by the Boltzmann equation, a balance equation for the number of particles that reside in a volume element of phase space at a given time originally set up for gases [55]. It has to be extended by quantum-mechanical scattering rates in the collision term, the band structure of the semiconductor to compute the group velocity, and the Pauli principle to account for the quantum-mechanical nature of semiconductor physics [56]. However, a direct numerical solution of this complicated equation using methods such as Monte Carlo simulation or the relaxation time approximation is difficult and time-consuming.

From a practical point of view, a small number of macroscopic state variables often proves to be sufficient for modeling the characteristics of realistic devices. To this end, conservation laws for the particle density, the particle flux, and the energy density of the particle are derived from the Boltzmann equation. A brief review of this derivation and the resulting macroscopic models is given in [56, 112].

Alternatively, Wachutka derived a framework of phenomenological transport theory [62, 63, 64] by applying the principles of irreversible thermodynamics [58, 59] to the many-particle system. Within this framework, the consistent formulation of carrier and heat transport including those physical mechanisms which are particularly relevant in wide bandgap semiconductors is guaranteed. This formulation is consistent with the corresponding model equations derived from the Boltzmann equation. A brief overview of its basic ideas and assumptions is given in section 2.1. Subsequently, special emphasis is paid to the modeling of impurities and anisotropic material properties in section 2.2 and 2.3, respectively, which have been implemented in a multi-dimensional general-purpose device simulation tool [47] in order to accurately modeling 4H/6H-SiC electronic devices. Finally, we discuss several aspects of the resulting set of basic model equations which can be identified as an extended electrothermal

drift-diffusion model on the basis of phenomenological thermodynamics.

## 2.1 Transport theory based on phenomenological irreversible thermodynamics

Macroscopic measurements sense only statistical averages of the microscopic states which are defined by their atomic coordinates and momenta $(q_i, p_i)$ with $1 \leq i \leq 3N$ where $N$ denotes the number of particles in the system. The macroscopic state is characterized by a distribution function $f(q_i, p_i, t)$ on the 6 N-dimensional phase space. Macroscopic quantities are obtained by means of a statistical average of the microscopic states over the phase space. Let $X(t)$ be a generic time-dependent macroscopic observable, every microscopic state $(q_i, p_i)$ will contribute with its microscopic value $x(q_i, p_i)$ and the statistical weight $f(q_i, p_i, t)$ [48]:

$$X(t) = \int x(q_i, p_i)\, f(q_i, p_i, t)\, d\overset{3N}{q}\, d\overset{3N}{p}. \tag{2.1}$$

The statistical definition of the second law of thermodynamics states that an energetically isolated system is said to be in thermodynamic equilibrium, if it is found with equal probability in each one of its accessible microscopic states [65]. Hence, a macroscopic state can be uniquely characterized by a certain set of macroscopic variables $(N, V, U, S, ...)$ which are statistically defined by

$$\text{particle number}\, N = \int f(q_i, p_i, t)\, d\overset{3N}{q}\, d\overset{3N}{p} \tag{2.2}$$

$$\text{volume}\, V = \int d\overset{3N}{q} \tag{2.3}$$

$$\text{total energy}\, U = \int E(q_i, p_i)\, f(q_i, p_i, t)\, d\overset{3N}{q}\, d\overset{3N}{p} \tag{2.4}$$

$$\text{entropy}\, S = -k \int f(q_i, p_i, t)\, ln(f(q_i, p_i, t))\, d\overset{3N}{q}\, d\overset{3N}{p}\,. \tag{2.5}$$

### 2.1.1 Local thermal equilibrium and fundamental Gibbs relations

A device structure can be partitioned in small volume elements, called cells, each of which considered as a small thermodynamic subsystem. Even if the device structure as a whole is driven far away from global thermodynamic equilibrium, each of the cells is supposed to be locally in equilibrium. That means, at a fixed position $\vec{r}$ and time $t$, any accessible state of the full structure can be uniquely characterized by local thermodynamic equilibrium variables and transport can be modeled as relaxation processes between these cells. By defining a composite thermodynamic system in each of the cells which comprises several simple subsystems, interactions between the free carriers, the semiconductor lattice, and impurities such as donors, acceptors, and deep traps are included (Fig. 2.1).

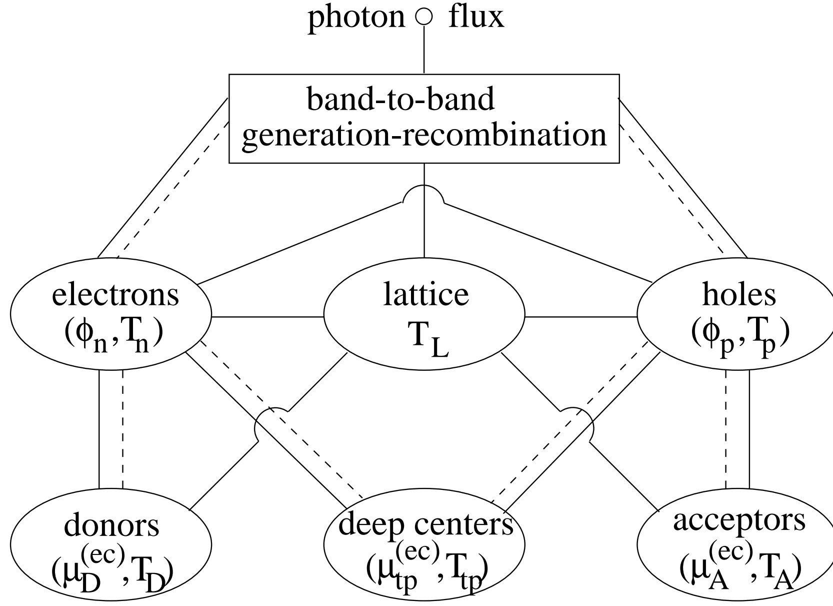


Figure 2.1: Composite thermodynamic system comprising host lattice, electron gas, hole gas, donors, acceptors, and a sequence of deep centers as subsystems. Solid lines denote energy exchange, dashed lines denote particle exchange between the respective thermodynamic subsystems [73].

Applying the first law of thermodynamics, we obtain fundamental Gibbs relations

$$\begin{aligned} du_n &= T\, ds_n + \mu_n^{(c)}\, dn \\ du_p &= T\, ds_p - \mu_p^{(c)}\, dp \\ du_L &= T\, ds_L \\ du_{tp} &= T\, ds_{tp} - \left(z^{occ} - z^{emp}\right)\left(\mu_{tp_{occ}}^{(c)} - \mu_{tp_{emp}}^{(c)}\right) dN_{tp}^{occ} \\ du_{el} &= \vec{E}\, d\vec{D} \end{aligned} \tag{2.6}$$

for these subsystems. Here, the local set of state variables have been chosen as the lattice temperature $T = T_\nu = T_{tp} = T_L$ which is assumed to equal the temperature of free carriers for simplicity[1], the chemical potentials $\mu_\nu^{(c)}$ of electrons and holes, the chemical potential $\mu_{tp}^{(c)}$ of each impurity $tp \in \{\text{traps}\}$, and the electric potential $\Psi$ which is defined by

$$\vec{E} = -\vec{\nabla}\Psi, \tag{2.7}$$

describing the electrostatic energy density $u_{el}$ distributed over all subsystems. The volume $V$ is eliminated by normalization to the unit volume. From Poisson's equation

$$\vec{\nabla}\left(\tilde{\varepsilon}\vec{\nabla}\Psi\right) = -\rho, \tag{2.8}$$

we conclude that $\Psi$ is not an independent thermodynamic state variable, but a functional of $(n, p, N_{tp})$. Thus we can eliminate the electrical degrees of freedom by replacing the chemical potentials $\mu_\nu^{(c)}$ and

[1]please refer to [62, 63, 64, 73] for the complete model.

$\mu_{tp}^{(c)}$ by there corresponding electrochemical potentials:

$$\mu_n^{(ec)} := \mu_n^{(c)} - q\Psi \tag{2.9}$$
$$\mu_p^{(ec)} := \mu_p^{(c)} - q\Psi \tag{2.10}$$
$$\mu_{tp}^{(ec)} := \mu_{tp_{occ}}^{(c)} - \mu_{tp_{emp}}^{(c)} - q\Psi\,. \tag{2.11}$$

The gradient of the electrochemical potential of free carriers

$$\vec{\nabla}\mu_\nu^{(ec)} = \vec{\nabla}\mu_\nu^{(c)} - \vec{\nabla}\Psi \tag{2.12}$$

can be intuitively interpreted as the driving force for carrier flow in a non-uniformly doped semiconductor. Hence the diffusion current resulting from a gradient of the chemical potential (Fick's diffusion law) is balanced by the repulsive electric field caused by the separation of electric charges (Ohm's law) in thermodynamic equilibrium. In electrical engineering it is convenient to measure $\mu_\nu^{(ec)}$ in units of a voltage

$$\mu_\nu{}^{(ec)} =: -q\Phi_\nu =: \mu_{\nu_0}^{(ec)} - q\phi_\nu\,, \tag{2.13}$$

where $\Phi_\nu$ denotes the so-called quasi-Fermi levels and $\phi_\nu$ are the quasi-Fermi potentials which refer to the intrinsic Fermi level as energy reference point (Fig. 2.2). We finally end up with a reduced set of fundamental Gibbs relations

$$\begin{aligned} du_n' &= T\,ds_n - q\Phi_n\,dn \\ du_p' &= T\,ds_p + q\Phi_p\,dp \\ du_L &= T\,ds_L \\ du_{tp}' &= T\,ds_{tp} - (z^{occ} - z^{emp})\,\mu_{tp}^{(ec)}\,dN_{tp}^{occc} \end{aligned} \tag{2.14}$$

without loosing any information about the complete system.

### 2.1.2 Gibbs-, Fermi-, and Boltzmann distributions

Considering the band structure originating from the quantum-mechanical nature of the material, the macroscopic state variables $X \in \left(n, p, N_{tp}^{occ}\right)$ which are the density of occupied states in the conduction band (electrons), in the valence band (holes), and the density of occupied centers of a given impurity species within the bandgap ($N_{tp}^{occ}$), respectively, are defined by

$$X = \int N(E,T)\,f(E,T)\,dE\,, \tag{2.15}$$

where $f(E,T)$ denotes the occupation probability of the individual states which are described by the respective density of states, $N(E,T)$, of the individual subsystems. In the case of holes, the density of empty states $(1-f)$ has to be substituted for $f$. Considering statistical physics, the occupation probability for an energy state with half integer spin is determined by the Fermi-Dirac distribution:

$$f(E,T) = \frac{1}{1+\exp\left[\frac{E-E_F}{kT}\right]}\,. \tag{2.16}$$

The Fermi energy $E_F$ can be interpreted as the energy of the quantum state with the occupation probability $f = 1/2$. It is identified by thermodynamic considerations as the electrochemical potential of the corresponding subsystem:

$$\mu^{(ec)}_{\nu,tp} = E_{F_{\nu,tp}} . \tag{2.17}$$

Hence, Eqs. (2.12) and (2.13) can be rewritten with Eq. (2.17) in the notation typically used in electrical engineering which will also be used in the following.

#### 2.1.2.1 Free carrier densities

In order to derive the density of free carriers, the integral in Eq. (2.15) is evaluated in the case of electrons to be

$$n(E_{F_n}, T) = N_C(T)\,\mathrm{F}_{1/2}\left[(E_{F_n} - E_C)/kT\right] , \tag{2.18}$$

where $N_C(T)$ is the effective density of states in the conduction band and $\mathrm{F}_{1/2}$ denotes the Fermi integral. Provided that $E_{F_n}$ is several $kT$ below $E_C$ in non-degenerate semiconductors, Eq. (2.16) can be approximated by the Boltzmann distribution obtaining

$$n = N_C(T)\exp\left[\frac{E_{F_n} - E_C}{kT}\right] . \tag{2.19}$$

In device simulation, the intrinsic density of free carriers

$$n_i(T) = N_C(T)\exp\left[\frac{E_i - E_C}{kT}\right] \tag{2.20}$$

is generally used as reference point defining the intrinsic Fermi energy $E_i$ which follows the electrostatic potential $\Psi$ in non-uniform semiconductors:

$$E_i = E_{i_0} - q\Psi . \tag{2.21}$$

Using Eqs. (2.21), (2.20), (2.17), and (2.13), we can rewrite Eq. (2.19) as

$$n = n_i(T)\exp\left(\frac{q(\Psi - \phi_n)}{kT}\right) \tag{2.22}$$

and similarly for holes

$$p = n_i(T)\exp\left(\frac{q(\phi_p - \Psi)}{kT}\right) . \tag{2.23}$$

In Fig. 2.2, the energy band diagram and the corresponding potential distribution of a reverse biased pn-junction are shown. Here, a negative potential has been applied to the anode whereas the cathode has been grounded. The quasi-Fermi potentials of electrons and holes equal to the applied potentials whereas the electric potential is shifted by the corresponding built-in potential, Eq. (2.93), at both contacts as outlined in section 2.5. The shape of the band edges follows the electric potential distribution with the quasi-Fermi levels given by Eq. (2.13). Considering Eqs. (2.22) and (2.23) and comparing

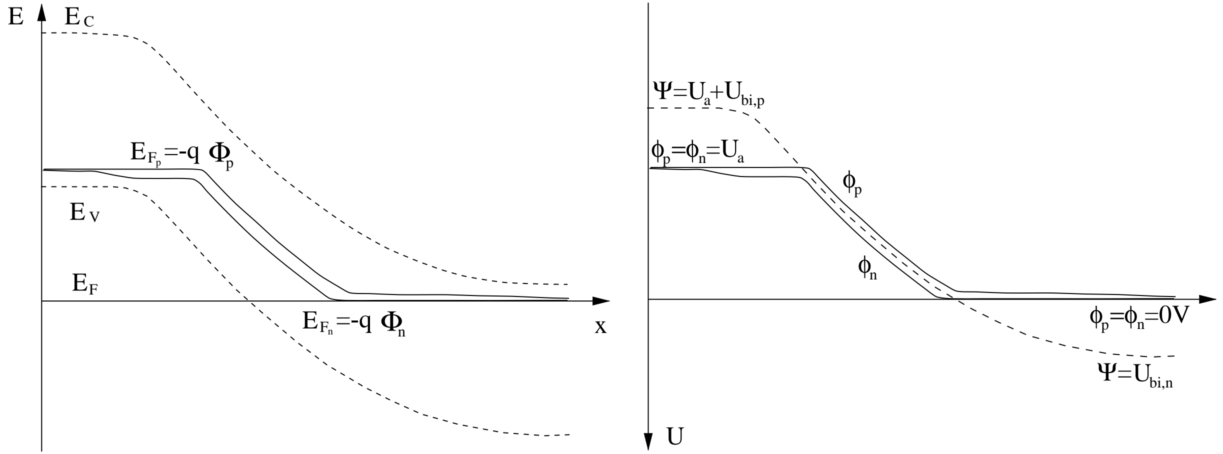


Figure 2.2: Energy band diagram (left) of a reverse biased pn-junction and the corresponding potential distribution (right) across the pn-junction.

Figs. 2.2 and 5.3, the relation between the free carrier densities and the quasi-Fermi potentials becomes evident.

Deviations from the carrier densities in thermodynamic equilibrium are given by the difference between the corresponding quasi-Fermi potentials:

$$n\,p = n_i^2 \exp\left(\frac{q\,(\phi_p - \phi_n)}{kT}\right) . \tag{2.24}$$

#### 2.1.2.2 Impurities

In the case of a discrete impurity level, we obtain from Eq. (2.15)

$$N_{tp}^{occ} = N_{tp}\, f_{tp}\,(E_{tp}) . \tag{2.25}$$

Generally, the number of final states available depends on the direction of a carrier transition. For instance, in the case of donors, there are two possible quantum states available for capturing an electron by an ionized (empty) donor and only one possible quantum state for each energy level within the conduction band available for emitting an electron from a neutral (occupied) donor. Using Eq. (2.16) for the ratio between occupied and empty impurity states

$$\frac{N_{tp}^{occ}}{N_{tp}^{emp}} = \frac{f_{tp}}{1-f_{tp}} = \frac{g_{tp}^{occ}}{g_{tp}^{emp}} \exp\left[\frac{E_{tp} - E_{F_{tp}}}{kT}\right] \tag{2.26}$$

with the number of quantum states $g_{tp}^{occ}$ and $g_{tp}^{emp}$ available for the capture and emission, respectively, we can define the degeneracy factor

$$g_{tp} = \frac{g_{tp}^{occ}}{g_{tp}^{emp}} \tag{2.27}$$

which is 0.5 in this case. Generalizing this concept, $f_{tp}$ is given by a Gibbs distribution [150]

$$f_{tp} = \frac{1}{1 + g_{tp} \exp\left[\frac{E_{tp} - E_{F_{tp}}}{kT}\right]} \tag{2.28}$$

controlled by the energetic difference between $E_{F_{tp}}$ and the energy level $E_{tp}$ of the impurity states. Energy-distributed traps are modeled by

$$N_{tp}^{occ} = \int_{E_V}^{E_C} \gamma_{tp}(E) P_{tp}(E) dE\,, \tag{2.29}$$

where $\gamma_{tp}(E)$ is the density of states per unit volume and energy and $P_{tp}(E)$ denotes the occupation probability for this state [151, 152, 153].

### 2.1.3 Balance equations and constitutive current relations

A balance equation can be formulated for each density of an extensive state variable in Eq. (2.14) with the generic structure

$$\frac{\partial x}{\partial t} + \mathrm{div}\vec{J}_x = \Pi_x \tag{2.30}$$

which include various source and sink terms for all the possible generation and loss processes by a production rate $\Pi_x$. The change of $x$ with time can arise from the local production rate $\Pi_x$ and the divergence of the current density div$\vec{J}_x$. From Eq. (2.30) we obtain in our case balance equations for the free carrier densities $\nu$, the density of involved impurity levels $N_{tp}$, the density of the total internal energy, and the density of the entropy,

$$\frac{\partial n}{\partial t} - \frac{1}{q}\vec{\nabla}\vec{J}_n = \Pi_n \tag{2.31}$$

$$\frac{\partial p}{\partial t} + \frac{1}{q}\vec{\nabla}\vec{J}_p = \Pi_p \tag{2.32}$$

$$\frac{\partial N_{tp}^{occ}}{\partial t} = \Pi_{tp} \tag{2.33}$$

$$\frac{\partial u_{tot}}{\partial t} + \vec{\nabla}\vec{J}_{u,tot} = 0 \tag{2.34}$$

$$\frac{\partial s_{tot}}{\partial t} + \vec{\nabla}\vec{J}_{s,tot} = \Pi_{s,tot}\,, \tag{2.35}$$

where $\Pi_{tp}$ is the production rate referring to the involved impurities (see section 2.2). The total internal energy density $u_{tot}$ and the total entropy density $s_{tot}$ are obtained by the sum of the corresponding quantities in all subsystems. The electrical current densities $\vec{J}_\nu$ in Eqs. (2.31) and (2.32) have been substituted for the particle current densities $\vec{j}_\nu$:

$$\vec{J}_n =: -q\,\vec{j}_n \;\; ; \;\; \vec{J}_p =: q\,\vec{j}_p\,. \tag{2.36}$$

From the balance equations, Eqs. (2.31) - (2.35), and the fundamental Gibbs relations, Eq. (2.14), we can deduce the total entropy production rate to be

$$\Pi_{s,tot} = -\vec{J}_n \vec{\nabla}\left(\frac{\Phi_n}{T}\right) - \vec{J}_p \vec{\nabla}\left(\frac{\Phi_p}{T}\right) + \vec{J}_{u,tot} \vec{\nabla}\left(\frac{1}{T}\right) + \frac{q}{T}(G-R)(\Phi_n - \Phi_p) . \tag{2.37}$$

Hence, an irreversible process is characterized by non-zero forces ("affinities") $\vec{\nabla}F_\alpha$ with $F_n = \Phi_n/T$, $F_p = \Phi_p/T$, and $F_u = 1/T$, taking the system towards the equilibrium state. The response of the system to this force are fluxes $\vec{J}_n$, $\vec{J}_p$, and $\vec{J}_{u,tot}$ which can be linearized in a vicinity of thermodynamic equilibrium by

$$\vec{J}_\alpha = \sum_\beta \tilde{L}_{\alpha\beta} \vec{\nabla} F_\beta + O\left(F_\beta\right) \tag{2.38}$$

with $O\left(F_\beta\right)$ being the higher order terms. In matrix notation, Eq. (2.38) is rewritten as

$$\begin{pmatrix} \vec{J}_n \\ \vec{J}_p \\ \vec{J}_{u,tot} \end{pmatrix} = \begin{pmatrix} \tilde{L}_{nn} & \tilde{L}_{np} & \tilde{L}_{nu} \\ \tilde{L}_{pn} & \tilde{L}_{pp} & \tilde{L}_{pu} \\ \tilde{L}_{un} & \tilde{L}_{up} & \tilde{L}_{uu} \end{pmatrix} \begin{pmatrix} -\vec{\nabla}\frac{\Phi_n}{T} \\ -\vec{\nabla}\frac{\Phi_p}{T} \\ \vec{\nabla}\frac{1}{T} \end{pmatrix} . \tag{2.39}$$

This expression is called the "constitutive current relations" with the matrix of linear transport coefficients, $\tilde{L}_{\alpha\beta}$. Stating Onsager's theorem [58, 59], it contains six independent matrix components which can be identified, after a linear transformation to the generally used gradients $-\vec{\nabla}\Phi_n$, $-\vec{\nabla}\Phi_p$, and $-\vec{\nabla}T$ (see section 2.4), as

$$\tilde{\sigma}_n > 0\,,\ \tilde{\sigma}_p > 0\,,\ \tilde{\sigma}_{np} = \tilde{\sigma}_{pn}\,,\ \tilde{\kappa} > 0\,,\ \tilde{P}_n > 0\,,\ \tilde{P}_p > 0\,. \tag{2.40}$$

Each of these coefficients which are the thermal conductivity tensor $\tilde{\kappa}$, the tensor of electric conductivity $\tilde{\sigma}_\nu$, and the tensor of thermoelectric power $\tilde{P}_\nu$ of electrons and holes, respectively, contains at most six independent components. $\tilde{\sigma}_{np} = \tilde{\sigma}_{pn}$ is a contribution to the electrical conductivity due to carrier-carrier scattering which can be neglected in many practical cases. The number of independent components is additionally reduced due to crystal symmetry in hexagonal polytypes (see section 2.3). Nonlinear current transport is included within this concept by linear transport coefficients dependent of the state variables (see chapter 3).

## 2.2 Carrier emission and capture kinetics

The balance equations, Eqs. (2.31) - (2.35), for the thermodynamic subsystems can be divided into those including and excluding fluxes. Particle and energy flow have been modeled by corresponding constitutive current equations. In this section, we want to focus on the carrier production rates defined in (2.31) - (2.33) which are strongly related to the impurity subsystems defined for each relevant impurity level $tp \in \{\text{traps}\}$ in the material. Let $N_{tp}^{occ}$ be the density of an impurity with a discrete energy level in the bandgap occupied by an electron. The corresponding balance equation, Eq. (2.33), reads

$$\frac{\partial N_{tp}^{occ}}{\partial t} = c_n^{tp} n N_{tp}^{emp} - e_n^{tp} N_{tp}^{occ} - c_p^{tp} p N_{tp}^{occ} + e_p^{tp} N_{tp}^{emp} \tag{2.41}$$

with

$$N_{tp}^{emp} = N_{tp} - N_{tp}^{occc}. \tag{2.42}$$

The reaction process between electrons, holes, and impurities is modeled by corresponding emission rates $e_{\nu}^{tp}$ and capture rates $c_{\nu}^{tp}$ of the free carriers which have to be multiplied with the concentrations of the involved reaction partners (Fig. 2.3). The right hand side of Eq. (2.41) which corresponds to $\Pi_{tp}$ in Eq. (2.33) yields an electron and a hole production rate:

$$\left(\frac{\partial n}{\partial t}\right)_{tp} = e_n^{tp} N_{tp}^{occ} - c_n^{tp} n N_{tp}^{emp} \tag{2.43}$$

$$\left(\frac{\partial p}{\partial t}\right)_{tp} = e_p^{tp} N_{tp}^{emp} - c_p^{tp} p N_{tp}^{occ}. \tag{2.44}$$

Hence, in a very general way, the production rates for electrons and holes which enter the free carrier balance equations, Eqs. (2.31) and (2.32), can be divided up in a contribution due to impurities and the contribution of all other carrier production rates $(G-R)$ such as band-to-band processes (Fig. 2.1):

$$\Pi_n = \left(\frac{\partial n}{\partial t}\right)_{tp} + (G-R) \tag{2.45}$$

$$\Pi_p = \left(\frac{\partial p}{\partial t}\right)_{tp} + (G-R). \tag{2.46}$$

### 2.2.1 Quasi-static approximation

Using the occupation probability $f_{tp}$ defined by Eq. (2.25) as an independent state variable, Eq. (2.41) can be rewritten as

$$\frac{\partial f_{tp}}{\partial t} = -\left(e_n^{tp} + e_p^{tp} + c_n^{tp} n + c_p^{tp} p\right) f_{tp} + e_p^{tp} + c_n^{tp} n. \tag{2.47}$$

For fixed (or very slowly varying) carrier concentrations n and p, the solution of Eq. (2.47) with respect to the steady state occupation probability $f_{tp}^{(0)}$ is

$$f_{tp} = f_{tp}^{(0)} + \left(f_{tp} - f_{tp}^{(0)}\right) \exp[-t/\tau_{tp}] \tag{2.48}$$

with

$$\tau_{tp} = \frac{1}{e_n^{tp} + e_p^{tp} + c_n^{tp} n + c_p^{tp} p} \tag{2.49}$$

dependent of the state variables $(n, p, T)$. It can be interpreted as a momentary time constant reflecting the response of the impurity state to a step-like change in the operating conditions. If $\tau_{tp}$ is short compared to the change of an external excitation, governed by a time constant $\tau_{ext}$,

$$\tau_{tp} \ll \tau_{ext}, \tag{2.50}$$

$f_{tp}$ can be assumed to follow instantaneously the corresponding change of the remaining state variables ("quasi-static approximation"). Therefore, it is determined by the stationary condition

$$\frac{\partial f_{tp}}{\partial t} = 0. \tag{2.51}$$

By combining Eqs. (2.51) and (2.47), we obtain an explicit relation

$$f_{tp}^{(0)} = f_{tp}^{(0)}(n,p,T) = \frac{e_p^{tp} + c_n^{tp} n}{e_n^{tp} + e_p^{tp} + c_n^{tp} n + c_p^{tp} p} . \tag{2.52}$$

Hence, the stationary trap occupation probability $f_{tp}^{(0)}$ is no longer an independent state variable and the balance equation, Eq. (2.47), of the impurity level is eliminated.

### 2.2.2 Carrier emission and capture coefficients

With Eq. (2.41) we have introduced four parameters for each relevant impurity level. However, by considering the case of thermodynamic equilibrium, the number of independent parameters can be reduced. In thermodynamic equilibrium, the electron production rate of the impurity level vanishes and Eq. (2.43) together with Eqs. (2.25), (2.28) and (2.19) yields

$$n_1^{tp} := \frac{e_n^{tp}}{c_n^{tp}} = g_{tp} N_C \exp\left[\frac{E_{tp} - E_C}{kT}\right] . \tag{2.53}$$

The electrochemical potentials (or quasi-Fermi energies) $\mu_\nu^{(ec)}$ and $\mu_{tp}^{(ec)}$ of all subsystems equal to one common Fermi energy $E_F$ in thermodynamic equilibrium. The ratio of the emission and capture coefficients in electrothermal equilibrium is thus determined by the ionization energy $E_{tp} - E_C$ of the energy level and is independent of any state variable. The quantity $n_1$ can be interpreted as the free electron density which would be available in the conduction band if $E_F$ equals the energy level $E_{tp}$ of the impurity. A corresponding equation is obtained for the ratio of emission and capture coefficients of holes:

$$p_1^{tp} := \frac{e_p^{tp}}{c_p^{tp}} = g_{tp}^{-1} N_V \exp\left[\frac{E_V - E_{tp}}{kT}\right] . \tag{2.54}$$

By introducing capture cross sections for electrons and holes

$$c_\nu^{tp} = \sigma_\nu^{tp}(T)\, v_{\nu_{th}} , \tag{2.55}$$

with the thermal velocity $v_{\nu_{th}}$ of electrons and holes

$$v_{\nu_{th}} = \sqrt{\frac{3kT}{m_\nu^*}} \tag{2.56}$$

we assume the capture and emission coefficients to be independent from any other state variable except $T$. Several models for the capture process are discussed in literature such as a cascade capture model resulting in a temperature dependence of $\sigma_\nu^{tp} = \sigma_{\nu_o}^{tp} T^{-2}$ [60], as well as a multi-phonon process resulting in a $\sigma_\nu^{tp}$ which is approximately independent of temperature [61]. We finally obtain with Eqs. (2.53) and (2.54)

$$e_n^{tp} := \sigma_n^{tp}(T)\, v_{n_{th}}\, g_{tp} N_C \exp\left[\frac{E_{tp} - E_C}{kT}\right] \tag{2.57}$$

$$e_p^{tp} := \sigma_p^{tp}(T)\, v_{p_{th}} \frac{1}{g_{tp}} N_V \exp\left[\frac{E_V - E_{tp}}{kT}\right] . \tag{2.58}$$

Therefore, three independent parameters $\sigma_n^{tp}$, $\sigma_p^{tp}$, and $E_{tp}$ are needed in order to model the carrier emission and capture kinetics of a discrete impurity level. It is assumed that Eqs. (2.57) and (2.58) keep valid under arbitrary stationary or non-stationary non-equilibrium conditions. Nonlinear corrections, e.g. resulting from the high-field band bending due to the Poole-Frenkle effect [101], have to be modeled by additional dependencies of these parameters on the state variables.

### 2.2.3 Classification of impurities

Classifying the character of an impurity level by means of the emission and capture rates entering Eq. (2.41), we distinguish generation-recombination centers, electron/hole traps, and donors/acceptors as shown in Fig. 2.3:

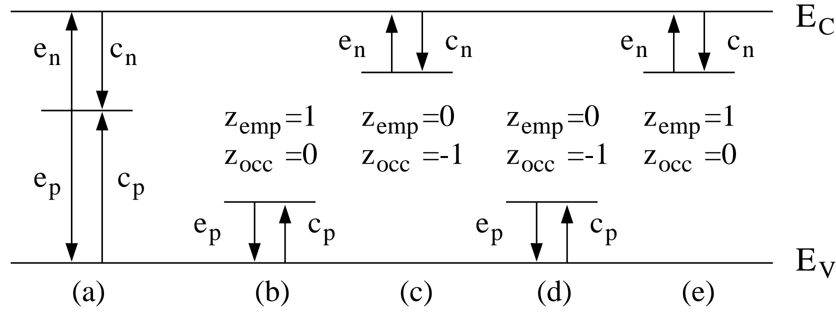


Figure 2.3: Energy diagram of different types of impurities: Generation-recombination centers (a), hole (b) and electron (c) traps, acceptors (d), and donors (e).

#### 2.2.3.1 Generation-recombination centers

Impurities with transition probabilities of the same order of magnitude to both, the conduction and the valence band, have usually energy levels in proximity of the mid gap. They generally act as recombination or generation centers with

$$\text{recombination center} \quad : \quad c_n^{tp}\, n \gg e_p^{tp} \;\wedge\; c_p^{tp}\, p \gg e_n^{tp} \tag{2.59}$$

$$\text{generation center} \quad : \quad c_n^{tp}\, n \ll e_p^{tp} \;\wedge\; c_p^{tp}\, p \ll e_n^{tp} \tag{2.60}$$

depending on the state variables $n$ and $p$. If $np \ll n_i^2$ ("depletion"), electrons from the valence band are trapped by the center[2] and subsequently emitted to the conduction band. Otherwise, electrons are captured from the conduction band and subsequently emitted to the valence band. By substituting

$$\tau_\nu^{tp} = \frac{1}{c_\nu^{tp} N_{tp}} \tag{2.61}$$

where $\tau_\nu^{tp}$ can be identified as the minority carrier lifetime at weak injection [154], the well known Shockley-Read-Hall generation rate [156, 157] is obtained from Eqs. (2.25), (2.52), (2.53), and (2.54)

[2] which corresponds to the emission of holes from the center to the valence band

at steady state:

$$(G-R)_{SRH}^{tp} = \frac{n_i^2 - np}{\tau_p^{tp}\left(n+n_1^{tp}\right)+\tau_n^{tp}\left(p+p_1^{tp}\right)}. \tag{2.62}$$

The net generation rate vanishes at electrothermal equilibrium and will be negative ("recombination") in the case of carrier injection $np \gg n_i^2$. The steady state non-equilibrium condition is generally characterized by a separation of the quasi-Fermi energies $E_{F_\nu}$ of electrons and holes, respectively. The quasi-Fermi energy of the impurity level as determined by Eq. (2.28) takes a value somewhere between these energies. The free carrier production rates of the impurity level, Eqs. (2.43) and (2.44), equal to $(G-R)_{SRH}^{tp}$.

#### 2.2.3.2 Dopants and deep traps

From Eqs. (2.57) and (2.58) an exponential increase of the corresponding emission coefficient is expected if the impurity level approaches one of the energy bands. The coupling to the corresponding energy band becomes dominant and the character of the impurity level changes to an electron or hole trap:

$$\text{electron trap} \;:\; c_n^{tp}\, n \gg e_p^{tp} \;\wedge\; c_p^{tp}\, p \ll e_n^{tp} \tag{2.63}$$

$$\text{hole trap} \;:\; c_n^{tp}\, n \ll e_p^{tp} \;\wedge\; c_p^{tp}\, p \gg e_n^{tp} \tag{2.64}$$

Usually the coupling of such "deep" traps to one of the bands can be neglected and only two independent parameters are needed to model the impurity level. However, there might exist impurities with a strongly unsymmetric coupling to both bands resulting in a characteristic somehow between a deep trap and a recombination-generation center.

Considering the physical nature of a hole trap ($e_n^{tp} = c_n^{tp} = 0$), we distinguish centers which accept electrons ("acceptor") and centers which yield electrons (this is the actual meaning of "hole trap"). In consequence, the charge number for the occupied state $z_{occ}^{tp}$ and the empty state $z_{emp}^{tp}$ are

$$\text{hole trap} \;:\; z_{occ}^{tp} = 0, \quad z_{emp}^{tp} = +1 \tag{2.65}$$

$$\text{acceptor} \;:\; z_{occ}^{tp} = -1, \; z_{emp}^{tp} = 0 \tag{2.66}$$

and similarly

$$\text{electron trap} \;:\; z_{occ}^{tp} = -1, \; z_{emp}^{tp} = 0 \tag{2.67}$$

$$\text{donor} \;:\; z_{occ}^{tp} = 0, \quad z_{emp}^{tp} = +1\,. \tag{2.68}$$

An electron/hole trap is also called an acceptor-like/donor-like trap in correspondence to the charge state of the occupied impurity level, respectively[3]. With a negligible coupling to one of the energy bands, only two independent parameters are needed to describe the impurity kinetics simplifying Eq. (2.41) and obtaining a contribution to the free carrier production rate in only one of the free carrier balance equations, Eqs. (2.45) or (2.46).

[3] In the literature, the term "acceptor-like/donor-like" trap is sometimes ambiguously used for a trap coupled only to the valence/conduction band, respectively.

If $e_\nu^{tp}$ is sufficiently large, the corresponding relaxation time $\tau_{tp}$ can be neglected and the quasi-static approximation can be applied. Because of the coupling to only one of the carrier subsystems, $E_{F_{tp}}$ equal to the corresponding $E_{F_\nu}$ and Eq. (2.28) is applicable. Using Eqs. (2.13), (2.25), and (2.28) the ionization degree of an acceptor is obtained by

$$N_A^- = \frac{N_A}{1 + g_A \exp\left[\frac{E_A - q\Phi_p}{kT}\right]} . \tag{2.69}$$

Unlike an acceptor, a donor is ionized after the emission of an electron. Thus, its ionization degree is obtained from Eq. (2.28) by $(1 - f_D)\, N_D$:

$$N_D^+ = \frac{N_D}{1 + g_D \exp\left[\frac{q\Phi_n - E_D}{kT}\right]} . \tag{2.70}$$

Here, the usually applied definition

$$g_D = g_{tp}^{-1} \tag{2.71}$$

for the degeneracy factor of donors is applied [154]. Using Eqs. (2.69) and (2.70) the quasi-static contribution of the dopants to the corresponding free carrier production rates, Eqs. (2.45) or (2.46), is obtained by the so-called "quasi-static derivative"

$$\frac{\partial f_{tp}}{\partial t} = \frac{\partial f_{tp}}{\partial \nu}\frac{\partial \nu}{\partial t} + \frac{\partial f_{tp}}{\partial T}\frac{\partial T}{\partial t} . \tag{2.72}$$

Similar considerations yield the occupation probabilities of deep traps.

The aforementioned considerations are valid for discrete single impurity levels within the bandgap. However, there may be physical reasons for a coupling of two discrete impurity levels or for groups of non-localized electron states which are distributed in energy within the bandgap [153]. The impurity kinetics presented in this chapter can be easily extended to such cases. Two coupled impurity levels are modeled by two balance equations, Eqs. (2.41), applying additionally coupling coefficients $e_{12}$ and $c_{12}$ (see Fig. 2.3 and appendix C). In case of distributed impurity levels, an integral form of the balance equation is obtained [151]. Furthermore, the same concept can be applied to model the surface charge at MOS interfaces resulting from the occupation of distributed traps within the oxid.

## 2.3 Generic model for anisotropic material properties

The hexagonal modifications of SiC comprise anisotropic material properties which require a tensorial formulation of all basic equations except for the impurity balance equations.

Basically, a tensor of rank two as defined in Eq. (2.40) has nine components. However, by investigating the crystal symmetry it is possible to identify the number of independent non-vanishing components of these tensors in bulk material with zero magnetic field. A tensor quantity, e.g. the conductivity tensor $\tilde{\sigma}_\nu$, will not be changed by a symmetry operation represented by an orthogonal matrix $\tilde{S}$:

$$\tilde{\sigma}_\nu = \tilde{S}\,\tilde{\sigma}_\nu\,\tilde{S}^T . \tag{2.73}$$

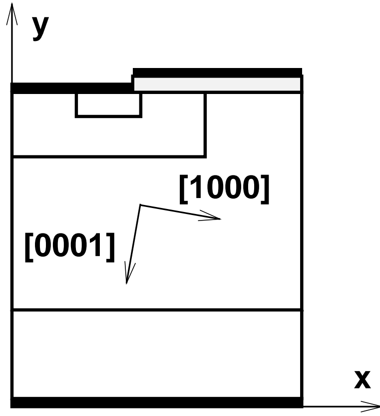


Figure 2.4: Relation between the crystallographic axes of the semiconductor lattice and the coordinate system of a device (DMOS).

The crystal structure of α-SiC defines a plane of physically equivalent directions and a distinguished direction orthogonal to this plane, the so-called ĉ-axis (Fig. 3.1). By applying Eq. (2.73) to all symmetry operations of the crystal, we obtain two independent components describing the conductivity parallel and orthogonal to the ĉ-axis for a coordinate system which coincides with the crystallographic axes of the semiconductor lattice:

$$\tilde{\sigma}_\nu = \begin{pmatrix} \sigma_{\nu_\perp} & 0 & 0 \\ 0 & \sigma_{\nu_\parallel} & 0 \\ 0 & 0 & \sigma_{\nu_\perp} \end{pmatrix}. \tag{2.74}$$

The isotropic current relations available in drift-diffusion simulation tools [47] have therefore to be extended to a tensor formulation. Using Eq. (2.74), the constitutive current relations, Eqs. (2.78), can be rewritten as

$$\vec{J}_\nu = \sigma_{\nu_\perp} \left(\tilde{1} + \Delta\tilde{\sigma}_\nu\right) \vec{\nabla}\phi_\nu = \left(\tilde{1} + \Delta\tilde{\sigma}_\nu\right) \vec{J}_\nu^{iso} \tag{2.75}$$

in the isothermal case with

$$\Delta\tilde{\sigma}_\nu = \begin{pmatrix} 0 & 0 & 0 \\ 0 & \frac{\sigma_{\nu_\parallel}}{\sigma_{\nu_\perp}} - 1 & 0 \\ 0 & 0 & 0 \end{pmatrix}. \tag{2.76}$$

The anisotropic current density $\vec{J}_\nu$ is obtained by a matrix multiplication from the original isotropic current density $\vec{J}_\nu^{iso}$ which is defined as the component perpendicular to the ĉ-axis. Eq. (2.75) can be discretized using the same scheme as in the case of galvanomagnetic current transport [68, 69] which accounts for the fact that, within the usually applied box integration method together with the Scharfetter-Gummel interpolation scheme (see appendix B), only the projection of the current along the edges of the grid is available. Due to this discretization scheme, the balance of the terminal currents can be affected depending on the grid imposing additional requirements to its quality. Using this techniques, three-dimensional investigations of silicon magnetotransistors [70] and piezoresistive sensors [71] have been demonstrated.

Since in general the wafer orientation and the device coordinate system does not coincide with the crystallographic axes of the semiconductor lattice, an orthogonal transformation $\tilde{D}$ has to be employed

$$\tilde{\sigma}_\nu^0 = \tilde{D}\,\tilde{\sigma}_\nu\,\tilde{D}^T \tag{2.77}$$

to obtain the anisotropic mobility tensor in diagonal form (Fig. 2.4). Here, $\tilde{D}$ describes the three-dimensional rotation transforming the device coordinate system to the crystal axes.

Generalizing this concept, $\tilde{P}_\nu$, $\tilde{\varepsilon}$, and $\tilde{\kappa}$ can be treated similarly. It is important to note that higher order effects such as the influence of very high electric fields (avalanche coefficients) or surface effects such as anisotropy in the vicinity of the MOS interface [72] are neglected.

## 2.4 Extended electrothermal drift-diffusion model

As outlined in the previous sections, the macroscopic description of a semiconductor device is given by the state variables $(\Psi, n, p, T, f_{tp})$ provided that the free carriers are in thermal equilibrium with the host lattice. This constriction mostly keeps valid as long as the investigated device structures are large compared to the mean free path of the carriers.

The electron and hole currents are driven by the gradients of the respective quasi-Fermi potentials, $\phi_n$ and $\phi_p$, and the temperature T, thereby reflecting drift and diffusion of carriers as well as their thermal diffusion induced by a non-uniform temperature distribution. The constitutive current relations for electrons and holes, Eq. (2.39), can be written in compact form as

$$\vec{J}_\nu = q\nu\tilde{\mu}_\nu\left(\vec{\nabla}\phi_\nu + \tilde{P}_\nu\vec{\nabla}T\right) . \tag{2.78}$$

Non-uniform temperature distributions are governed by a heat flow equation which is derived from the constitutive current relation for the energy, Eq. (2.39), the corresponding balance equation, Eq. (2.34), and the fundamental Gibbs relations, Eq. (2.14). It accounts for all potential heating mechanisms such as Joule heat, recombination heat, and Peltier and Thomson heat:

$$c\frac{\partial T}{\partial t} - \vec{\nabla}\left(\tilde{\kappa}\vec{\nabla}T\right) = -\vec{\nabla}\left(\left(\tilde{P}_nT + \phi_n\right)\vec{J}_n + \left(\tilde{P}_pT + \phi_p\right)\vec{J}_p\right) , \tag{2.79}$$

The distributions of the electron and hole densities, $n$ and $p$, obey the carrier balance equations, Eqs. (2.31) and (2.32),

$$\frac{\partial n}{\partial t} - \frac{1}{q}\vec{\nabla}\vec{J}_n = (G-R) + \sum_D \frac{\partial N_D^+}{\partial t} + \sum_e \frac{\partial N_e^-}{\partial t} + \sum_{tp}\left(e_n^{tp}N_{tp}^{occ} - c_n^{tp}n\left(N_{tp} - N_{tp}^{occ}\right)\right) \tag{2.80}$$

$$\frac{\partial p}{\partial t} + \frac{1}{q}\vec{\nabla}\vec{J}_p = (G-R) + \sum_A \frac{\partial N_A^-}{\partial t} + \sum_h \frac{\partial N_h^+}{\partial t} + \sum_{tp}\left(e_p^{tp}\left(N_{tp} - N_{tp}^{occ}\right) - c_p^{tp}pN_{tp}^{occ}\right) \tag{2.81}$$

which are also known as electron and hole continuity equations. In the equations above, the current relations, Eq. (2.78), have to be substituted for the electron and hole current densities, $\vec{J}_n$ and $\vec{J}_p$, respectively. Boltzmann statistics, Eqs. (2.22) and (2.23), establishes the relation between carrier densities and the quasi-Fermi potentials, while substituting the effective intrinsic density $n_{i,eff}$ for $n_i$ allows including bandgap narrowing in highly-doped device regions (see section 3.2). The right-hand sides of Eqs. (2.80) and (2.81) represent a net carrier generation rate, Eqs. (2.45) and (2.46), which is composed of contributions from band-to-band transitions (e.g. Auger recombination, impact ionization) and external excitation, summarized in the term $(G-R)$, and contributions arising from transitions through deep and shallow energy states in the bandgap. The latter are splitted up following the classification outlined

in section 2.2.3. Their dynamical behavior is controlled by additional balance equations which can be written using Eqs. (2.41) and (2.42) as

$$\frac{\partial N_{tp}^{occ}}{\partial t} = -\left(e_n^{tp} + e_p^{tp} + c_n^{tp} n + c_p^{tp} p\right) N_{tp}^{occ} + \left(e_p^{tp} + c_n^{tp} n\right) N_{tp}\,. \tag{2.82}$$

Due to the coupling to only one of the energy bands, Eq. (2.82) is simplified to

$$\frac{\partial N_A^-}{\partial t} = -\left(e_p^A + c_p^A p\right) N_A^- + e_p^A N_A \tag{2.83}$$

$$\frac{\partial N_h^+}{\partial t} = -\left(e_p^h + c_p^h p\right) N_h^+ + c_p^h p N_h \tag{2.84}$$

for acceptors and hole traps and similarly

$$\frac{\partial N_D^+}{\partial t} = -\left(e_n^D + c_n^D n\right) N_D^+ + e_n^D N_D \tag{2.85}$$

$$\frac{\partial N_e^-}{\partial t} = -\left(e_n^e + c_n^e n\right) N_e^- + c_n^e n N_e \tag{2.86}$$

for donors and electron traps, respectively.

For each relevant energy state, one of these equations has to be solved in addition to Eqs. (2.79) - (2.81), augmenting the complete set of dynamic equations by an additional independent state variable. The charged energy states in the bandgap contribute to the total electrical charge density on the right-hand side of Poisson's equation

$$\begin{aligned}\vec{\nabla}\left(\tilde{\varepsilon}\vec{\nabla}\Psi\right) &= q\Bigg(n - p + \sum_A N_A^- - \sum_D N_D^+ + \sum_D N_h^+ - \sum_A N_e^- - \\ &\qquad \sum_{tp}\left(z_{emp}^{tp}\left(N_{tp} - N_{tp}^{occ}\right) + z_{occ}^{tp} N_{tp}^{occ}\right)\Bigg)\end{aligned} \tag{2.87}$$

which completes the set of $4 + \sum(tp + D + A + e + h)$ coupled differential equations for the vector of independent state variables $(n, p, \Psi, T, N_{tp}^{occ}, N_A^-, N_D^+, N_e^-, N_h^+)$. Here, the impurity balance equations, Eqs. (2.82) - (2.86), differ from the remaining equations since they are simple algebraic equations with respect to space variables.

The time scales on which the individual state variables respond to a step-like excitation can differ by many orders of magnitude depending on material and structural parameters as well as on the nature of the external excitation. Generally, local heating is a very fast process, whereas thermal diffusion occurs on a much longer time scale. Concerning the dynamic behavior of the impurities, we may apply the quasi-static approximation (see section 2.2.1) to obtain an explicit expression $N_{tp}^{occ}$ as a function of $(n, p, T)$ so that the number of independent state variables is reduced. For generation-recombination centers, we obtain the well known Shockley-Read-Hall generation rate (see sections 2.2.3 and 3.6) representing the partial steady-state generation-recombination rate of electron-hole pairs through the energy state $tp$, which may be substituted on the right-hand side of Eqs. (2.80) and (2.81) for the respective term in the summation over all impurity states. By analogy, the quasi-static approximation

of the concentrations of the ionized donors and acceptors can be deduced from Eqs. (2.69) and (2.70) together with Eq. (2.13) and using Eqs. (2.22) and (2.23), respectively:

$$N_A^- = \frac{N_A}{1+g_A \frac{p}{N_V} \exp\left[\frac{E_A-E_V}{kT}\right]} \quad (2.88)$$

$$N_D^+ = \frac{N_D}{1+g_D \frac{n}{N_C} \exp\left[\frac{E_C-E_D}{kT}\right]} . \quad (2.89)$$

The quasi-static approximation of the impurity balance equations allows us to systematically tailor the complexity of the model equations according to the needs of the problem under consideration. Only those generation-recombination centers, deep traps and dopants which exhibit long ionization time constants (comparable to the switching time of the device) have to be included in the set of balance equations, Eqs. (2.82) - (2.86). For instance, the electrothermal transient simulation of a high-power SiC pn-diode with a boron doped drift region can be achieved by applying the quasi-static approximation to the shallow donor (N) and including one acceptor balance equation (2.83) for boron and one deep trap balance equation (2.82) for the boron related D-center ending up with six equations.

At low current ratings, self-heating effects generally can be neglected by assuming a homogeneous temperature distribution within the device (isothermal approximation), thus eliminating Eq. (2.79) and the contribution due to the gradient of temperature in Eq. (2.78). Finally, all time derivatives vanish at steady state operating conditions.

## 2.5 Boundary conditions

Assuming charge neutrality and electrothermal equilibrium, the ideal ohmic boundary condition is obtained by the solution of

$$n-p+\sum_A N_A^- - \sum_D N_D^+ + \sum_D N_h^+ - \sum_A N_e^- - \sum_{tp}\left(z_{emp}^{tp}\left(N_{tp}-N_{tp}^{occ}\right)+z_{occ}^{tp} N_{tp}^{occ}\right)=0 \quad (2.90)$$

with respect to the majority carrier concentration and applying the mass-action law:

$$p = \frac{n_i^2}{n} . \quad (2.91)$$

The electrostatic potential is given by (see Fig. 2.2)

$$\psi = U_{applied} + U_{bi} , \quad (2.92)$$

with the externally applied contact potential $U_{applied}$ and the built-in potential [154]

$$qU_{bi} = kT \ln\left(\frac{n_{n0}p_{p0}}{n_i^2}\right) \approx kT \ln\left(\frac{N_D^+ N_A^-}{n_i^2}\right) \quad (2.93)$$

which is determined by the majority carrier concentrations given by Eqs. (2.90) and (2.91). They equal the corresponding concentrations of ionized dopants provided that the influence of deep traps can be neglected.

For gate contacts, the electrostatic potential is taken as

$$\psi = U_{applied} + \phi_{MS}\,, \tag{2.94}$$

where $\phi_{MS} = \phi_M - \phi_S$ is the work function difference between metal and semiconductor relative to an intrinsic semiconductor. All other boundaries are given by ideal Neumann boundary conditions.

Following Wachutka [62] but neglecting the difference in thermo-powers between the semiconductor and the metal, thermally insulating surfaces are described by

$$\kappa \frac{\partial T}{\partial N} = 0 \tag{2.95}$$

whereas thermally conducting surfaces can be alternatively modeled by Dirichlet or inhomogeneous Neumann boundary conditions:

$$\text{Neumann} \quad : \quad \kappa \frac{\partial T}{\partial N} = \frac{1}{R_{th}}\left(T_{ext} - T\right) \tag{2.96}$$

$$\text{Dirichlet} \quad : \quad T = T_{ext}\,. \tag{2.97}$$

# Chapter 3

# Modeling of 4H/6H-SiC material properties

The specific properties of device materials enter the model equations, Eqs. (2.78) - (2.82), in the form of physical parameters such as the effective intrinsic density $n_{i,eff}$, the transport coefficients ($\tilde{\mu}_\nu$, $\tilde{\kappa}$, $\tilde{P}_\nu$), the electric permitivity $\tilde{\varepsilon}$, the heat capacity $c$, the emission and capture coefficients ($e_\nu^{tp}$, $c_\nu^{tp}$), and all the parameters appearing in $(G-R)$. Each of these parameters may depend on the state variables as well as external parameters. A widely favored pragmatic approach is to rely on phenomenological material parameter models [56, 112] which, after careful calibration to experimental data, makes it possible to combine physically-based predictive simulation with numerical practicability.

In the following sections, these models are systematically reviewed with respect to the measured data currently available for 4H- and 6H-SiC, respectively, completed by theoretically calculated material parameters. The resulting parameter set is evaluated by comparing measured and simulated characteristics of pn-diodes and JFETs within a wide range of operation conditions (see chapter 5). Thereby, the sensitivity of certain parameters due to variations in process technology and the impact of the error range of measured material parameters on simulated device behavior is shown.

## 3.1 General material characteristics and process technology

This section briefly summarizes some basic attributes of SiC as material for electronic semiconductor applications. More detailed information can be obtained in the referenced reviews.

SiC exhibits a one-dimensional polymorphism called polytypism. There are a large number of different SiC polytypes which are characterized by the stacking sequence of the tetrahedrally bonded Si-C bilayers. While the individual bond lengths and local atomic environments are nearly identical, the overall symmetry of the crystal is determined by the stacking period. There are three possible positions available for each SiC bilayer with respect to its adjacent bilayers. All maintain the tetrahedral bonding scheme of the crystal. Depending on the stacking order, the type of bonding between Si and C in those bilayers is either of a zinc-blende (cubic) or wurtzite (hexagonal) nature, leading to inequivalent lattice sites in all polytypes with mixed bonding schemes. The different polytypes are categorized by their stacking periodicity and bonding type. 4H- and 6H-SiC are hexagonal polytypes (which are also

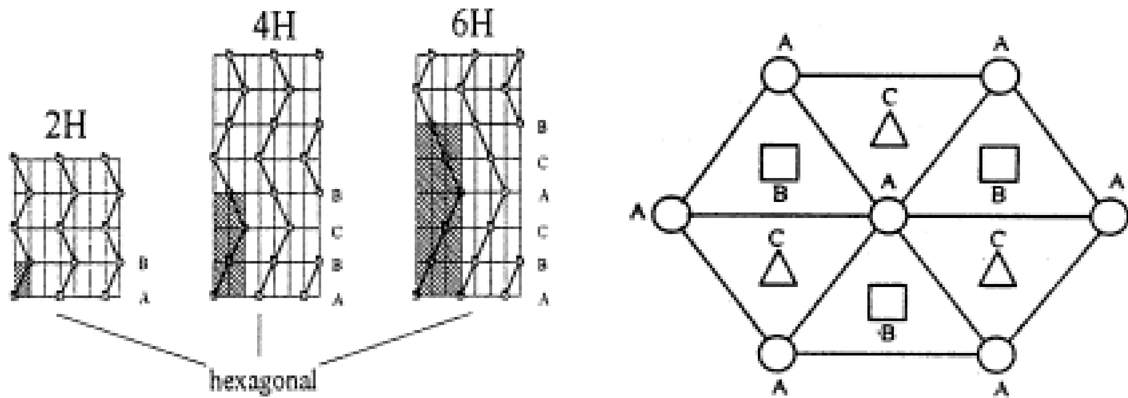


Figure 3.1: Stacking sequence of 2H-, 4H-, and 6H-SiC and corresponding atomic positions.

referred to as α-SiC in literature) with a stacking sequence of ABCB and ABCACB, respectively (Fig. 3.1).

A major technological challenge has been the growth of single-phase material. Substrates are grown by using a sublimentation technique. SiC is transported in the vapor phase to a SiC seed crystal driven by a temperature gradient with typical process temperatures of 2100-2400 K. Historically, first 3C- and 6H-SiC have been commercially available. 4H-SiC is becoming more important because of superior electronic properties. To date, n- and p-conducting 4H- and 6H-SiC wafers are commercially available up to 75 mm of diameter.

The most serious problem of substrate growth is currently the formation of the so-called micropipes, large screw dislocations which are basically voids propagating from the top to the bottom of the substrate [74]. They continue propagating during epitaxial growth which is typically realized by chemical vapor deposition (CVD). Presently, reliable growth of epi-layers with a background doping below $10^{14}\,\mathrm{cm}^{-3}$ is achievable using single wafer vertical CVD systems [75]. In view of the future release of commercial applications, epitaxial growth using multi-wafer vertical CVD systems has been reported [75].

Doping of SiC layers can only be achieved by ion implantation and in-situ doping during epitaxial growth because of the very low diffusion rates of all known dopants [18]. Implantation depths of 300-500 nm for N and Al as well as up to 900 nm for B can be achieved. Thus, only rather shallow junctions are technologically feasible if selective doping is required. Alternatively, mesa pn-junctions can be fabricated using reactive ion etching (RIE) of in-situ doped epi-layers. Additionally, many different intrinsic and extrinsic defects related to the incorporation of transition metals or doping centers are present in state-of-the-art 4H- and 6H-SiC epi-layers. These defects strongly depend on the fabrication process which has been experimentally reviewed in [76] for 4H- and 6H-SiC.

High-power and high-temperature applications require the availability of highly reliable contacts which do not degrade over time. Theory and technology of ohmic contacts are reviewed for instance in [77]. At present, specific contact resistances below $10^{-6}\,\Omega\mathrm{cm}^2$ on highly-doped n-type SiC are reported, whereas ohmic contacts on p-type SiC are more critical and specific contact resistances larger than $10^{-4}\,\Omega\mathrm{cm}^2$ are currently reported.

Intensive technological research has qualified the Schottky diode as the most promising device for

the first SiC commercial application [34]. But the theory of Schottky contacts to SiC is still rather incomplete and presently reported Schottky diodes show by far too large reverse leakage currents [32].

The most important parameters of state-of-the-art $SiC - SiO_2$ interfaces such as the density of interface traps $D_{it}$ and the density of fixed positive charges at the interface $Q_F$ are still insufficient for general commercial device applications. However, continuous improvement of the related theory, characterization and process technology has been achieved over the recent years [78, 79, 80].

## 3.2 Effective density of states and intrinsic carrier density

The bandgap as well as the structure of the conduction and the valence band in its vicinity basically determine the electronic properties of a semiconductor material. Calculations of the band structure [81] yield an indirect bandgap located between the maximum of the valence band at the Γ-point and the minimum of the conduction band at the M-point for 4H-SiC, whereas the conduction band of 6H-SiC has a camel's back structure with a minimum lying on the ML-axis in the brillouin zone (Fig. 3.2).

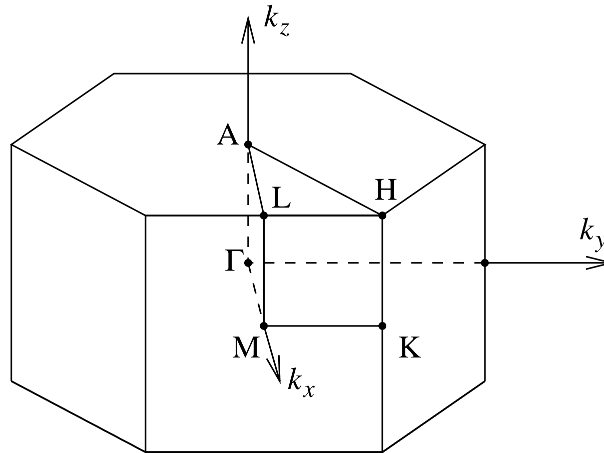


Figure 3.2: First hexagonal brillouin zone of α-SiC.

Photoluminescence measurements yield an exciton bandgap $E_{gx}$ of 3.023eV [82] and 3.265eV [83] at $T = 4\,\mathrm{K}$ for 6H- and 4H-SiC, respectively. Absorption measurements [84] in α-SiC (likely 6H-SiC) yield the temperature dependence of $E_{gx}$ between $4\,\mathrm{K} < T < 200\,\mathrm{K}$ and $300\,\mathrm{K} < T < 700\,\mathrm{K}$, respectively. The measured data can be piecewise fitted by

$$E_g(T) = E_g^{T_0} - \alpha^{E_g} \frac{T^2}{\beta^{E_g} + T} \tag{3.1}$$

using the parameter sets A and C given in Tab. 3.1. Alternatively, a third parameter set B approximates the measured data with a deviation smaller than the possible error range given in [84] as shown in Fig. 3.3 for 6H-SiC. The respective temperature dependence of 4H-SiC is assumed to be similar as long as no further experimental data is available. There are no reliably measured values for the binding energy $E_x$ of free excitons in any SiC polytype [85] which are required in order to obtain the indirect bandgap

$E_g = E_{gx} + E_x$. As presently measured values for $E_x$ ranges from 10-80 meV [85], a mean indirect bandgap may be assumed by shifting $E_{gx}$ by 40 meV for 4H- and 6H-SiC, respectively.

| | $E_g^{T_0}$ (6H) [eV] | $E_g^{T_0}$ (4H) [eV] | $\alpha^{E_g}$ [eV/K] | $\beta^{E_g}$ [K] | range [K] |
|---|---|---|---|---|---|
| set A | 3.023 | 3.265 | $3.3 \cdot 10^{-4}$ | $1.05 \cdot 10^{3}$ | 4-200 |
| set B | 3.023 | 3.265 | $3.3 \cdot 10^{-2}$ | $1.00 \cdot 10^{5}$ | 4-600 |
| set C | 3.1 | 3.342 | $3.3 \cdot 10^{-4}$ | 0 | 300-700 |

Table 3.1: Parameter sets describing the measured exciton bandgap of 4H- and 6H-SiC dependent of temperature.

The effective density of states entering Eq. (2.19) is obtained by a parabolical approximation of the conduction and the valence band in k-space [154]:

$$N_C = 2M_C \left( \frac{2\pi m_e^* kT}{h^2} \right)^{\frac{3}{2}} . \tag{3.2}$$

$M_C$ is the number of equivalent minima in the conduction band and $m_e^*$ is the density-of-states effective mass for electrons, given by

$$m_e^* = (m_{M\Gamma} \cdot m_{MK} \cdot m_{ML})^{\frac{1}{3}} , \tag{3.3}$$

calculated with the effective masses along the principal axes of the ellipsoidal energy surface. In Tab. 3.2, the widely accepted values of the electron effective masses of 4H/6H-SiC are compiled which have been measured by optically detected cyclotron resonance (ODCR) [86, 87].

Similarly, the density-of-states effective mass of holes is given by

$$N_V = 2 \left( \frac{2\pi m_p^* kT}{h^2} \right)^{\frac{3}{2}} . \tag{3.4}$$

The first ODCR measurements of the effective mass of holes have been reported recently for 4H-SiC [88]. The corresponding parameters are compiled in Tab. 3.2 together with calculated values for 6H-SiC [89]. The temperature dependence of $m_\nu^*$ is expected to be relevant only for electrons at low temperatures [90].

| | $m_{M\Gamma}$ | $m_{MK}$ | $m_{ML}$ | $m_e^*$ | $M_C$ | $m_{h_\perp}$ | $m_{h_\parallel}$ | $m_h^*$ |
|---|---|---|---|---|---|---|---|---|
| 4H-SiC | 0.58 | 0.31 | 0.33 | 0.39 | 3 | 0.59 | 1.60 | 0.82 |
| 6H-SiC | $0.42^a$ | | 2.0 | 0.71 | 6 | $0.58^b$ | $1.54^b$ | $0.80^b$ |

Table 3.2: Electron and hole effektive mass in 4H/6H-SiC at 300 K. ($^a$ corresponds to the transversal mass, $^b$ theoretical values)

The quasi-Fermi potentials $\phi_\nu$ are equal to zero in electrothermal equilibrium. Hence, using Eqs. (2.24)

together with (2.22) and (2.23), the intrinsic density of free carriers reads

$$n_i = \sqrt{N_C \cdot N_V} \cdot exp\left(-\frac{E_G}{2kT}\right). \tag{3.5}$$

Due to the wide bandgap, this quantity is smaller by about 16 orders of magnitude when comparing 6H-SiC with Si (Fig. 3.3). This becomes relevant in electronic devices when exceeding the extrinsic carrier concentration at high temperatures. At lower temperatures, it should not be interpreted as real carrier density but rather as quantifying the probability for thermal band-to-band generation. By determining the boundary conditions of the basic partial differential equation set (see section 2.5) and the deviation from electrothermal equilibrium in various generation-recombination models (see section 3.6), it becomes one of the key parameters for device simulation.

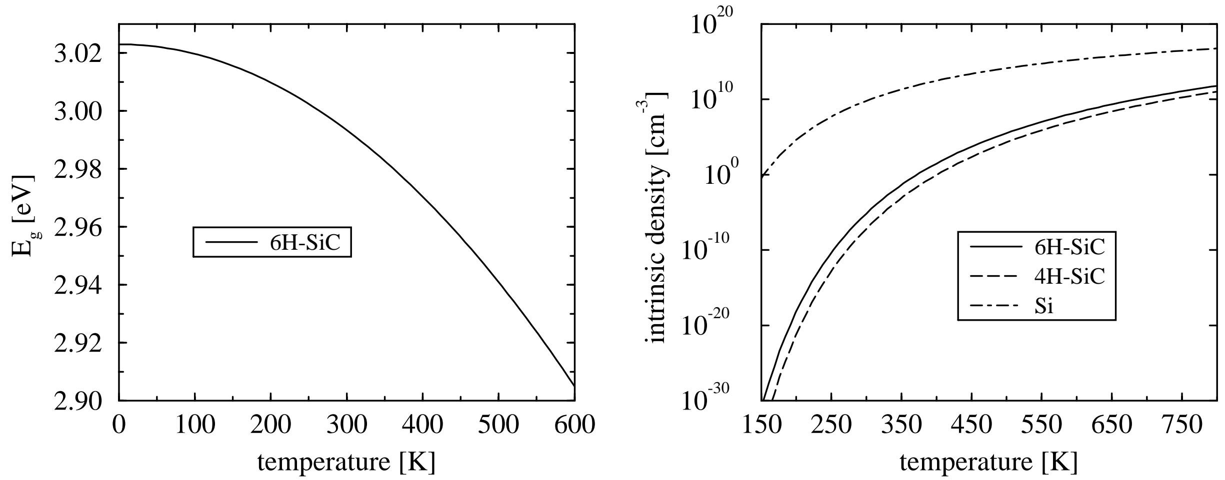


Figure 3.3: Temperature dependence of bandgap energy in 6H-SiC (left - set B of Tab. 3.1) and intrinsic carrier density of Si, 4H-SiC, and 6H-SiC (right).

Eq. (3.5) is based on the parabolic approximation of the conduction and the valence band [154]. Rigorous calculations of the density of states reveal that this approximation overestimates the free carrier concentration in Al-doped 4H-SiC by approximately 60 % [94]. Furthermore, the exponential dependence of $n_i$ on $E_g$ introduces a rather large uncertainty of this parameter. Therefore, its resulting overall error range can hardly be estimated.

The modification of the density of states by heavy doping leads to an additional influence which is generally modeled by rigid shifts of the band edges, the so-called “bandgap narrowing”. Apparent bandgap narrowing models have been established for Si based on measurements of the quantity $\mu_n n_i^2$ in npn-transistors [56, 91, 92]:

$$\Delta E_g = C_\nu^{BGN} \cdot \left(F + \sqrt{F^2 + 0.5}\right), \quad F = ln\left(\frac{N_D + N_A}{N_\nu^{BGN}}\right). \tag{3.6}$$

Recently, Lindefelt [93] published calculated band edge displacements for 4H/6H-SiC. In Tab. 3.3, the parameters obtained by adapting Eq. (3.6) to these results are listed. Compared to Si, a larger

$\Delta E_g$ is expected in n-type material for 4H- and 6H-SiC, respectively, whereas approximately the same displacements are obtained in p-type material for both polytypes.

| | $C_n^{BGN}$ [eV] | $N_n^{BGN}$ [cm$^{-3}$] | $C_p^{BGN}$ [eV] | $N_p^{BGN}$ [cm$^{-3}$] |
|---|---|---|---|---|
| 4H-SiC | $2.0 \cdot 10^{-2}$ | $1.0 \cdot 10^{17}$ | $9.0 \cdot 10^{-3}$ | $1.0 \cdot 10^{17}$ |
| 6H-SiC | $9.0 \cdot 10^{-3}$ | $1.0 \cdot 10^{17}$ | $9.0 \cdot 10^{-3}$ | $1.0 \cdot 10^{17}$ |

Table 3.3: Calculated bandgap narrowing parameters in n-type and p-type 4H- and 6H-SiC, respectively.

As Boltzmann statistics will not keep valid within highly-doped ($N > 10^{19}\,\mathrm{cm}^{-3}$) regions, Fermi statistics has to be used by introducing a correcting factor [56]

$$n_{i,eff} = n_i \gamma_{BGN} \tag{3.7}$$

with

$$\gamma_{BGN} = \frac{F_{1/2}\left[x + \frac{\Delta E_g}{2kT}\right]}{F_{1/2}[x]}, \quad x = \frac{E_i - E_C + q(\psi - \phi)}{kT} \tag{3.8}$$

and approximating the Fermi integral $F_{1/2}$ [112]. The resulting relative influence on $n_i$ is shown in Fig. 3.4.

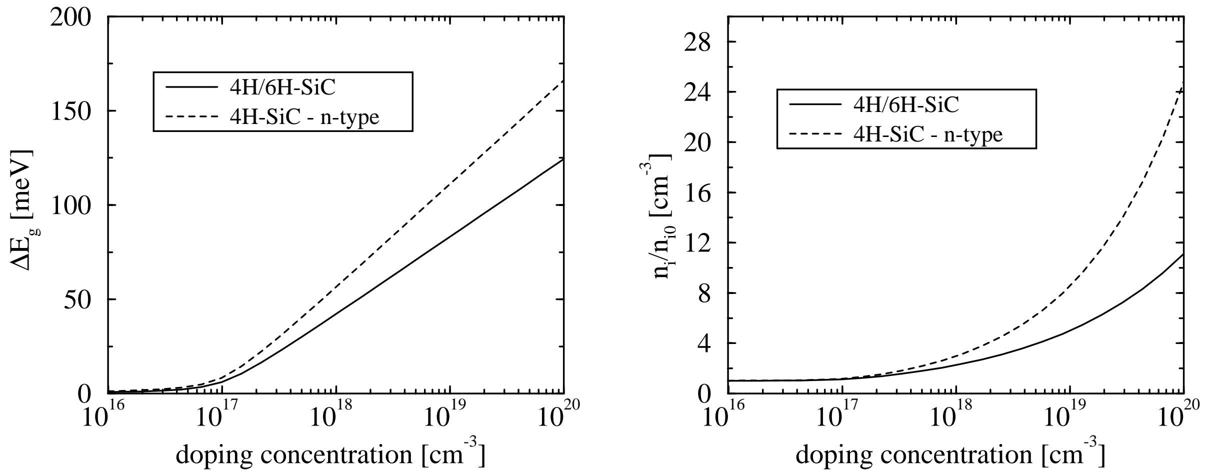


Figure 3.4: Bandgap narrowing in 4H-SiC and 6H-SiC (left) and corresponding influence on the intrinsic carrier density (right).

As mentioned in section 5.1, the exponential part of the IV characteristics of a pn-diode is very sensitive to $n_i$ (see Eq. (5.1)). Using the parameters of this section and neglecting any shift of the bandgap due to the exciton binding energy, a consistent quantitative agreement between experiment and simulation is obtained within a wide temperature range for several devices by only adjusting the SRH lifetimes. Therefore, although the effect of an incorrect $n_i$ may be partly compensated by the extracted SRH lifetimes and further influences, these parameters can be seen as a good reference for state-of-the-art

SiC device simulation. Further coupled experimental and theoretical work would allow to effectively minimize the possible error range of $n_i$.

## 3.3 Dielectric constant

Using data available on the refractive indices, their dispersion, and on phonon energies obtained by Raman scattering, Patrick et al. published 1970 the two tensor components of the static dielectric constant of 6H-SiC [110]. They found a ratio of anisotropy $\varepsilon_\perp/\varepsilon_\parallel = 0.96$ with $\varepsilon_\perp = 9.66$ and $\varepsilon_\parallel = 10.03$. In a more recent investigation, Ninomiya et al. obtained $\varepsilon_\perp = 9.76$ and $\varepsilon_\parallel = 9.98$ [111]. Thus these values are well agreed upon within a very small error boundary. However, up to now, no values seem to be available for 4H-SiC. Therefore, the values of 6H-SiC have to be used. Since 4H-SiC has a somewhat larger bandgap than 6H-SiC, one may expect the dielectric constants of this polytype to be somewhat smaller [113]. Additionally, the ratio of anisotropy may differ as the anisotropy of 4H-SiC seems to be generally weaker.

## 3.4 Free carrier mobilities

The free carrier mobilities are the transport parameters relating the gradient of the quasi-Fermi potential to the corresponding current flow (see Eq. (2.78)). They are derived from relaxation times $\tau_\nu^{rel}$ which describe the average time between the scattering events of free carriers. Assuming a single isotropic scattering process, they can be defined by

$$\mu_\nu = \frac{q\tau_\nu^{rel}}{m_\nu^*}. \tag{3.9}$$

However, there are various scattering mechanisms which determine the free carrier mobilities such as acoustical and optical phonon scattering, piezoelectric and polar scattering, ionized and neutral impurity scattering as well as scattering at vacancies, dislocations, and surfaces. Due to the complex nature of these mechanisms, phenomenological models have been developed for the various experimentally observed mobility phenomena in Si devices [112]. The contributions from different scattering processes can be combined using the simple Mathiesen rule [112]

$$\frac{1}{\mu_\nu^{low}} = \sum_i \frac{1}{\mu_\nu^i} \tag{3.10}$$

provided that they can be considered as independent mechanisms. Due to the diagonal form of the mobility tensor of α-SiC, this concept can also be applied to its independent components in the principal axes system (see section 2.3). However, a rigorous modeling of the anisotropic properties of α-SiC will be a challenge to semiconductor transport theory. A first attempt to calculate the anisotropy of the Hall mobility in n-type α-SiC based on detailed information about the band structure is reported in [116].

The transport parameters of semiconductors may significantly depend on the process technology. Therefore, reported mobility data from the period before wafers with a defined polytype in acceptable

quality were available can hardly be used to investigate state-of-the-art devices. Hall measurements of the bulk epitaxial free carrier mobility tensor components of 4H- and 6H-SiC have been reported by Schaffer et al. [114] and Schadt et al. [115].

### 3.4.1 Acoustic-phonon and ionized-impurity scattering

The measurement results of Schaffer et al. [114] for $\mu_\perp$ of n-type (N) and p-type (Al) 4H/6H-SiC within a large doping range at 300 K are shown as symbols in Fig. 3.5. Acoustic-phonon and ionized-impurity

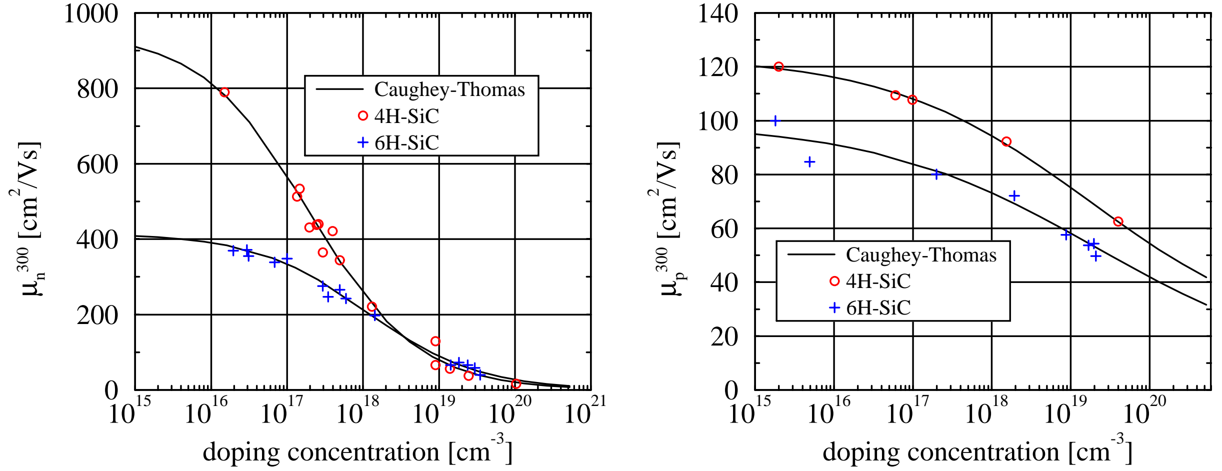


Figure 3.5: Doping dependence of Hall mobility in n-type (N) and p-type (Al) 4H/6H-SiC.

scattering are not independent of each other. Thus, Eq. (3.10) can not be used and a combined model is needed. The data of Fig. 3.5 can be modeled using the phenomenological model of Caughey-Thomas [117]:

$$\mu_\nu^{ac,ii}(N,T) = \mu_\nu^{min} + \frac{\mu_\nu^{T_0} \cdot \left(\frac{T}{T_0}\right)^{\alpha_\nu^{mob}} - \mu_\nu^{min}}{1 + \left(\frac{N_D+N_A}{N_\nu^{mob}}\right)^{\gamma_\nu^{mob}}}. \tag{3.11}$$

The corresponding parameters are listed in Tab. 3.4. The measured electron mobility in 4H-SiC is about twice that of 6H-SiC for a total impurity concentration less than $10^{17}\,\mathrm{cm}^{-3}$. Additionally, the hole mobility in 4H-SiC is $20-30\,\%$ larger than in 6H-SiC over the entire measured impurity range. Schaffer et al. investigated over 100 4H- and 6H-SiC wafers and analyzed in detail the temperature dependence $\mu(T)$ of both polytypes. He obtained constant temperature coefficients with values between $1.8 \leq \alpha_\nu^{mob} \leq 2.2$ depending on the measured sample for temperatures larger than 300 K in both polytypes. It is demonstrated that the ionization of deeper levels can affect the measured temperature coefficient $\alpha_\nu^{mob}$ explaining the large range of reported values. Since the observed temperature coefficients are lying between 1.5 which would be characteristic for acoustical-mode phonon scattering and 2.5 which would be characteristic for optical-mode phonon scattering, it appears that other scattering mechanisms contribute less to limit the mobility in high-quality bulk material [118, 119].

The anisotropic characteristics of the Hall mobilities have been investigated independently by Schaffer

| polytype | $\nu$ | $\mu_{\perp}^{T_0}$ $[\frac{cm^2}{Vs}]$ | $\mu_{\nu}^{min}$ $[\frac{cm^2}{Vs}]$ | $N_{\nu}^{mob}$ $[cm^{-3}]$ | $\gamma_{\nu}^{mob}$ |
|---|---|---|---|---|---|
| 6H-SiC | n | 415 | 0.0 | $1.11 \cdot 10^{18}$ | 0.59 |
| | p | 99 | 6.8 | $2.10 \cdot 10^{19}$ | 0.31 |
| 4H-SiC | n | 947 | 0.0 | $1.94 \cdot 10^{17}$ | 0.61 |
| | p | 124 | 15.9 | $1.76 \cdot 10^{19}$ | 0.34 |

Table 3.4: Caughey-Thomas parameter for $\mu_{\nu_{\perp}}$ in 4H/6H-SiC.

et al. using epitaxial layers grown on $[1\bar{1}00]$ and $[11\bar{2}0]$ surfaces, and Schadt et al. using samples sawed out directly from a single crystal. Whereas a large anisotropic Hall mobility ratio $\mu_{\perp}/\mu_{\parallel} = 5$ was obtained in 6H-SiC, only a small anisotropic effect with $\mu_{\perp}/\mu_{\parallel} = 0.8$ was observed in 4H-SiC. Thus, the largest Hall mobility is related to a current flow parallel to the ĉ-axis in 4H-SiC and perpendicular to the ĉ-axis in 6H-SiC. No dependence on the impurity concentration has been reported for these ratios. On the other hand, a rather large dependence on temperature for these ratios has been reported by Schadt et al. for both polytypes for $100\,\mathrm{K} < T < 600\,\mathrm{K}$. However, Schaffer et al. proved that the influence of deeper levels could result in such a temperature dependence. They obtained no temperature dependence of these ratios between $100\,\mathrm{K} < T < 600\,\mathrm{K}$ for high-quality epi-layers. Thus, the concept of modeling the anisotropy of the bulk mobility is also applicable within this temperature range and for arbitrary impurity concentrations. No anisotropy of the Hall mobility has been observed for p-conducting material.

In conclusion, experimental data for the Hall mobility of electrons and holes including anisotropic effects is available for high-quality bulk epitaxial 4H- and 6H-SiC within a wide range of impurity concentration and temperature. A negative temperature coefficient $\alpha_{\nu}^{mob}$ has been reported between $100\,\mathrm{K} < T < 600\,\mathrm{K}$. The Hall mobility equals approximately the drift mobility $\mu_{\nu} = \mu_{H_{\nu}}/r_H$ with $r_H \approx 1$ [120]. The data can be well described by the model of Caughey-Thomas including the temperature dependence for $T > 300\,\mathrm{K}$. Although the mobility parameters depend on technology, Tab. 3.4 can serve as a base for evaluating measured device characteristics. Good agreement has been obtained for numerical simulations of JFETs (see section 5.2). However, in order to perform predictive quantitative simulations, these parameters have to be calibrated by measured data of the material under investigation.

### 3.4.2 Carrier-carrier and surface scattering

There are important scattering mechanisms for SiC devices for which no experimental or theoretical data is yet available. Carrier-carrier scattering significantly influences the characteristics of Si high-power bipolar devices at high current ratings. In addition, the surface current transport parameters which are especially relevant in MOS devices are rather unknown. Therefore, corresponding silicon models and parameters have to be used, rescaled by fitting simulated device characteristics to measured data.

Carrier-carrier scattering is modeled using a model of Choo [121]:

$$\mu_{np} = \frac{D\left(\frac{T}{T_0}\right)^{\frac{3}{2}}}{\sqrt{np}} \cdot \left[ ln \left( 1 + \bar{F} \left(\frac{T}{T_0}\right)^2 (pn)^{-\frac{1}{3}} \right) \right]^{-1} . \tag{3.12}$$

In Fig. 3.6, the dependence of the mobility resulting from Eq. (3.12) is plotted for Si along a cutline where n equals p (solid line). The curves for 4H- and 6H-SiC are obtained by rescaling the parameters for Si such that the influence of this scattering mechanism sets on approximately at the same doping concentration.

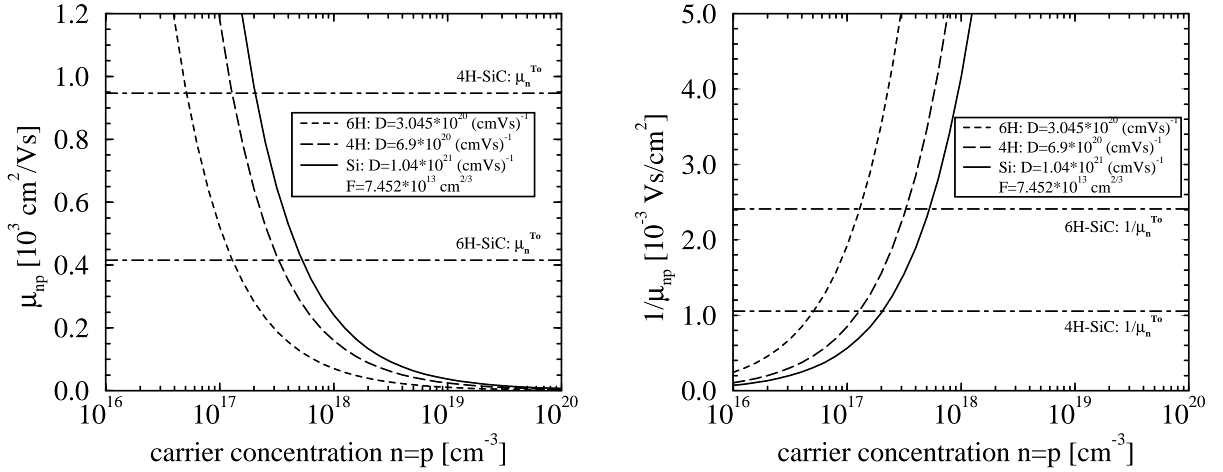


Figure 3.6: Influence of model parameters of carrier-carrier-scattering.

Similarly, the physical mechanisms at MOS interfaces in SiC are not well understood. However, it is necessary to account for reduced channel mobilities in real MOS devices. In Silicon, mobility degradation at MOS interfaces can be modeled using a model of Lombardi et al. [122]:

$$\mu_\nu^{acs} = \frac{B}{F_\perp} + \frac{C\left(\frac{N}{N_0}\right)^\lambda}{F_\perp^{\frac{1}{3}}\left(\frac{T}{T_0}\right)} \tag{3.13}$$

$$\mu_\nu^{rs} = \frac{\delta}{F_\perp^2} . \tag{3.14}$$

It accounts for contributions from surface acoustic phonon scattering (acs) and surface roughness scattering (rs) as function of the electric field normal to electron and hole current, respectively. Using these parameters, experimental data can be empirically fitted to account for such effects in numerical investigations (see section 5.3).

### 3.4.3 High-field drift velocity saturation

The heating of free carriers at high electric fields results in a saturation of the drift velocity

$$\vec{v}_\nu = \tilde{\mu}_\nu \cdot \vec{E} \tag{3.15}$$

originating from various scattering mechanisms such as optical phonon scattering, phonon dispersion, phonon absorption as well as emission, and the energy band non-parabolicity [56]. The experimental data [123, 124] shown in Fig. 3.7 can be modeled by the widely used expression of Canali et al. [125]:

$$\mu_{\nu_{\perp,\parallel}} = \frac{\mu^{low}_{\nu_{\perp,\parallel}}}{\left[1 + \left(\frac{\mu^{low}_{\nu_{\perp,\parallel}} \cdot \left|\vec{E}\cdot\vec{J}_\nu\right| / \left|\vec{J}_\nu\right|}{v^{sat}_{\nu_{\perp,\parallel}}}\right)^{\alpha^{sat}_\nu}\right]^{\frac{1}{\alpha^{sat}_\nu}}} . \tag{3.16}$$

The combined low field mobility resulting from Eq. (3.10) will be reduced by the influence of the electric field component parallel to the current flow. Here, the temperature dependence of $v^{sat}_\nu$ can be modeled by

$$v^{sat}_{\nu_{\perp,\parallel}}(T) = v^{sat}_{\nu_{0\perp,\parallel}} \cdot \left(\frac{T}{T_0}\right)^{\delta^{sat}_\nu} \tag{3.17}$$

and

$$\alpha^{sat}_\nu(T) = \alpha^{sat}_{\nu_0} \cdot \left(\frac{T}{T_0}\right)^{\beta^{sat}_\nu} . \tag{3.18}$$

The first measurements published by Muench et al. in 1977 [123] using n-type α-SiC epi-layers on Lely crystals have been updated recently by Khan et al. [124] using standard n-type and p-type 4H- and 6H-SiC epi-layers at several temperatures (Tab. 3.5 and Fig. 3.7). All measured data refers to a current flow perpendicular to the ĉ-axis. No measured data of holes is presently available.

| | $v^{sat}_{n_0}$ [cm/s] | $\alpha^{sat}_n$ | $\delta^{sat}_n$ | $\beta^{sat}_n$ |
|---|---|---|---|---|
| 4H-SiC | $2.2 \cdot 10^7$ | 1.2 | $-0.44$ | 1 |
| 6H-SiC | $1.9 \cdot 10^7$ | 1.7 | $-1$ | 1.25 |

Table 3.5: Model parameters of electron saturation velocity in 4H- and 6H-SiC.

Recent Monte Carlo simulations for 4H-SiC [126] which extend earlier work [127, 128] by including more precisely the non-parabolic band structure excellently agree to the measured data. In addition, these investigations reveal a lower electron saturation velocity $v^{sat}_{n_\parallel} = 1.8 \cdot 10^7\,\mathrm{cm/s}$ parallel to the ĉ-axis in 4H-SiC with an anisotropic factor of $v^{sat}_{n_\perp}/v^{sat}_{n_\parallel} = 1.16$. Furthermore, no significant difference between bulk and surface saturation velocity is expected if the same scattering mechanisms are dominant in α-SiC as in Si [129].

## 3.5 Thermal properties

The thermal material properties are modeled by the tensors of thermoelectric power $\tilde{P}_\nu$ for electrons and holes, the heat capacity $c$, and the tensor of the thermal conductivity $\tilde{\kappa}$.

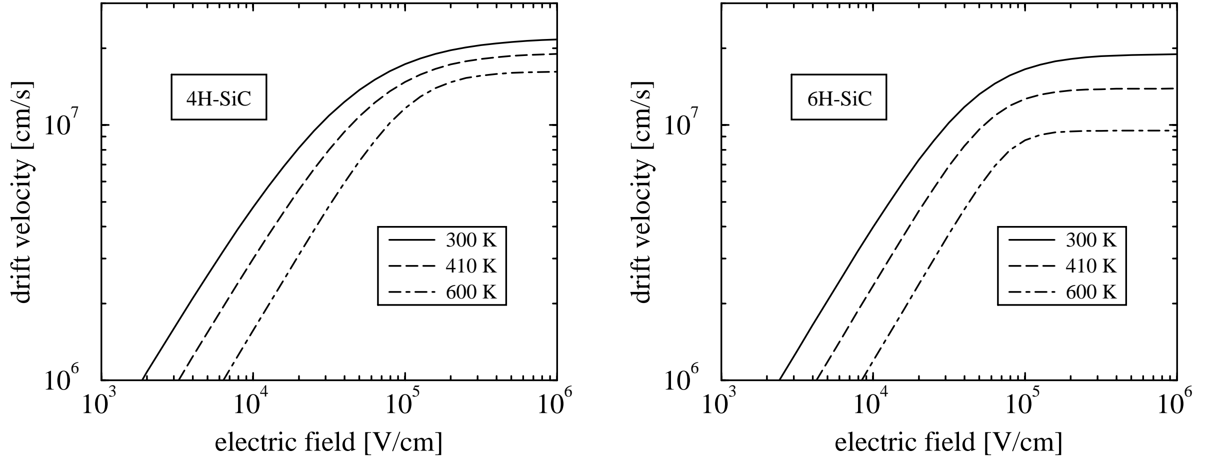


Figure 3.7: Saturation of the electron drift velocity with increasing electric field in 4H- (left) and 6H-SiC (right).

No measured data about the tensors of thermoelectric power $\tilde{P}_\nu$ is available, up to now. Hence, corresponding values measured for Si have to be used [47, 130, 131]. However, their influence can be neglected for the class of device applications considered in this work.

The measured data which is available for the heat capacity of α-SiC [132] can be adapted to [51]

$$c(T) = A_c + B_c T + C_c T^2 + D_c T^{-2}. \tag{3.19}$$

Similarly, the references available for experimental data of the thermal conductivity [133, 134, 135] can be adapted to [51]

$$\kappa(T) = \frac{1}{A_\kappa + B_\kappa T + C_\kappa T^2}. \tag{3.20}$$

The corresponding parameters are given in Tab. 3.6. Furthermore, the anisotropic ratio of 6H-SiC has been experimentally determined to $\kappa_\perp/\kappa_\| = 0.7$ [134] independent of temperature and doping concentration.

| | $A_c$ [$\mathrm{Jkg^{-1}K^{-1}}$] | $B_c$ [$\mathrm{Jkg^{-1}K^{-2}}$] | $C_c$ [$\mathrm{Jkg^{-1}K^{-3}}$] | $D_c$ [$\mathrm{Jkg^{-1}K}$] |
|---|---|---|---|---|
| c | 1026 | 0.201 | 0 | $-3.66 \cdot 10^7$ |
| | $A_\kappa$ [$\mathrm{cmKW^{-1}}$] | $B_\kappa$ [$\mathrm{cmW^{-1}}$] | $C_\kappa$ [$\mathrm{cmW^{-1}K^{-1}}$] | – |
| κ | $2.5 \cdot 10^{-3}$ | $2.75 \cdot 10^{-4}$ | $1.3 \cdot 10^{-6}$ | – |

Table 3.6: Model parameter for heat capacity and thermal conductivity of α-SiC.

These parameters are quite important for simulating transient high-power device applications. However, a calibration with respect to measured electrothermal device characteristics is still missing but is currently planned in another work [136].

## 3.6 Carrier generation and recombination

In section 2.4, the carrier production rate of the continuity equations, Eqs. (2.80) and (2.81), has been divided into contributions arising from impurities and those arising from band-to-band generation or recombination. Referring to the classification of impurities presented in section 2.2.3, generation-recombination centers are modeled within the limits of the quasi-static approximation including various physical mechanisms. Apart from a possible external optical generation rate [47], the relevant band-to-band processes in wide bandgap materials are basically Auger recombination and the corresponding inverse process, impact ionization, which determines the avalanche generation rate.

### 3.6.1 Generalized field-dependent Shockley-Read-Hall statistics

As shown in section 2.2.3, the balance equation for each generation-recombination center yields a Shockley-Read-Hall (SRH) rate [156, 157] within the quasi-static approximation. The indiviual characteristic properties of generation-recombination centers depend strongly on technology and, therefore, they are usually lumped together in quantities like effective electron and hole lifetimes, ending up with one effective single level SRH rate in analogy to Eq. (2.62):

$$(G-R)_{SRH} = \frac{n_{i,eff}^2 - n\,p}{\tau_p(N,T,E)\,(n+n_1) + \tau_n(N,T,E)\,(p+p_1)}\,. \tag{3.21}$$

Here, the SRH parameters $\tau_\nu$ and $\nu_1$ defined in section 2.2.3 describe the apparent electronic properties of the dominant recombination-generation center in a device. Various physical mechanisms may influence this process. Generally, a doping dependence of $\tau_\nu$ is experimentally observed in Si technology [95, 96, 97] and is empirically modeled by the so-called Scharfetter relation:

$$\tau_\nu(N,T) = \tau_\nu^{min} + \frac{\tau_\nu(T) - \tau_\nu^{min}}{1 + \left(\frac{N_D+N_A}{N_\nu^{SH}}\right)^{\gamma_\nu^{SRH}}} \tag{3.22}$$

with

$$\tau_\nu(T) = \tau_\nu^{T_0}\left(\frac{T}{T_0}\right)^{\alpha_\nu^{SRH}}\,. \tag{3.23}$$

Eq. (3.22) can be basically regarded as a fit formula to account for experimental facts which are strongly dependent on process technology. There is no experimental data available to extract the corresponding parameters for $\alpha$-SiC. Therefore, parameters typical for Si devices may be used in order to qualitatively account for those effects.

Principally, any field dependence of the SRH lifetimes can originate from either the Franz-Keldysh effect (band-state field effect) or from the Poole-Frenkel effect (bound-state field effect). The Franz-Keldysh effect leads to a non-vanishing tunneling probability for electrons and holes to a recombination center in the bandgap as a consequence of a change in the density of states near the band edges under the influence of a strong electric field [98]. The resulting recombination (or generation) process is no longer purely vertical, but accompanied by a tunneling process into virtual multi-phonon states as illustrated in Fig. 3.8, where $l$ and $l'$ are the number of phonons involved. The Poole-Frenkel effect occurs

in the case of charged recombination centers. The electronic structure of the localized states in the bandgap is distorted by a strong electric field, thus lowering the thermal energy barrier for generation or recombination [101]. Both effects are modeled by introducing a corresponding field-enhancement factor $g_\nu(E)$ (see appendix C):

$$\tau_\nu(N,T,E) = \frac{\tau_\nu(N,T)}{1+g_\nu(E)}. \tag{3.24}$$

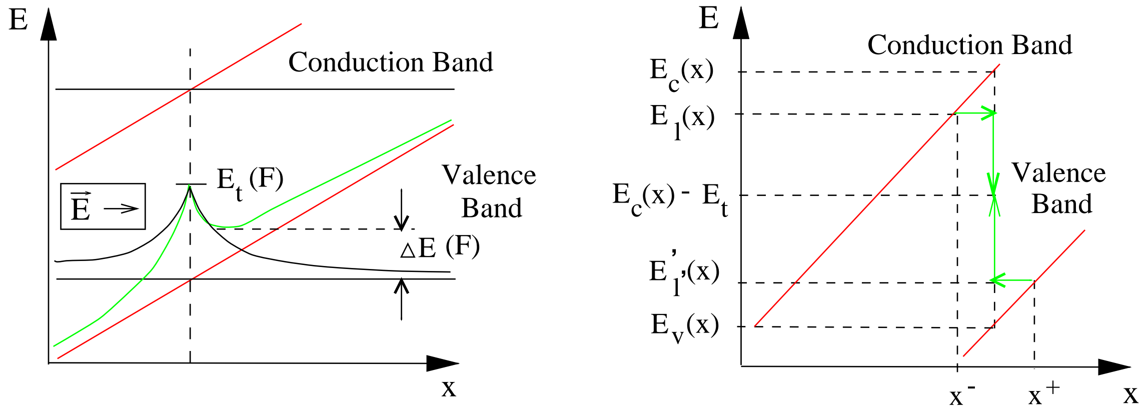


Figure 3.8: Schematic energy diagram illustrating the Poole-Frenkel (left) and the Franz-Keldysh (right) effect.

The extension of the conventional single level SRH toward coupled defect-level generation-recombination [100] is briefly summarized in appendix C. It may partly explain excess leakage currents in reverse biased pn-diodes as shown in section 5.1.3.

Furthermore, a formula structurally equivalent to the bulk SRH rate models surface related generation-recombination by the recombination velocities $v_\nu$:

$$(G-R)^{SRH}_{surface} = \frac{n^2_{i,eff} - n\,p}{v_p^{-1}\,(n+n_1) + v_n^{-1}\,(p+p_1)}. \tag{3.25}$$

### 3.6.2 Auger recombination

Being a 3-particle process, Auger recombination is only relevant at high carrier concentrations. The Auger recombination rate is proportional to the product of the concentrations of the respective reaction partners [102, 103]:

$$R^{Au} = (C_n n + C_p p)(n p - n_{i,eff}^2) \,. \tag{3.26}$$

Here, $C_\nu$ denotes the Auger coefficient of electrons and holes, respectively. For 6H-SiC, they have been for the first time estimated to $C_n = C_p = (3.0 \pm 0.5) \cdot 10^{-29} \, \frac{\mathrm{cm}^6}{\mathrm{s}}$ [104] by means of transient measurements of the stored charge of pn-diodes during switch-off.

### 3.6.3 Impact ionization

The acceleration of free carriers within a high electric field finally results in generating free carriers by impact ionization. This process corresponds to the inverse process of Auger recombination. It is modeled by the reciprocal of the mean free path which is called the impact ionization coefficient. The corresponding avalanche generation rate can be expressed by

$$G_{ava} = \frac{1}{q} \left( \alpha_n j_n + \alpha_p j_p \right) \,. \tag{3.27}$$

The impact ionization coefficients are modeled by the well known Chynoweth law [107]:

$$\alpha_\nu = a_\nu \gamma_a \exp\left( -\frac{b_\nu \gamma_a}{\vec{E} \cdot \frac{\vec{J}_\nu}{|\vec{J}_\nu|}} \right) , \tag{3.28}$$

with

$$\gamma_a = \frac{\tanh(h\omega_{op}/2kT_0)}{\tanh(h\omega_{op}/2kT)} \,. \tag{3.29}$$

The factor $\gamma_a$ with the optical phonon energy $h\omega_{op}$ expresses the temperature dependence of the phonon gas against which the carriers are accelerated [47]. Presently, there is only one report available on measured impact ionization coefficients at different temperatures [106]. A positive temperature gradient has been found which is an important desirable property for power devices.

| | $a_n$ [cm$^{-1}$] | $b_n$ [V/cm] | $a_p$ [cm$^{-1}$] | $b_p$ [V/cm] |
|---|---|---|---|---|
| 4H-SiC | $3.44 \cdot 10^6$ | $2.58 \cdot 10^6$ | $3.24 \cdot 10^7$ | $1.9 \cdot 10^7$ |
| 6H-SiC | $1.66 \cdot 10^6$ | $1.27 \cdot 10^7$ | $5.18 \cdot 10^6$ | $1.4 \cdot 10^7$ |

Table 3.7: Average impact ionization coefficients of electrons and holes 4H- and 6H-SiC.

Generally, the impact ionization coefficients of electrons are significantly smaller than those of holes. A review of the published data on impact ionization coefficients has been first published by Ruff et al. [49, 50, 113]. The extracted average parameter set (Tab. 3.7) is superceeded by newer measurements [105, 106] which yield an about 20 % larger critical electric field.

It is important to note that the measured data rely on uniform avalanche breakdown with all possible influence of structural defects and edge termination excluded. There is experimental evidence that elementary screw dislocations reduce the breakdown voltage of a pn-junction [108, 109]. Considering such findings and the spread of measured data, the avarage parameters seem to be a good base for numerical simulations which should be calibrated to the applied process technology.

No explicitly measured data about anisotropic impact ionization coefficients is available so far. Adaption to available measured data may indicate an anisotropic ratio $a_{n_\perp}/a_{n_\parallel} = 1/3.5$.

# Chapter 4

# Incomplete ionization of dopants

In section 3.1 some general aspects concerning process technology and impurities in 4H- and 6H-SiC have been discussed. The controlled incorporation of shallow impurity levels acting as donors or acceptors is one of the key processes of semiconductor device technology and the resulting n-doped and p-doped regions are the basic functional components of semiconductor devices besides rectifying metal-semiconductor contacts and MOS interfaces.

The most important dopant centers for 4H- and 6H-SiC have been so far nitrogen (N) acting as donor as well as aluminum (Al) and boron (B) acting as acceptors. N and other donor impurities are assumed to occupy the carbon sites, Al atoms substitute only on the Si sublattice, whereas B may substitute on both sites [137]. The long unit cell of 4H- and 6H-SiC leads to inequivalent lattice sites divided into a cubic-like configuration of the first- and second-neighbor atoms and a hexagonal-like atomic configuration. At present, only few and very limited microscopic theory on shallow impurity levels in SiC polytypes is available [138]. The macroscopic parameters introduced in section 2.2, however, are accessible by several measurement methods such as infrared absorption, the Hall effect, thermal and optical admittance spectroscopy, and deep level transient spectroscopy. Whereas the ionization energies reported in the seventies and eighties scattered within a range of more than 100 meV [137, 139], recently published data [139, 140, 141, 142, 144, 145, 146, 147, 148, 149] generally only vary by about 10-15% (Tab. 4.1). It should be mentioned that various possible sources of error (see section 4.2) and the uncertainty about several material constants will probably result in comparable scatter when comparing the data of different publications and different measurement methods. Whereas different ionization energies

$$\Delta E_A = E_A - E_V \qquad \Delta E_D = E_C - E_D \tag{4.1}$$

of the inequivalent lattice sites have been measured for N, their site dependence seems to be at least very weak for Al and B[1].

Due to the rather large ionization energies, incomplete ionization of these dopants in 4H- and 6H-SiC will affect the device behavior within a wide range of operation conditions. The most important effect is a substantial increase of the bulk resistance dependent on temperature and doping concentration

[1] To date, experimental evidence [142, 141] on the site dependence of Al and B is at least questionable as it results from analytical fittings of a TAS conductance peak using several energy levels with different trap concentration. Particularly, the influence of serial resistances can significantly influence the results of TAS as shown in section 4.2.2.

| | 6H-SiC | 4H-SiC |
|---|---|---|
| Al | $210 \pm 20$ | $210 \pm 20$ |
| B | $320 \pm 20$ | $320 \pm 20$ |
| $N_{hex}$ | $80 \pm 10$ | $50 \pm 5$ |
| $N_{cub}$ | $140 \pm 10$ | $90 \pm 10$ |

Table 4.1: Ionization energies (in meV) of N, Al, and B in 4H/6H-SiC (Tab. 4.3).

which can be deduced from equilibrium considerations. Additionally, the measurement of the emission coefficients, Eqs. (2.57) and (2.58), within a wide range of temperature which was not available up to now will enable us to conclude about the limits of validity of the quasi-static approximation, Eqs. (2.88) and (2.89), and the impact of dynamic ionization on device characteristics beyond these limits (see section 5.4).

## 4.1 Electrothermal equilibrium

Electrothermal equilibrium is characterized by a constant Fermi energy $E_F = E_{F_V}$ which equals the quasi-Fermi energies of electrons and holes. Hence, from the neutrality condition

$$n + N_A^- = p + N_D^+ \tag{4.2}$$

and the corresponding Gibbs distributions, Eqs. (2.88) and (2.89), we obtain an explicit relation for the ionization degree of a single donor level in n-type material

$$\xi_D = \frac{N_D^+}{N_D} = \frac{-1 + \sqrt{1 + 4 g_D \frac{N_D}{N_C} \exp\left(\frac{E_C - E_D}{kT}\right)}}{2 g_D \frac{N_D}{N_C} \exp\left(\frac{E_C - E_D}{kT}\right)} \tag{4.3}$$

and similarly

$$\xi_A = \frac{N_A^-}{N_A} = \frac{-1 + \sqrt{1 + 4 g_A \frac{N_A}{N_V} \exp\left(\frac{E_A - E_V}{kT}\right)}}{2 g_A \frac{N_A}{N_V} \exp\left(\frac{E_A - E_V}{kT}\right)} \tag{4.4}$$

in p-type material. Using the values of Tab. 4.1, the ionization degree of Al and B calculated with Eq. (4.4) is shown in Fig. 4.1 as function of temperature and doping concentration. At room temperature and $N_A = 10^{16}\,\mathrm{cm}^{-3}$, only 60 % of Al and 14 % of B are ionized. $\xi_A$ decreases with increasing center concentration and decreasing temperature which finally leads to the freeze-out of holes at low temperatures.

As can be seen in Fig. 4.2, the error range for acceptors given in Tab. 4.1 leads to an uncertainty of about $\pm 20\%$ of $\xi_A$ for Al.

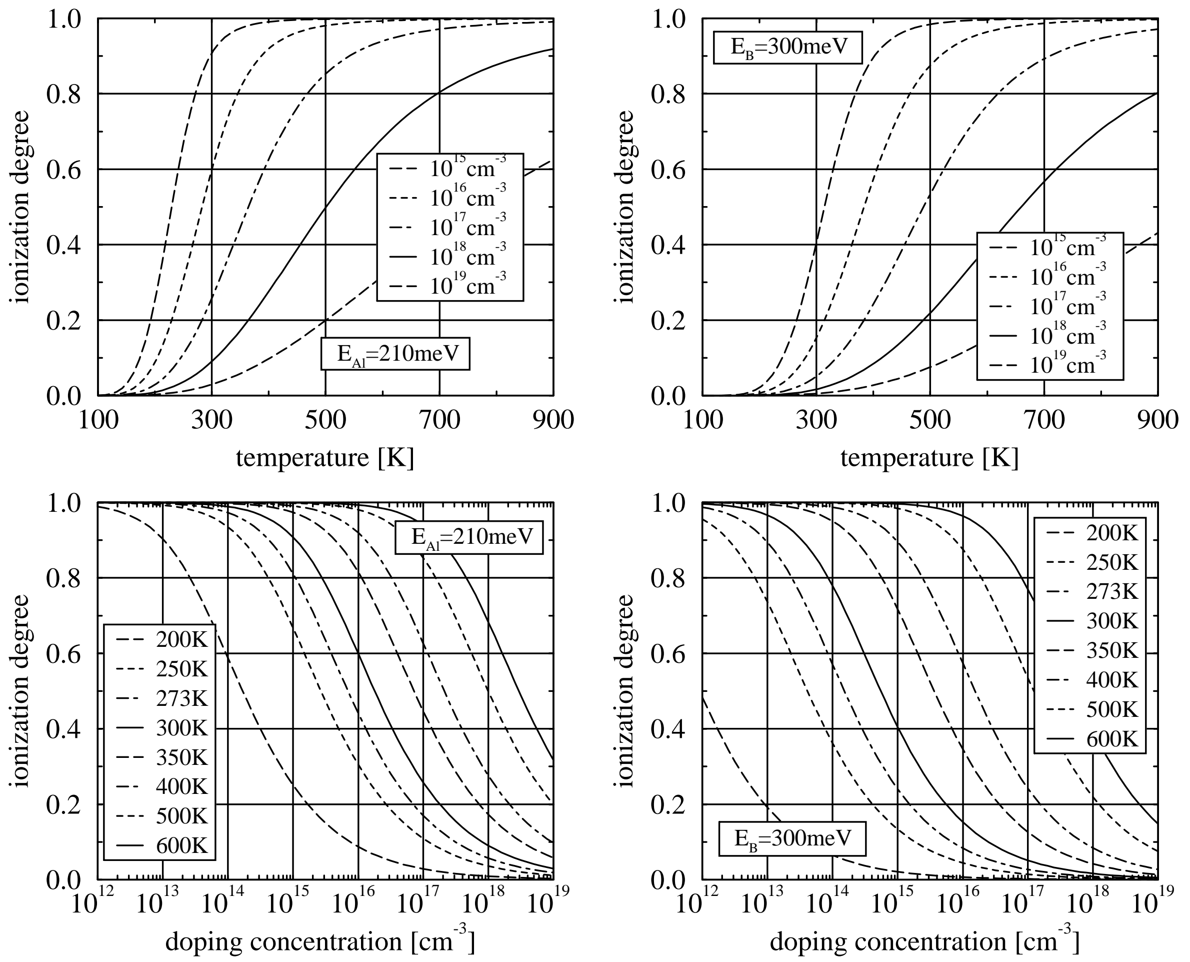


Figure 4.1: Ionization degree of Al (left) and B (right) in electrothermal equilibrium.

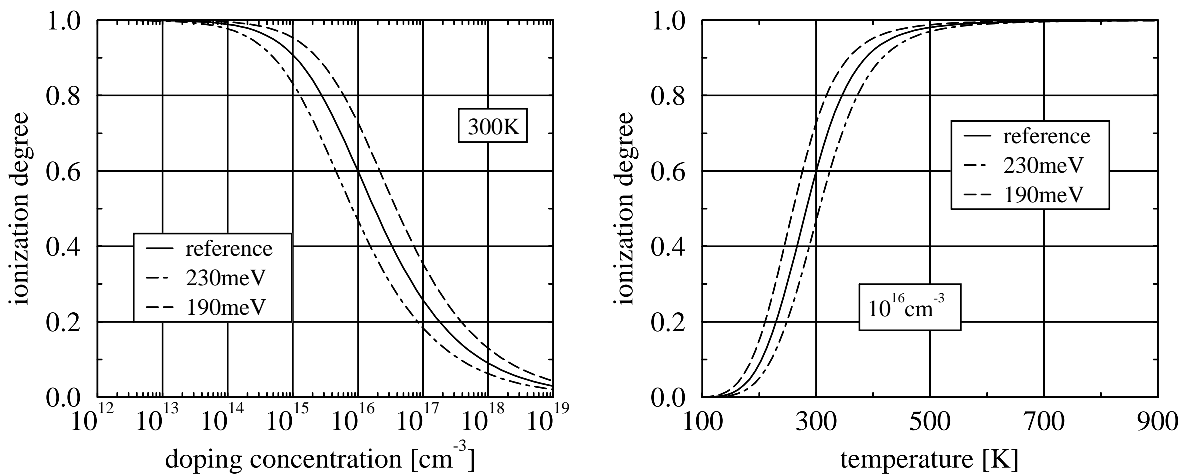


Figure 4.2: Influence of the ionization energy on the ionization degree of Al.

In case of N, the site dependence of the ionization energy has been reliably confirmed by experiment [143, 144]. As there are two cubic and one hexagonal lattice site in 6H-SiC and only one cubic and hexagonal lattice site in 4H-SiC, we obtain from the neutrality condition, Eq. (4.2),

$$n = N_{D_{hex}}^{+} + m \cdot N_{D_{cub}}^{+} \tag{4.5}$$

with $m = 2$ for 6H-SiC and $m = 1$ for 4H-SiC, respectively. In electrothermal equilibrium, Eq. (4.5) together with Eq. (2.89) yields a cubic relation for $E_F$. The resulting $\xi_D(T, N_D)$ is shown in Fig. 4.3. Incomplete ionization of N becomes only relevant at low temperatures and high doping concentrations. Here, more than 90 % of N is ionized for temperatures above 250 K and $N_D < 10^{16}\,\mathrm{cm}^{-3}$.

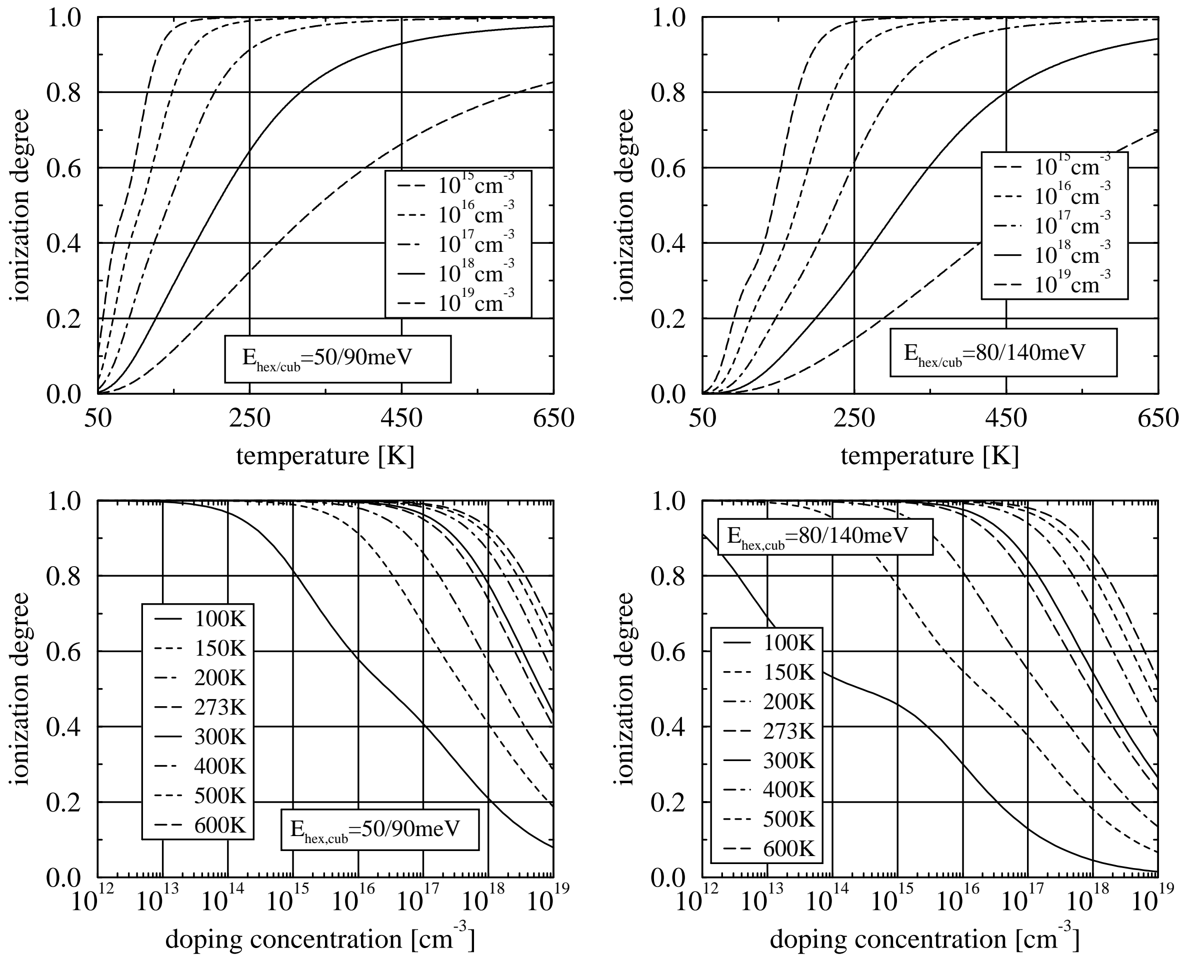


Figure 4.3: Ionization degree of N in 4H-SiC (left) and 6H-SiC (right) in electrothermal equilibrium.

In order to simplify calculations, a two-level donor is often approximated by a mean effective ionization energy $E'_D$ in literature [49, 113, 190]. At room temperature and $N_D < 10^{18}\,\mathrm{cm}^{-3}$, an error below 1% and 4% is obtained with $E'_D = 75\,\mathrm{meV}$ and $E'_D = 125\,\mathrm{meV}$ for 4H- and 6H-SiC, respectively (Fig. 4.4). The two-level system, however, becomes more and more evident at lower temperatures or center concentration as the deeper level can not yield any longer free carriers (Fig. 4.5).

Apart from the high injection conditions, the calculated ionization degree shown in Figs. 4.1 and 4.3 is

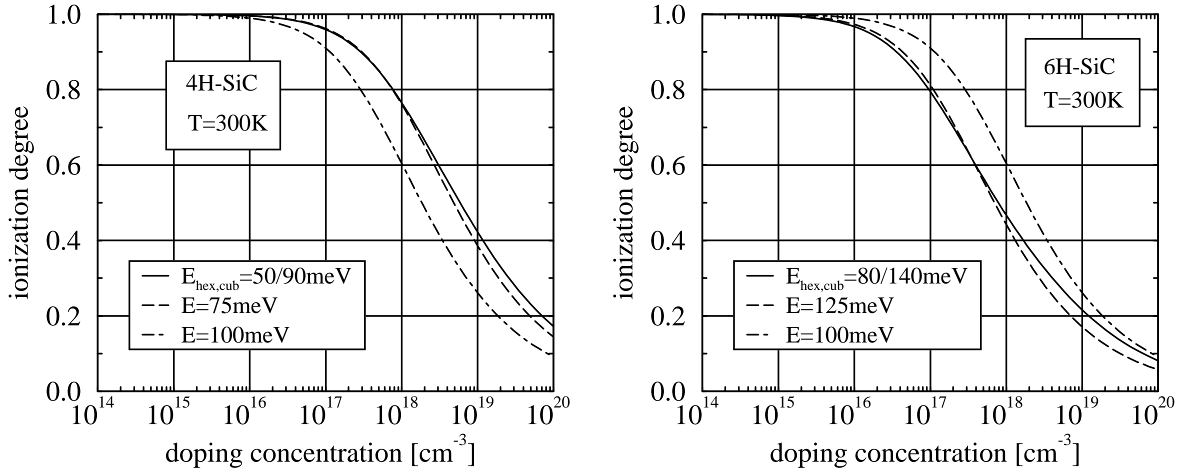


Figure 4.4: Approximation of a two-level donor by a mean effective ionization energy $E'_D$ for 4H-SiC (left) and 6H-SiC (right).

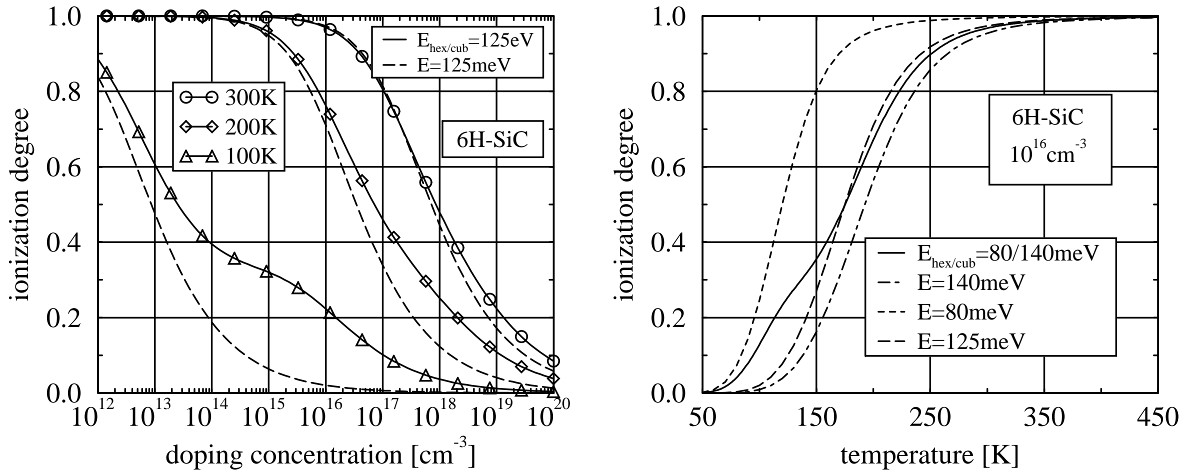


Figure 4.5: Error induced by a mean effective ionization energy $E'_D$ for 6H-SiC.

also obtained in neutral regions during stationary non-equilibrium conditions ("quasi-static approximation"). They can therefore be used to estimate the free carrier concentration in neutral regions which determine the corresponding serial resistance, provided that compensation effects are negligible.

The concentration of free carriers is reduced if compensating deep impurities or dopants of the opposite type are available. The ionization degree is again obtained by the solution of an appropriate formulated neutrality equation as shown in Fig. 4.6 for an Al-doped semiconductor with a compensating N impurity. Here, compensation effects become relevant for compensation ratios larger than 5 %. At higher doping concentrations and compensation ratios, the free carrier density will be smaller than the density of available dopant centers even at rather large temperatures[2].

[2]Please note that the ionizaion energy may decrease at large doping concentrations [211]. Hence, the figures presented in this section may keep valid only up to $10^{19}$ cm$^{-3}$.

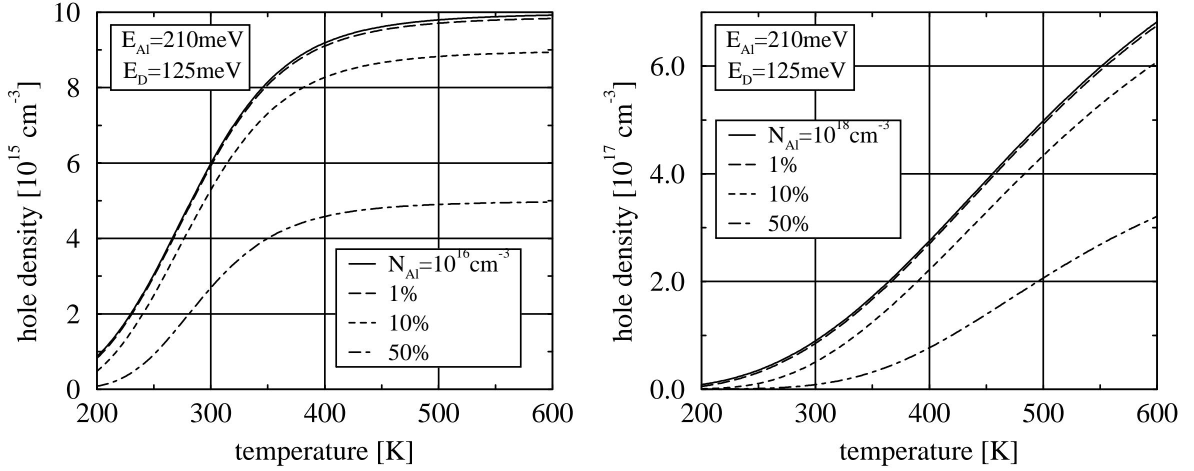


Figure 4.6: Influence of N-compensation on the free carrier density of an Al-doped layer at different compensation degrees and doping concentrations.

## 4.2 Measurement of ionization time constants

Whereas the static properties of incomplete ionized dopants are governed by their energetic level, the transient properties need to be described by emission and capture coefficients (see section 2.2.2) which are directly related to the capacitive response obtained by thermal admittance spectroscopy (TAS) and deep level transient spectroscopy (DLTS). Both methods basically yield the emission coefficient $e_V^{tp}$ as function of temperature within a limited temperature range.

Using Eqs. (2.57) or (2.58) together with Eq. (2.55) for donors or acceptors, respectively, the Arrhenius plot of the measured $(e_V^{tp}, T)$ pairs of values

$$\log\left(\frac{T^{2+\alpha}}{e_{n,p}}\right) = \frac{\Delta E_{D,A}}{k\ln(10)}\frac{1}{T} + \log\left(\frac{1}{\sigma^0_{n,p}\gamma_{n,p}}\right) \tag{4.6}$$

gives a straight line whose slope is a measure of $\Delta E_{D,A}$ and whose intercept with the $y$-axis is a measure for $\sigma^0_V$. Here, all additional parameters are summarized to

$$\gamma_{n,p} = \sqrt{96\pi^3} g_{D,A}^{-1} M_{C,V} \frac{k^2}{h^3} m^*_{e,p}\,. \tag{4.7}$$

As the temperature measurement range of TAS is well below the usually applied operation ranges for power devices which comprises temperatures larger than 230 K, a temperature extrapolation of $e_V^{tp}$ using Eqs. (2.57) or (2.58) is needed. Even though DLTS is not usually applied to investigate shallow centers, it can be used to extend the temperature range obtained from TAS. In this way, the temperature extrapolation of emission coefficients measured by TAS can be compared to independently measured values at lower temperatures.

Various types of pn- and Schottky-diodes of 4H/6H-SiC and up to 3 similar diodes of each type were measured. The samples were manufactured by Daimler-Benz AG, Frankfurt, using epitaxial layers and substrates of Cree Research Inc., Durham, NC. All diodes are planar and directed along the c-axis

(apart from the off-axis angle due to the epitaxial growth) with an active area of $A = 2.69 \cdot 10^{-3}\text{cm}^2$. The pn-junctions were formed by ion implantations approximately achieving box profiles. The $p^+n$-diodes were implanted with Al and B, the $n^+p$-diodes with N, respectively. In order to electrically activate the implantations, the samples were annealed at 1800 K. Schottky contacts were realized using titanium. An overview of the used samples is given in Tab. 4.2. Further details about the measurement setup can be found in [181].

| sample | | 6PN | 6S | 6NP | 4PN | 4S |
|---|---|---|---|---|---|---|
| polytype | | 6H | 6H | 6H | 4H | 4H |
| type | | $p^+n$ | n – Schottky | $n^+p$ | $p^+n$ | n – Schottky |
| implantation[a] | $[\text{cm}^{-3}]$ | $2.5 \cdot 10^{19}$ | - | $5.0 \cdot 10^{19}$ | $2.5 \cdot 10^{19}$ | - |
| depth | $[\mu\text{m}]$ | 0.5 | - | 0.6 | 0.5 | - |
| epitaxial layer | $[\text{cm}^{-3}]$ | $1.3 \cdot 10^{16}$ | $1.3 \cdot 10^{16}$ | $2.5 \cdot 10^{16}$ | $4.9 \cdot 10^{15}$ | $6.0 \cdot 10^{15}$ |
| thickness | $[\mu\text{m}]$ | 8 | 8 | 5 | 9 | 9 |

Table 4.2: Data of measured samples ([a]implanted atomic concentration).

All samples were characterized using CV and IV measurements to obtain the doping concentrations and the serial resistances which were estimated from the linear slope of the forward IV characteristics at high current densities (Fig. 4.7).

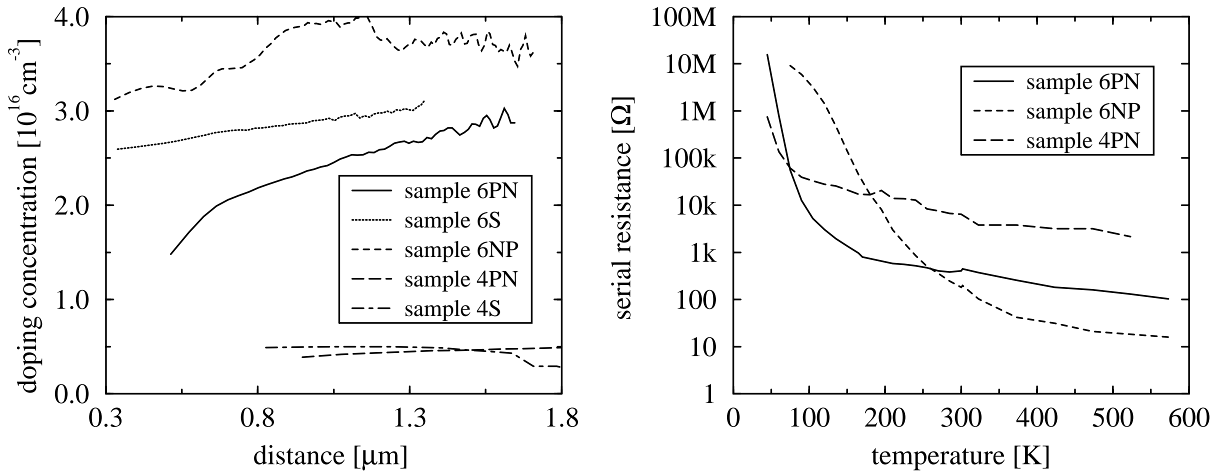


Figure 4.7: Serial resistance and doping profile of the investigated samples.

In the following sections, thorough investigations on measured TAS and DLTS data reveal the influence of serial resistances on these measurement methods. It is shown that $e_p^A$ of Al as the shallowest acceptor has to be measured with $p^+n$-diodes in order to preserve the direct relation between the measured signal and the quantity to be measured. Here, numerical investigations are needed to understand the measured TAS spectra which differ from those expected by standard TAS theory.

### 4.2.1 Thermal admittance spectroscopy (TAS)

Thermal admittance spectroscopy is based on the measurement of the conductance or capacitance of a reverse biased pn- or Schottky-junction dependent on temperature or frequency [182, 183].

In Fig. 2.2, the simulated band diagram of a reverse biased B-doped $n^+$p-diode is plotted. Far away from the junction within the p-region, the quasi-Fermi energy $E_{F_p}$ of holes nearly equals to its bulk value in electrothermal equilibrium. For $T < 350\,\mathrm{K}$ and $N_A = 2.5 \cdot 10^{16}$, the ionization energy $\Delta E_A$ is smaller than $E_{F_p} - E_V$ in correspondence to $\xi < 0.5$ (Fig. 4.1). If a small AC voltage is additionally applied, holes will be captured and emitted by the acceptor center in the vicinity of the crossing point between $E_A$ and $E_{F_p}$ at the edge of the depletion region. In Fig. 4.8, the transient evolution of the space charge region is shown for $\tau_p^A < T_{ac}$ ("quasi-static" signal) and $\tau_p^A > T_{ac}$ ("dynamic" signal) where $T_{ac}$ denotes the period of a sinusoidal voltage.

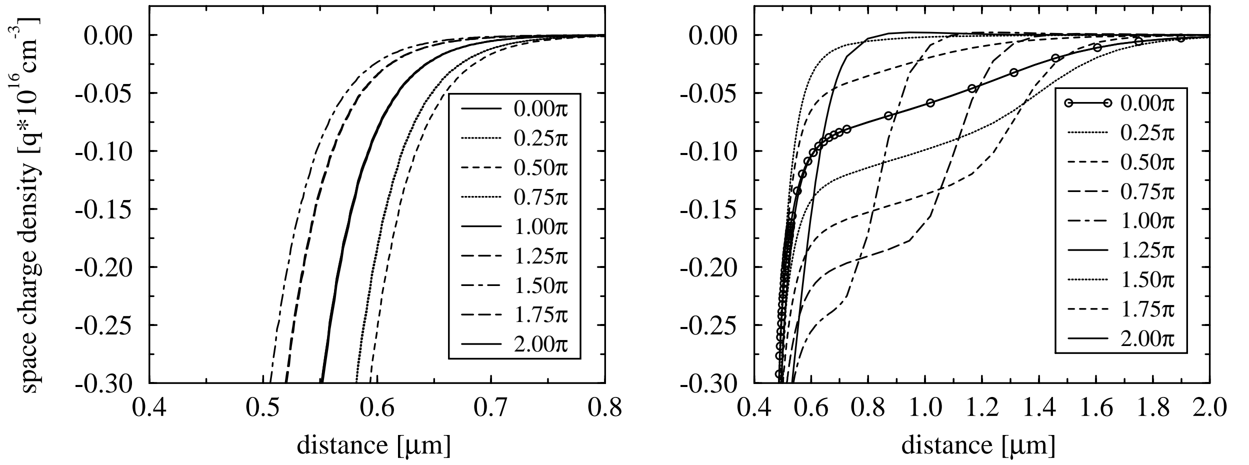


Figure 4.8: Transient evolution of the edge of the space charge region during one period for quasi-static (left) and dynamic (right) TAS signal.

For small frequencies and high temperatures, the emission and capture processes are faster than the external excitation. Here, the extension of the depletion region can be described by

$$w(t) = \sqrt{\frac{2\varepsilon_r\varepsilon_0(U_0 + U_{ac}(t) + U_{bi})}{q \cdot N_A}}\,. \tag{4.8}$$

As given in Eqs. (2.49), (2.55), and (2.58), the ionization time constant $\tau_A$ becomes larger than the period of the applied AC voltage with increasing frequency or decreasing temperature (see also Fig. 4.27). The basic mechanism of the resulting dynamically enlarged depletion region obtained in this case is analyzed in detail in section 5.4.1 by investigating the response of a pn-junction to a step-like excitation.

Whereas the minimum depletion region width always occurs at the minimum bias at $1.5\,\pi$, the maximum extension of the space charge region of the dynamic signal occurs already at $0.25\,\pi$, before the maximum bias at $0.5\,\pi$. The corresponding capacitance is reduced as the modulated charge at the edge

of the space charge region is smaller in this case. Finally, with $\tau_A \gg T_{ac}$, no ionization of acceptors takes place during one period and the high-frequency capacitance determined by the charge available in the neutral region at electrothermal equilibrium is obtained. Comparing both cases at $0.00\pi$, it becomes clear that the dynamic signal corresponds to a non-equilibrium situation with holes bound to the acceptor even though $E_{F_p} > E_A$. The resulting energy losses lead to a transition of the conductance $G(\omega)$ at constant temperature from its low-frequency value to a larger high-frequency value.

Constant temperature TAS spectra are obtained by plotting $C(\omega)$ or $G(\omega)$ with the temperature as parameter yielding low-to-high frequency transitions with $C_{LF} > C_{HF}$ and $G_{LF} < G_{HF}$. Alternatively, constant frequency TAS spectra can be evaluated by plotting $C(T)$ or $G(T)$ with the frequency as parameter. Here, a similar high-to-low temperature transition of the capacitance is obtained with $C_{HT} > C_{LT}$, whereas the conductance $G(T)$ shows a maximum because $e_p^A$ approaches zero with decreasing temperature. From analytical calculations can be concluded, that these inflection or maximum points are direct proportional to $e_p^A$,

$$e_\nu = k_{C,G}^{\omega,T} \cdot \omega, \tag{4.9}$$

with slightly different proportionality factors $k_{C,G}^{\omega,T}$ depending on the type of the TAS spectra [182]. For instance, $k_C^\omega = 1/1.98$ and $k_C^T = 1/1.825$ is obtained for the constant temperature and the constant frequency TAS spectrum of the capacitance, respectively.

Within the one-sided abrupt junction approximation, the peak heights of the spectra can be related to the impurity concentration by

$$G = \frac{e_\nu \omega^2}{e_\nu^2 + \omega^2} \frac{N_{tp}}{\nu} \sqrt{\frac{\varepsilon q N_D}{2(U_{bi} - U)}} \tag{4.10}$$

for the conductance and

$$C = \frac{e_\nu^2}{e_\nu^2 + \omega^2} \frac{N_{tp}}{\nu} \sqrt{\frac{\varepsilon q N_D}{2(U_{bi} - U)}} \tag{4.11}$$

for the capacitance [184]. However, it will be shown in the following section that serial resistances can significantly alter the peak heights and that Eqs. (4.10) and (4.11) keep not valid for signals arising from the highly-doped region of a pn-junction.

The measured temperature spectra of capacitance and conductance of sample 6PN, 4PN, and 6S are given in Fig. 4.9 - 4.11, respectively. From the extracted $\Delta E_{D,A}$, the observed peaks in sample 4PN (Fig. 4.9), for instance, can be related to B, Al, and the cubic site of N from high to low temperatures whereas the increasing signal at the lowest temperature is due to the freeze-out of free carriers as shown in the following section.

### 4.2.2 Simulation of TAS: Serial resistances and doping profiles

Both measurement methods, TAS and DLTS, are based on measuring the admittance of a pn- or Schottky-diode. Thus, additional serial resistances can significantly influence the results. Equating

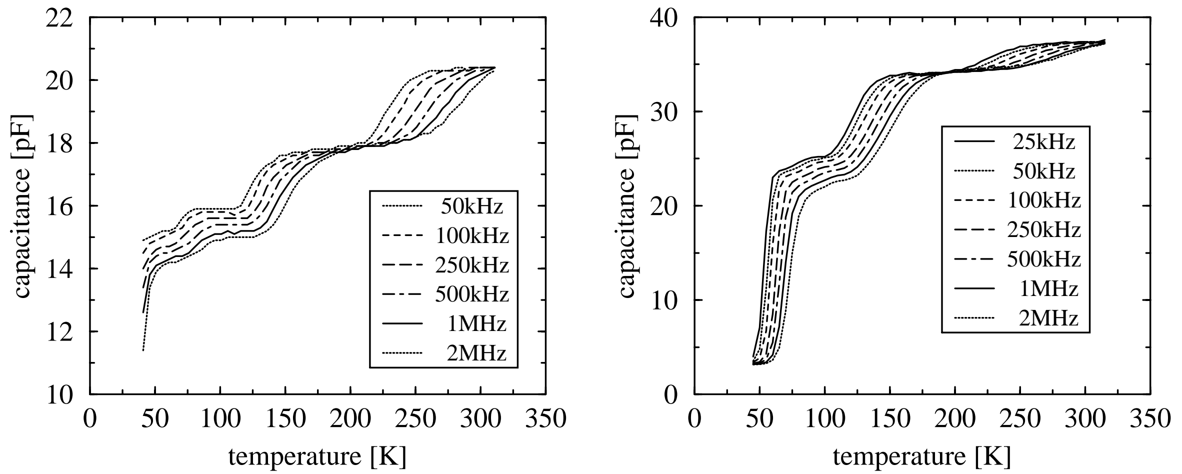


Figure 4.9: Measured TAS capactiance spectra of sample 4PN (left) and 6PN (right).

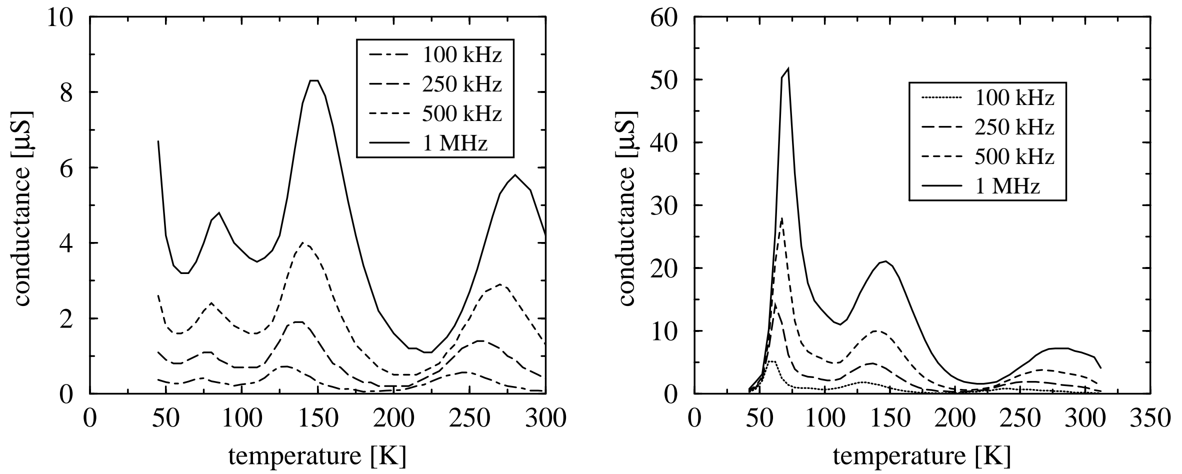


Figure 4.10: Measured TAS conductance spectra of sample 4PN (left) and 6PN (right).

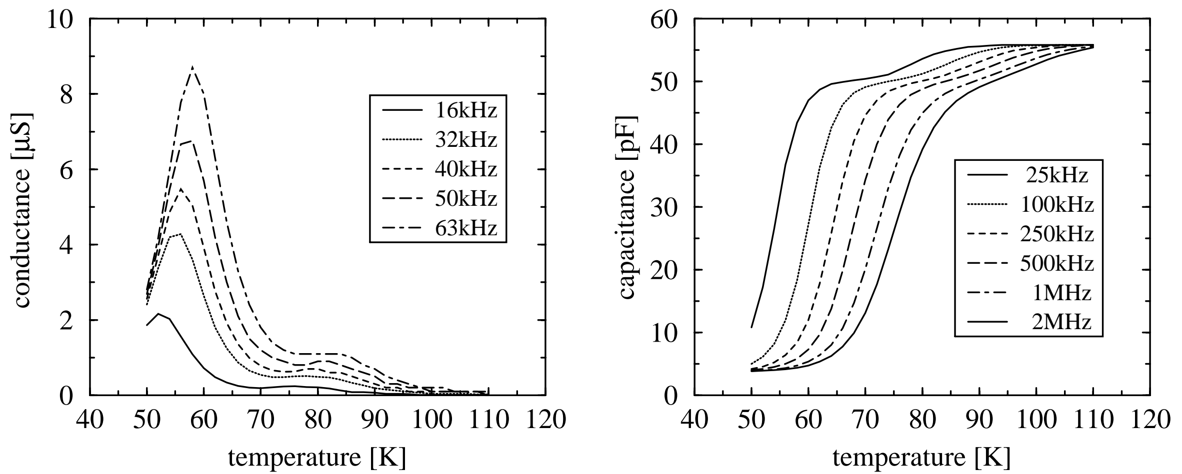


Figure 4.11: Measured TAS conductance (left) and capacitance (right) spectra of sample 6S.

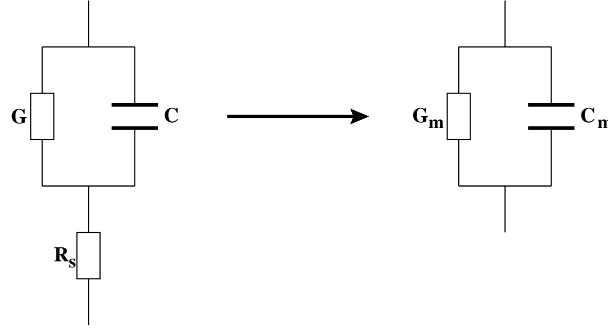


Figure 4.12: Equivalent circuit of admittance measurement.

the admittance of the equivalent circuit including and excluding a serial resistance (Fig. 4.12), the relation between real and measured capacitance and conductance reads

$$G^{-1} = \frac{1}{G_m - R_s(\omega^2 C_m^2 + G_m^2)} - 2R_s \tag{4.12}$$

$$C = \frac{C_m}{(1 - G_m R_s)^2 + (\omega C_m R_s)^2} \tag{4.13}$$

or similarly

$$G_m = \frac{G(1+GR_s) + \omega^2 C^2 R_s}{(1+GR_s)^2 + (\omega C R_s)^2} \tag{4.14}$$

$$C_m = \frac{C}{(1+GR_s)^2 + (\omega C R_s)^2}\,. \tag{4.15}$$

Neglecting the junction conductance $G$, we obtain by Eq. (4.15)

$$\omega_c C R_s = 1 \Longrightarrow C_m = C/2\,. \tag{4.16}$$

Hence, a serial resistance will dominate the measured capacitance if $\omega$ approaches the cut-off frequency $\omega_c$ defined by Eq. (4.16). Besides the contact resistances, the serial resistance of a diode is composed of the layer resistance of the substrate, the epi-layer, and the implanted region, respectively:

$$R_s(T) = \sum_i^{layers} \frac{1}{q\nu^{(i)}(T)\mu_\nu^{(i)}(T)} \frac{l^{(i)}}{A}\,. \tag{4.17}$$

The density of free carriers $\nu^{(i)}$ will be reduced with decreasing temperature due to incomplete ionization of the dopants. As shown in Fig. 4.19, this freeze-out process exponentially sets on at lower temperatures depending on the ionization energy and the center concentration.

#### 4.2.2.1 Simulation of TAS spectra

In Fig. 4.13, the simulated (see appendix B) constant temperature TAS conductance and capacitance spectra of an $n^+p$-diode are shown. First, the capacitive signal arising from the center dynamics

of the acceptor of the p-layer ("dynamic signal") is obtained before the freeze-out process (see Eq. (4.15)) becomes dominant ("freeze-out signal") as described previously. Using Eqs. (4.4) and (4.17), the resistance of the p-doped epi-layer and substrate at $T = 220\,\mathrm{K}$ is calculated to $89\,\Omega$ which results in $f_c = 120\,\mathrm{MHz}$. At lower frequencies, the transition of the capacitance from its low-frequency to high-frequency value is observed with $e_p^A$ given by the inflection point and Eq. (4.9). With increasing temperature, this point is exponentially shifted towards higher frequencies as given by Eq. (2.58). As expected, the G(f) curve shows a corresponding inflection point. Subsequently, the conductance further increases with increasing frequency as given by Eq. (4.14).

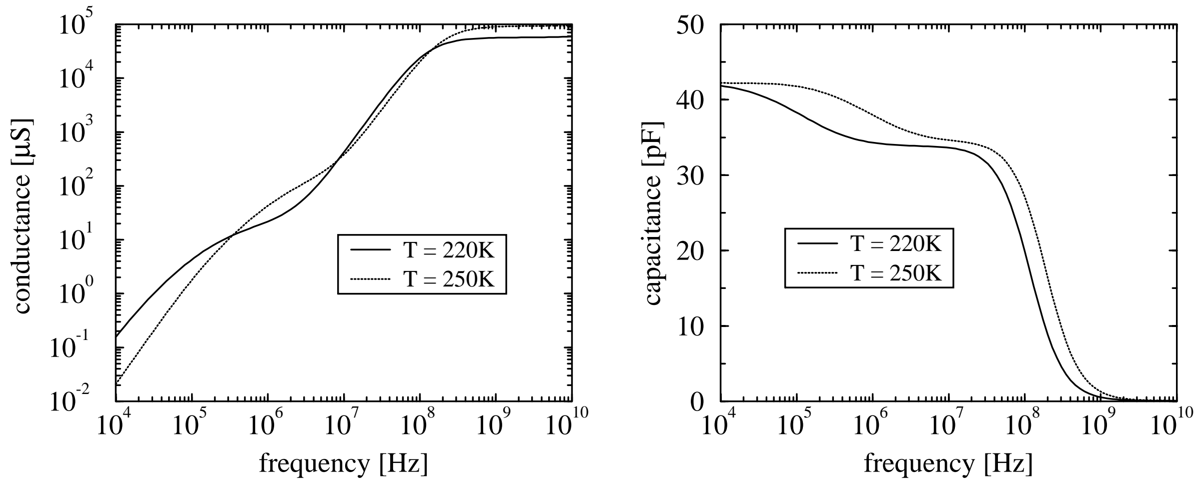


Figure 4.13: Simulated constant temperature TAS conductance (left) and capacitance (right) spectra of an $n^+$p-diode.

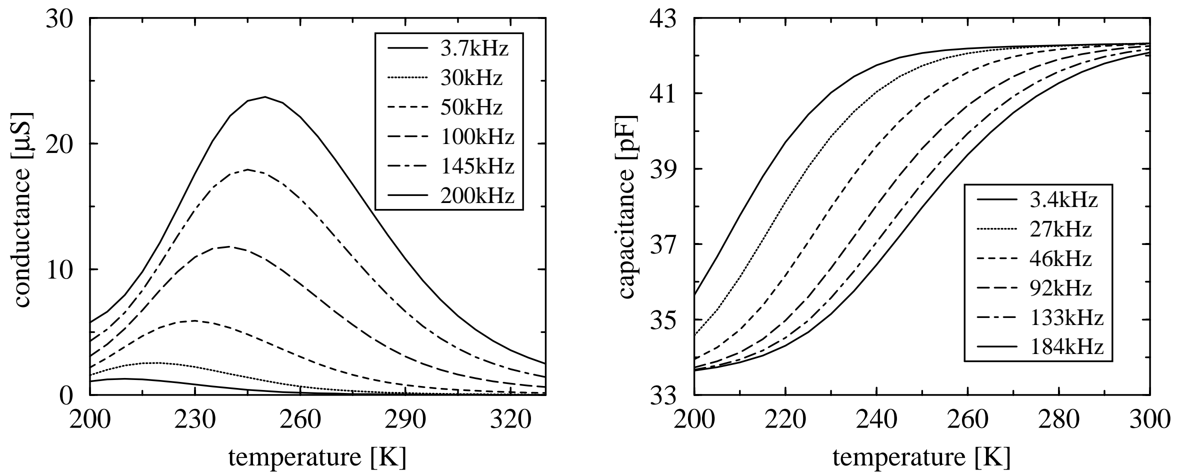


Figure 4.14: Simulated constant frequency TAS conductance (left) and capacitance (right) spectra of an $n^+$p-diode: "Dynamic signal".

Performing such simulations at various temperatures and subsequently extracting C and G at a given frequency yield the corresponding constant frequency TAS spectra (Figs. 4.14 and 4.15) which can be

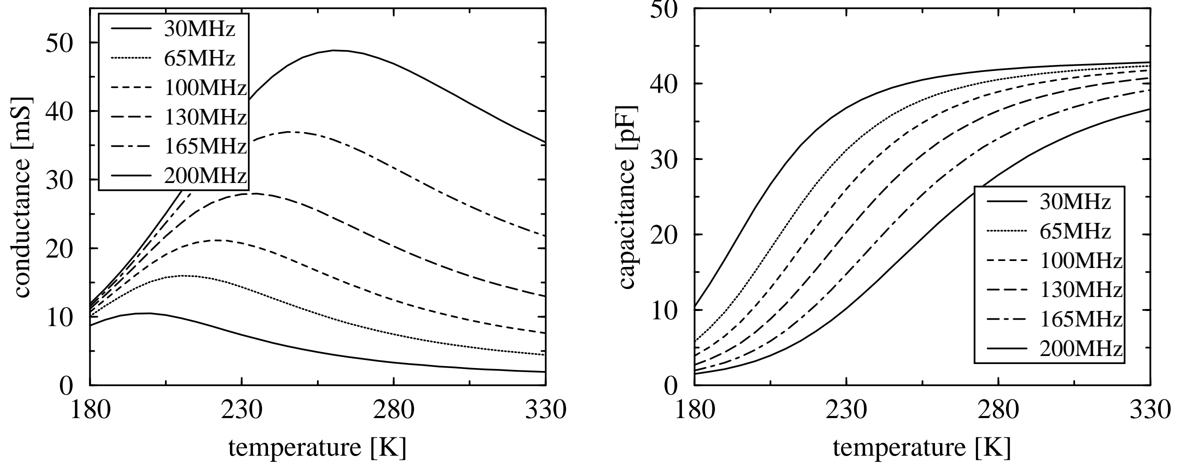


Figure 4.15: Simulated constant frequency TAS conductance (left) and capacitance (right) spectra of a $n^+$p-diode: “Freeze-out signal”.

directly compared with the measured TAS spectra. As can be seen, the information obtained by constant temperature and constant frequency TAS is identical with respect to both, the extracted emission coefficient $e_p^A$ and the peak height. However, the simulation of the capacitive constant temperature thermal admittance spectrum is less critical with respect to time and numerical limits[3]. Therefore, it will be used for all further investigations even though no direct comparison between measured and simulated data is achieved.

#### 4.2.2.2 Evaluation of “freeze-out signal”

It is obvious that the freeze-out signal should not be evaluated according to Eq. (4.6). Assuming a power law for the temperature dependence of the mobility $\mu_\nu(T) = \mu_\nu^{T_0}\,(T/T_0)^{\alpha_\nu^{mob}}$ (see Eq. (3.11)) and using Boltzmann statistics, Eq. (2.19), the modified Arrhenius plot

$$\log\left(\frac{\omega}{T^{\frac{3}{2}+\alpha_\nu^{mob}}}\right) = \frac{\left|E_{C,V} - E_{F_{n,p}}\right|}{k\ln(10)}\frac{1}{T} + y_i' \tag{4.18}$$

gives a straight line whose slope is a measure for the quasi-Fermi energy $E_{F_\nu}$, provided that this energy is nearly independent of temperature [186]. This holds for compensated materials where $E_{F_{n,p}}$ equals $E_{D,A}$ at low temperatures (Fig. 4.19). Thus, the shallow energy level which governs the freeze-out process is obtained. For instance, using Eq. (4.6) for the peak of $150\,\mathrm{K} < T < 250\,\mathrm{K}$ of the conductance spectrum of sample 6NP (Fig. 4.16), the very small extracted value of $\Delta E_A = 150\,\mathrm{meV}$ clearly indicates that this peak arises from the freeze-out of holes in the substrate and epi-layer. Depending on the mobility temperature coefficient $\alpha_\nu^{mob}$, the modified Arrhenius plot (4.18) yields an ionization energy $\Delta E_A$ of about 200 meV as expected for Al. However, besides the uncertainties of this method due to its direct dependence on $\alpha_\nu^{mob}$ [185], this extraction method does not yield the capture cross section $\sigma_\nu^{tp}$ which is needed to characterize the dynamic behavior of the center.

[3]The impact of the extremely small values of the minority carrier density leads to a larger low temperature limit of the simulated conductive TAS spectrum compared to the simulated capacitive TAS spectrum.

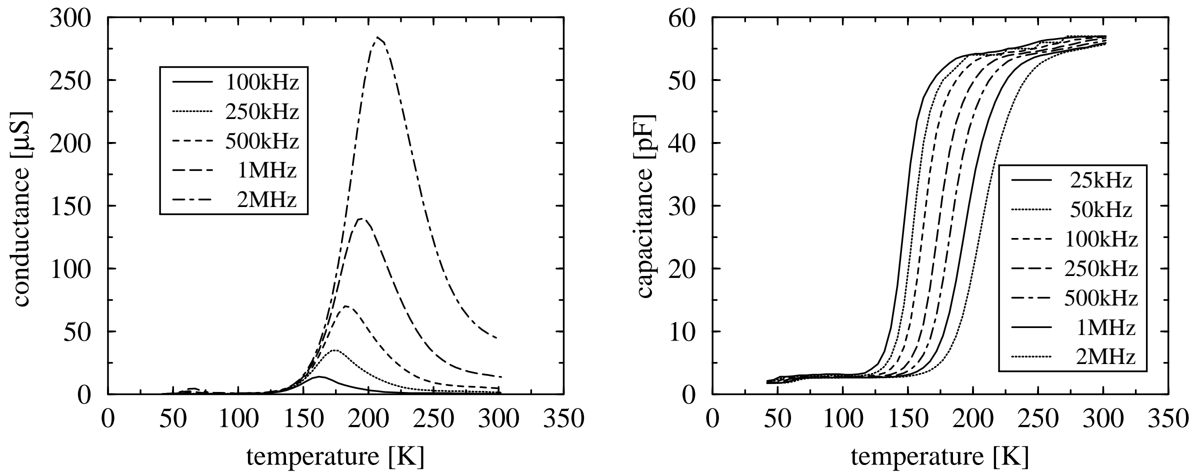


Figure 4.16: Measured TAS conductance (left) and capacitance (right) spectra of sample 6NP.

This finding is corroborated by the simulated constant temperature TAS spectrum of capacitance of sample 6NP (Fig. 4.17), confirming the significance of the freeze-out of holes as the dominant process. The freeze-out signal dominates the dynamic signal which can be visualized by specifying an artificially high conductivity in the p-substrate in order to reduce the serial resistance.

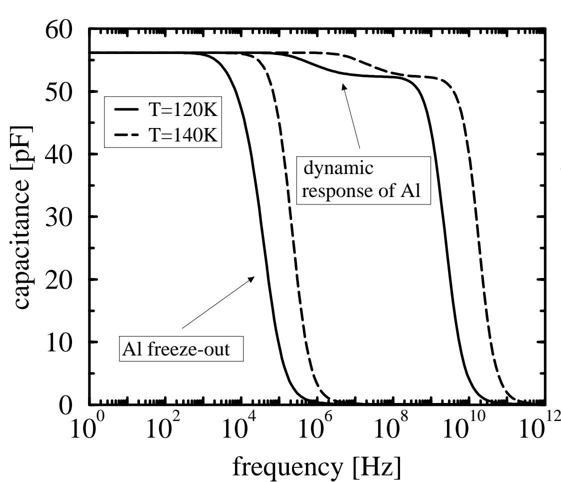


Figure 4.17: Simulation of sample 6NP with a realistic ($5\,\frac{\mathrm{cm}^2}{\mathrm{Vs}}$, left curves) and an artificially high ($10^6\,\frac{\mathrm{cm}^2}{\mathrm{Vs}}$, right curves) mobility.

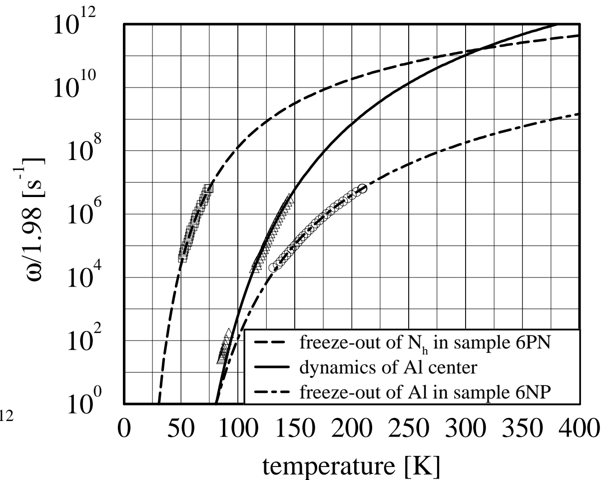


Figure 4.18: Freeze-out diagram of Al of sample 6PN and 6NP.

#### 4.2.2.3 Concept of TAS applied to the highly-doped part of a pn-junction

Eq. (4.17) gives evidence that mainly the ohmic resistances of substrate and epi-layer contribute to $R_s$ because of the larger layer thickness $l$ and the lower doping concentration compared with the implanted layer. Using a $p^+$n-diode instead of an $n^+$p-diode, the shallowest center in the lowly doped layers is

no longer Al but the hexagonal site of N resulting in a freeze-out of free carriers at significantly lower temperatures.

In order to calculate the $p^+$-layer resistance, Eq. (4.2) together with Eqs. (2.88), (2.89), and (2.19) must be solved with respect to $E_F$. Inserting the values given in Tabs. 4.1 and 4.2 (assuming 10 % electrical activation of the implanted acceptors), we obtain a temperature dependence of $E_F$ and $R_s$ as given in Fig. 4.19. Comparing this data with the measured serial resistance (Fig. 4.7) reveals good agreement within the freeze-out region at lower temperatures. At higher temperatures, on the other hand, significantly higher measured values are obtained which are probably due to poor non-linear contact resistances on the p-type implanted layer[4].

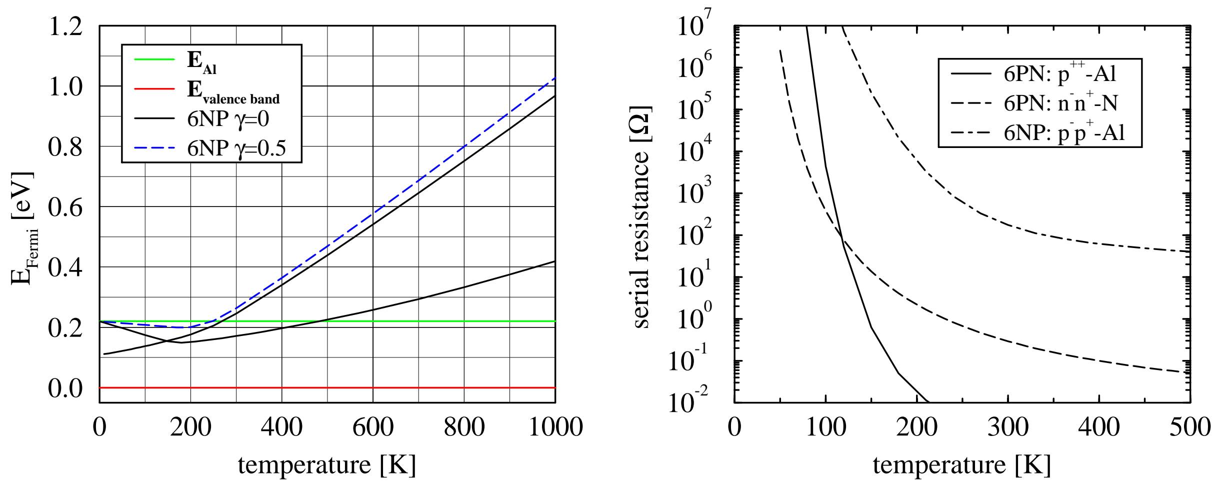


Figure 4.19: Calculated Fermi energy (left) and corresponding serial resistance (right) of samples 6NP and 6PN.

Using this data, the freeze-out characteristics of sample 6PN and sample 6NP with respect to the dynamic signal of Al in 6H-SiC can be compared by constructing a so-called "freeze-out diagram" as shown in Fig. 4.18. The measured (symbols) pairs of value $\left(\frac{\omega}{k_C^\omega}, T\right)$ of sample 6PN and their extrapolation (lines) are plotted together with the corresponding pairs of value obtained by the freeze-out signals from sample 6PN and 6NP. The solid curve corresponds to the dynamic signal $e_p = \frac{\omega}{k_C^\omega}$ (see Eqs. (2.58) and (4.9)) of Al as shown in Fig. 4.32. The freeze-out curves of sample 6NP and 6PN are obtained by evaluating the peaks of the corresponding freeze-out signals using the conventional Arrhenius plot, Eq. (4.6). It can be seen that the freeze-out signal of sample 6NP is obtained at larger temperatures thus suppressing the signal arising from the dynamics of Al. The freeze-out signal of sample 6PN, on the other hand, sets on at lower temperatures, thus enabling the reliable characterization of Al using this structure.

Similar considerations can now be taken into account for B. In Fig. 4.21, the "freeze-out diagram" of sample 6NP assuming a B-doped epi-layer is shown. Here, the simulated freeze-out curve appears

[4]The serial resistance of sample 6PN and 4PN has been extracted from the linear slope of the forward IV characteristics (Fig. 4.7) which probably overestimates the real serial resistance in reverse direction as the metal-semiconductor system of the ohmic contact (which has possibly rectifying characteristics at low temperatures) is forward biased in this case.

at lower temperatures as the curve obtained by the measured (symbols) pairs of values $\left(\frac{\omega}{k_C^\omega}, T\right)$ and their extrapolation (lines) which corresponds to B in Fig. 4.32. Hence, the freeze-out process becomes dominant at temperatures below those at which the dynamic signal of B is obtained and both signals are well separated in the simulated constant temperature TAS spectrum of capacitance (Fig. 4.20). This finding results from the smaller capture cross section $\sigma_p$ of B compared with Al. Therefore, TAS performed on B-doped n$^+$p- or Schottky-diodes with sufficiently low $R_s$ and ohmic contact resistances can be interpreted using Eq. (4.6) and yields the correct emission coefficients. However, dependent on $R_s$ of the investigated sample, the situation might arise that both effects are visible within the same temperature range which would then lead to a broadened peak in the spectrum as already reported for Schottky diodes with B as the shallowest center [142].

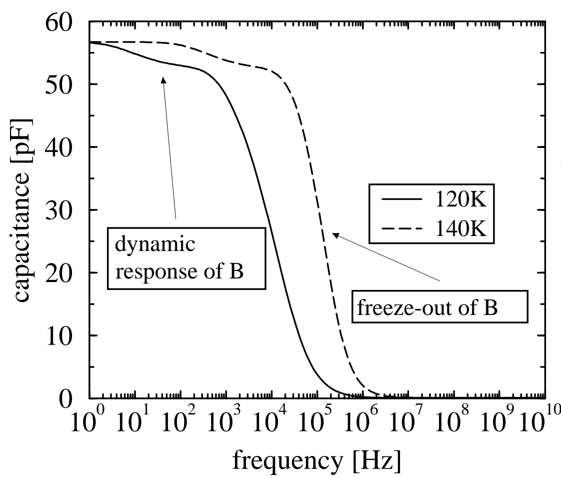


Figure 4.20: Simulation of sample 6NP assuming a B-doped epi-layer.

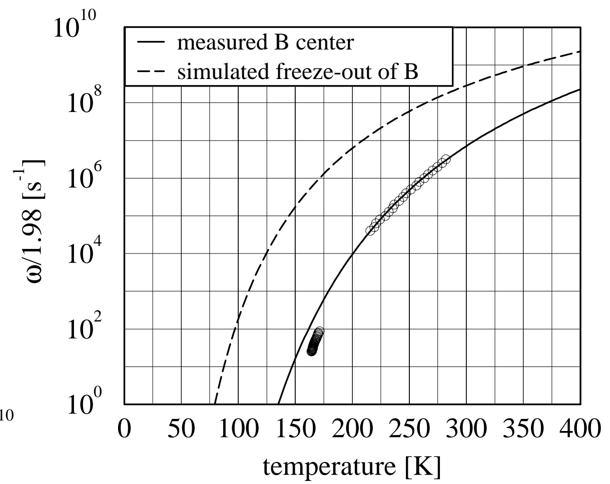


Figure 4.21: Freeze-out diagram of B of sample 6NP.

The effect of $R_s$ can also be estimated from the capacitance spectrum of TAS (Fig. 4.9). If $R_s$ is negligible, no frequency dependence of capacitance is obtained between two neighboring peaks as it can be seen between the peaks related to Al and B. On the other hand, the decreasing measured capacitance with increasing frequency between the peaks of Al and $N_c$ can be clearly related to the corresponding increase of $R_s$. At a given temperature, the influence of $R_s$ reduces the measured capacitance more at higher frequencies, thus significantly altering the obtained peak heights. The extracted quantities $\Delta E_{D,A}$ and $\sigma_{n,p}$, however, are not influenced by this effect provided that $R_s$ varies only moderately with temperature.

#### 4.2.2.4 Evaluation of TAS signals arising from the highly-doped part of a pn-junction

In general, TAS measurements are performed at Schottky-diodes or at the lowly doped region of pn-diodes. TAS theory relies on the one-dimensional, one-sided abrupt junction approximation which will not be valid when evaluating signals arising from the highly doped region of a pn-diode.

The p$^+$-region of sample 6PN is about three orders of magnitude shorter than the width of the depletion

region in the $n^-$-region. Hence, the capacitive dynamic signal of B and Al in sample 6PN would intuitively expected to be very small. Additional effects must be relevant as the measured dynamic signals are in the same order of magnitude than those expected from signals arising from dopant centers in lowly doped regions.

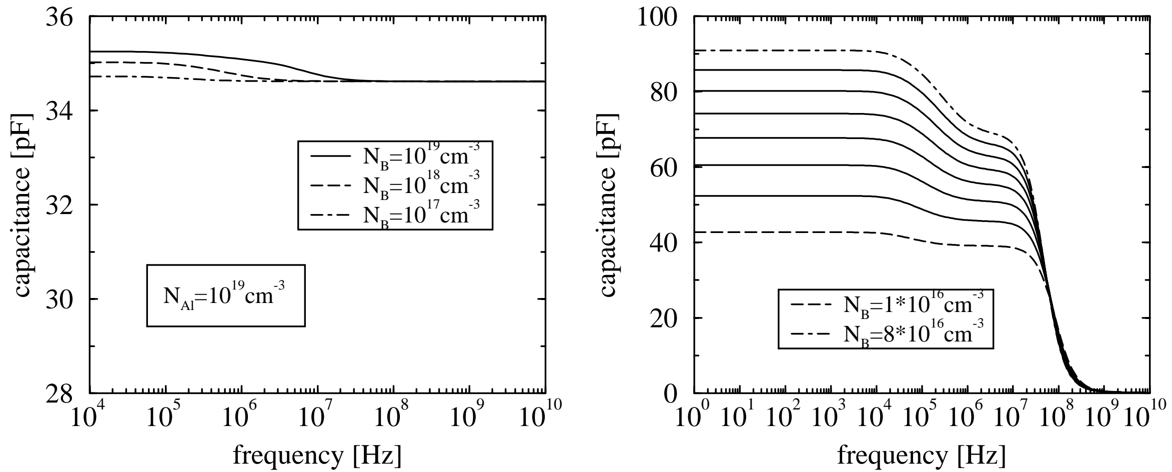


Figure 4.22: Dependence of B dynamic signal on center concentration in sample 6PN (left) and 6NP (right).

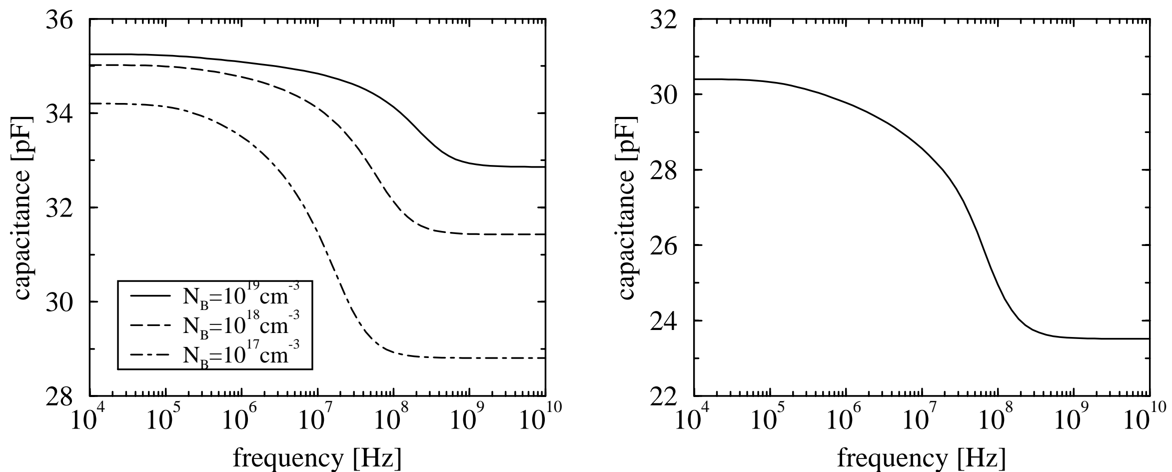


Figure 4.23: B dynamic signal in sample 6PN excluding (left) and including (right) the center profile of Fig. 4.24.

In order to understand the TAS signals arising from the highly doped part of a pn-junction, two different case studies are investigated: (a) B acting as an additional acceptor below Al (two-level system), and (b) B acting as single acceptor (one-level system) within a $p^+$-layer.

In Fig. 4.22, the simulated dynamic signal of B for case (a) is shown dependent of the center concentration, assuming the structural data of sample 6PN and 6NP, respectively. The signal of both samples increases with increasing center concentration as given by Eq. (4.11).

Performing the same simulation for case (b) with B as shallowest acceptor (without Al), this finding is

also obtained with sample 6NP. However, significant larger dynamic signals are observed with sample 6PN which decrease with increasing acceptor concentration (left part of Fig. 4.23). The inflection point due to the dynamic signal, however, occurs at the same frequency in all cases.

For low doping concentrations, the crossing point of the energy level of the investigated center and the corresponding quasi-Fermi energy is always situated at the edge of the depletion region. All centers within the depletion region are ionized due to the electric field. Considering the band diagram of sample 6PN at the operation point (Fig. 4.24), it becomes clear that the crossing point of the quasi-Fermi energy $E_{F_p}$ and the acceptor level $E_A$ is situated very close to the junction at $0.5\,\mu$m. The major difference between the B signals of sample 6PN and 6NP is that the dynamic signal arises approximately near the maximum of the space charge density at $x_m$ within the $p^+$ depletion region as shown in Fig. 4.24. In contrast to the situation in lowly doped regions, incomplete ionization occurs at this point within the depletion region as well because of the high center concentration.

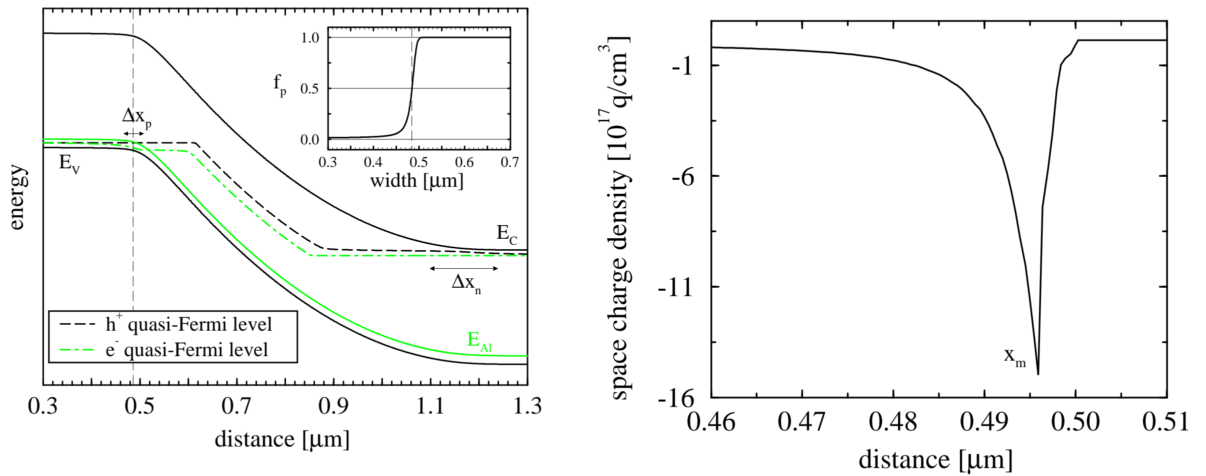


Figure 4.24: Energy band diagram of sample 6PN at the operation point including the occupation propability of Al (left) and corresponding space charge density (right).

The basic mechanisms leading to the observed findings can be understood by considering the schematic of the depletion regions within both, the highly-doped and the lowly-doped region at the operation point (Fig. 4.25). As non-ionized acceptors are generally still available at $x_m$ within the highly-doped region, the charge is modulated predominantly in the vicintiy of this point at low frequencies.

In case (a) at high frequencies with $\tau_B \gg T_{ac}$, most of the charge required to sustain the external AC bias is still available at $x_m$ (Al centers) and only a small fraction of the modulated charge is shifted to the edge of the depletion region $w_{0-2}$. Therefore, $\Delta C_{LF-HF} = C_{LF} - C_{HF}$ is only very small. $C_{HF}$ is independent of $N_B$, as the junction capacitance is mainly determined by the doping concentration of the $n^-$-region and $x_m$ depends only weakly on $N_B$ provided that $N_B < N_{Al}$ (left part of Fig. 4.22).

In case (b) at high frequencies, the region where the charge is modulated is completely shifted from $x_m$ to $w_{0-2}$, thus leading to a larger $\Delta C_{LF-HF}$ (Fig. 4.23 left). Here again, the edge of the depletion region $w_{0-2}$ dependents only weakly on $N_B$ as the ionization degree $\xi$ within the depletion region can still alter. The dynamic extension of the depletion region width decreases with increasing center concentration as

the charge yet available within the neutral region at electrothermal equilibrium increases. Hence, the increase of $C_{LF}$ will be smaller than the increase of $C_{HF}$. Thus, $\Delta C_{LF-HF}$ decreases with increasing center concentration.

Dynamic signals arising from the lowly-doped region of a pn-junction will increase with increasing $N_B$ because of $w_{max}/w_\infty(\xi)$ and $\xi(N)$ as shown in section 5.4.1 and appendix E.

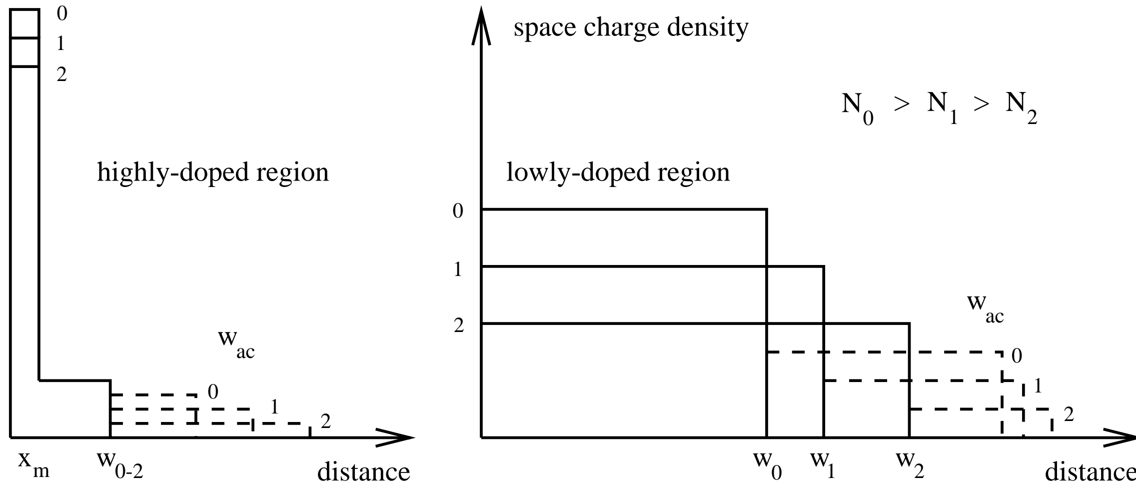


Figure 4.25: Schematic evolution of the space charge regions with TAS dynamic signal arising from the highly-doped (left) and the lowly-doped (right) region of a pn-junction dependent on doping concentration.

#### 4.2.2.5 Influence of doping profile

Any conclusions regarding the magnitude of the dynamic signal of Al must be qualitative because of the influence of the serial resistance. However, comparing the measured (Fig. 4.9) and simulated (left part of Figs. 4.22 and 4.23[5]), it seems that only a small fraction of the implanted Al is electronically active.

In the case of B acting below Al as a two-level system which corresponds to case (a) in the previous section, measured peaks are significantly larger than the simulated ones. This finding can be explained by the fact that identical box profiles have been assumed for both, Al and B. It is well known that B is incorporated deeper and additionally diffuses during the annealing process. Therefore, a more realistic doping profile of sample 6PN probably consists of an Al box profile and a deeper B profile with unknown shape as shown in Fig. 4.26. Here, a rather deep gaussian profile was assumed in order to demonstrate the effect on the resulting constant temperature TAS spectrum (Fig. 4.23). In the right part of Fig. 4.26, the corresponding distribution of the space charge density is shown. The positive space charge density within the $p^+$-region (part III) results from diffusion of holes from the Al box profile.

The transition of $C_{LF}$ to $C_{HF}$ corresponds to a shift of the modulated charge from part III to part I in Fig. 4.26, thus leading to a more than 100 % larger magnitude of the signal compared to Fig. 4.22.

[5]The magnitude of a signal is independent of the center species.

There is only a minor influence on the static forward IV and CV characteristics by introducing such an additional gaussian profile. Additionally, no influence on the freeze-out characteristics of the $p^+$-layer can be observed as only the neutral layers located behind the edges of the depletion region contribute to the serial resistance. Hence, the large measured magnitude of the signal of B in sample 6PN can be considered as indirect proof for the existence of a doping profile qualitatively shaped as shown in Fig. 4.26.

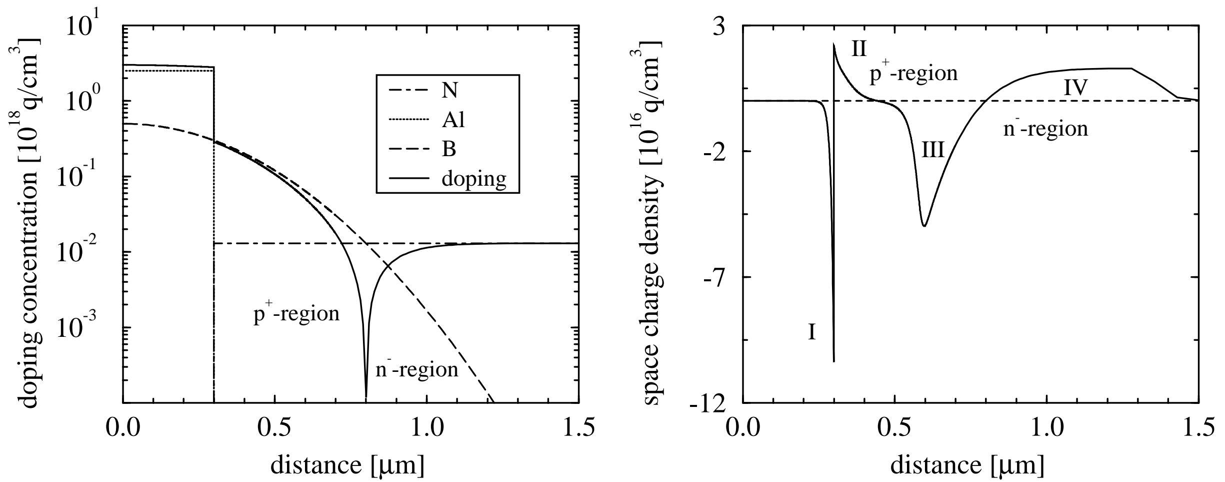


Figure 4.26: Doping profile of sample 6PN (left) and corresponding space charge region at at the operation point (right).

### 4.2.3 Deep level transient spectroscopy (DLTS)

DLTS is based on the measurement of the transient evolution of the capacitance of a Schottky- or pn-junction as sketched schematically in Fig. 4.27. A short “filling pulse” is applied to a reverse biased junction. It should not forward bias the junction, but only reduce the width of the depletion region[6]. After switching back to the initial reverse bias operation point, free carriers will be emitted by donors and deep traps with an energy level beyond the corresponding quasi-Fermi energy in order to relax towards electrothermal equilibrium. Again, this corresponds to a dynamically extended depletion region with a transition of a dynamically reduced capacitance to its stationary value. Hence, the emission coefficient of the investigated center is directly measured just as in the case of the TAS. However, this process must be slow enough in order to being able to detect the transient change in capacitance. Considering Eqs. (2.57) and (2.58), this implies a temperature range well below that of TAS. Therefore, DLTS is generally used to characterize deep levels acting in addition to the shallow doping centers of an investigated structure.

[6]This corresponds to DLTS using majority carriers. We do not consider DLTS using minority carriers which is performed by forward biasing a junction.

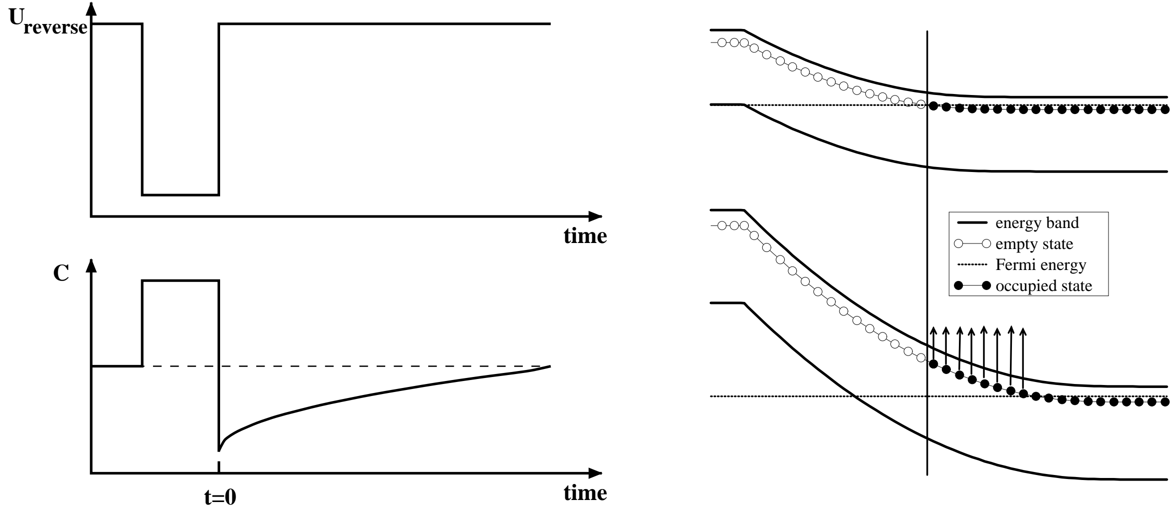


Figure 4.27: Response of the capacitance during DLTS measurement (left) and corresponding energy diagram (right).

#### 4.2.3.1 Basic theory

A general theory for DLTS is given for instance in [187]. Applying the parallel plate capacitance approximation of a reverse biased one-dimensional abrupt junction, the dynamically extended depletion region after switching back to the reverse operation point at $t = 0$ (Fig. 4.27) is given by

$$w(t) = \sqrt{\frac{2\varepsilon(U_{bi} - U)}{q\left(N_0 - N_{tp}^{occ}(t)\right)}} \tag{4.19}$$

resulting from the charge arising of a shallow impurity level with concentration $N_0$ which is partly compensated by the occupied deep traps $N_{tp}^{occ}(t)$. The corresponding transient capacitance is calculated by

$$C(t) = \frac{\varepsilon A}{w(t)} = A\sqrt{\frac{\varepsilon q N_0}{2(U_{bi} - U)}\left(1 - \frac{N_{tp}^{occ}(t)}{N_0}\right)} \tag{4.20}$$

to be

$$C(t) = C_0\sqrt{1 - \frac{N_{tp}\exp[-e_{\nu}^{tp}t]}{N_0}} \tag{4.21}$$

with

$$C_0 = A\sqrt{\frac{\varepsilon q N_0}{2(U_{bi} - U)}}. \tag{4.22}$$

Eq. (4.22) can be approximated by

$$C(t) = C_0\left(1 - \frac{N_{tp}\exp[-e_{\nu}^{tp}t]}{2N_0}\right) \tag{4.23}$$

provided that $N_0 \gg N_{tp}$. The difference of the capacitance at two instants of time is thus given by

$$\Delta C_{1,2} = C(t_2) - C(t_1) = C_0 \frac{N_{tp}}{2N_0} (\exp[-e_\nu t_1] - \exp[-e_\nu t_2]) \tag{4.24}$$

which yields a maximum when plotted as function of temperature ("classical" DLTS spectrum). With

$$\frac{d\Delta C_{1,2}}{de_n} = 0 \Longrightarrow e_n^{max} = \frac{\ln\left(\frac{t_2}{t_1}\right)}{t_2 - t_1}. \tag{4.25}$$

we obtain $(e_\nu^{tp}, T)$ pairs of values by varying the time window of measurement $(t_1, t_2)$. Considering the signal arising from the transient ionization of a single deep dopant center such as Al, the concentration $N_A^{occ} = N_A - N_A^{emp}(t)$ of ionized dopants has to be substitued for $(N_0 - N_{tp}^{occ}(t))$ in Eq. (4.19) which corresponds to sustituting $N_A$ for $N_0$ in Eq. (4.21).

The approximation of $C(t)$ by Eq. (4.24) is thus no longer valid similar to the case of high trap concentrations. Hence, Eq. (4.21) has to be used instead and a modified DLTS spectrum ("quadratic" DLTS spectrum) is obtained by squaring the measured capacitance at $t_1$ and $t_2$,

$$\Delta C_{1,2}^2 = C(t_2)^2 - C(t_1)^2 = \left(C_0 \frac{N_{tp}}{N_0}\right)^2 (\exp[-e_n t_1] - \exp[-e_n t_2]), \tag{4.26}$$

again yielding Eq. (4.25) as condition for a maximum. For instance, the maximum obtained by Al in sample 6PN (Fig. 4.28) is shifted by about 1.15 K which would correspond to an error of about 50 % for $e_p$ if this peak would be evaluated using Eq. (4.24) ("classical" DLTS spectrum) instead of Eq. (4.26) ("quadratic" DLTS spectrum)[7].

In Fig. 4.28, the measured DLTS spectra of sample 4PN and 6PN are shown. The peaks are identified as $N_{cub}$, Al and B in sample 4PN, and Al, and B in sample 6PN from the left to the right, respectively.

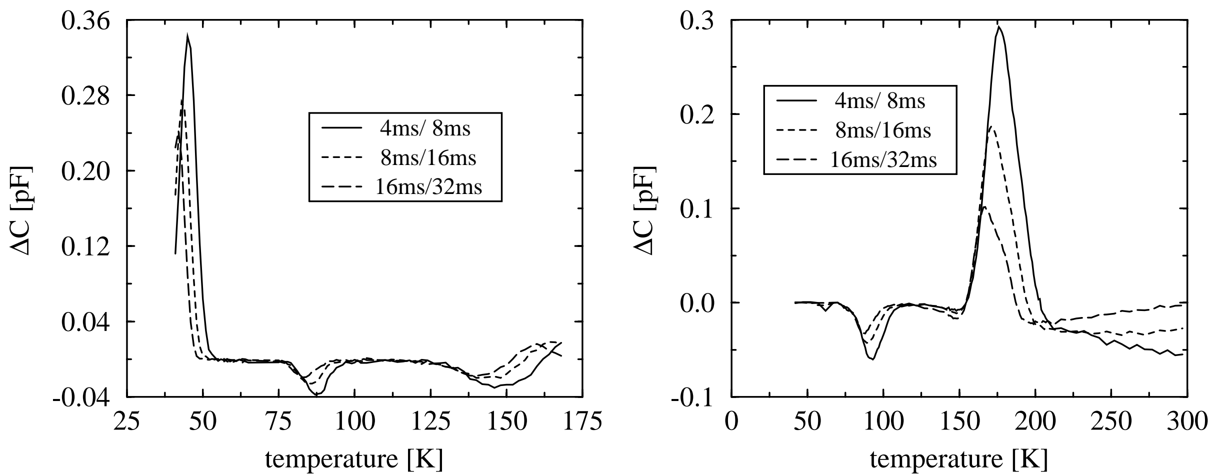


Figure 4.28: DLTS spectra of sample 4PN (left) and 6PN (right).

[7] All DLTS plots shown in this section are based on the "classical" DLTS spectrum for convenience. However, the data shown in Fig. 4.32 and Tab. 4.3 is evaluated using Eq. (4.26).

#### 4.2.3.2 Influence of serial resistance

Note that some of the observed DLTS peaks are minima. This is a consequence of the serial resistance. By differentiating Eq. (4.13),

$$\begin{aligned}\Delta C &= \frac{dC}{dC_m}\Delta C_m \\ &= \frac{(1-G_mR_s)^2-(\omega C_mR_s)^2}{((1-G_mR_s)^2+(\omega C_mR_s)^2)^2}\Delta C_m\,, \end{aligned} \tag{4.27}$$

we obtain as condition for the transition of a maximum to a minimum in the DLTS spectrum in the case of a constant serial resistance:

$$C_m > \frac{1-G_mR_s}{\omega R_s}. \tag{4.28}$$

Using Eqs. (4.26) and (4.13), the influence of a constant serial resistance can be calculated as shown in Fig. 4.29. No temperature shift of the maximum of a "classical" DLTS spectrum occurs which corresponds to the validity of Eq. (4.24). After changing the sign, the magnitude of the signal first increases again with increasing $R_s$ before it finally disappears at a very large $R_s$. The "quadratic" DLTS spectrum, on the other hand, is significantly distorted by a constant $R_s$ and must be corrected for $R_s > 1\,\mathrm{k\Omega}$.

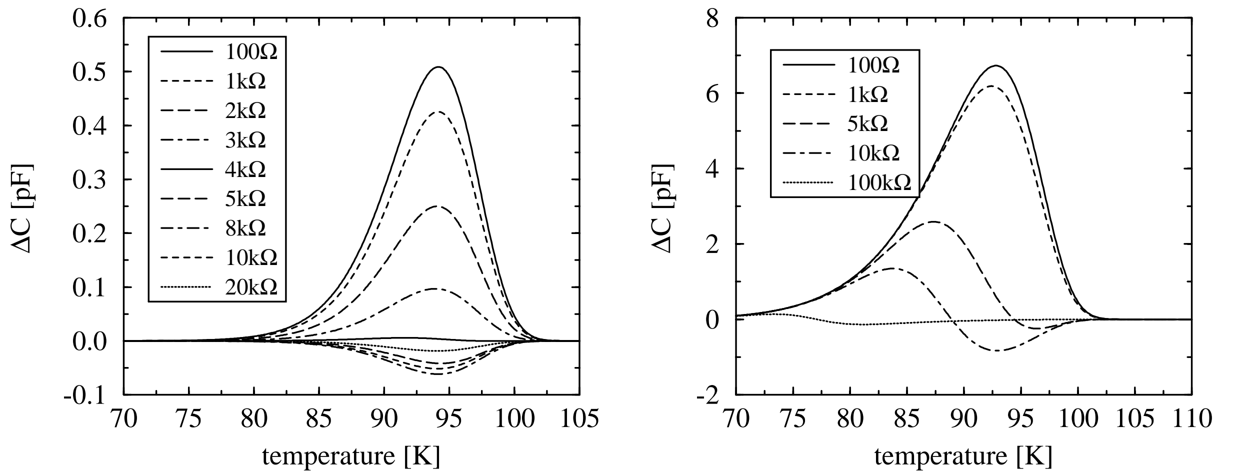


Figure 4.29: Influence of a constant serial resistance on a "classical" (left) and a "quadratic" (right) DLTS signal.

Considering the calculated serial resistance of sample 6PN shown in Fig. 4.19, it becomes evident that $R_s$ already significantly increases within the temperature range of the measured B signal (Fig. 4.28). Using this serial resistance dependent on temperature to calculate the DLTS spectrum of Al, we observe a minimum with a rather small signal height for both, the "classical" and the "quadratic" DLTS spectrum (Fig. 4.30). The transition of an undistorted DLTS signal towards this minimum can be visualized by scaling $R_s(T)$. The double peak structure obtained in the "quadratic" DLTS spectrum with constant $R_s$ (Fig. 4.29) is observed in both cases only during this transition. The temperature shift

of the minimum is below 3 K within the range of measured peaks for Al (see Fig. 4.28), leading to an error of $e_p$ about 100% when evaluating the distorted signal.

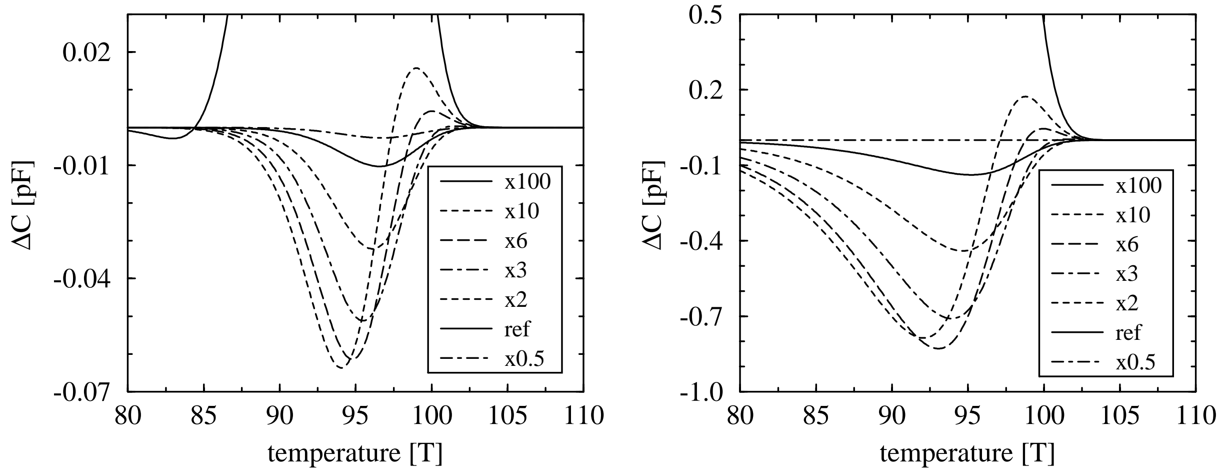


Figure 4.30: Influence of calculated temperature dependent serial resistance on a "classical" (left) and a "quadratic" (right) DLTS signal.

Considering the fact that the real serial resistance can not be precisely measured[3], it becomes clear that any correction of the measured DLTS spectra would not be very reliable and the results of DLTS within these operating conditions can only be regarded as a very coarse estimation. The analytical calculations shown in Figs. 4.29 and 4.30 yield a rough estimate of the qualitative and quantitative characteristics of the real DLTS spectrum. As a result, a double-peak structure due to the large serial resistance would be expected in case of sample 6NP because of the long and lowly Al-doped epilayer which is experimentally confirmed as shown in Fig. 4.31.

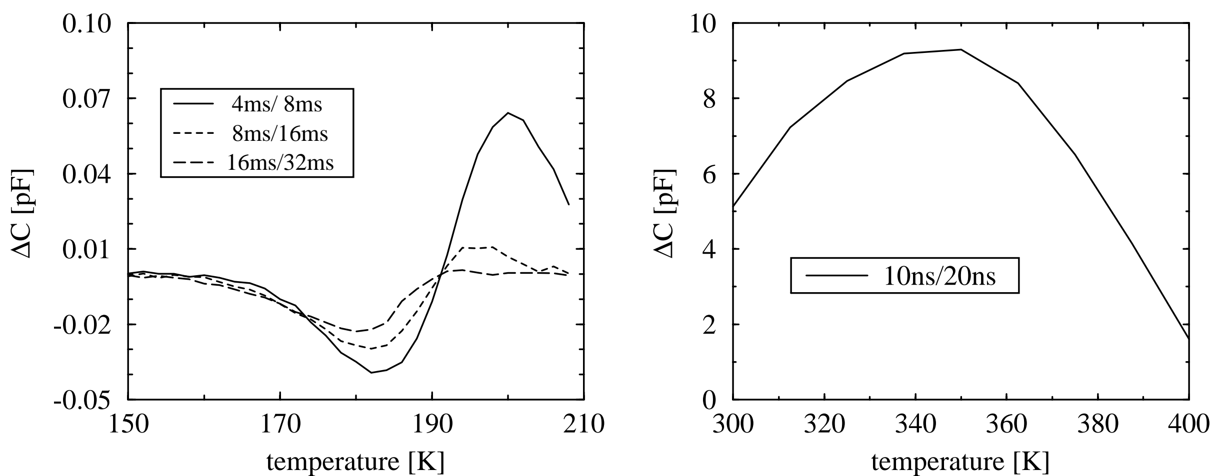


Figure 4.31: Measured DLTS spectrum of sample 6NP (left) and simulated DLTS spectrum of sample 6PN at high temperatures (right).

The fact that Al as shallowest acceptor in a $p^+$n-diode can be detected using DLTS is also confirmed by the freeze-out signal of sample 6PN obtained by TAS at 1 MHz at temperatures lower than 75 K (Fig. 4.9). The Al values obtained by DLTS are measured at the same frequency above this temperature (80 - 90 K).

#### 4.2.3.3 DLTS at the highly-doped part of a pn-junction

The general theory of DLTS presented in the previous section is based on homogeneously doped, abrupt junctions, and the parallel plate capacitance approximation. It can not be directly applied to a signal obtained from the highly-doped region of a pn-junction. Therefore, the measurement of the ionization time constants of Al and B using DLTS has to be confirmed by numerical simulation. Here, the low temperatures und the corresponding extremely low minority carrier concentrations prevent from directly comparing measured and simulated data. Significant convergence problems have been observed for temperatures below 150 K.

However, the principal characteristics of DLTS signals arising from the highly-doped region of a pn-junction can also be investigated at higher temperatures by extracting the emission coefficient from a simulated DLTS spectrum of sample 6PN using Eq. (4.25). To this end, a reverse voltage pulse with a very short risetime superimposed by an alternate sinusoidal bias is applied to a pn-junction in electrothermal equilibrium. The resulting transient $U(t)$ response has to be multiplied with the signal of a reference source in order to obtain the transient capacitance $C(t)$ (see appendix B). Evaluating such simulated data as function of temperature using Eq. (4.26) yields the DLTS spectrum shown in the right part of Fig. 4.31. Inserting the temperature $T = 335\,\mathrm{K}$ of the maximum and the parameters of B given in Tab. 4.3 into Eq. (2.58) results in the same emission coefficient as obtained by Eq. (4.26). Hence, Eq. (4.26) can also be applied to DLTS peaks arising from the highly-doped region of a pn-junction.

## 4.3 Ionization energy and capture cross sections of N, Al, and B in 4H/6H-SiC

A plot of the measured emission coefficients of B, Al, and the cubic site of N in 4H- and 6H-SiC versus temperature is shown in Fig. 4.32. The lower values were measured with DLTS, the higher ones with TAS which is the more suitable method in this case as values can be detected over nearly three orders of magnitude. Moreover, these values are closer to the temperature range of interest for device applications.

The Arrhenius plot, Eq. (4.6), of all maxima observed in the different samples yield straight lines with very small standard deviations. Tab. 4.3 summarizes $\Delta E_{D,A}$ and $\sigma_{n,p}$ which were extracted from TAS measurements using Eq. (4.6) for the two models of $\sigma_{n,p}(T)$, respectively. Signals due to the hexagonal site of N can not be clearly separated from the freeze-out of free carriers as shown in section 4.2.2. Therefore, the extracted data of those signals is rather uncertain and was excluded from Tab. 4.3.

Using Eqs. (2.57) and (2.58) together with Eq. (2.55) and the data of Tab. 4.3, the values obtained by TAS were extrapolated for temperature independent capture cross sections (solid line) and $\sigma_\nu \propto$

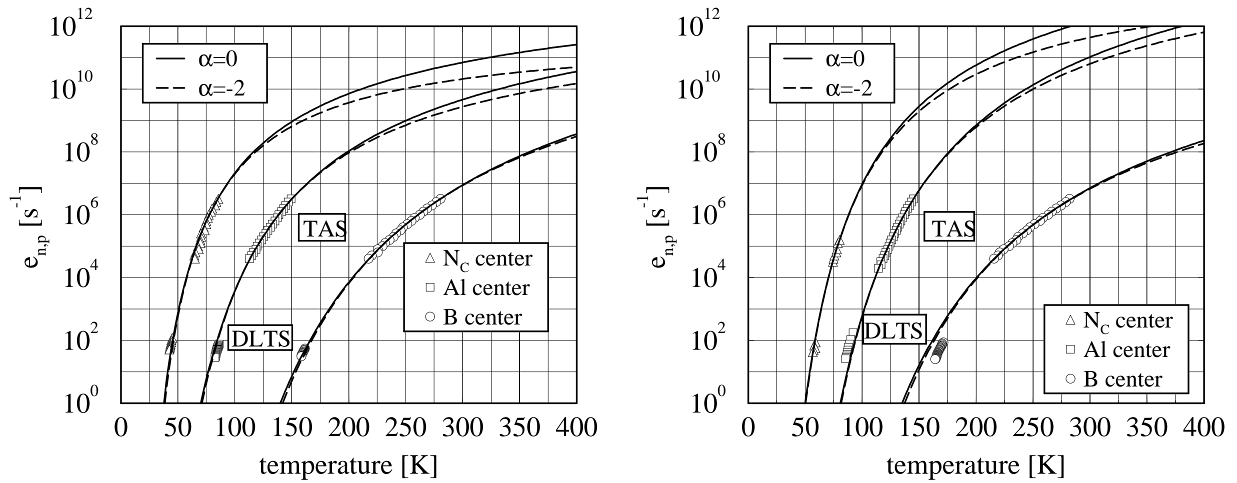


Figure 4.32: Measured (symbols) and extrapolated (lines) emission coefficients of $N_c$, Al and B in 4H-SiC (left) and 6H-SiC (right) for capture cross sections independent (solid) and dependent (dashed) of temperature.

$T^{-2}$ (dashed line). The extrapolation shows an excellent agreement between the values independently measured by TAS and DLTS, confirming its validity towards lower temperatures. Therefore, it should give at least a valid approximation for the high-temperature range. Only this range is affected by the uncertainty of the correct temperature dependence of $\sigma_\nu$. Smaller $e_\nu$ are resulting from $\sigma_\nu \propto T^{-2}$ and can be interpreted as worst-case estimation for evaluating transient incomplete ionization effects in 4H/6H-SiC devices.

| center | | $\alpha = 0$ | | $\alpha = -2$ | | measured in sample |
|---|---|---|---|---|---|---|
| | | $\Delta E$[meV] | $\sigma_\nu$[cm$^2$] | $\Delta E$[meV] | $\sigma_{\nu_0}$[cm$^2$K$^2$] | |
| 6H | $N_{cub}$ | 127 | $3.22 \cdot 10^{-13}$ | 140 | $1.42 \cdot 10^{-8}$ | 6S |
| 6H | Al | 225 | $4.49 \cdot 10^{-12}$ | 240 | $2.90 \cdot 10^{-7}$ | 6PN |
| 6H | B | 300 | $3.71 \cdot 10^{-15}$ | 343 | $1.67 \cdot 10^{-9}$ | 6PN |
| 4H | $N_{cub}$ | 77 | $7.92 \cdot 10^{-15}$ | 90 | $3.57 \cdot 10^{-10}$ | 4S |
| 4H | Al | 189 | $2.58 \cdot 10^{-13}$ | 208 | $2.57 \cdot 10^{-8}$ | 4PN |
| 4H | B | 312 | $2.10 \cdot 10^{-14}$ | 375 | $9.69 \cdot 10^{-9}$ | 4PN |

Table 4.3: Ionization energies and capture cross sections obtained by TAS.

# Chapter 5

# Simulation of 4H/6H-SiC devices

In section 2 to 4, the basic framework for the simulation of SiC electronic devices has been outlined and identified as an extension of the electrothermal drift-diffusion transport model which has been widely used for design and optimization of Si devices for many years [112]. The extensions have been introduced in order to properly account for specific physical mechanisms especially relevant to SiC. It is the scope of this chapter to systematically evaluate the applicability of this approach to state-of-the-art SiC devices, first by comparing simulated and measured device characteristics within a wide range of operation conditions and, second, by investigating the impact of the implemented models on the device characteristics. The latter results yield the basis for qualitatively estimating the relevance of these models for a specific device design and allow for appropriate validation by measurement.

## 5.1 The PN-junction - Evaluation of material parameters and models

Being one of the basic building blocks of electronic devices, we first consider the pn-junction by investigating the stationary forward and reverse characteristics of several 6H-SiC pn-diodes. In the following sections, a detailed numerical analysis of measured forward and reverse pn-diode characteristics within a wide temperature range will be given. The influence of various possible physical models is analyzed and the results are discussed with respect to a simplified analytical one-dimensional pn-diode theory [154, 155] in order to evaluate their specific impact on device characteristics.

#### (a) Basic analytical theory

Assuming an abrupt pn-junction, low injection conditions, and Boltzmann statistics, the one-dimensional IV characteristics of a pn-diode can be analytically described by

$$J(U) = \frac{qW n_i}{2\tau_{R-G}} \left( \exp\left[\frac{qU}{2kT}\right] - 1 \right) + q \left( \sqrt{\frac{kT}{q}\frac{\mu_n}{\tau_n}}\frac{n_i^2}{N_A^-} + \sqrt{\frac{kT}{q}\frac{\mu_p}{\tau_p}}\frac{n_i^2}{N_D^+} \right) \left( \exp\left[\frac{qU}{kT}\right] - 1 \right) . \quad (5.1)$$

The total current density consists of two contributions: the current arising from carrier recombination[1] within the depletion region and the current carried by minority carrier diffusion[2]. Generally, the recombination mainly arises within the lowly-doped area of the depletion region. Therefore, $\tau_{R-G}$ can be identified as the corresponding minority carrier lifetime $\tau_n$ or $\tau_p$ in this case (see section 3.6.1). In reverse direction, $\tau_{R-G}$ denotes the so-called generation lifetime.

The bulk recombination current is coupled to the diffusion current via the diffusion length

$$L_\nu = \sqrt{D_\nu \tau_\nu} \tag{5.2}$$

with $D_\nu$ being the diffusion constant given by the Einstein relation:

$$D_\nu = \frac{kT}{q}\mu_\nu\,. \tag{5.3}$$

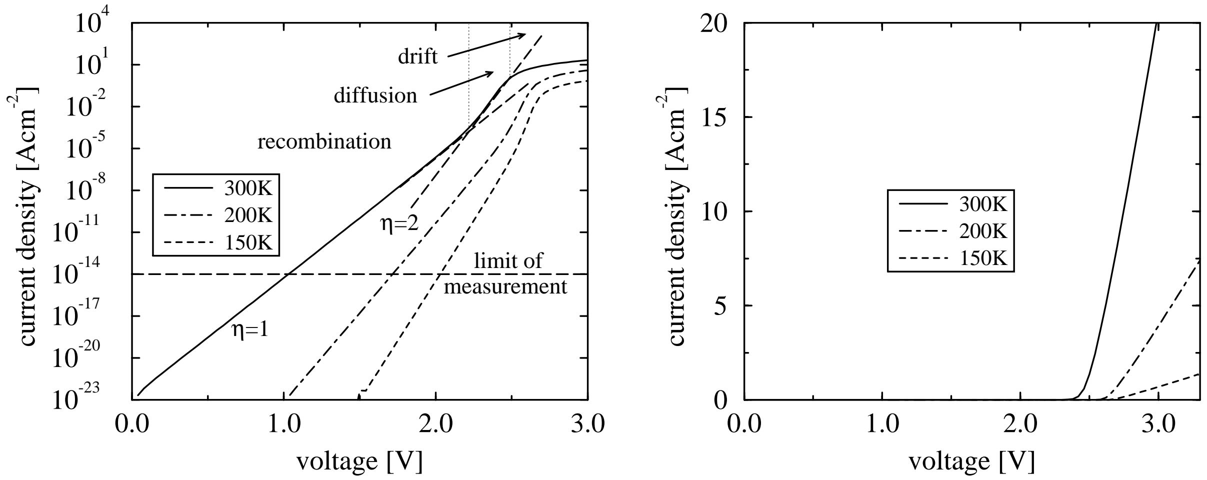


Figure 5.1: Logarithmic (left) and linear (right) plot of theoretical forward-biased 6H-SiC pn-diode IV characteristics.

In Fig. 5.1, the simulated forward characteristics of a pn-diode are shown on a logarithmic and a linear scale. Substituting Eq. (5.1) with

$$J(U) \propto \exp\left[\frac{qU}{\eta \cdot kT}\right] \tag{5.4}$$

with $\eta$ being the ideality factor, the different parts of the forward characteristics yield straight lines in a logarithmic plot with $\eta = 2$ and $\eta = 1$ for the recombination and diffusion current, respectively. The recombination current which is basically determined by the ratio of $n_i/\tau_{R-G}$ dominates the characteristics up to $J = 3 \cdot 10^{-3}\,\mathrm{Acm}^{-2}$. The diffusion current is determined by the corresponding diffusion properties (expressed by $\sqrt{kT\mu_\nu/q\tau_\nu}$) and the density of injected minority carriers at the edge of the depletion regions (expressed by $n_i^2/N_{D,A}^{+,-}$). At high current ratings, the voltage drop across the epi-layer and the substrate results in approximately linear IV characteristics.

[1]Generation in the case of a reverse biased pn-diode.

[2]Please refer to [154] and [155] for more details about analytical pn-diode theory.

In the part of the characteristics dominated by the drift current, self-heating effects may affect the measured data as well as several additional factors arising from e.g. contact resistances, Auger recombination, and carrier-carrier scattering [154]. Therefore, we will restrict our investigations in section 5.1.2 to the recombination and diffusion part of the IV characteristics.

Currently measured reverse characteristics [159, 160, 161, 162, 163, 164, 165, 166, 167, 168, 169] are far from the theoretical expectations based on Eq. (5.1) and will be only qualitatively investigated in section 5.1.3 with respect to extended SRH generation models.

#### (b) Structural parameters of investigated devices

In Tab. 5.1, the structural parameters of the investigated diodes are compiled. Sample D1 (Fig. 5.2) is a vertical $p^+n$-diode with a circular mesa design (Fig. 5.2) which has been fabricated and characterized by Cree research [158]. It has been used as reference for several publications [49, 176]. An abrupt junction was formed by an N-doped and an Al-doped epi-layer and passivated by thermally grown $SiO_2$. Ohmic contact materials for the p-side and n-side were sintered Al and Ni, respectively.

| sample | | | D1 | | | D2 | | | D6 | | |
|---|---|---|---|---|---|---|---|---|---|---|---|
| polytype | | | 6H | | | 6H | | | 6H | | |
| type | | | $p^+n$ - mesa | | | $p^+n$ - planar | | | $n^+p$ - planar | | |
| area | $[cm^2]$ | | $5.19 \cdot 10^{-2}$ | | | $1.3 \cdot 10^{-4}$ | | | $9.6 \cdot 10^{-4}$ | | |
| 1st layer | $[cm^{-3}]$ | $[\mu m]$ | Al | $1.0 \cdot 10^{18}$ | 1.0 | Al[a] | $5.0 \cdot 10^{19}$ | 0.5 | N[a] | $5.0 \cdot 10^{19}$ | 0.5 |
| 2nd layer | $[cm^{-3}]$ | $[\mu m]$ | N | $2.3 \cdot 10^{16}$ | 6.0 | N | $7.8 \cdot 10^{15}$ | 10.0 | Al | $2.5 \cdot 10^{16}$ | 5.0 |
| substrate | $[cm^{-3}]$ | $[\mu m]$ | N | $4.5 \cdot 10^{19}$ | 330 | N | $1.3 \cdot 10^{18}$ | 287 | Al | $4.3 \cdot 10^{18}$ | 420 |

Table 5.1: Structural parameters of investigated samples ([a]implanted atomic concentration).

Sample D2 and D6 are implanted vertical planar pn-diodes fabricated by Daimler-Benz AG, Research & Technology, on commercial 6H-SiC wafers with an Al-doped and an N-doped epilayer [177], respectively (Fig. 5.2). A junction with an abrupt box profile was formed by ion implantation of Al and N, respectively. For junction passivation, first a thin $SiO_2$ layer was deposited by thermal oxidation, and then its thickness was increased to $1.5\,\mu$m by CVD deposition. Contacts were formed using a titanium metalization on the n-side and an aluminum/titanium layer sequence on the p-side.

### 5.1.1 Basic considerations

Let us first discuss some basic properties of a SiC pn-junction in order to analyze the conceptual applicability of the drift-diffusion model to wide bandgap semiconductors and to outline the general impact of their properties on the simulation of wide bandgap devices.

As outlined in section 4.1, the Fermi energy in electrothermal equilibrium is given by the neutrality condition and is determined by the concentrations and electronic properties of the relevant dopant centers. Neglecting compensation effects, the majority carrier density is thus given by the density of

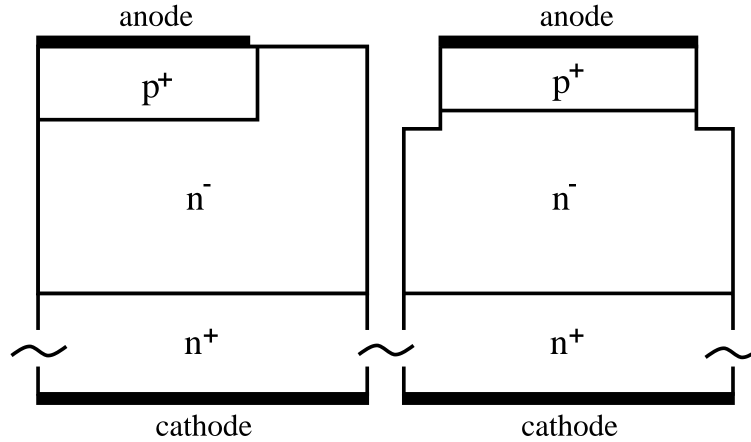


Figure 5.2: Schematic of lateral implanted (left - D2 and D6) and mesa-structured epitaxial (right - D1) pn-diodes.

the respective ionized dopant centers. The density of minority carriers, on the other hand, is extremely small because of the wide bandgap and the corresponding large distance between the Fermi energy and the minority carrier energy band (see Eqs. (2.22), (2.23), and Fig. 2.2). For instance, we obtain a minority carrier density of about $10^{-28}\,\mathrm{cm}^{-3}$ in the epi-layer of sample D6 at room temperature (Fig. 5.3). Evidently, the applicability of thermo-statistical methods becomes very questionable at those values.

#### 5.1.1.1 Statistical limit

By defining $N_{min} = 100$ carriers within the active volume $V = A_{\mathrm{D6}} \cdot 5 \cdot 10^{-4}\ \mathrm{cm}^3$ as the statistical limit for sample D6, the density of free carriers determining the contact current at different operation conditions must be larger than $n_{min} = N_{min}/V = 2.1 \cdot 10^8\,\mathrm{cm}^{-3}$. Using the analytical relation for the recombination current, Eq. (5.1), to estimate the minimum voltage needed for exceeding $n_{min}$,

$$U > U_{min} = \frac{2kT}{q} \ln\left(\frac{n_{min}}{n_{i,eff}}\right) , \tag{5.5}$$

we obtain $U_{min} \approx 1.5\,\mathrm{V}$ at room temperature. This leads to $J_{min} \approx 10^{-10}\,\mathrm{Acm}^{-2}$ (Fig. 5.1) which yield a minimum contact current of $I_{min} = J_{min} \cdot A_{D6} \approx 10^{-13}\,\mathrm{A}$ which is very close to the limits of the measurement setup. In Fig. 5.3, the internal distribution of the free carrier densities of the forward biased sample D6 (Fig. 5.6) at different operation points is plotted. At $U = 1.5\,\mathrm{V}$, the current is clearly dominated by recombination within the depletion region which mainly occurs within a narrow region of about 30 nm (Fig. 5.4). At this point, the free carrier densities determining the current are in the order of $n_{min}$ confirming the estimation of Eq. (5.5). $U_{min}$ increases with decreasing temperature because of the corresponding decrease of $n_{i,eff}$. At a temperature as low as 150 K, we obtain $U_{min} \approx 2.3\,\mathrm{V}$ which again yields $J_{min} \approx 10^{-10}\,\mathrm{Acm}^{-2}$. This is corroborated with the decrease of $U_{bi}$ with increasing temperature, thus yielding a minimum current density $J_{min}$ approximately independent of temperature.

The second part of the forward IV characteristics is dominated by the diffusion of injected minority carriers. The density of injected minority carriers within the transition region between the first and

second part is much larger than $n_{min}$ as shown in Fig. 5.3. Hence, the application of statistical methods is justified for all measured forward current characteristics investigated in section 5.1.2 and the limit for applying statistical methods approximately coincides with the limitations of today's standard measurement equipment.

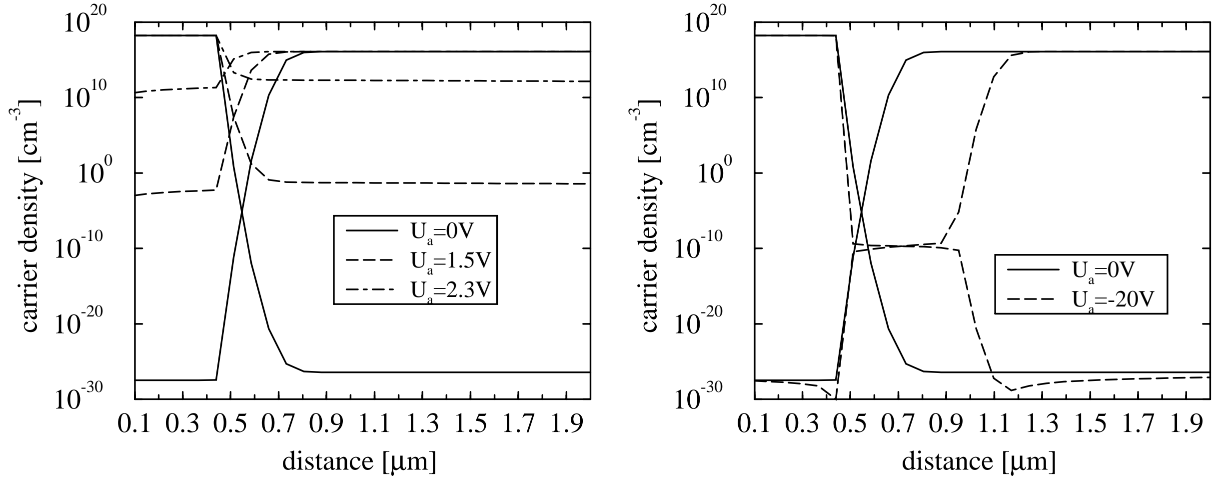


Figure 5.3: Electron and hole density distribution of forward- (left) and reverse-biased (right) pn-junction at $T = 300\,\mathrm{K}$.

Neglecting the various sources for surface leakage currents, the reverse current density is determined by the carriers generated within the depletion region which are subsequently extracted by the electric field. They can be estimated by

$$n \approx \frac{J}{q v_{sat}} \tag{5.6}$$

which yields $n \approx 10^4\,\mathrm{cm}^{-3}$ at 623 K. Therefore, although $n_{i,eff}$ is larger than $n_{min}$ at those high temperatures, there is less than one carrier in the active volume at stationary conditions. Hence, even at high temperatures beyond 600 K, the applicability of statistical methods is questionable (see section 5.1.3). However, it should be noted that similar considerations apply to reverse biased Si diodes with long minority carrier lifetimes at temperatures below 300 K.

### 5.1.1.2 Validity of the quasi-static approximation

At operating conditions with dominating recombination (low injection as well as high injection), the relaxation time constant $\tau_{tp}$ (see section 2.2.1) is short because of the large concentration of at least one free carrier species in Eq. (2.49) confirming the validity of the quasi-static approximation. In the case of prevailing carrier generation, however, $\tau_{tp}$ becomes extremely large in wide bandgap materials due to the very low intrinsic density. Therefore it is even under steady-state conditions very questionable whether the SRH-model, Eq. (2.62), can be applied.

#### 5.1.1.3 Numerical instabilities

Apart from these considerations, any drift or diffusion current carried by very low carrier concentrations will hardly be numerically treatable as the driving forces are basically determined by the difference of very small numbers (see Tab. B.2). This results in various numerical instabilities which have to be accounted for in order to achieve reliable simulation results.

Typically, the reverse characteristics of power diodes are investigated with respect to optimizing the breakdown characteristics[3]. If the measured leakage currents are sufficiently small, they are of minor interest to the designer. Although in disagreement with measurement and therefore neglected, they have to be numerically handled which requires advanced domain integration techniques [178] to simulate current densities as low as to $10^{-20}\,\mathrm{Acm}^{-2}$. It has been observed at those numerically critical situations that small deviations of the free carrier densities during the Newton iteration process can lead to an artificially avalanche breakdown below the critical field (see Eq. (3.27)) The usually applied work-around in such a case is to perform the simulations at artificially high temperatures [50, 51]. An alternative pragmatic approach which does not artificially affect the remaining internal properties is the specification of an additional external generation rate limiting the minimum current density to values above $10^{-10}\,\mathrm{Acm}^{-2}$.

Furthermore, the enormous difference of more than 28 orders of magnitude between majority and minority carriers (Fig. 5.3) must be properly resolved by the grid in order to avoid numerical artifacts in the forward characteristics as shown in Fig. 5.4. Considering the ideality factor defined by Eq. (5.4) which is extracted from the simulated forward characteristics, it can be seen that the maximum distance between a one-dimensional grid must be smaller than 3 nm in case of sample D6 in order to obtain reliable results.

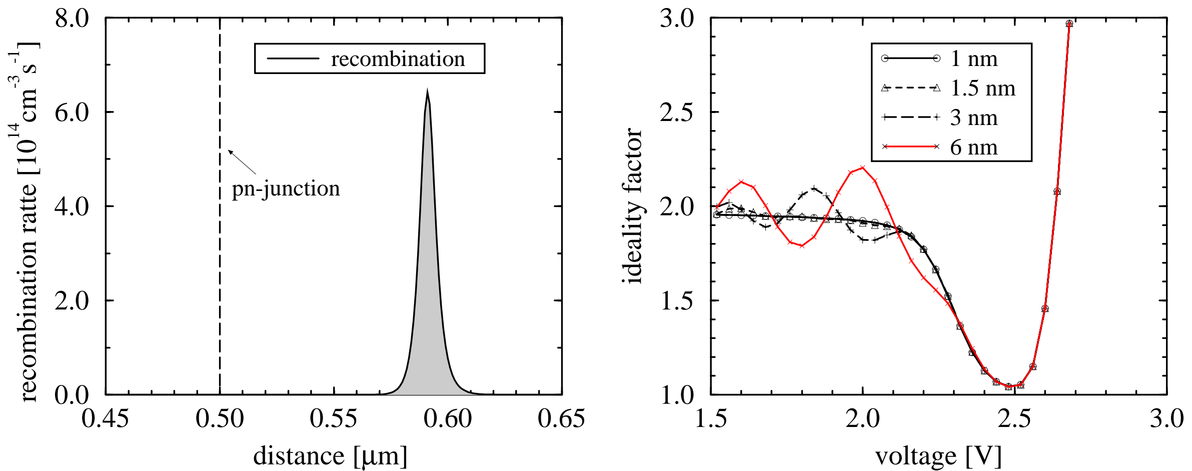


Figure 5.4: Localization of recombination rate at $U = 1.5\,\mathrm{V}$ (left) and influence of discretization on the ideality factor (right).

Finally, it must be assured that no internal hard-coded numerical quantities are limiting dependent variables because of corroborated artificial gradients and other numerical artifacts.

[3]For instance, the investigation of the electric field distribution at the junction termination.

## 5.1.2 Forward characteristics

The recombination and diffusion dominated part of the forward biased pn-diode IV characteristics are well suited as references for parameter evaluation and calibration because several possible sources of error can be excluded. First of all, contact resistance and self heating effects can be neglected due to the rather low current ratings. Furthermore, carrier-carrier scattering and Auger recombination is not relevant in this part of the characteristics.

### 5.1.2.1 Influence of surface recombination

Considering Fig. 5.2, there are basically two different recombination mechanisms which may determine the recombination current of sample D6: First bulk recombination within the depletion region along the junction and second surface related recombination as modeled by Eq. (3.25). While the surface recombination velocities $v_\nu$ do not influence the diffusion dominated part of the characteristics, the bulk recombination current is coupled to the diffusion current by the minority carrier lifetimes $\tau_\nu$ and to a minor extend by the free carrier mobilities (see Eq. (5.2)) as long as the diffusion lengths are smaller than the layer thickness of the diffusion regions [154].

In Fig. 5.5, the corresponding simulated current characteristics are shown, adjusted to the measured recombination current at 299 K by $\tau_n^{T_0}$ =67 ns and $v_n = 10^6\,\mathrm{cm/s}$, respectively. By assuming surface recombination and neglecting any bulk recombination, the corresponding diffusion current is far too small, limited by the layer thickness of the diffusion regions due to the corresponding large diffusion lengths. Combining the maximum values for the bulk free carrier lifetimes[4] with surface recombination underestimates the diffusion current by more than 100 %.

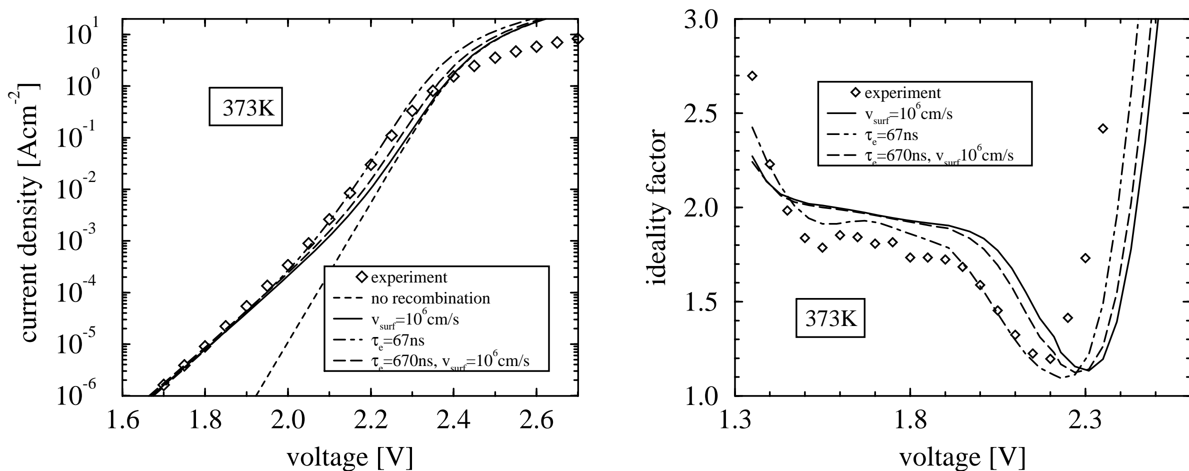


Figure 5.5: Forward characteristics of sample D6 at 373 K including and excluding surface recombination.

There are several publications which report on edge dominated recombination current in SiC diodes by investigating the forward IV characteristics as a function of the perimeter/area ratio [166, 167, 170,

[4] up to several microseconds as published so far [166, 167, 170, 171, 172]

171]. However, they all refer to investigations on mesa-structured diodes. Because of the extremely large extracted value of $v_n$ which is about two orders of magnitude larger than the data reported in [166, 167] and the resulting deviations obtained in the diffusion-dominated part of the characteristics, it is assumed that surface-related recombination can be neglected in sample D6 and similarly in sample D2.

The recombination current is mainly determined by a small area close to the junction (Fig. 5.4). As shown in Fig. 5.12 and also reported in [173], significant implantation damage has been observed within the implanted regions which may explain the rather low minority carrier lifetime determining the recombination current of sample D6.

#### 5.1.2.2 Temperature dependence of SRH lifetimes

In Fig. 5.6, the temperature dependent forward characteristics of sample D6 are shown together with the corresponding ideality factor extracted for 373 K and 623 K. Here, the default parameters, as outlined in chapter 3 and 4, have been used and the minority carrier lifetime parameter $\tau_n^{T_0}$ of the Scharfetter relation, Eqs. (3.22) and (3.24), has been adjusted such that the simulated recombination current at 299 K agrees with the measured data. Although an overall qualitative agreement is observed, deviations up to a factor of 2 are obtained at higher temperatures within the recombination and diffusion part of the characteristics, respectively.

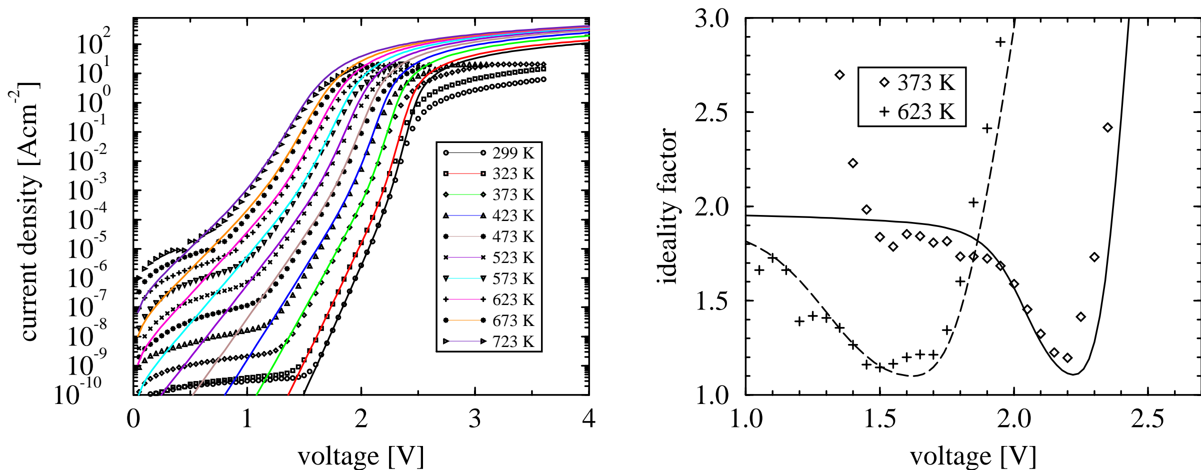


Figure 5.6: Temperature dependent forward characteristics of sample D6 excluding temperature coefficient of the SRH-lifetimes.

The disagreement between measured and simulated data below a certain threshold voltage depending on temperature (Fig. 5.6) still has to be clarified. However, similar behavior at very low current ratings has been observed by other groups [166, 175].

The recombination current is determined by the intrinsic density $n_i$ and the appropriate minority carrier lifetime (see Eq. (5.1)). The temperature dependence of $n_i$, on the other hand, is basically determined by $E_g(T)$ which should not vary among the investigated samples. Assuming a power law for the temperature dependence of the SRH lifetimes, Eq. (3.24), with $\tau_n^{T_0} = 67$ ns and $\alpha_\nu^{SRH} = 1.64$, the simulated

characteristics agree excellently with the measured data within the complete temperature range (Fig. 5.7) for both the recombination-dominated and diffusion-dominated part of the IV characteristics.

A similar finding is obtained in case of sample D2. In Fig. 5.8, the simulated IV characteristics with $\tau_n^{T_0} = 11$ ns and $\alpha_\nu^{SRH} = 3.6$ are shown which again agree very good with the measured data within the recombination- and diffusion-dominated range. In Fig. 5.10, the resulting temperature dependence of $\tau_n^{T_0}$ for sample D2 and D6 is compared to measured data for 4H-SiC [172] and 6H-SiC [104] confirming that reasonable temperature coefficients $\alpha_\nu^{SRH}$ have been extracted.

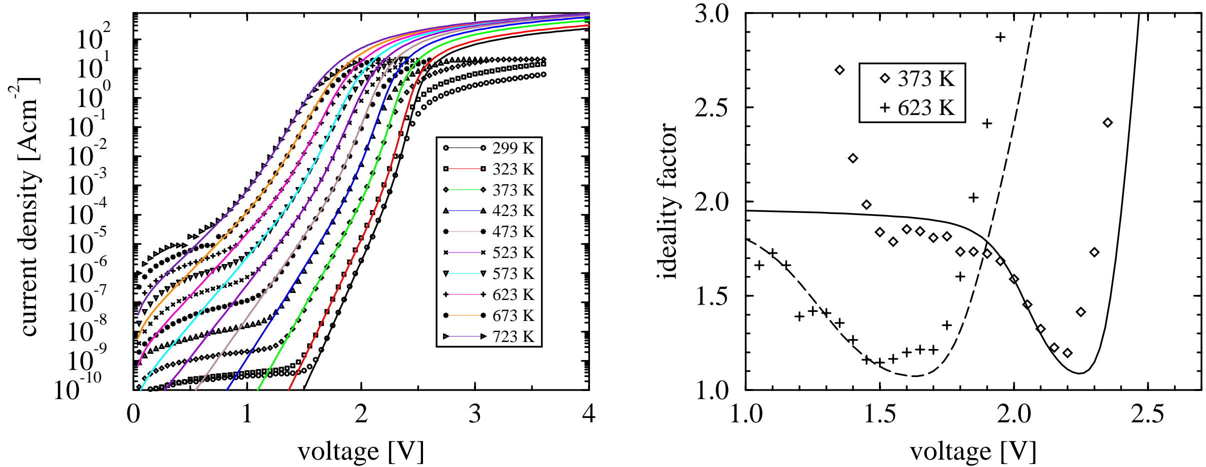


Figure 5.7: Temperature dependent forward characteristics of D6 including temperature coefficient of the SRH-lifetimes.

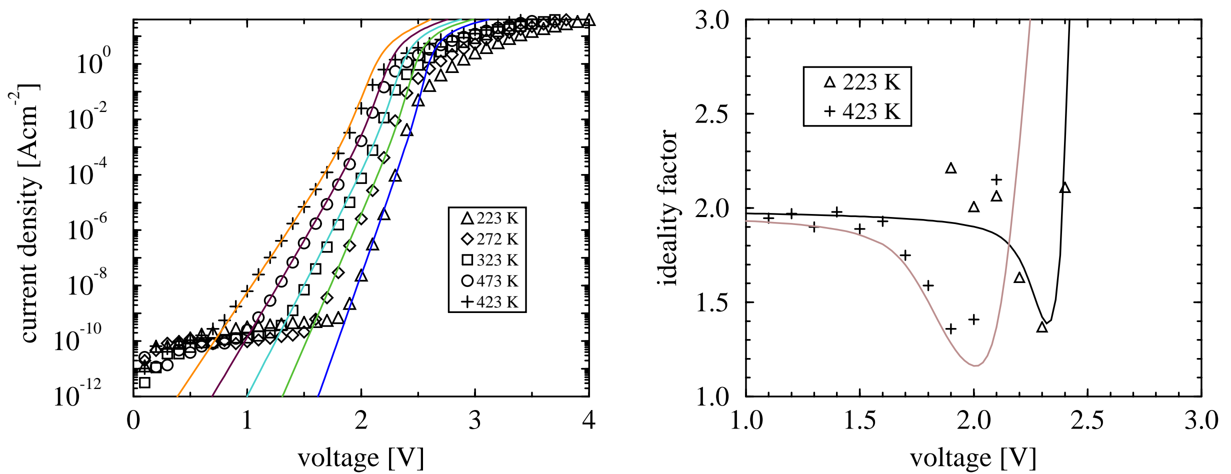


Figure 5.8: Temperature dependent forward characteristics of sample D2 including a temperature coefficient of the SRH-lifetimes.

#### 5.1.2.3 Field-dependent SRH lifetimes

Basically, two different field-related mechanisms may affect the recombination current as outlined in section 3.6.1. Due to the low electric fields at forward-biased pn-junctions and the non-degenerately doped material, it turns out that only the Poole-Frenkel effect can possibly influence the forward characteristics of the investigated pn-diodes. In Fig. 5.9, the corresponding simulated characteristics of sample D6 are shown excluding any additional temperature dependence of $\tau_n^{T_0} = 540\,\text{ns}$ adjusted to the recombination current at 299 K. The exponential factor of Eq. (C.5) yields a current density

$$J \propto J_{SRH} \exp\left[\frac{q}{2kT}\sqrt{\frac{qE}{\pi\varepsilon}}\right]. \tag{5.7}$$

Therefore, the influence of the Poole-Frenkel effect is larger at lower temperatures. We obtain a similarly good agreement between simulated and measured data within the recombination-dominated range as in case of using a minority carrier lifetime dependent of temperature. The larger value of $\tau_n^{T_0}$ results from its field-related reduction within the recombination-dominated part of the characteristics.

The simulated diffusion current, however, is too small as this enhancement of recombination decreases with rising current densities because of the decreasing field at the junction. In addition, a larger ideality factor is obtained in the recombination dominated range which is also in disagreement with the measured data. Therefore, any field-related effects can be excluded as a possible explanation for the measured characteristics of sample D6 and similarly of sample D2.

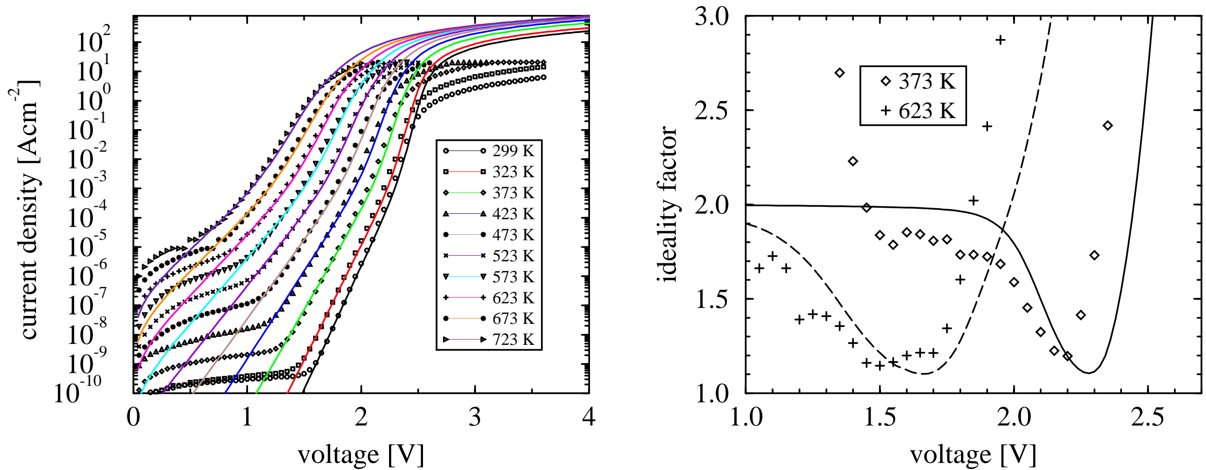


Figure 5.9: Temperature dependent forward characteristics of sample D6 including field-dependent SRH lifetimes due to the Poole-Frenkel effect.

Pelaz et al. reported on the Poole-Frenkel effect as a possible explanation for the forward characteristics of sample D1 [176]. However, the data can similarly be modeled by temperature-dependent SRH-lifetimes. The reported measured data is not sufficient to draw further conclusions about which effect is more likely. Furthermore, the Poole-Frenkel effect may only be relevant in some devices as it requires the existence of charged recombination centers.

#### 5.1.2.4 IV characteristics at high current ratings

In most device applications, the linear range of the forward IV characteristics is the most important. No comparison between measured and simulated data has been undertaken in this range because of a lack of reliably measured data. It is essential to avoid any self-heating effects during measurement. Furthermore, the influence of contact resistance during measurement has to be minimized. Besides the SRH bulk recombination, Auger processes and carrier-carrier scattering reducing the free carrier mobilities may impact within that operation range.

In Fig. 5.10, the influence of the latter on the forward voltage drop at a given current density is shown. As long as the minority carrier lifetimes are well below one microsecond, SRH bulk recombination will also dominate this range of the characteristics. Further simulated data on SiC pn-diodes at high current ratings can be found in [50, 51].

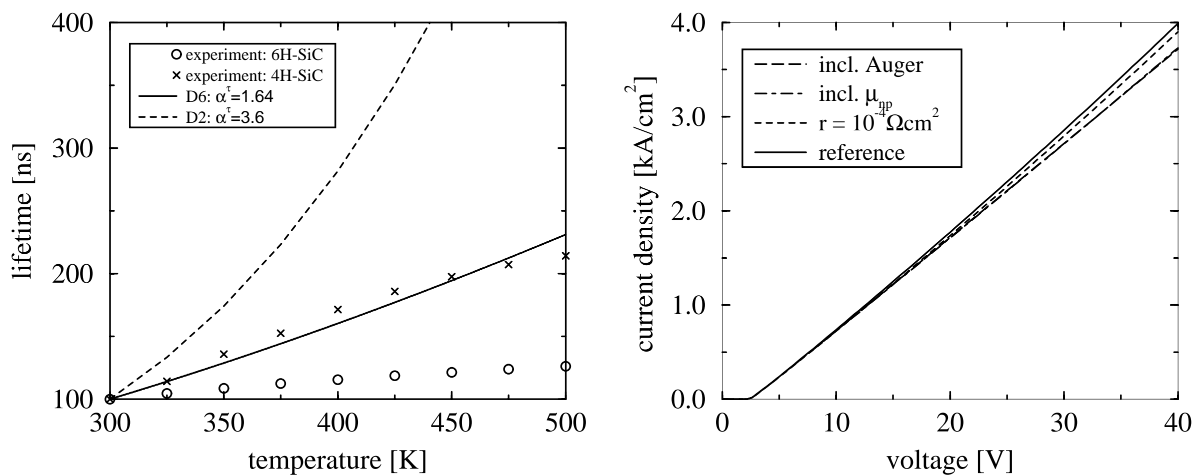


Figure 5.10: Normalized temperature dependence of SRH-lifetimes (left) and influence of carrier-carrier scattering, Auger recombination, and contact resistances at high current ratings (right). The experimental data is taken from [172] and [104] for 4H- and 6H-SiC, respectively.

#### 5.1.2.5 Discussion of material parameters

There are several uncertainties among the material parameters which may affect the quantities entering Eq. (5.1). Accounting for the unknown exciton binding energy by shifting the exciton bandgap by 40 meV as outlined in section 3.2, the characteristics corresponding to Fig. 5.7 are obtained with $\tau_n^{T_0} =$ 26 ns and a similar temperature coefficient $\alpha_\nu^{SRH} = 1.64$ (Fig. 5.11). In this case, the diffusion current is underestimated by a factor of 4 due to the larger bandgap and the corresponding lower intrinsic density. This finding may be partly compensated for by a reduced concentration of ionized donors $N_D^+$ which may result from a smaller percentage of electronically active implanted atoms. On the other hand, the ionization energy may be somewhat smaller as a result of the high doping concentrations (see chapter 4). Furthermore, the bandgap-narrowing parameters are only based on theoretical calculations (see section 3.2). It should be noted, that most of the aforementioned uncertainties will reduce the simulated

diffusion current compared to the simulation results given in Fig. 5.7 which is in disagreement with the measured data.

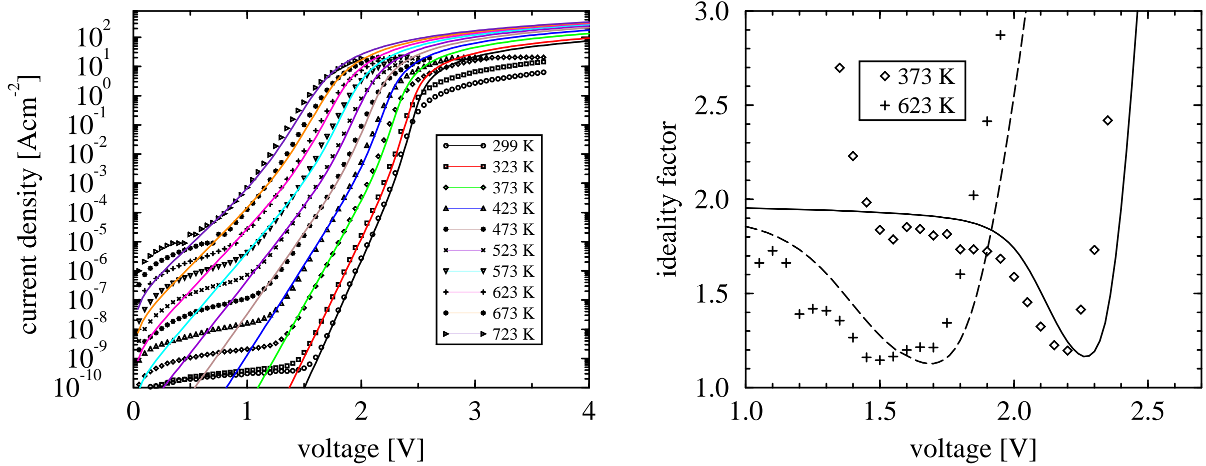


Figure 5.11: Temperature dependent forward characteristics of sample D6 including temperature coefficient of the SRH-lifetimes and a 40 meV shift of the bandgap.

Finally, we can not exclude a doping profile as shown for instance in Figs. 5.12 and 4.26 in the case of sample D6, since its box profile has been confirmed by SIMS measurements which get rather inaccurate for doping concentrations below $10^{17}\,\mathrm{cm}^{-3}$. CV measurements used to obtain the doping concentration of the p$^{-}$-region will probably not detect such an effective doping gradient. However, only minor differences are observed in the simulated characteristics. The extracted $\tau_n^{T_0} = 89$ ns is larger in this case due to the lower doping concentration within the area determining the recombination current near the junction. Similarly, a larger $\tau_n^{T_0}$ would be obtained if the ratio of $\tau_n^{T_0}/\tau_p^{T_0} = 5$ is overestimated.

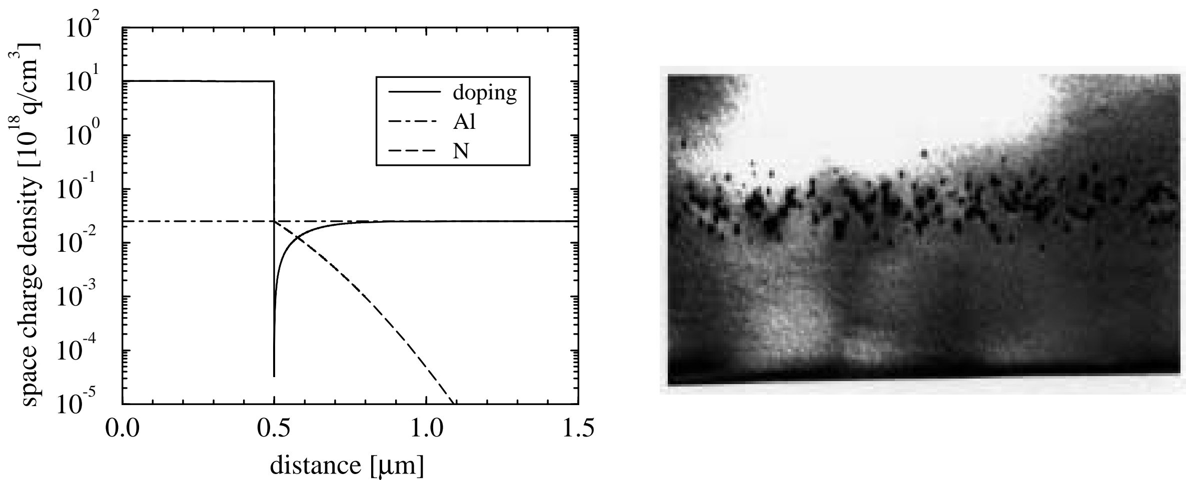


Figure 5.12: Possible effective doping profile of sample D6 (left) and REM picture showing implantation damage in the vicinity of the pn-junction (right).

#### 5.1.2.6 Summary

The recombination- and diffusion-dominated forward characteristics of two pn-diodes have been simulated within a large temperature range with excellent agreement to measured data using a single material parameter set (see appendix A) by adjusting the technology-dependent SRH minority carrier lifetimes. The set of material parameters collected in chapter 3 and 4 can be regarded as a basis for numerical investigations which should be carefully updated with respect to further experimental data and the specific process technology of a given device. The investigated range of the forward IV characteristics of pn-diodes is particularly well suited for calibrating the material parameters. However, although most of the relevant parameters are known within rather small error ranges, it seems questionable to draw any conclusions with respect to certain other parameters (e.g. band-gap narrowing) from the observed agreement due to the large number of possible influences.

### 5.1.3 Reverse characteristics

Apart from the theoretical aspects discussed in section 5.1.1, any investigations on reverse pn-junction characteristics are presently qualitative due to the large variations of measured data even between devices originating from neighboring positions on a single wafer.

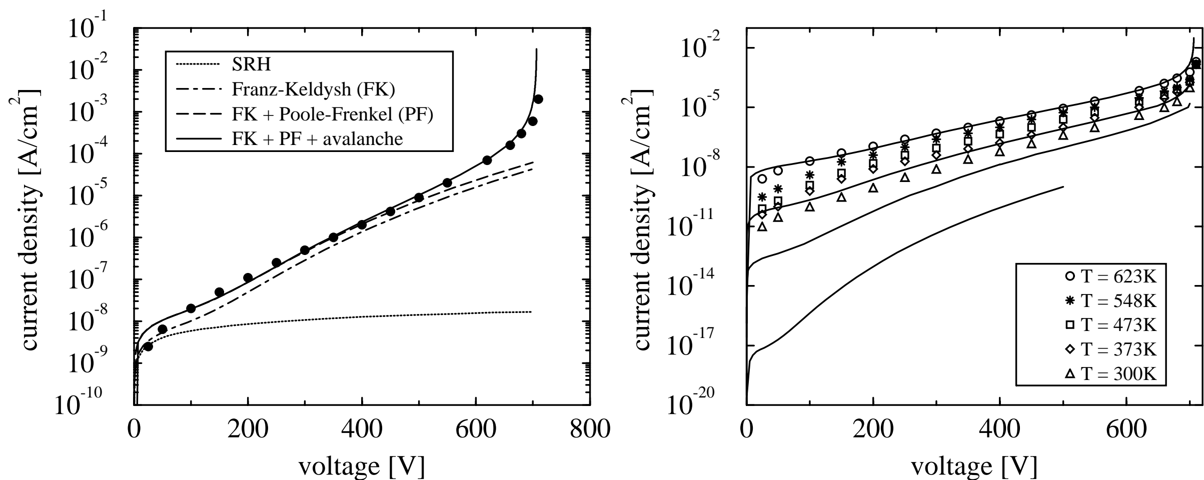


Figure 5.13: Influence of different generation models on the reverse current density of sample D1 at 623 K (left) and field-dependent reverse characteristics for $300\,\mathrm{K} < T < 623\,\mathrm{K}$ (right).

Based on the generalized SRH statistics outlined in section 3.6.1 and appendix C, the simulated and measured reverse characteristics of sample D1 are shown in Fig. 5.13. Here, $\tau_n^{T_0}$ has been adapted such that the low field current density agree between simulation and measurement at 623 K. At this temperature, the influence of the different field-related extensions is demonstrated: the standard SRH model, the tunnel-assisted SRH model (Franz-Keldysh effect), both tunnel-assisted SRH recombination and Poole-Frenkel effect in combination ("FK + PF"), and impact ionization included ("FK + PF + avalanche"). At this rather high temperature, it is possible to model the measured data by field-enhanced single energy level SRH generation. Without any field-enhancements, the generation current

is proportional to the depletion region width, thus showing a square root dependence on voltage. The Franz-Keldysh effect alters the generation current by several orders of magnitude at larger voltages before impact ionization sets on at about 700 V. As expected, the influence of the Poole-Frenkel effect is small in this high-field range because only one of the minority carrier lifetimes, $\tau_n^{T_0}$ or $\tau_p^{T_0}$ is reduced.

Since the exact energy level $E_{tp}$ of the recombination-generation center in the bandgap is not known, a numerical investigation of this influence has been performed (see Eqs. (2.53), (2.54), and (2.62)). Generation centers are generally most effective at mid-gap energy levels. Therefore, a large deviation of the energy level from mid-gap results in even lower reverse current densities together with a more pronounced temperature dependence.

#### 5.1.3.1 Temperature activation of reverse current

Considering the complete measured temperature range, it becomes obvious that there are significant differences between simulated and measured data at lower temperatures (Fig. 5.13). As given by Eq. (5.1), the generation current in a reverse-biased diode originating from thermal excitation of free electrons and holes via a single recombination-generation center is proportional to the ratio $n_i/\tau_{R-G}$. Hence, the temperature dependence of the reverse current is predominantly governed by that of the intrinsic density $n_i(T)$. Therefore, plotting the logarithm of the reverse current density at $U = 100\,\mathrm{V}$ against $1/T$,

$$\ln J \propto \frac{E_a}{kT}, \tag{5.8}$$

gives a straight line with $E_a = E_g(T)/2$ (Fig. 5.14). As a consequence, the current decreases to a value as low as $10^{-20}\,\mathrm{Acm}^{-2}$ (Fig. 5.13). The field-dependence due to the Franz-Keldysh effect reduces $E_A$ only at higher voltages.

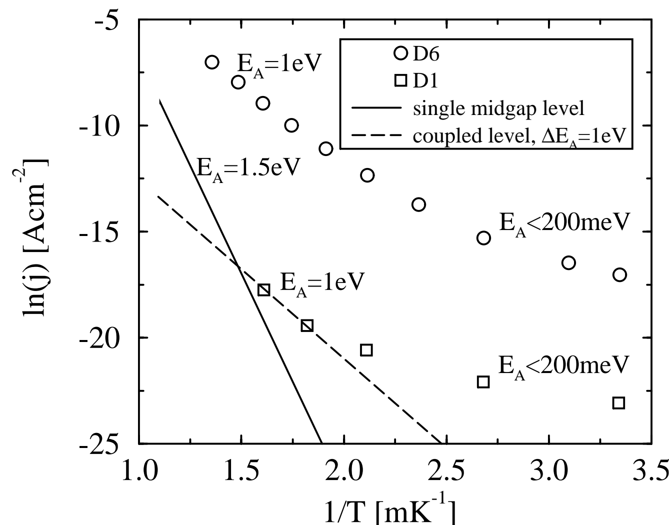


Figure 5.14: Arrhenius plot of experimental and calculated reverse current density.

Although the reverse current density of sample D1 is far below that of sample D6, both samples show activation energies of the reverse current density between 0.2 and 1 eV. An experimental characteriza-

tion of electron-hole generation in SiC has yielded similar activation energies for defect-related generation [170]. In recent years, the maximum reverse current density has been reduced more and more by technological progress and is approaching the measurement limits. Similarly, its field-dependence has also been significantly reduced [26]. However, no temperature activation of the reverse characteristics approaching $E_g/2$ has been reported so far.

There are two basic questions arising from the aforementioned considerations: 1st) Does the observed current originate from the bulk or from the edge of a device, and 2nd) which is the dominating physical mechanism?

There are several experimental investigations showing that the recombination current of forward-biased mesa-structured pn-junctions is primarily related to the edge of the device [171, 173]. The large statistical variations of measured reverse currents make it very difficult to draw any conclusions from experimental investigations of the dependency of reverse current on the ratio of area to perimeter. However, Kimoto et al. reported on an experimentally confirmed edge-dominated reverse current of mesa-structured pn-junctions based on those measurements at 406 K and 466 K [167]. The observed current density in that paper is significantly larger than that of sample D1 which also has a mesa-structured design.

The experimentally observed activation energy as given by Eq. (5.8) allows us to draw some basic conclusions with respect to the basic physical mechanism. Any low-field bulk or edge-related thermal excitation of free electrons and holes via a single energy level recombination-generation center as modeled by the SRH statistics, Eq. (2.62), will be thermally activated with $E_a \geq 1.5\,\text{eV}$. Hence, all presently published measured data of reverse pn-junction characteristics can not be explained by this process. However, extending it to coupled defect-level recombination-generation gives a possible explanation for the observed characteristics as outlined below.

#### 5.1.3.2 Coupled defect-level generation current

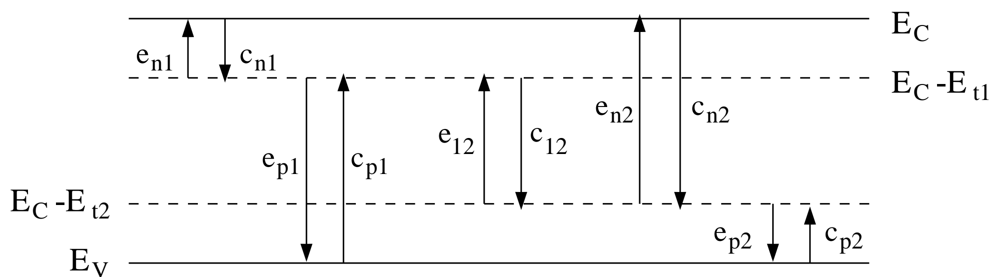


Figure 5.15: Energy diagram of two coupled defect levels and corresponding emission and capture rates.

In Fig. 5.15, a schematic energy diagram of two coupled defect levels is shown. The corresponding quasi-static recombination rate is given by Eqs. (C.7)-(C.12) [100]. Basically, there are three different transition paths available by such a system: the single energy level transition $R_{1,2}$ via the respective

energy level $E_{t_1,t_2}$ with similar thermal activation and the interlevel transition modeled by the internal rate $r_{12}$. Interlevel transition is obtained by $\tau_{p1} \to \infty$ and $\tau_{n2} \to \infty$ or similarly by $\tau_{n1} \to \infty$ and $\tau_{p2} \to \infty$. Either the transition between the energy level and the corresponding energy band, $\tau_{p1}$ or $\tau_{n2}$, or the interlevel transition $r_{12}$ is rate-limiting. In the latter case, one obtains from Eq. (C.7)

$$R \to r_{12} \frac{np - n_i^2}{(n+n_1)(p+p_2)} \to \begin{cases} -r_{12} & \text{for } np \ll n_i^2 \\ r_{12} & \text{for } np \gg n_i^2 \end{cases} \tag{5.9}$$

which shows together with Eqs. (C.11) and (C.11) that the resulting current is activated by the energetic distance of the coupled energy levels. Hence, it is possible to obtain activation energies below $E_g/2$ in such a situation.

A very interesting finding is obtained if the interlevel transition is not limited by the internal rate $r_{12}$. Here, the recombination rate is given by

$$R = R_{12} - \sqrt{R_{12}^2 - \frac{np - n_i^2}{\tau_{n1}\tau_{p2}(1-\varepsilon)}} \tag{5.10}$$

with

$$R_{12} = \frac{(n+n_1)(p+p_2)}{2r_{12}\tau_{n1}\tau_{p2}(1-\varepsilon)} + \frac{\tau_{n1}(p+p_1) + \tau_{p2}(n+n_2)}{2\tau_{n1}\tau_{p2}(1-\varepsilon)}. \tag{5.11}$$

If the energy level coupled to the valence band lies in the lower half of the bandgap and the energy level coupled to the conduction band lies in the upper half of the bandgap, $R$ is dominated by the second term of the square root which corresponds to $S_{12}$ in Eq. (C.7) and is therefore given by $n_i/\sqrt{\tau_{n1}\tau_{p2}(1-\varepsilon)}$. Hence, the reverse current is activated in this case by $E_a = E_g/2$ independent of the energy level of both centers. This finding is a consequence of $r_{12} \to \infty$ which results in equal chemical potentials of both centers. The term $S_{12}$ originates from the equilibrium condition of the quasi-static approximation, assuring that $R$ is vanishing in electrothermal equilibrium with $np = n_i^2$. If both energy levels are situated below $E_g/2$, we obtain $E_a = \max(E_{t_1}, E_{t_2})$ by Eq. (5.10) and similarly $E_a = \max(E_g - E_{t_1}, E_g - E_{t_2})$ for $E_{t_1,t_2} > E_g/2$.

Hence, modeling the experimental finding of $0.2\,\text{eV} < E_a < 1\,\text{eV}$ at low electric fields by thermal excitation of free electrons and holes via impurities requires an electronic structure of at least two coupled centers including a rate-limiting internal transition rate. They may be related to structural defects in the material or at the edge of a device as the probability for coupled impurities decreases rapidly with increasing distance in space. The reverse characteristics of sample D1 can be adjusted to $E_a = 1\,\text{eV}$ by specifying $E_{t_1} = 1\,\text{eV}$ and $E_{t_2} = 2\,\text{eV}$ with $\tau_{n1} = 10\,\text{ns}$ and $\tau_{p2} = \tau_{n1}/5$. The forward recombination current is generally dominated by the most effective single level recombination path yielding similar IV characteristics as described in section 5.1.2.

It should be noted that also several other physical mechanisms may be involved which could lead to the measured characteristics. Further experimental data is required together with a thorough theoretical analysis to clarify the underlying physical mechanisms of the observed excess leakage currents.

## 5.2 The JFET - Concept of inverse modeling

Simulation of SiC devices have so far been mostly qualitatively related to measured data due to the various possible uncertainties of material and structural parameters. On the other hand, further progress in process technology would be enhanced by a well-based interpretation of measured data which can significantly be improved by applying the concept of inverse modeling. This concept basically comprises the extraction of unknown or uncertain parameters by detailed quantitative numerical investigations of measured device characteristics.

The junction field effect transistor (JFET), being a unipolar device without any Schottky or MOS interface for which accurate models are not yet available, is excellently suited for evaluating the applicability of this concept to state-of-the-art SiC devices. Hence, numerical simulations of various JFET devices have been performed with a view to quantitatively reproducing the measured device characteristics within a wide temperature range and various bias conditions.

### 5.2.1 Characterization of implanted-gate 6H-SiC JFET

A generalized cross-section of an implanted-gate 6H-SiC JFET is shown in Fig. 5.16. The device is basically a four-terminal n-channel normally-on JFET, which allows separate control of top and bottom gates. Due to the trench isolation, it can easily be integrated with other active and passive devices for planar circuits and has therefore been fabricated at Daimler-Benz AG, Research & Technology, with a view to evaluating its benefits for high-temperature applications [190, 194]. Al implantation in an

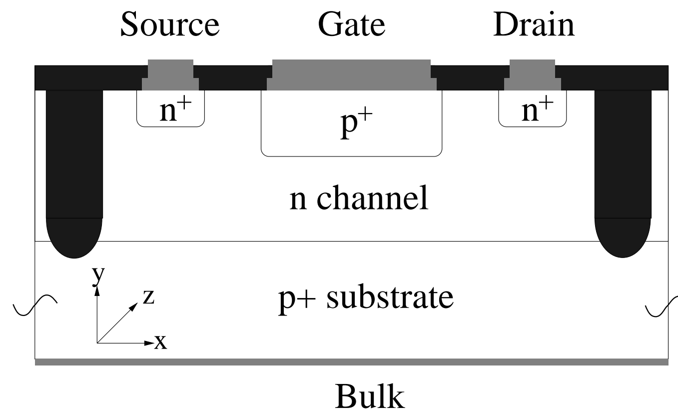


Figure 5.16: Cross section of implanted top-gate JFET structure.

n-type epi-layer on a p-type commercial substrate [177] was used to form the $p^+$-gate. The source and drain regions were fabricated by the implantation of N. Contacts were realized using Ti and Al/Ti for the n-type and p-type regions, respectively. Five devices were investigated, each with different ratios of channel width to channel length as compiled in Tab. 5.2. All devices could be completely pinched-off to below 100 pA and showed good saturation of the drain current up to 400°C. CV-measurements were performed to obtain information about the doping concentration of the epi-layer.

| sample | L [$\mu$m] | Z [$\mu$m] | $N_{A,gate}$ [cm$^{-3}$] | $N_{D,channel}$ [cm$^{-3}$] | $N_{A,substrate}$ [cm$^{-3}$] |
|---|---|---|---|---|---|
| J10/5 | 5 | 10 | $3 \cdot 10^{19}$ | $8 \cdot 10^{16}$ | $3 \cdot 10^{18}$ |
| J10/20 | 20 | | | | |
| J100/5 | 5 | 100 | | | |
| J100/10 | 10 | | | | |
| J100/20 | 20 | | | | |

Table 5.2: Structural data of investigated 6H-SiC samples.

#### 5.2.1.1 Basic characteristics

The basic characteristics of this JFET can be analyzed by considering a simplified analytical model as briefly outlined in appendix D [189, 190]. The device properties are mainly determined by the channel properties which are parameterized in this model by its thickness $a$, its length $L$, its width $Z$, the doping concentration $N_{ch}$, and the mobility $\mu_{ch}$. In Fig. 5.18, the internal distribution of electron current density, space charge, and the effective electron mobility as determined by Eq. (3.11) and (3.16) are shown for sample J10/5 at $U_{GS} = 0$ V and $U_{DS} = 4$ V. The current flow is concentrated in the middle of the channel between the depletion regions of both pn-junctions. The lateral potential difference between source and drain leads to the larger extension of the depletion regions near the drain as outlined in appendix D. Any high-field reduction of the channel mobility can be neglected within the investigated range of channel lengths (Fig. 5.18). Therefore, only a minor difference is obtained when comparing the results of the analytical model, Eqs. (D.10) and (D.18), with those obtained by simulation of sample J10/5, assuming a homogeneous channel doping concentration and abrupt junctions.

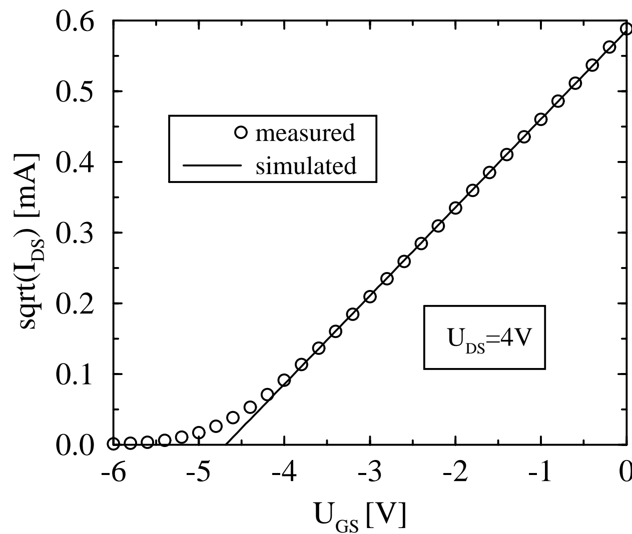


Figure 5.17: Graphical extraction of threshold voltage $U_{th}$.

With increasing negative potential $U_G$ at the gate, the region available for the current is more and more reduced until the channel is finally pinched off. This defines the threshold voltage $U_{th} = -4.7\,\text{V}$ as

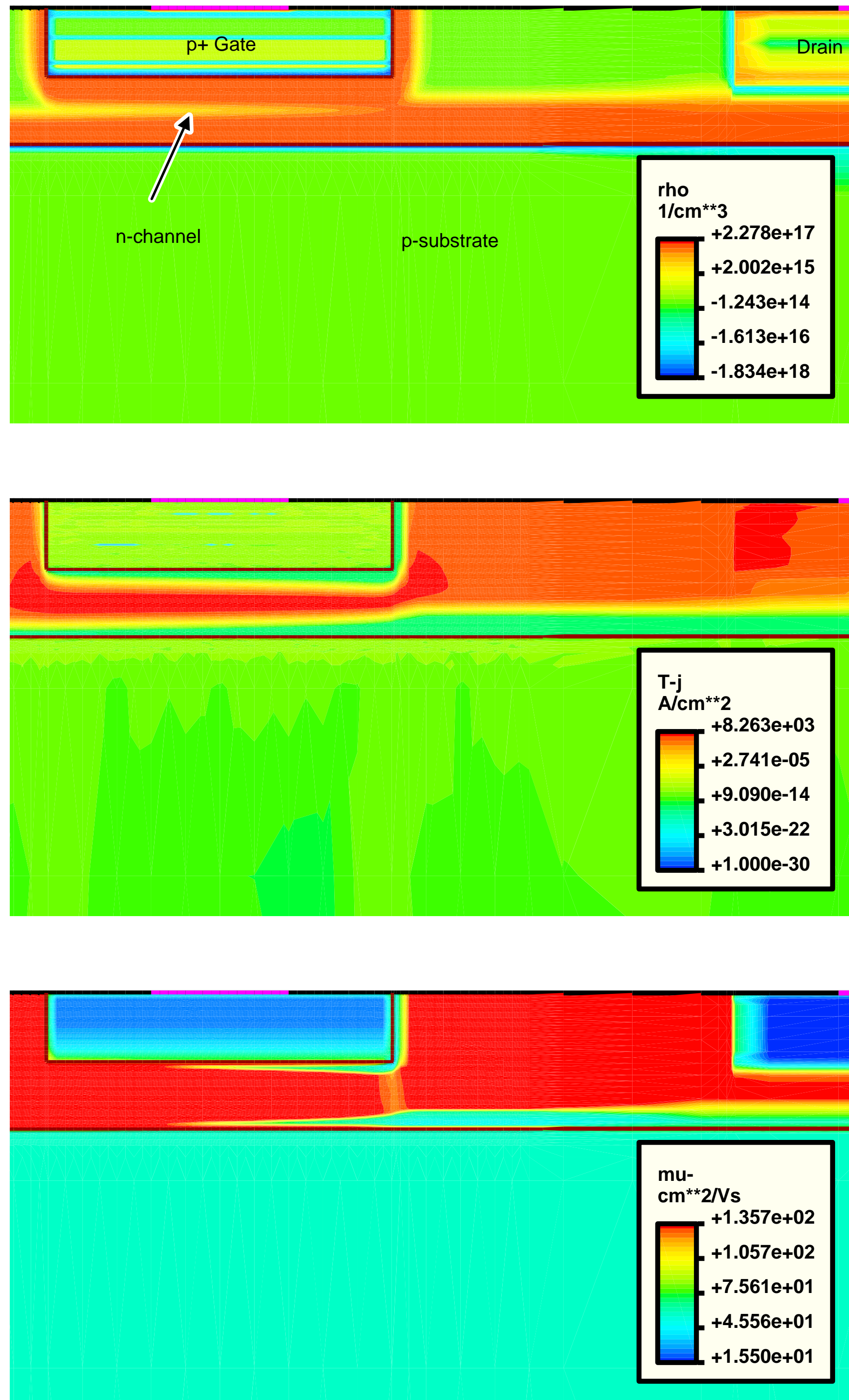


Figure 5.18: Distribution of space charge density, current density, and electron mobility at $U_{GS} = 0\,\text{V}$ and $U_{DS} = 4\,\text{V}$.

shown in Fig. 5.17. Considering Eq. (D.20) it becomes clear that the curvature of the transfer characteristics is mainly determined by $a$ and $N_{ch}$ whereas $\mu_{ch}$ only acts as a linear factor. Thus, the transfer characteristics very sensitively sense the channel thickness at a given doping concentration $N_{ch}$. In the case of sample J10/5, a variation $a \pm 10\,\text{nm}$ together with appropriate readjusting of $\mu_{ch}$ to fit $I_{DS}$ at $U_G = 0\,\text{V}$ leads to a significant different curvature of the transfer characteristics whereas only a minor impact on the output characteristics is observed (Fig. 5.19). Similar results are obtained when varying $N_{ch}$ at a given thickness $a$ and again readjusting $\mu_{ch}$.

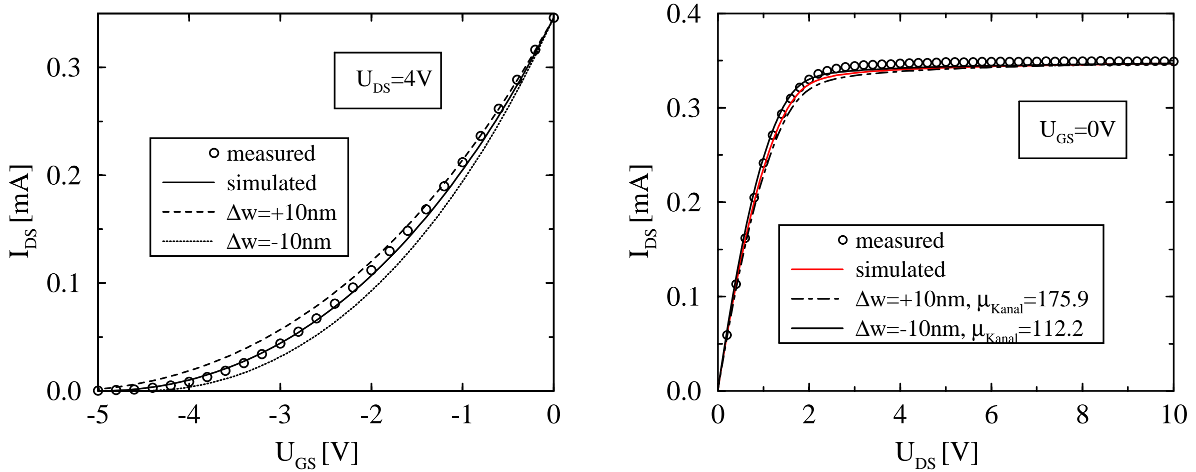


Figure 5.19: Influence of channel width on transfer (left) and output (right) characteristics of sample J10/5 at $T = 423\,\text{K}$.

| sample | a [nm] | $\mu_{channel}$ [$\frac{cm^2}{Vs}$] | $U_T$ [V] | $N_K$ [$cm^{-3}$] | $\mu'_{channel}$ [$\frac{cm^2}{Vs}$] |
|---|---|---|---|---|---|
| J10/5 | 503 | 135.3 | -4.7 | $7.4 \cdot 10^{16}$ | 135.3 |
| J10/20 | - | - | -4.1 | $7.2 \cdot 10^{16}$ | 73.1 |
| J100/5 | 620 | 96.7 | -11.2 | $1.1 \cdot 10^{17}$ | 71.3 |
| J100/10 | 620 | 92.2 | -10.9 | $1.1 \cdot 10^{17}$ | 68.0 |
| J100/20 | - | - | -11.7 | $1.2 \cdot 10^{17}$ | 61.1 |

Table 5.3: Comparison of extracted data of all investigated samples.

In Tab. 5.3, the measured threshold voltages $U_{th}$ are given for all investigated devices. The large variations of $U_{th}$ can be mapped to either variations in thickness or doping concentration of the n-type epi-layer. Quantitative information is obtained by adapting $a$ and $\mu_{ch}$ at a given doping concentration $N_{ch} = 8 \cdot 10^{16}\,\text{cm}^{-3}$ or by adapting $N_{ch}$ and $\mu_{ch}$ at a given channel thickness $a = 500\,\text{nm}$ in order to fit the corresponding transfer characteristics as shown in Fig. 5.20. In both cases, the resulting mobility should be approximately constant as this property is not expected to vary significantly across the wafer. This is precisely obtained by the simulation results of all samples except sample J5/10 (Tab. 5.3). Comparing both cases for one given sample, a larger extracted value for the mobility is found in the case of a larger channel width.

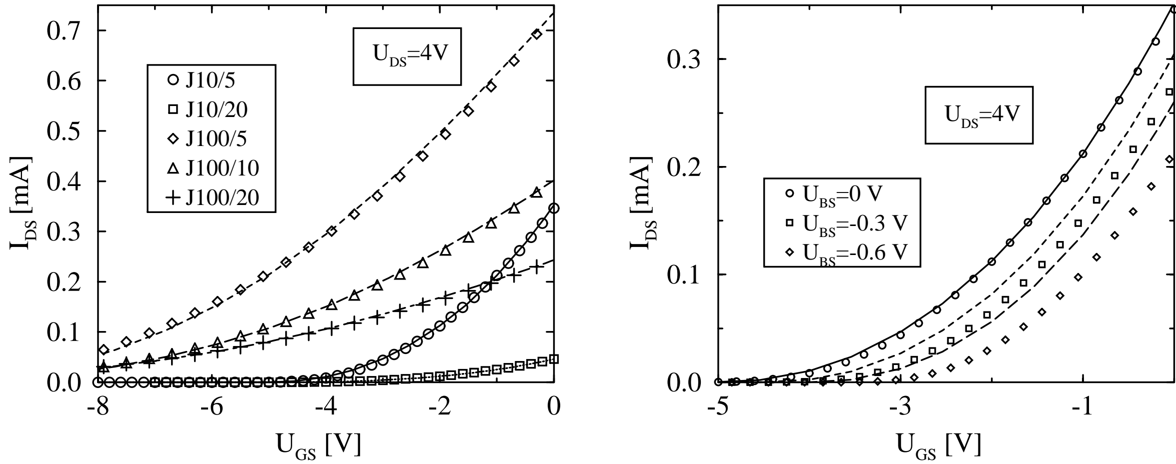


Figure 5.20: Comparison of the transfer characteristics of all investigated samples (left) and measured (symbols) and simulated (lines) transfer characteristics of sample J10/5 at different base potentials and $T = 423\,\mathrm{K}$ (right).

The extracted values for possible variations of $N_{ch}$ and $a$ are realistic as the thickness of the epi-layer as well as the doping concentration may vary across the wafer by such values [191, 192]. However, considering Fig. 3.5 and Eq. (3.11), a channel mobility of about $180\,\mathrm{cm}^2/\mathrm{Vs}$ would be expected at $T = 300\,\mathrm{K}$. Therefore, a large difference is obtained between the extracted material parameter and the theoretically expected value which will be further discussed in the following section.

#### 5.2.1.2 Inhomogeneous channel properties

The base contact which basically acts as second gate in this device yields additional information about the channel properties. By comparing the measured transfer characteristics of sample J5/10 at different base potentials with simulated data using the same extracted channel parameters as given in Tab. 5.3, significant disagreement is obtained with decreasing base potentials (Fig. 5.20). The variation of the measured $I_D \sim \sqrt{U_{BS}}$ confirms that the channel is controlled by the depletion region at the substrate junction $w_B$. However, any readjustment of $N_{ch}$ and $a$ in order to fit to the bottom-gate transfer characteristic $g_{mB}(U_{BS})$ would also result in a change of the simulated top-gate control characteristics $g_{mT}(U_{GS})$ (Fig. 5.19). Analyzing all relevant device parameters proves that only a non-uniform effective channel doping concentration $N_{ch,eff}$ can explain such findings. This leads to a shift of the conducting channel towards the substrate resulting in a larger influence of $U_{BS}$ without changing the top-gate transfer characteristics. Two different configurations have been found which can be adapted to the measured data. The first case consists of an effective doping profile near the gate junction as sketched in Fig. 5.21 possibly caused by doping tails from the gate implantation [173, 193] or by large implantation damage (Fig. 5.12) introducing deep centers in the channel compensating the channel doping (Fig. 5.22).

A rather large gradient must be assumed to be able to adapt the measured data in that case. Apart from the fact that an effective doping profile as shown in Fig. 5.21 seems to be rather unrealistic, the corresponding simulation still yields a significant disagreement below the threshold voltage as shown by

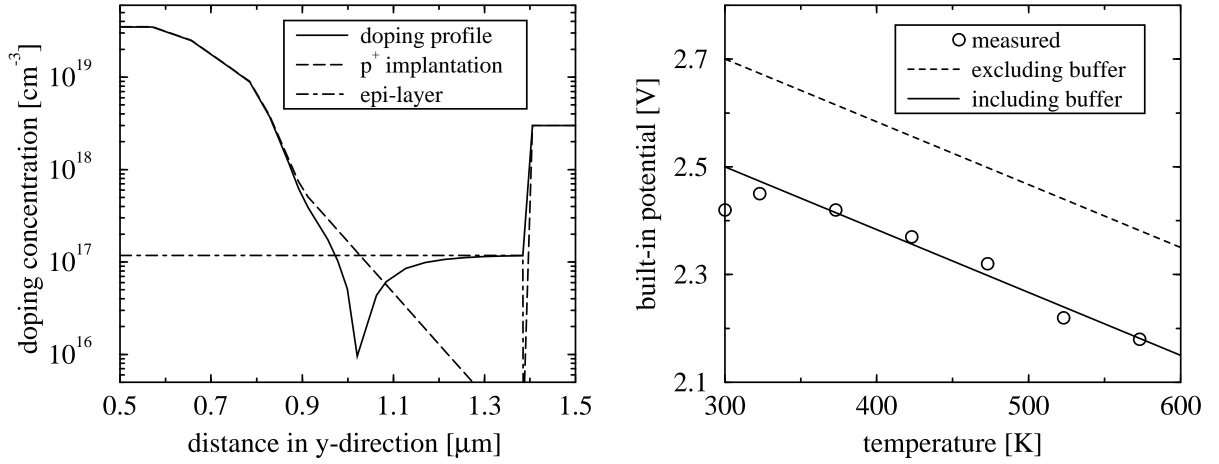


Figure 5.21: Doping profile due to compensated channel doping (left) and influence of a buffer layer between substrate and channel on built-in potential (right).

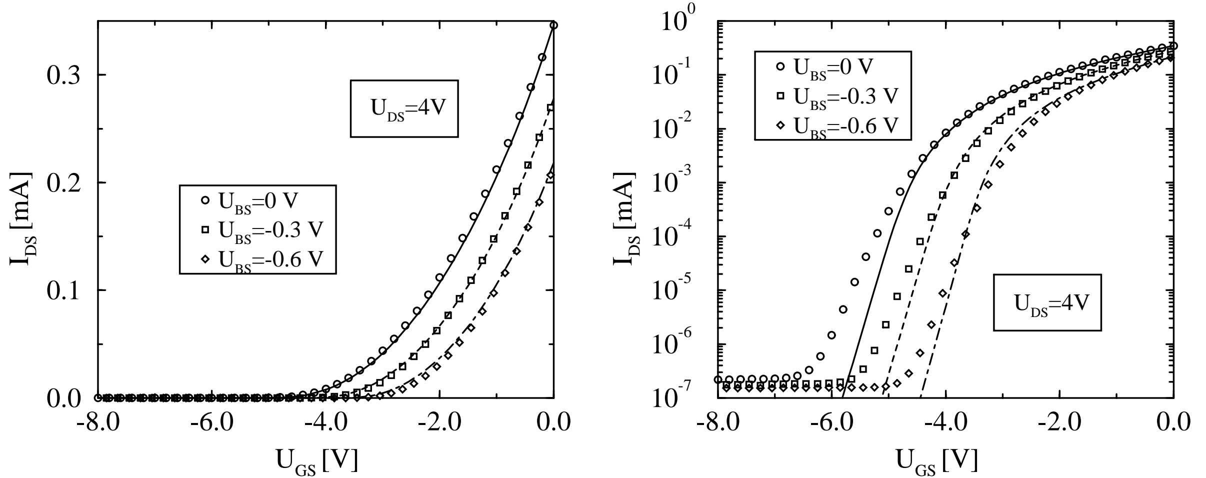


Figure 5.22: Influence of doping profile on linear (left) and logarithmic (right) plot of the transfer characteristics of sample J10/5 at $T = 423\,\mathrm{K}$.

a logarithmic plot of the transfer characteristics (Fig. 5.22). Furthermore, considering the data obtained by CV-measurements at the pn-junction between channel and substrate, the built-in potential extracted from the intercept with the y-axis of the CV-plot [154] yields about 0.2 V larger built-in potential than expected [194]:

$$C \equiv \frac{\varepsilon\varepsilon_0}{W} = \sqrt{\frac{q\varepsilon\varepsilon_0 N_{ch}}{2}} \cdot (V_{bi} \pm V)^{-1/2} \,. \tag{5.12}$$

This finding could be explained by assuming a thin $n^+$-buffer layer between p-substrate and n-type epi-layer. Such a layer may have been used by the manufacturer to enhance the quality of the epi-layer. The existence of such a buffer layer could not be clarified with the manufacturer. By defining a buffer thickness of 3 nm and an n-type doping concentration of $N_{buf} = 7 \cdot 10^{17}\,\mathrm{cm}^{-3}$, excellent agreement between measured and simulated data is obtained including the sub-threshold region of the transfer characteristics (Fig. 5.23), the output characteristics (Fig. 5.24), and the the built-in potential

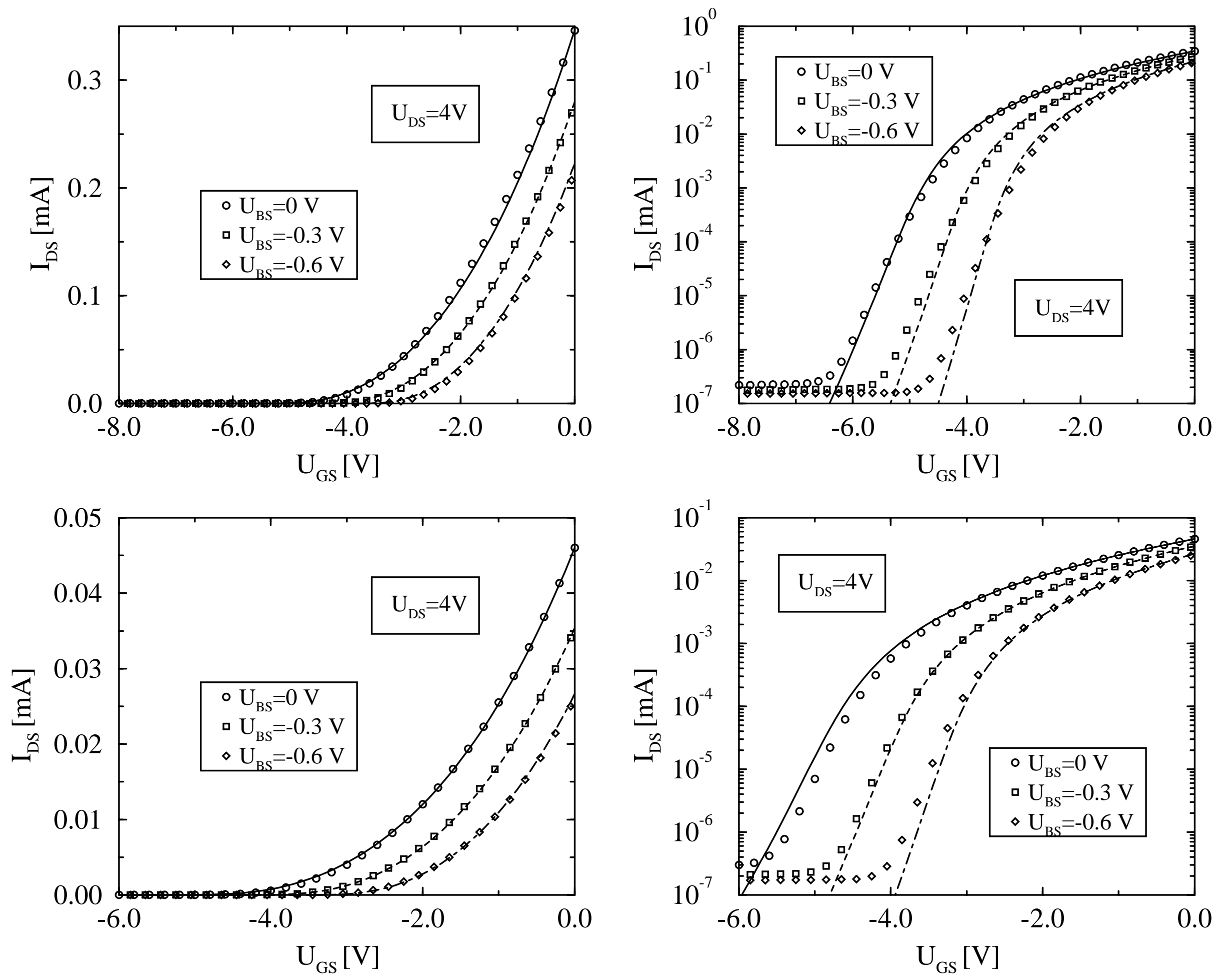


Figure 5.23: Influence of $n^+$-buffer layer on linear (left) and logarithmic (right) plot of the transfer characteristics of sample J10/5 (first row) and J10/20 (second row) at $T = 423\,\mathrm{K}$.

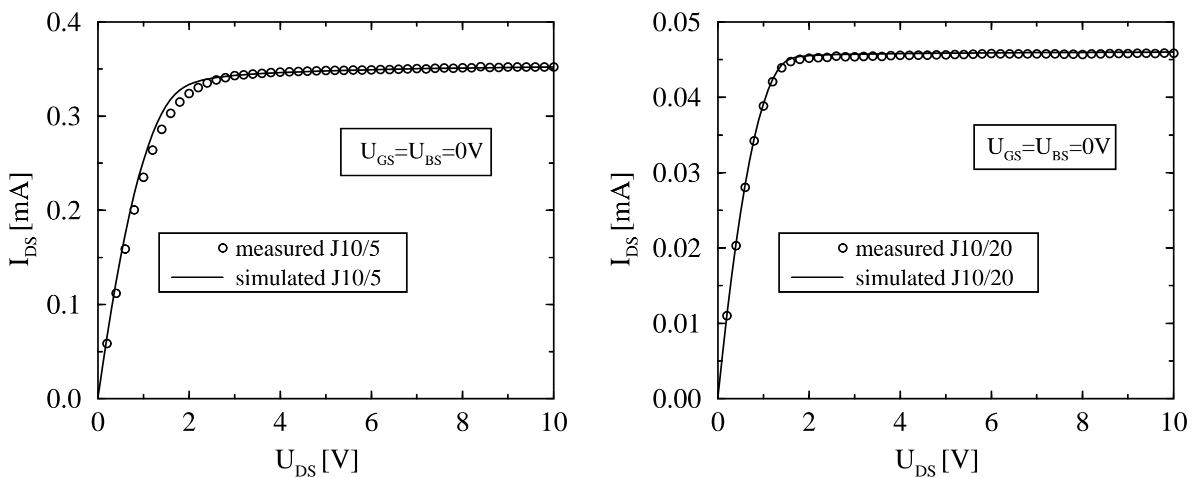


Figure 5.24: Influence of $n^+$-buffer layer on output characteristics of sample J10/5 (left) and sample J10/20 (right) at $T = 423\,\mathrm{K}$.

extracted from simulated CV-characteristics (Fig. 5.21). Furthermore, a larger effective channel mobility is extracted compared to the results obtained with an inhomogeneous channel doping profile, nearly approaching the theoretically expected value. Similar agreement is obtained for sample J10/20 with $N_{buf} = 4.6 \cdot 10^{16}\,\mathrm{cm}^{-3}$ as shown in Fig. 5.23 and 5.24.

Obviously, it is not possible to extract the exact shape of the effective channel doping profile or buffer layer. Furthermore, both configurations may be relevant. However, the relevance of inhomogeneous channel properties has been proven by numerical simulation. It has been found that despite of a good agreement between measured and simulated data, the extracted parameters of the top-gate analysis have to be reviewed carefully with respect to the bottom-gate characteristics. This is only accessible by numerical simulation as no analytical approach is available in this case.

#### 5.2.1.3 Temperature dependence of channel properties

The temperature dependence of the device characteristics is mainly determined by two physical mechanisms within the investigated range of 300 - 623 K (Fig. 5.25). At high temperatures, the drain saturation current $I_{DSS}$ clearly follows the expected potential law $\mu_n(T) = \mu_n^{T_0} \cdot (T/T_0)^{\alpha_n^{mob}}$ (see section 3.4.1). A temperature coefficient $\alpha_n^{mob} = -1.77$ for the channel mobility is obtained for all investigated samples which has been reported for high-quality epitaxial material [114], indicating that implantation damage is negligible within the conducting channel. At lower temperatures, the increasing mobility with decreasing temperature is partly compensated by the onset of incomplete ionization of the channel doping and a point of inflection is obtained below 300 K. At lower temperatures, the contact resistance may also be relevant.

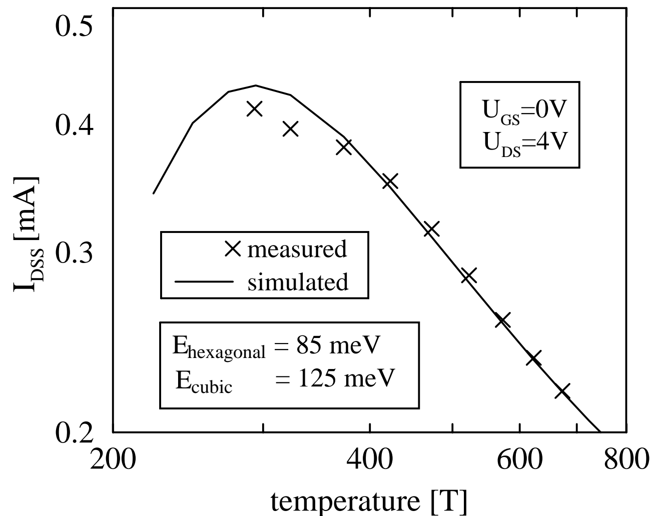


Figure 5.25: Temperature dependence of drain saturation current of sample J10/5 at $U_{BS} = 0\,\mathrm{V}$.

### 5.2.2 Extraction of channel length of buried-gate 6H-SiC JFET

As a further reference device for evaluating SiC device simulation, a buried-gate, n-channel, depletion-mode 6H-SIC JFETs purchased from CREE Research, Inc. [177] has been investigated (Fig. 5.26). The structure parameters, as given by the manufacturer, have been reexamined by CV- and TEM-measurements of one reference sample (Tab. 5.4).

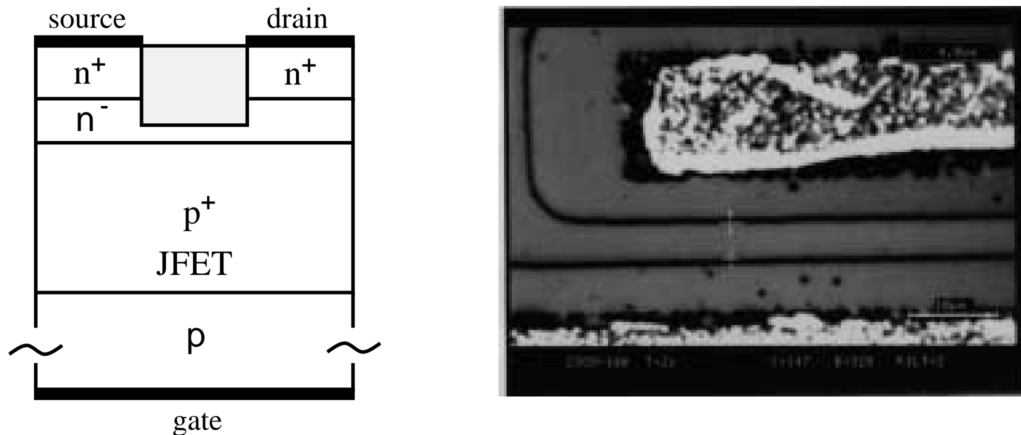


Figure 5.26: Cross section of buried-gate JFET structure (left) and REM picture showing the channel length of the device (right).

| | | |
|---|---|---|
| $n^+$-contact layer | [cm$^{-3}$] | $4.5 \cdot 10^{18}$ |
| n-channel layer | [cm$^{-3}$] | $2.1 \cdot 10^{17}$ |
| $p^+$-epi-layer | [cm$^{-3}$] | $1.4 \cdot 10^{18}$ |
| substrate | [cm$^{-3}$] | $2 \cdot 10^{17}$ |
| channel thickness | [nm] | 180 |
| channel length | [$\mu$m] | 2 |

Table 5.4: Structural data of buried-gate JFET

We applied the same strategy for extracting the channel parameters as outlined in section 5.2.1. By adapting the channel thickness and the channel carrier mobility to fit the transfer characteristics, a significant disagreement between measured and simulated output characteristics still remains (Fig. 5.27). While analyzing all relevant device parameters, no consistent parameter set fitting both, transfer and output characteristics has been found. Possible inhomogeneous channel properties or any buffer layers (see section 5.2.1) have been found to only minor influence the output characteristics. We therefore investigated the influence of all relevant parameters including the channel length. It is well known [154] that a short channel length sensitively influences the saturation behavior of the output characteristics. This so-called "short-channel effect" is characterized by a non-zero slope of the drain current in the output characteristics above the pinch-off voltage of the device. The corresponding slope decreases with increasing channel length. We obtained excellent agreement between measured and simulated data when assuming $L_{ch} = 4\,\mu$m (Fig. 5.28).

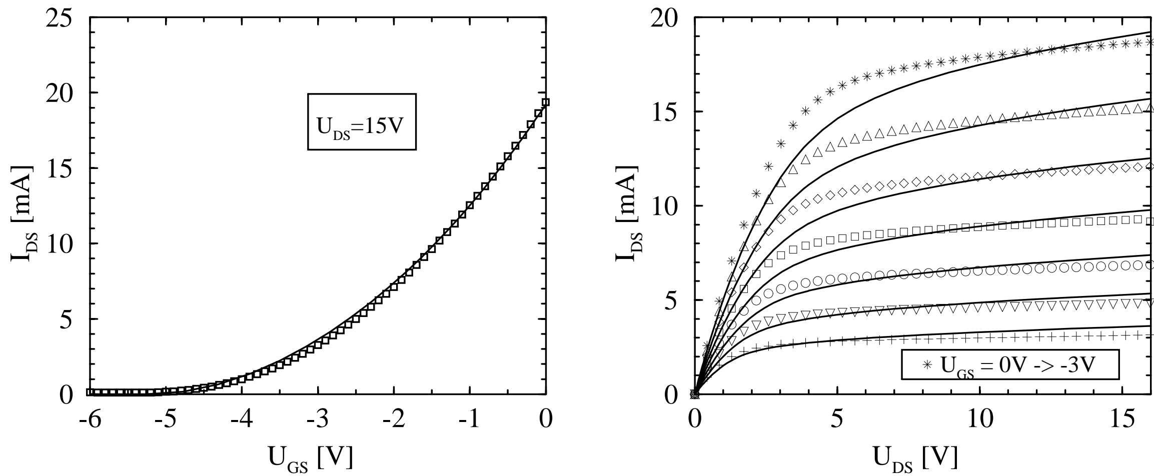


Figure 5.27: Transfer (left) and output (right) characteristics of buried-gate JFET assuming a channel length $L_{ch} = 2\,\mu$m at $T = 273\,$K.

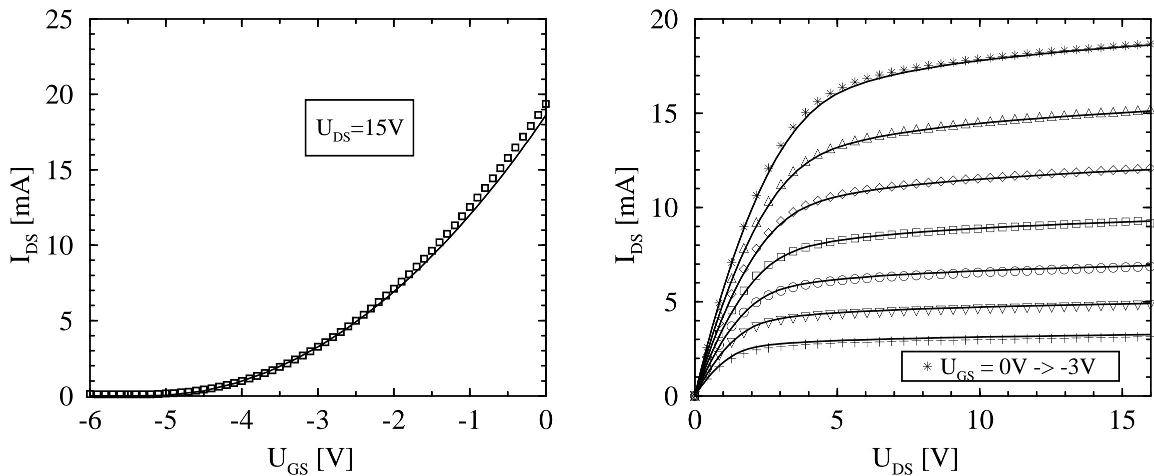


Figure 5.28: Transfer (left) and output (right) characteristics of buried-gate JFET assuming a channel length $L_{ch} = 4\,\mu$m at $T = 273\,$K.

As any variation of $L_{ch}$ by more than 100% seemed to be rather unrealistic, the investigated sample itself has also been examined using TEM. It turned out that the channel length of this sample differed from that of the initially characterized reference sample of the same product. The predicted $L_{ch}$ has been confirmed as shown in Fig. 5.26 demonstrating that the concept of inverse modeling is applicable to such devices.

## 5.3 Impact of anisotropic material properties on device characteristics

As commercial device applications are presently nearly exclusively based on isotropic semiconductor materials (Si, GaAs), there is only minor and very qualitative knowledge about the various influences arising from anisotropic properties of a given material on the characteristics of complex device structures.

| | $\varepsilon_{\perp}/\varepsilon_{\parallel}$ | $\mu_{n\perp}/\mu_{n\parallel}$ | $\mu_{p\perp}/\mu_{p\parallel}$ | $\kappa_{\perp}/\kappa_{\parallel}$ |
|---|---|---|---|---|
| 4H-SiC | - | 0.8 | 1 | - |
| 6H-SiC | 0.96 | 5 | 1 | 0.7 |

Table 5.5: Measured anisotropic ratios of 4H- and 6H-SiC material parameters.

In Tab. 5.5, the anisotropic ratio $x_{\perp}/x_{\parallel}$ of several relevant material properties is given for 4H- and 6H-SiC (see chapter 3). For 4H-SiC, only the anisotropic ratio of the free carrier mobilities has been experimentally investigated. Comparing this property between both polytypes in the case of electrons reveals their largely differing anisotropic behavior.

Restricting our investigations to the electronic properties, $\tilde{\mu_\nu}$ and $\tilde{\varepsilon}$, their basic influence on device characteristics can be classified as 1st) changing the properties of bulk resistive or capacitive regions within a device, and 2nd) the corresponding implicit influence on regions which control the transfer characteristics of active devices.

In the following, several effects of both categories within typical device structures are investigated. If not indicated explicitly, the vertical direction of a device is assumed to be parallel to the ĉ-axis, since most substrates commercially available today have the polished surface perpendicular to the ĉ-axis[5]. All simulations are performed with the material parameters of 6H-SiC applying different anisotropic ratios in order to working out their general influence on device characteristics.

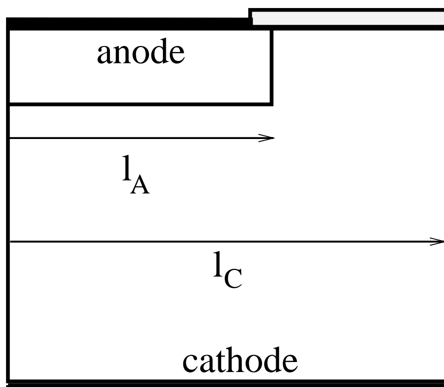


Figure 5.29: Schematic of a pn-diode with varying length of edge termination.

[5]neglecting the off-axis angle due to the epitaxial growth.

### 5.3.1 Planar 6H-SiC pn-diode characteristics

Let us first consider a planar 6H-SiC pn-diode as sketched in Fig. 5.29. We compare the forward IV characteristics for three different ratios of $l_A/l_C$ including and excluding anisotropic current transport with the wafer surface perpendicular and parallel to the ĉ-axis. Neglecting any influence arising from the edge of the device ($l_A/l_C = 1$), a quasi one-dimensional vertical current flow is obtained. Therefore, no difference is observed between an anisotropic simulation and an isotropic calculation with $\mu_n = \mu_{n_{\|}}$ (Fig. 5.30).

On the other hand, when decreasing the ratio $l_A/l_C$, the contributions of the lateral electron transport lead to an increasing influence of the anisotropic electron mobility and a rescaled isotropic simulation yield different IV characteristics (Figs. 5.30 and 5.32)[6]. With $l_A/l_C = 0.5$, for instance, the on-resistance of an anisotropic simulation with the ĉ-axis parallel to the wafer surface ($\mu_n^{lat} < \mu_n^{vert} = \mu_n^{iso}$) is larger compared to the corresponding isotropic case. It is interesting to note that any anisotropic mobility ratio ($\mu_n^{lat}$ larger or smaller than $\mu_n^{vert} = \mu_n^{iso}$) increases the on-resistance.

A different situation occurs at higher current ratings or a smaller ratio $l_A/l_C$ (Fig. 5.32). The voltage drop needed to carry a normalized current density exceeding 2.1 kA/cm$^2$ is larger for $\mu_n^{vert} > \mu_n^{lat}$ compared to $\mu_n^{vert} < \mu_n^{lat}$ assuming the anisotropic ratio of 6H-SiC. This, at a first glance, completely unexpected situation is explained by the internal electric potential distribution (Fig. 5.31). A reduced lateral mobility leads to a larger lateral voltage drop underneath the wafer surface (Fig. 5.32). The respective lateral electric field forces a large lateral current flow which significantly increases the on-resistance of the device (Fig. 5.31). For $\mu_n^{vert} < \mu_n^{lat}$, on the other hand, the current flow is localized within the active area of the device. Again the anisotropic mobility ratio results in a slightly larger on-resistance compared to the respective isotropic case (Fig. 5.32).

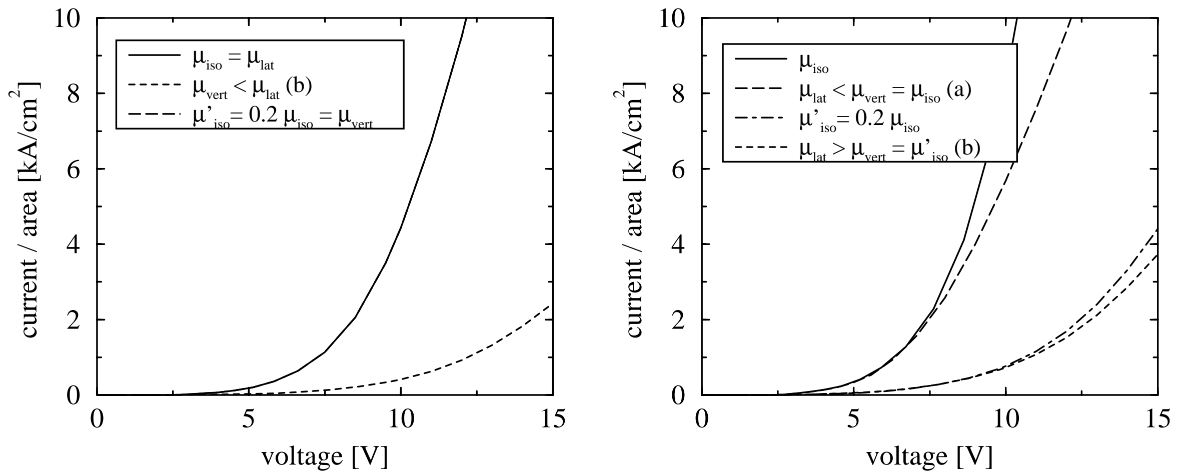


Figure 5.30: Forward IV characteristics of a pn-diode with $l_A/l_C = 1$ (left) and $l_A/l_C = 0.5$ (right).

Hence, it is shown that the redistribution of the electric potential in bulk regions leads to rather unexpected characteristics even in mainly one-dimensional structures. As a result, for instance, the onset

[6]In this section, we investigate on samples with different orientation of the ĉ-axis: (a) $\mu_{lat} = \mu_{\|}$ and (b) $\mu_{lat} = \mu_{\perp}$ with $\mu_{lat}$ denoting the mobility parallel to the wafer surface (Fig. 5.31).

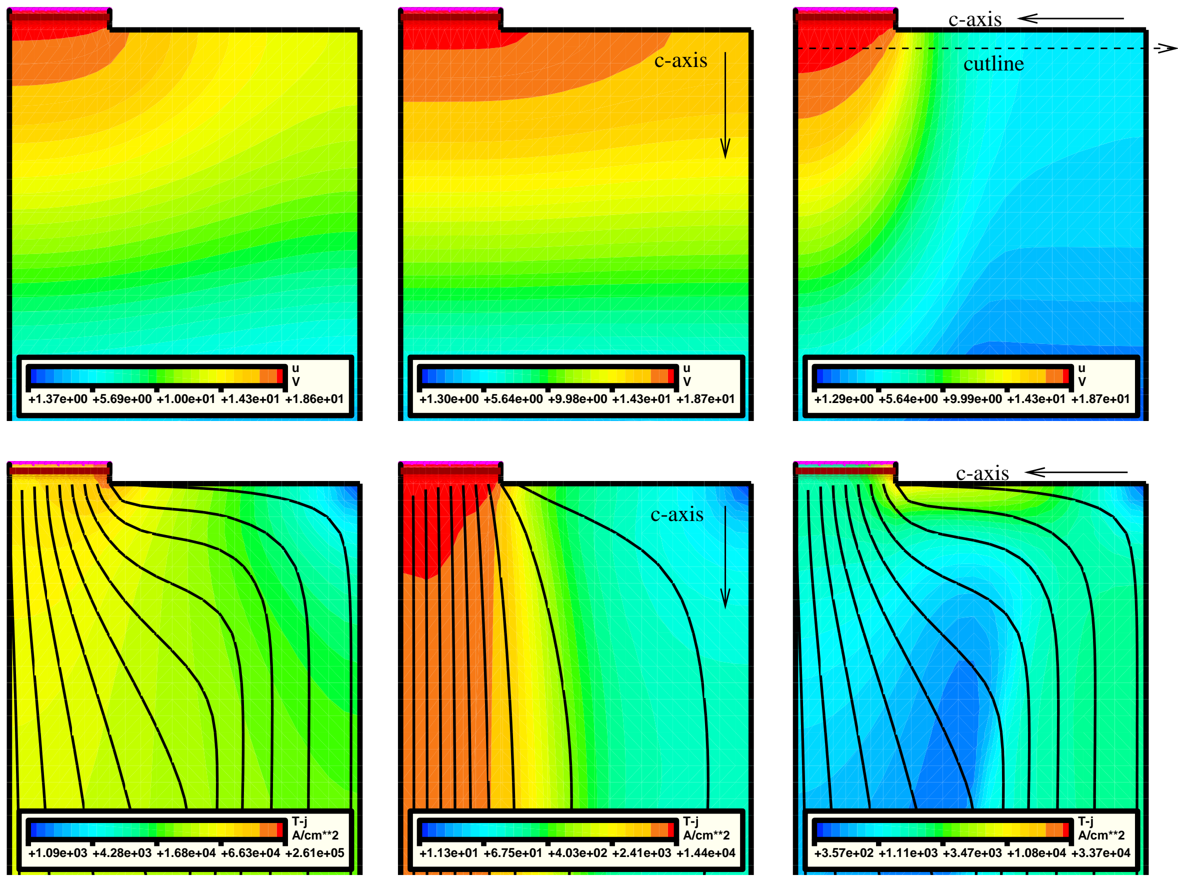


Figure 5.31: Distributions of electric potential (first row) and current density (second row ) within a planar pn-diode at high injection levels excluding (left) and including anisotropic current transport with the ĉ-axis perpendicular (middle - case (a)) and parallel (right - case (b)) to the wafer surface.

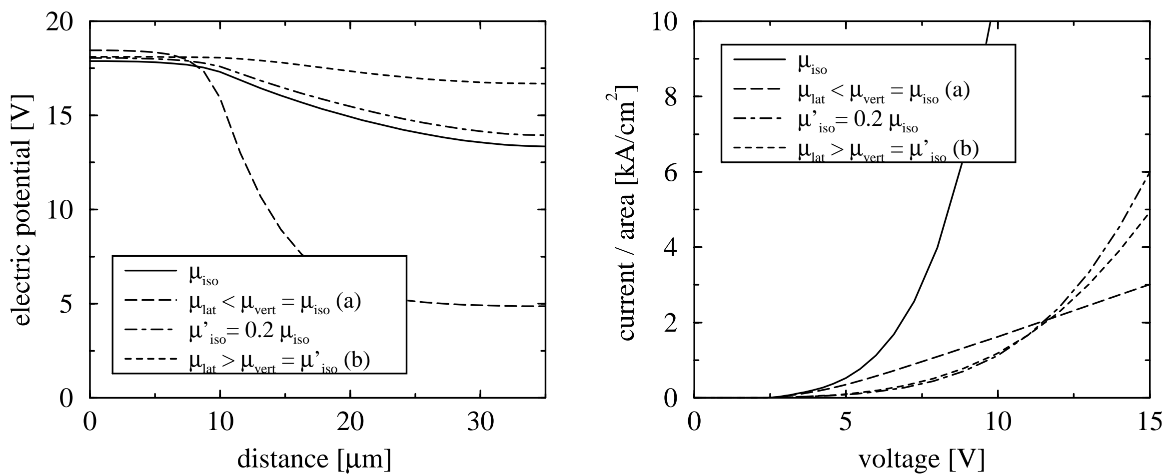


Figure 5.32: Lateral distribution ($l_A/l_B = 0.3$) of electric potential (see cutline in Fig. 5.31) including and excluding anisotropic current transport (left) and corresponding forward IV characteristics (right).

voltage for punch-through at a p-doped guard ring of an n-Schottky diode would be unexpectedly altered.

Apart from the influence of anisotropic material properties arising from the generally more complex two-dimensional structure of active devices such as MOSFETs, JFETs, BJTs, and thyristors, the influence of a redistributed electric potential on regions which control their transfer characteristics add an additional degree of complexity. With a view to demonstrating the basic effects of anisotropy within those devices, different types of structures are investigated including and excluding anisotropic material properties. If not explicitely mentioned, the lateral mobility component $\mu_{lat} = \mu_{\perp}$ is set to the same value as used for the isotropic simulations.

### 5.3.2 UMOS and lateral JFET characteristics

Considering first device structures with prevailing one-dimensional current flow within the predominant resistive components, we intuitively expect only a minor influence of the anisotropic mobility. In Fig. 5.34 the output characteristics of a trench-gated MOSFET (UMOS) as sketched in Fig. 5.33 (a) and a lateral JFET as sketched in Fig. 5.33 (b) are plotted.

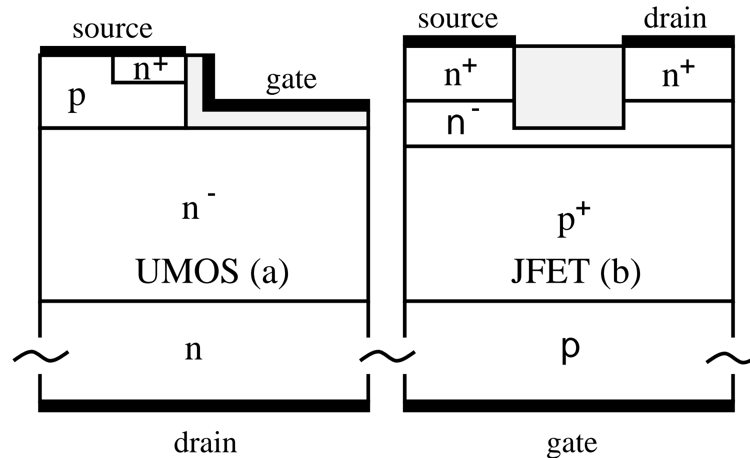


Figure 5.33: Schematic of an UMOS and a lateral JFET.

The current flow in the UMOS is mostly oriented in a vertical direction due to the vertical channel along the sidewall of the trench. Hence, the electron mobility along the ĉ-axis, $\mu_{n_{\parallel}}$, dominates and an isotropic calculation using a reduced electron mobility $\mu_n^{iso} = \mu_{n_{\parallel}}$ is shown to be a quite good approximation. The resulting specific on-resistance will be slightly underestimated because of the lateral components of current flow in the drift zone beneath the trench. Within this operation area, the influence of the anisotropic ratio of $\tilde{\varepsilon}$ can almost be neglected. However, the anisotropic $\tilde{\varepsilon}$ could easily be relevant within more complicated UMOS structures [113] which have been proposed to reduce the maximum electric field occurring at the corner of the trench.

In the lateral JFET the current flow is oriented in both, vertical and lateral directions within different regions of the device. However, the influence of the regions with lateral current flow can be neglected

due to their high doping concentration and the corresponding high conductivity. Again, the output characteristics are well approximated by an isotropic calculation using the lateral mobility, $\mu_n^{iso} = \mu_{n_\perp}$ and the vertical electric permitivity, $\varepsilon^{iso} = \varepsilon_{||}$.

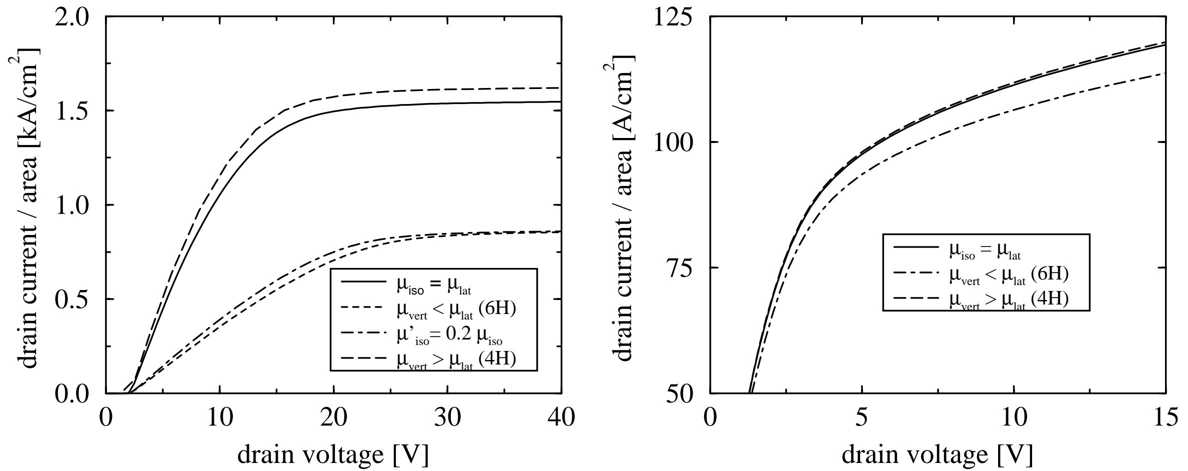


Figure 5.34: Influence of anisotropic transport properties on UMOS output characteristics at $U_G = 20\,\mathrm{V}$ (left) and lateral JFET output characteristics at $U_G = 0\,\mathrm{V}$ (right).

### 5.3.3 DIMOS characteristics

Reliability problems due to the field crowding at the trench corners of the UMOS and the currently superior effective channel mobilities for channel orientations perpendicular to the ĉ-axis motivated prototyping of power MOSFETs with lateral channel orientations [179, 180].

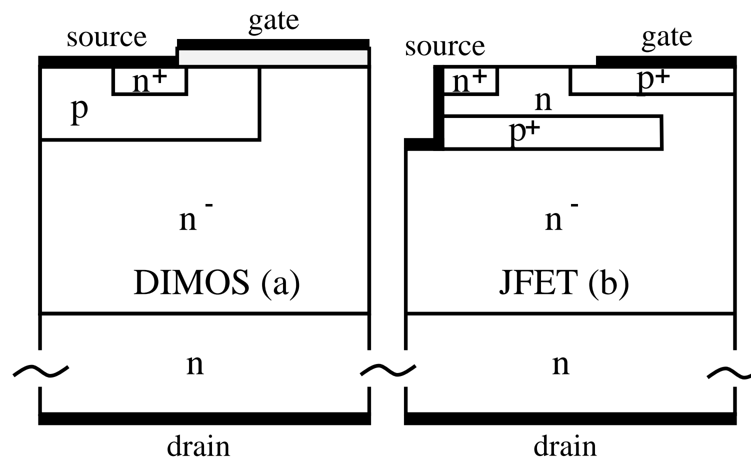


Figure 5.35: Schematic of a DIMOS and a vertical JFET.

In Fig. 5.35 (a), the cross section of a DIMOS as discussed in [49, 50] is sketched which was first realized by Shenoy et al. [179]. In this case, the on-state current flows first in a lateral direction

underneath the gate, while it is redistributed in the drift region forming a vertical flow parallel to the ĉ-axis. Neglecting any contributions arising from the drain and source contact resistance as well as the $n^+$-source region, the on-resistance $r_{on}$ of this device is determined by contributions arising from the channel resistance $r_{ch}$, the resistance of the accumulation layer in the drift region below the oxide $r_{accu}$, the JFET resistance of the region below the accumulation layer $r_{jfet}$, the drift layer resistance $r_{drift}$, and the substrate resistance $r_{sub}$.

For 6H-SiC we find that $r_{on}$, which is the most important parameter of such a device, is significantly reduced when we compare an isotropic simulation of the output characteristics assuming $\mu_n^{iso} = \mu_{n\perp}$ with that based on the anisotropic transport model (Fig. 5.36). This is primarily the combined effect of the different contributions to $r_{on}$ with $r_{ch}$ and $r_{drift}$ generally dominating. Thus, the isotropically calculated on-resistance scales with the electron mobility: $r_{on} \propto 1/\mu_n$. Here, only the vertical current components are affected by including an anisotropic mobility. Therefore, the ratio of $r_{on}^{6H}/r_{on}^{iso\perp}$ is strongly dependant on the percentage of vertical resistive components to the complete on-resistance, which is determined by structural and material properties and the applied gate voltage. Using the standard parameter set evaluated in chapter 3 and neglecting any reduction of the effective channel mobility caused by the $SiC - SiO_2 -$interface, we obtain a value of 3.5 for this ratio.

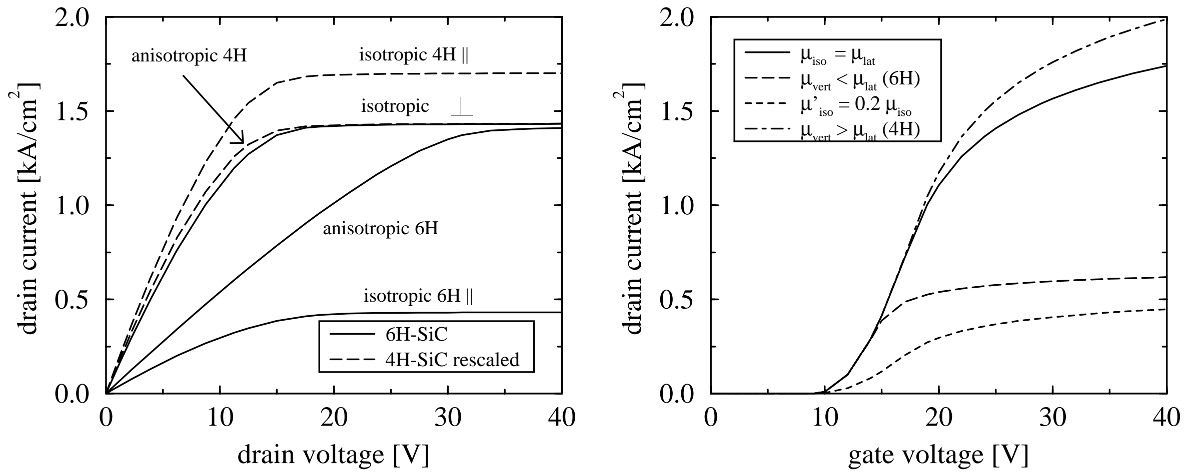


Figure 5.36: Influence of anisotropic transport properties on DIMOS output characteristics at $U_G = 20\,\text{V}$ (left) and transfer characteristics at $U_D = 10\,\text{V}$ (right).

The drain saturation current $I_{DSS}$, on the other hand, is mainly determined by the effective channel mobility $\mu_n^{eff}$, and the electron saturation velocity $v_n^{sat}$. This is corroborated by plotting the $\mu_n^{eff}$ underneath the gate (Fig. 5.37), which is reduced from the value of $200\,\text{cm}^2/\text{Vs}$ obtained by Eq. (3.11) to below $90\,\text{cm}^2/\text{Vs}$ due to high lateral electric field. For a reduced $\mu_n^{iso} = \mu_{n\parallel}$, we conclude from Eq. (3.15) that $v_n^{sat}$ will be reached at a higher electric field and $I_{DSS}$ is exclusively determined by the pinch-off of the inversion layer at the drain side of the channel. Here, we obtain $I_{DSS}^{iso\perp}/I_{DSS}^{iso\parallel} = 3.2$ for the ratio of saturation current of the isotropic simulations with $\mu_n^{iso} = \mu_{n\perp}$ and $\mu_n^{iso} = \mu_{n\parallel}$, whereas $I_{DSS}$ remains unaffected in the anisotropic case (Fig. 5.36).

Fig. 5.38 shows the current flowlines in the device during on-state including and excluding anisotropic transport properties. The current crowding occurring in the transition region between lateral and vertical

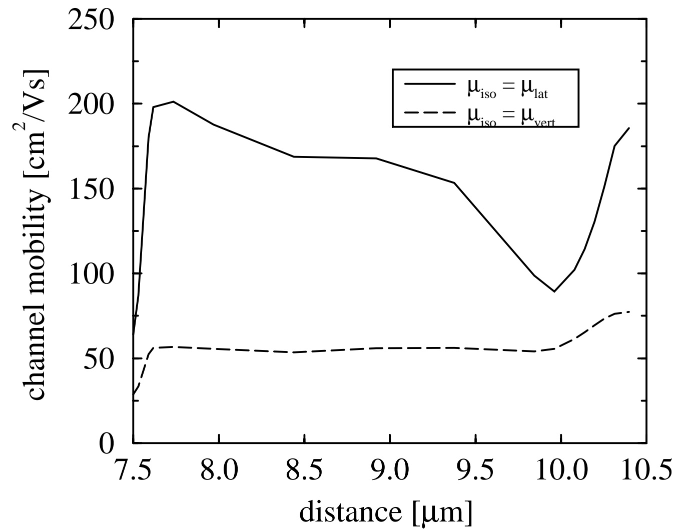


Figure 5.37: Field-dependent effective channel mobility along the channel.

current flow in the anisotropic simulation results from the larger extension of the accumulation layer underneath the gate (Fig. 5.39), which is affected by the potential redistribution as a consequence of the anisotropic electrical conductivity.

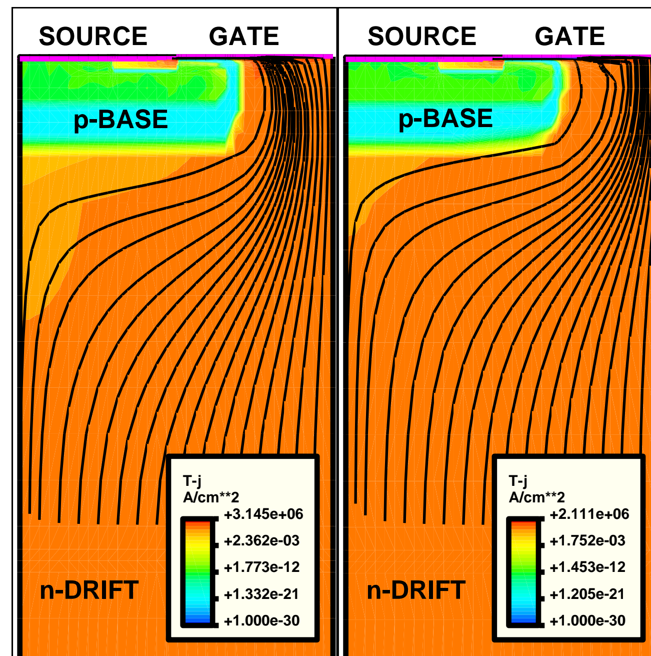


Figure 5.38: Current flowlines in a DIMOS cell during on-state with anisotropic transport properties excluded (left) and included (right).

In 4H-SiC, on the other hand, the smaller anisotropic ratio of the mobility results in much smaller differences between the anisotropic and the isotropic simulation (Fig. 5.36). However, it increases with

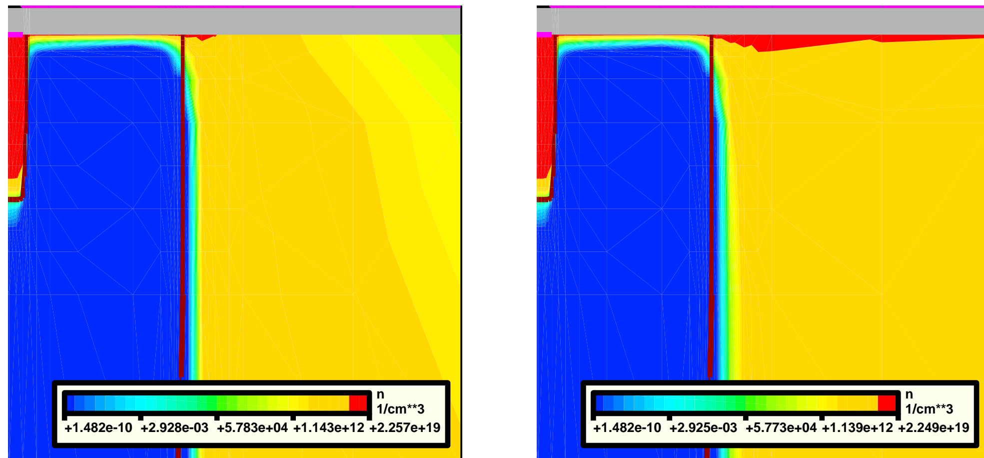


Figure 5.39: Accumulation region within the drift region below the gate with anisotropic transport properties excluded (left) and included (right).

rising gate voltage. Beyond the threshold voltage, the transfer characteristics of both, 4H- and 6H-SiC, differ significantly from the rescaled isotropic calculations. $I_{DS}$ of a 6H-SiC device becomes nearly independent of $U_{GS}$ for $U_{GS} > 20\,\mathrm{V}$ due to the increasing contribution of $r_{drift}$, whereas $I_{DS}$ of a 4H-SiC device depends even more on $U_{GS}$.

### 5.3.4 Vertical high-power JFET characteristics

The current flow within vertical power JFETs [35], as sketched in Fig. 5.35 (b) is very similar to that of the DIMOS mentioned above and a comparable influence of anisotropic transport properties on the output characteristics is obtained (Fig. 5.40 left). Here, the lateral mobility of the channel and the vertical mobility of the drift layer primarily determines the IV characteristics. In this case, however, the anisotropic permitivity $\tilde{\varepsilon}$ must also be considered as shown in Figs. 5.40 and 5.41. The influence of the anisotropic ratio of $\tilde{\varepsilon}$ is demonstrated by comparing different configurations assuming an isotropic mobility. It is shown that the anisotropic properties of this device are sufficiently modeled by only accounting for $\tilde{\mu}_n$ and using $\varepsilon^{iso} = \varepsilon_{\|}$.

### 5.3.5 Summary

State-of-the-art SiC DIMOS devices exhibit an effective channel mobility of about $30\,\mathrm{cm}^2/\mathrm{Vs}$ [180]. The rather poor effective channel mobility in 6H-SiC which is even worse in 4H-SiC qualifies the vertical 4H-SiC JFET as the most attractive candidate for the first commercial active power device application [21]. It has been shown that the behavior of such a device is sufficiently accurate approximated by isotropically rescaled material parameters during on-state. However, one should keep in mind that implicit effects could lead to unexpected results even for low anisotropic ratios and the blocking characteristics will be sensitively affected by $\tilde{\varepsilon}$. Finally, both, the controlling mechanisms and the main current flow, will be significantly influenced if the anisotropic carrier transport is relevant in bipolar

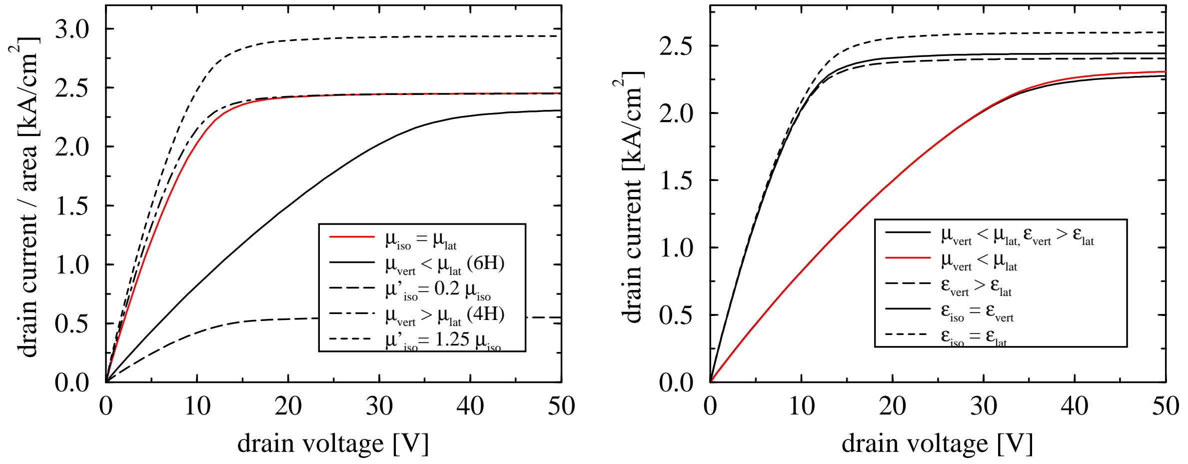


Figure 5.40: Influence of anisotropic transport properties on vertical JFET output characteristics at $U_G = 0\,\mathrm{V}$.

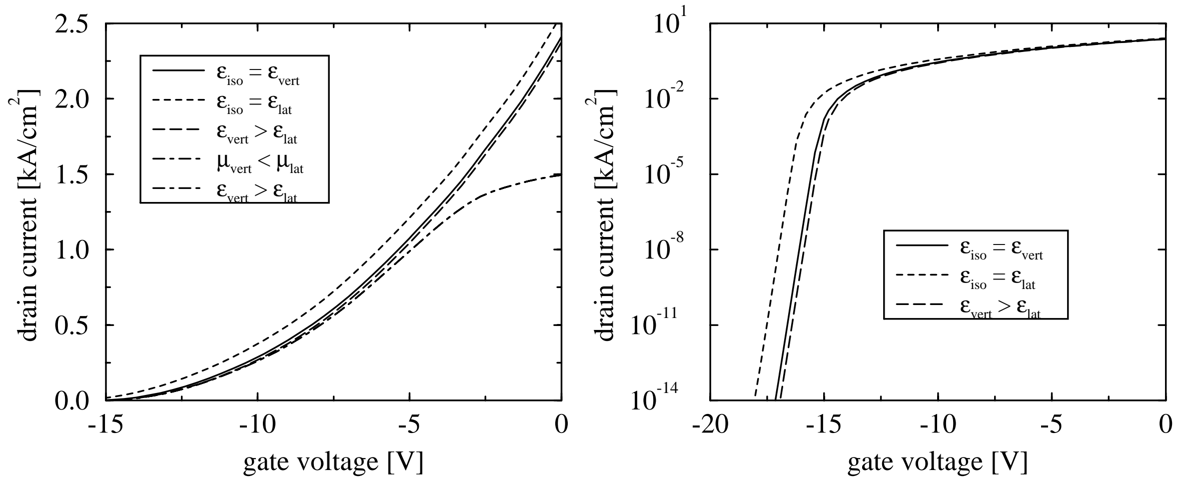


Figure 5.41: Influence of anisotropic transport properties on vertical JFET transfer characteristics at $U_D = 20\,\mathrm{V}$.

active devices such as BJTs and thyristors. In such cases, an accurate anisotropic transport model will be indispensable.

## 5.4 Dynamics of incomplete ionization of dopants

One of the most promising advantages of SiC high-power devices is their fast switching capability due to the strongly reduced stored charge at high current ratings compared to corresponding Si devices. It is therefore of major importance to know about the transient limits imposed by the electronic properties of the mostly used dopants in 4H- and 6H-SiC devices. In the interior of the depletion regions, the values of

$$\tau_A = \frac{1}{e_p^A + c_p^A\, p} \approx \frac{1}{e_p^A} \qquad \text{(acceptor)} \tag{5.13}$$

and

$$\tau_D = \frac{1}{e_n^D + c_n^D\, n} \approx \frac{1}{e_n^D} \qquad \text{(donor)} \tag{5.14}$$

given by Eq. (2.49) may be interpreted as ionization time constants of acceptors and donors, respectively. These quantities are crucial for analyzing the effect of incomplete ionization on the device behavior. In Fig. 5.42, the ionization time constants of $N_c$, Al, and B in 4H- and 6H-SiC, respectively, are given as function of temperature as determined in section 4.2 (see Fig. 4.32).

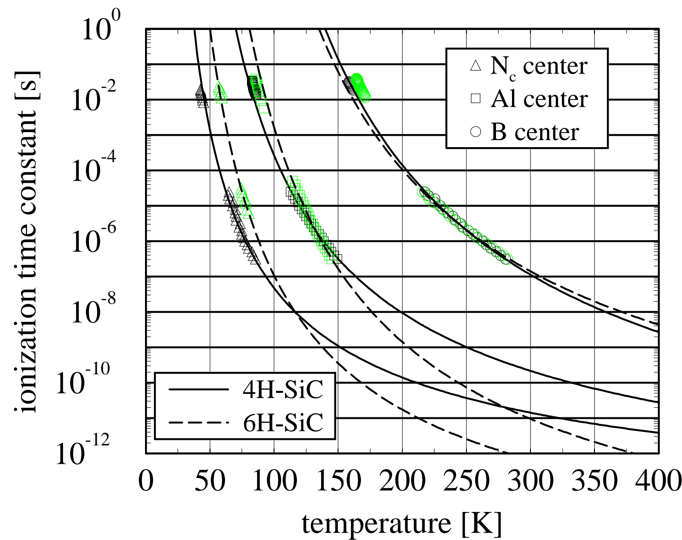


Figure 5.42: Temperature dependence of ionization time constants of N (cubic site), Al and B in 4H-SiC (solid lines) and 6H-SiC (dashed lines) with $\sigma_V^{tp}$ independent of temperature (see Fig. 4.32).

N and Al show ionization time constants shorter than 1 ns in the temperature range above 250 K. Hence, their dynamic behavior is intuitively expected not to influence today's power device applications whereas the ionization time constant of B, on the other hand, may be critical up to temperatures as high as 400 K. A detailed quantitative study of the major effects of dynamic dopant ionization on the behavior of SiC devices will be given in the following sections. Any other deep dopant or trap potentially relevant to 4H- and 6H-SiC (e.g. the boron-related D-center [188]) will qualitatively perform in a similar way and can be treated as analogous to these results.

### 5.4.1 PN-junction characteristics

Considering Eqs. (5.13) and (5.14) it becomes clear that dynamic ionization effects will be dominated by the emission of free carriers from impurity centers since the time constants of other charging or discharging effects will be drastically reduced by the presence of free carriers in neutral regions or under high injection conditions. Therefore, the basic mechanism of dynamic ionization is demonstrated by the dynamic response of a zero-biased pn- or Schottky-junction to a reverse bias pulse as illustrated by Figs. 5.43 and 5.44.

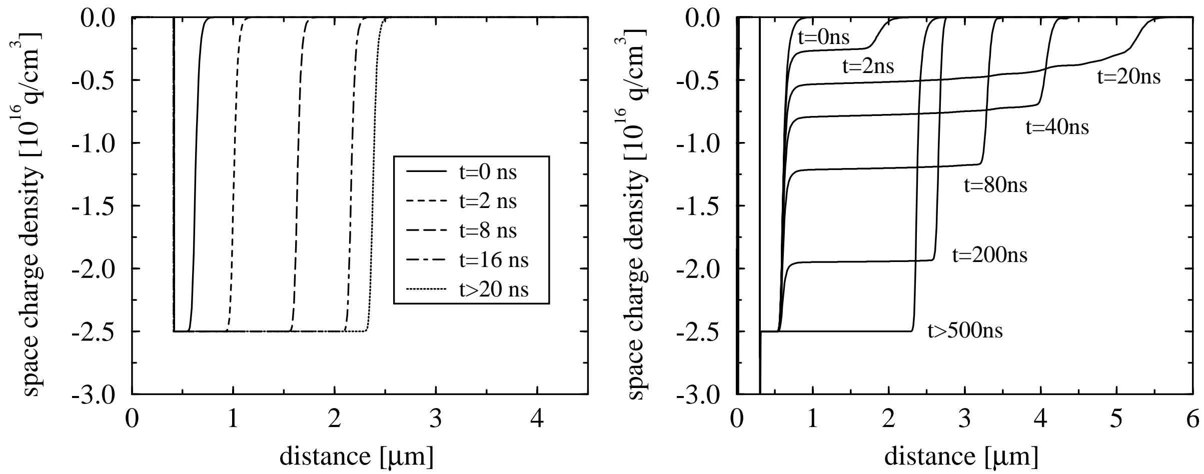


Figure 5.43: Transient response of the depletion region of an Al-doped (left) and B-doped (right) 6H-SiC $n^+$p-diode during a 100 V/20 ns reverse bias ramp at 300 K.

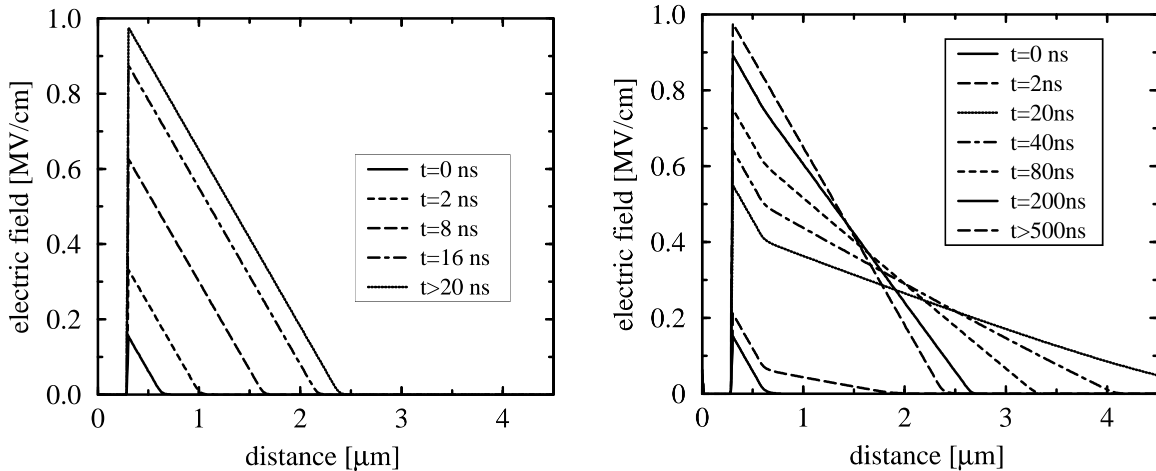


Figure 5.44: Transient electric field distribution of an Al-doped (left) and B-doped (right) 6H-SiC $n^+$p-diode during a 100 V/20 ns reverse bias ramp at 300 K.

Applying a reverse bias pulse of 100 V with a risetime of 20 ns, first only that portion of B which is ionized under electrothermal equilibrium contribute to the space charge within the low-doped region. Hence, a dynamically enlarged depletion region is formed in order to provide the charge required for

sustaining the bias voltage. The maximum width of the dynamically extended depletion region occurs when the final reverse bias is reached after 20 ns. Subsequently, the gradual ionization of the still unionized acceptors within the depletion region results in a relaxation towards the depletion region width in equilibrium governed by the ionization time constant $\tau_p^B = 100$ ns at 300 K as given in Fig. 5.42. Considering an Al-doped epi-layer, the complete background charge is quasi-instantaneously effective to build up the electric field and the maximum width of the depletion region is already reached by the end of the pulse at $t = 20$ ns. The dynamically inhomogeneous depletion region in the case of B leads to a varying gradient of the electric field. The maximum electric field at the pn-junction is not reached before 500 ns.

A systematic understanding of this effect can be obtained by an analytical model [195] outlined in appendix E which has been confirmed by these simulations. In Fig. 5.45, the resulting maximum extension of the depletion region $w_{max}$, normalized with respect to the width $w_\infty$ at $t \to \infty$ is plotted with the degree of ionization in electrothermal equilibrium $\xi$ as parameter. This normalization allows the elimination of the final voltage $U_{max}$. Here, the background doping $N_B$ and the ionization energy of the impurity are indirectly entered by $\xi$. As expected, there is no dynamically extended width of the deple-

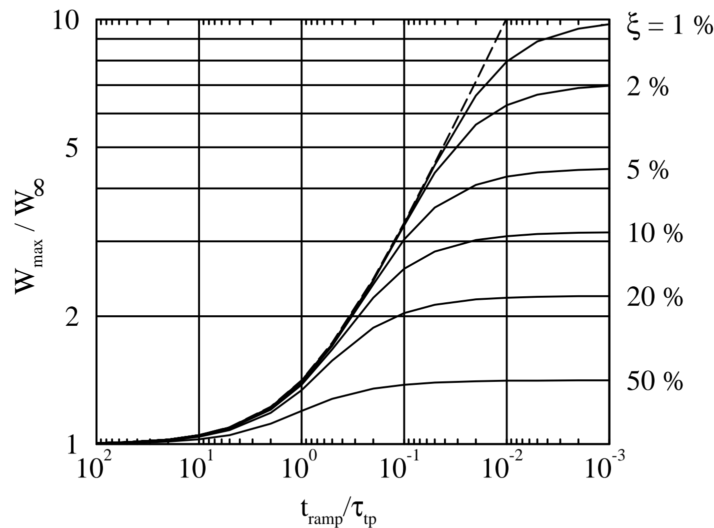


Figure 5.45: Influence of different rise times of a reverse bias pulse on the normalized dynamic extension of the depletion region at several degrees of ionization $\xi$ [195].

tion region at slowly varying voltage ramps ($t_{ramp} >> \tau_{tp}$). On the other hand, it is obvious that at very rapidly varying voltage ramps ($t_{ramp} << \tau_{tp}$), the final voltage is reached before significant ionization takes place. The extension of the depletion region is limited by

$$w_{max} = \sqrt{\frac{2\varepsilon}{qN_B\xi}(U_{bi} - U_{max})} = \frac{w_\infty}{\sqrt{\xi}}, \tag{5.15}$$

as a result of the charge which is quasi-instantaneously available due to the ionized dopants in electrothermal equilibrium. Here, it is interesting to note that the normalized maximum dynamic depletion width, $w_{max}/w_\infty$, is independent of $dU/dt$ but only depends on the ionization degree $\xi$ in electrothermal equilibrium.

Beside these extreme cases, the most interesting situation occurs for $t_{ramp} \approx \tau_{tp}$, since the ionization of a significant amount of centers takes place during the ramping period. Under these conditions $w_{max}$ does not exceed a certain limiting value, which depends on the ratio $t_{ramp}/\tau_{tp}$ but is independent of the equilibrium degree of ionization. There is strong evidence that the relationship between $w_{max}$ and $t_{ramp}/\tau_{tp}$ in this case can be described by

$$\frac{w_{max}}{w_\infty} = \sqrt{1+\frac{\tau_{tp}}{t_{ramp}}}\,. \tag{5.16}$$

Unlike in the case of trap states which is sensitive to the quality of the material, the electrical properties of dopants should not scatter significantly in state-of-the-art SiC devices. Hence, the information given by Fig. 5.45 together with the measured ionization time constants (Fig. 5.42) and the degree of ionization in electrothermal equilibrium (Figs. 4.1 and 4.3) yields an easy-to-use method to quantitatively predict the relevance of dynamic ionization of N, Al, and B in 4H- and 6H-SiC devices.

For instance, considering the example shown in Figs. 5.43 and 5.44, we obtain from Fig. 4.1 $\xi = 10\%$ for B at 300 K and $N_B = 2.5 \cdot 10^{16}\,\mathrm{cm}^{-3}$. With $\tau_p^B = 100\,\mathrm{ns}$, $w_{max}/w_\infty$ is expected to be 2.3 for a pulse rise time of 20 ns as obtained by the numerical simulation (Fig. 5.43). On the other hand, $t_{ramp}/\tau_p^{Al} = 2000$ confirm the validity of the quasi-static approximation when using Al instead of B.

These results can be generalized with respect to impurities acting as deep traps. A hole trap in p-type material, for instance, capture free holes provided by a shallow acceptor. They act as positive background charge partly compensating the negative charge of the ionized acceptors if the emission of these holes within depletion regions can not follow the external excitation. Therefore, a dynamically extended depletion region is similarly obtained which relaxes towards an equilibrium state when the trapped holes are emitted and the corresponding compensating positive charge vanishes. The quantitative characteristics are again determined by the kinetic parameters $e_V^{tp}$ and $c_V^{tp}$ of the deep level as well as the free carrier density in the neutral region and the density of trapped carriers $N_h^+$ in electrothermal equilibrium which is given by the neutrality condition, Eq. (4.2). However, quantitative investigations on impurities acting as deep traps similarly require detailed knowledge of their electronic properties as well as center concentrations and profiles which may sensitively depend on process technology.

### 5.4.2 Dynamic punch-through

It is quite obvious that dynamic ionization will influence the transient device behavior in many ways. For instance, the delay time until a pn-diode starts sustaining the reverse voltage while switching it from on-state to off-state will be prolonged provided that the switching phase is not dominated by the dynamics of the injected excess carriers. Similarly, the capacitive properties of a device will be significantly altered due to transient currents caused by the emission of free carriers from yet not ionized centers. Therefore, the usage of B or other comparable deep dopants should be omitted whenever possible.

However, there may arise situations where the use of B can hardly be avoided due to its specific properties such as the possibility of forming deeper implantation profiles. In such cases, the basic phenomenon of dynamically enlarged depletion regions may lead to dynamic punch-throughs (PT) in all

devices which contain back-to-back pn-junction configurations such as BJTs, certain JFETs, vertical MOSFETs, non-punch-through IGBTs, and thyristors (Fig. 5.46).

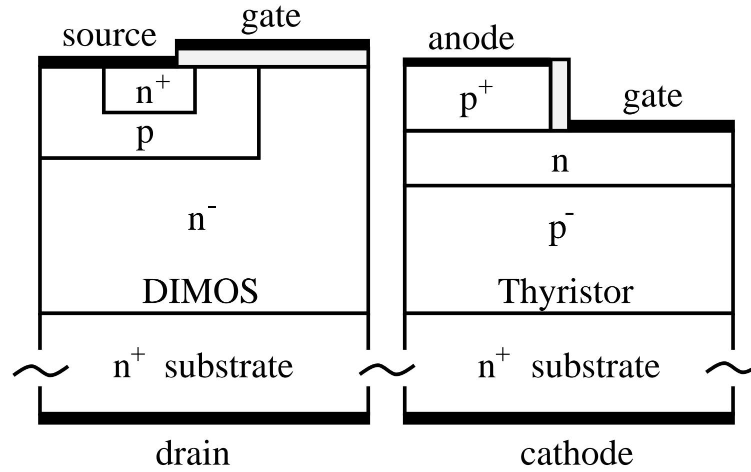


Figure 5.46: Schematic view of a 6H-SiC double-implanted MOSFET (left) and a 4H-SiC thyristor (right).

The basic mechanisms of onset and carrier transport during PT are described in [154, 196, 197]. An exponential rise of current will appear across the reduced barrier as soon as the opposing depletion regions come into contact (Fig. 5.49). In Fig. 5.47, the PT characteristics of an $n^+pn^+$ structure simulated under stationary conditions are compared with those simulated under transient conditions, but within the validity of the quasi-static approximation. In both cases, PT sets on at about 450 V nearly independent of temperature. For lower voltages, the theoretical reverse leakage current caused by SRH generation (see section 5.1) is observed in the stationary case, whereas a capacitive current independent of temperature flows in the transient case.

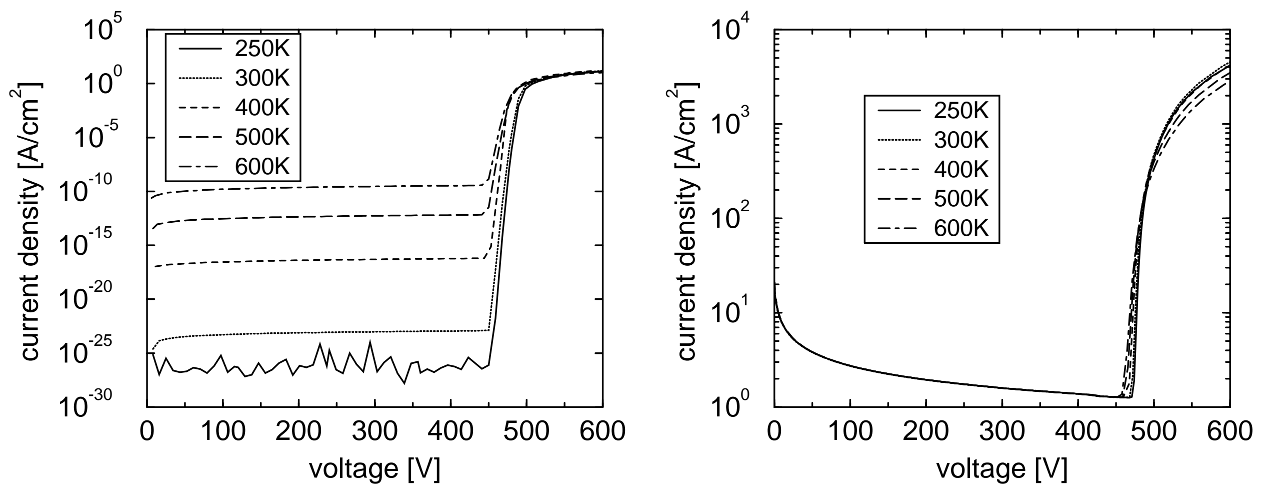


Figure 5.47: Simulated PT characteristics of an $n^+pn^+$-structure under stationary (left) and quasi-static transient (right) conditions.

If dynamic ionization is relevant within such a structure, completely different transient IV characteristics would be obtained. In Fig. 5.48, the corresponding current density is plotted for several temperatures with a pulse rise time of 1 $\mu$s. No PT is observed at 300 K and the capacitive current, present during the rise of voltage, falls down quickly as soon as the final voltage of 400 V is reached at 1 $\mu$s. Subsequently, the current is supported by the ionization of the remaining non-ionized acceptors, resulting in an exponential decrease of current governed by the ionization time constant $\tau_p$. At lower temperatures, the exponential increase of current indicates that PT occurs at the $n^+p$-junction. The onset of PT occurs earlier with decreasing temperature because the dynamic extension of the depletion region gets larger. Two different phases can be distinguished in the current waveform after the final voltage in a PT situation has been reached. First, the current drops down very fast due to the detaching of the depletion regions. Secondly, an exponential decay governed by the ionization time constant $\tau_p$ is subsequently observed, with a slower decay at decreasing temperatures due to the increasing ionization time constants.

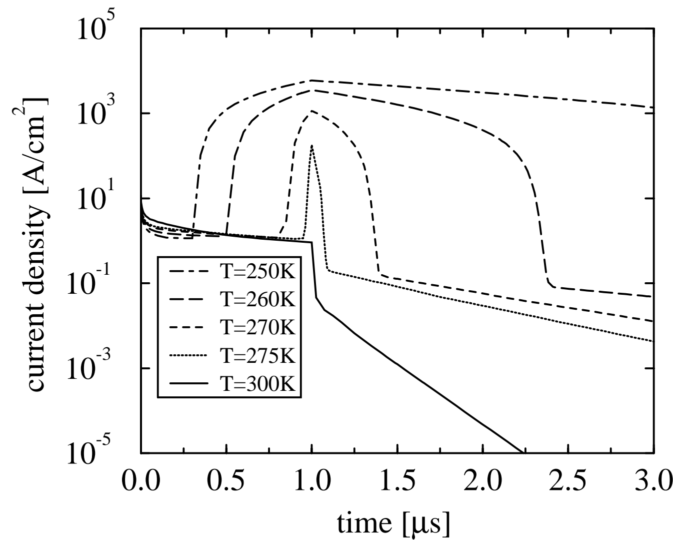


Figure 5.48: Transient dynamic PT characteristics of an $n^+pn^+$-structure.

It should be noted that such current transients would only be measurable if the density of electrical power is limited by designing rather thin test structures. In Fig. 5.49, the current transients assuming a B implantation with a $10^{16}\,\mathrm{cm}^{-3}/1.7\mu\mathrm{m}$ box profile and an N implantation with a $10^{18}\,\mathrm{cm}^{-3}/0.5\,\mu\mathrm{m}$ box profile in a $10^{19}\,\mathrm{cm}^{-3}$ N-doped layer are shown. The qualitative characteristics are similar while the total power loss density of $6\,\mathrm{kW/cm}^2$ is not sufficient to damage the structure within the applied time scale of several 10 ns.

A candidate for observing such dynamic PT effects is the first 6H-SiC double-implanted MOSFET (DIMOS) reported in [179] with a principal structure as sketched in Fig. 5.46. Being an unipolar device, however, it contains an $n^+pn^-$-back-to-back junction configuration. The gate threshold voltage gives an upper limit for the doping concentration of the p-base. In addition, the depth of the p-layer is limited as the $n^+$- and the p-regions are realized by two subsequent ion implantation steps. As a consequence, the depletion region will also extend into the p-region when a negative bias is applied to the source, as in the off-state (no current through the channel). B is required as acceptor for the p-region in order to

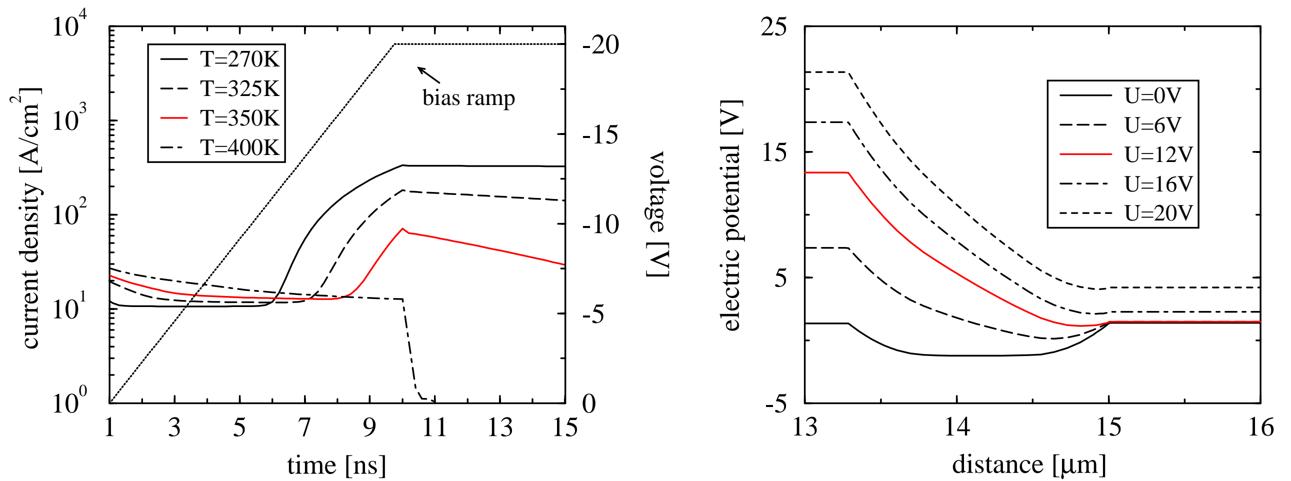


Figure 5.49: Current transients (left) and potential distribution across the n$^+$pn$^+$ structure at 325 K (right) of dynamic PT during a 20 V/10 ns bias ramp.

realize a sufficiently deep junction. Assuming a B implantation box profile of $N_A = 5 \cdot 10^{17}\,\mathrm{cm}^{-3}/1\,\mu\mathrm{m}$ and a N source implantation of $N_D = 10^{19}\,\mathrm{cm}^{-3}/0.5\,\mu\mathrm{m}$ in an epi-layer with a doping concentration of $N_D = 10^{16}\,\mathrm{cm}^{-3}$, the electrothermal simulation of a 500 V/100 ns reverse bias ramp at 300 K leads to onset of dynamic PT at 330 V well below the stationary measured breakdown voltage. In Fig. 5.50 the distributions of current density and temperature are shown at the instant of onset of PT (first row) and at 500 V (second row). During the onset of PT, a current filament starts to form in the vicinity of the n$^+$p-junction. There is also a slight temperature increase at this location, but the overall temperature rise is still insignificant. Due to the highly localized current flow within the current filament, Joule heating leads to a hot spot which eventually destroys the device.

Similarly, thyristor device design have to account for dynamic ionization effects if B is used to form p-layers. The common layer sequence known from Si thyristors has to be reversed in SiC thyristors because no adequate p-conducting substrate is currently available. Hence, the lowly doped base region has to be p-doped. As a thyristor represents a feed-back structure, a dynamic PT would destroy the device by initiating localized current filaments. This effect has yet been observed in Si thyristors doped with gold for carrier lifetime control [198]. The first switching-on of such a device is most critical, as the temperature is still low with the corresponding ionization time constant $\tau_p$ being larger compared to those at operation temperatures. This situation has been simulated comparing a B-doped with an Al-doped epi-layer, using the 4H-SiC thyristor structure as sketched in Fig. 5.46 which was recently reported in [199]. The voltage blocking $p^-$-layer is 4.5 $\mu$m thick with an acceptor concentration of $2.8 \cdot 10^{16}\,\mathrm{cm}^{-3}$. The n$^-$-base has a thickness of 0.55 $\mu$m and a doping concentration of $4.5 \cdot 10^{17}\,\mathrm{cm}^{-3}$.

Fig. 5.51 displays the cathode current density as a function of time at a temperature of 300 K, as it results from an anode forward bias pulse from 0 to 350 V, with two different rise times, namely 100 ns and 10 ns, respectively. The gate has been shortenend to the anode in order to avoid a capacitive forward breakover of the device. With a rise time of 100 ns, the device keeps the forward blocking state for an Al-doped (full line) as well as for a B-doped (dotted line) p$^-$-base region (left part of Fig. 5.51). Reducing the rise time by a factor of 10, the dynamically extended depletion region in the base leads to a dynamic PT failure for the B-doped base, which is expressed in the exponentially rising cathode

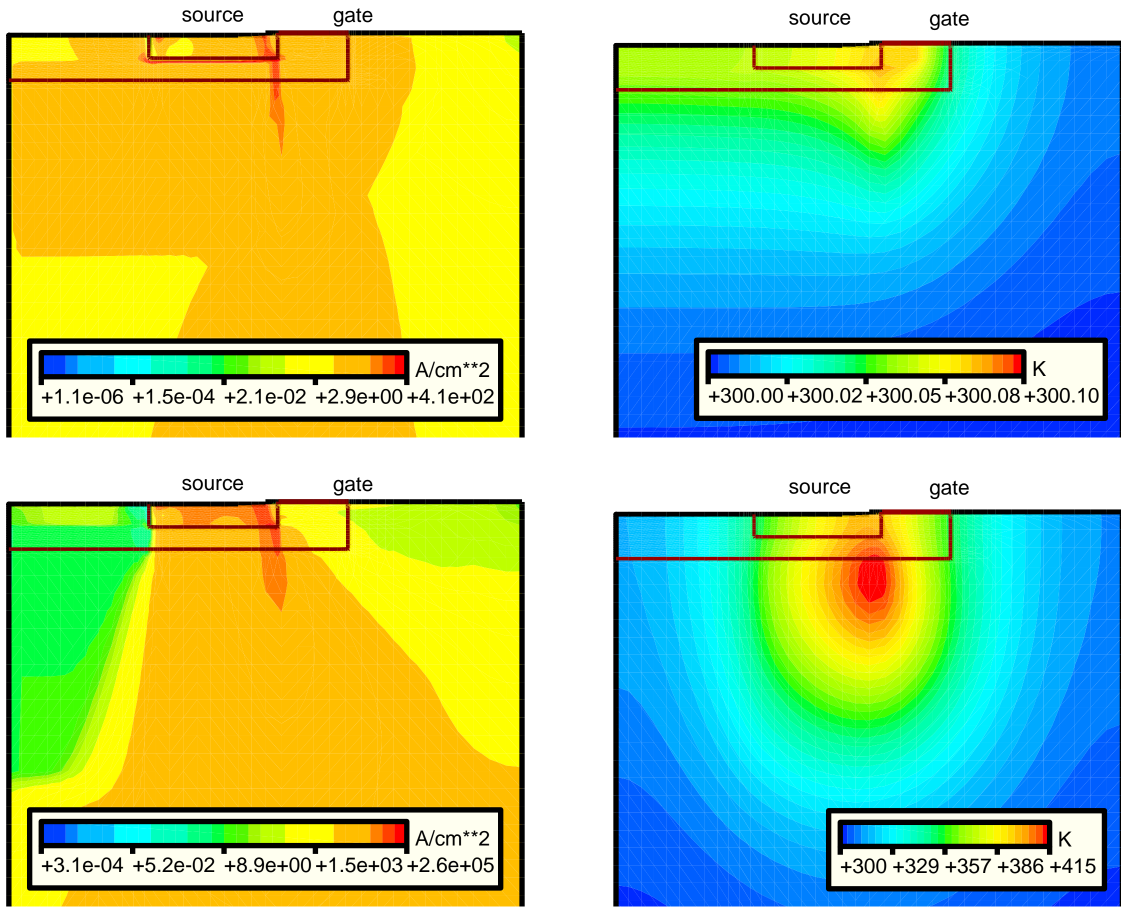


Figure 5.50: Distributions of current density (left) and temperature (right) during dynamic punch-through in a power DIMOS. First row: onset of punch-through at -330 V. Second row: formation of current filament at -500 V.

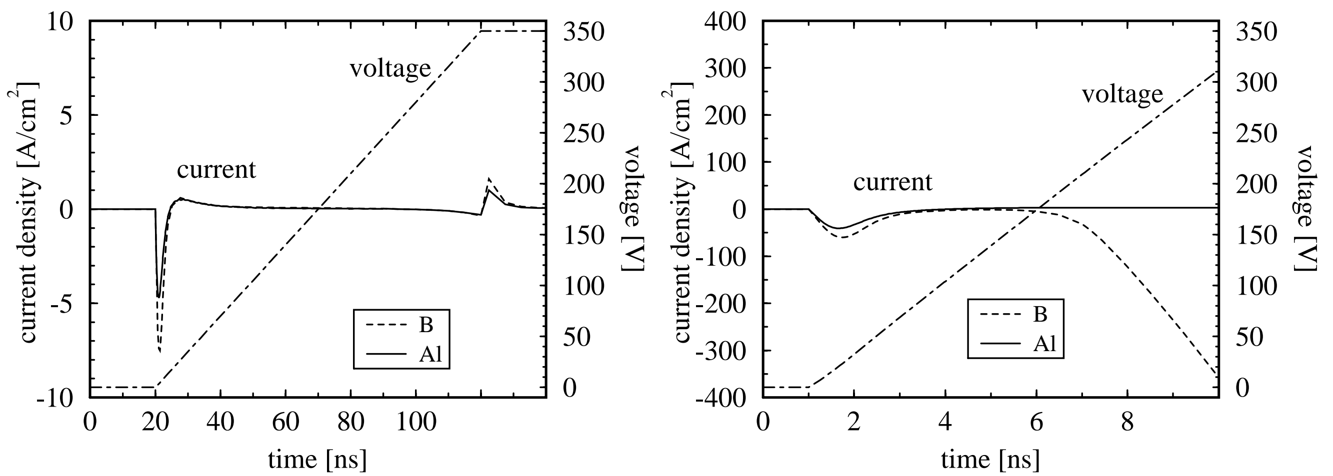


Figure 5.51: 4H-SiC thyristor response to a 350 V forward blocking bias pulse with a rise time of 100 ns (left) and 10 ns (right) at 300 K.

current density, whereas the Al-doped device is able to stay in the forward blocking state (right part of Fig. 5.51). At the beginning of the pulse, capacitive load currents can be observed in both cases. With a $p^+$-buffer layer at the substrate side of the base which is often used to reduce the cathode emitter efficiency [200], this PT would be avoided because the depletion regions are terminated at the buffer.

### 5.4.3 Impact ionization and dynamic ionization

Dynamic ionization leads to the emission of free carriers within the dynamically extended depletion region as discussed in section 5.4.1. Considering Figs. 5.43 and 5.44, it becomes clear that this mechanism will result in an additional drift current due to the large electric field within the depletion region as schematically shown in Fig. 5.52. Hence, the question arises, whether the breakdown characteristics of a junction will be altered by such an additional contribution to the avalanche generation rate[7].

First experimental indications of such an influence have been reported by Neudeck [52, 53], who observed a reduction of the statically measured breakdown voltage in 4H- and 6H-SiC pn-diodes subjected to single-shot reverse bias pulses with a rise time of 1 ns. Corroborated by numerical calculations of the expected transient currents [54], he assumed that this finding results from the generation of free carriers from non-ionized dopants and deep traps within the high-field area of the depletion region. A detailed understanding of the underlying mechanisms require systematic investigations based on simulations including self-consistently impurity kinetics and impact ionization.

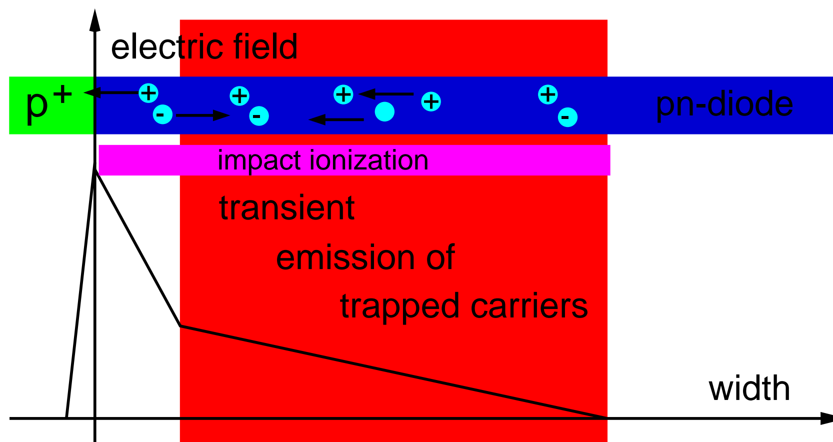


Figure 5.52: Schematic relation between dynamic emission of free carriers, electric field distribution, and impact ionization of a reverse biased pn-junction.

[7]Note, that this mechanism should not be mixed up with the usually called “dynamic avalanche” resulting from excess space charge in the lowly-doped region while switching off a diode caused by the kinetic characteristics of injected free carriers [201].

#### 5.4.3.1 Non-punch-through diode design

Let us first consider the $n^+p$-structure by analyzing the dynamic characteristics of sample D6 (Fig. 5.2 and Tab. 5.1) assuming a very long epi-layer (non-punch-through diode design). Applying a 1000 V/1 $\mu$s reverse bias pulse at 300 K, this structure shows avalanche breakdown at 680 V for both, an Al-doped ("quasi-static" case) and a B-doped ("dynamic" case) p-layer (Fig. 5.53).

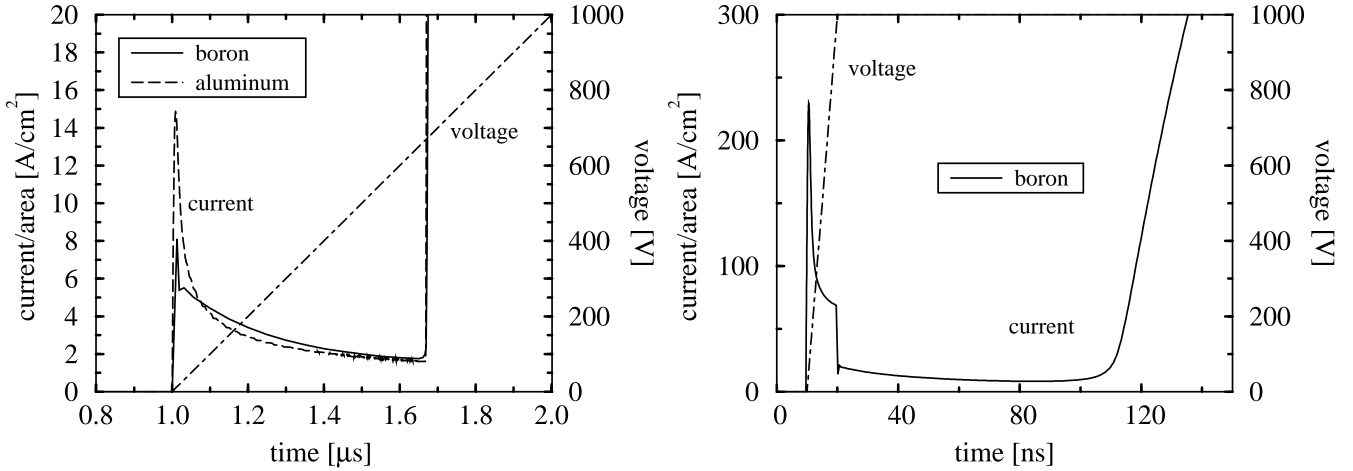


Figure 5.53: Transient current of a B-doped (full lines) and an Al-doped (dotted line) $n^+p$-junction during a 1000 V reverse bias pulse with a rise time of 1 $\mu$s (left) and 10 ns (right) at 300 K.

In Fig. 5.54, the distribution of the avalanche generation rate $G_{ava}$ as calculated by Eqs. (3.27) - (3.29) and the electric field within the depletion region are shown at different time instants. As expected, an excess avalanche generation rate $G_{ava}^{dyn}$ is observed in the vicinity of the dynamically extended depletion region after 100 ns in the dynamic case. On the other hand, the reduced maximum electric field results at the same time in a smaller $G_{ava}^{dyn}$ near the pn-junction. As most of the B is ionized after 500 ns, only minor differences in the electric field distribution are observed. However, the remaining non-ionized centers still contribute to $G_{ava}^{dyn}$. Additionally, the resulting drift current within the depletion region now leads to a larger $G_{ava}^{dyn}$ near the junction where $G_{ava}^{dyn}$ has been smaller than $G_{ava}^{qs}$ at 1.1 $\mu$s. Finally, right before avalanche breakdown occurs at 1.671 $\mu$s, only minor differences are observed between both cases.

A completely different finding is obtained when applying a shorter 1000 V/10 ns reverse bias pulse to the same structure. Whereas the identical breakdown voltage $U_b = 680$ V is obtained in the quasi-static case, the diode is first able to sustain the complete reverse bias of 1000 V in the dynamic case (Fig. 5.53). After the end of the pulse, a remaining transient current proves that further ionization takes place within the depletion region which finally leads to a breakdown more than 90 ns after the end of the pulse. Considering the corresponding distribution of $G_{ava}$ and the electric field, it becomes clear that the large dynamic extension of the depletion region results in a much smaller maximum electric field at the pn-junction (Fig. 5.55). The critical field is reached not before $t = 110$ ns by further ionization of B centers and the corresponding reduction of the depletion region width. The breakdown voltage is determined by the ionization integrals. They, in turn, depend sensitively on the region around the

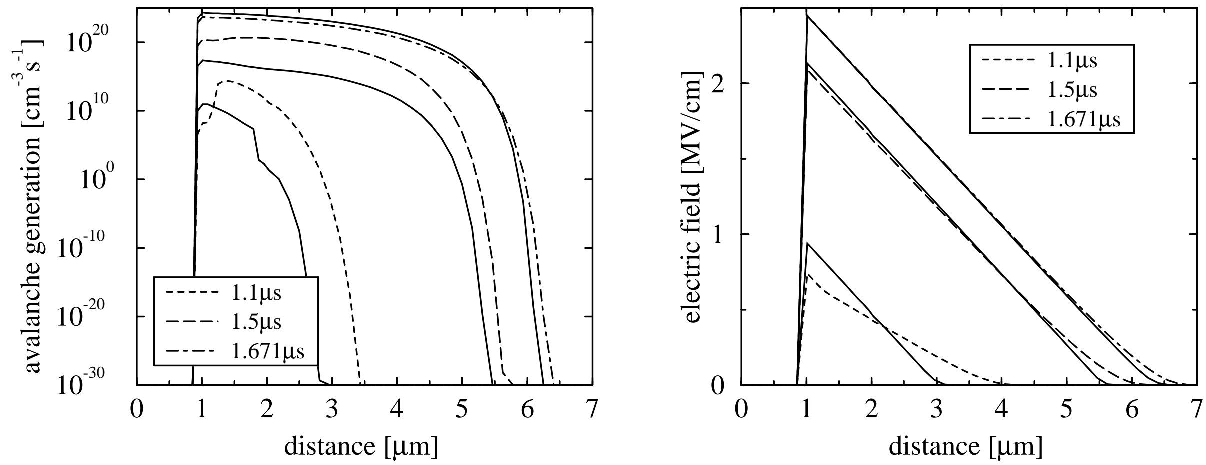


Figure 5.54: Avalanche generation rate (left) and electric field distribution (right) within the depletion region of a B-doped (dotted lines) and a Al-doped (full lines) $n^+p$-diode in NPT design during a 1000 V reverse bias pulse with a rise time of 1 $\mu$s at 300 K.

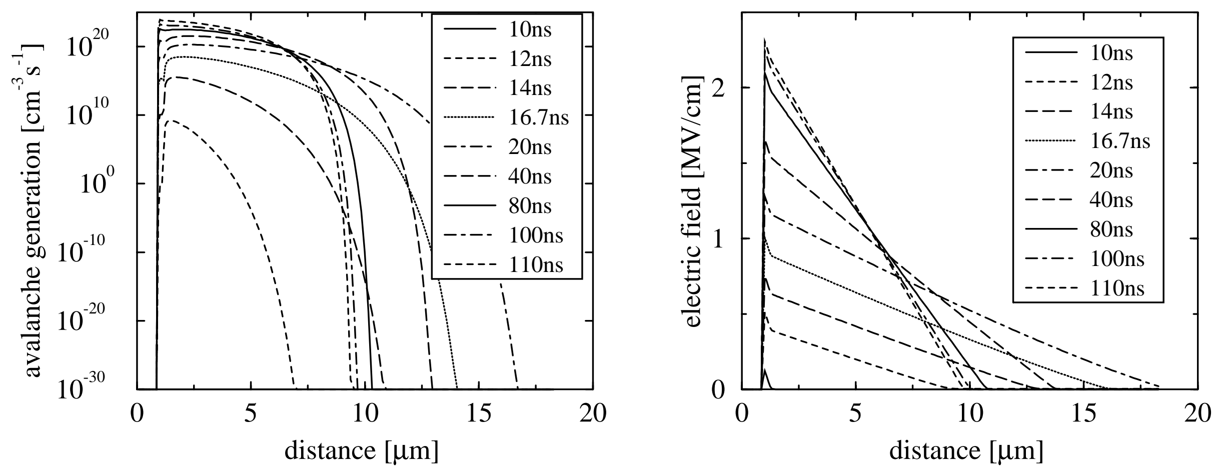


Figure 5.55: Avalanche generation rate (left) and electric field distribution (right) within the depletion region of a B-doped $n^+p$-junction in NPT-design during a 1000 V reverse bias pulse with a rise time of 10 ns at 300 K.

maximum electric field. It should be noted that a slightly reduced maximum electric field is obtained at breakdown in this case (Figs. 5.54 and 5.55).

#### 5.4.3.2 Punch-through diode design

Considering the same $n^+p$-structure but with a much shorter lowly-doped drift region (PT design), the maximum electric field is mainly determined by the length of the drift layer (Fig. 5.56). Nevertheless, a smaller breakdown voltage $U_b = 470$ V is obtained in the quasi-static case compared to $U_b = 525$ V in the dynamic case. As shown in Fig. 5.57, the avalanche generation rate in the quasi-static case dominates as soon as the electric field approaches the critical field.

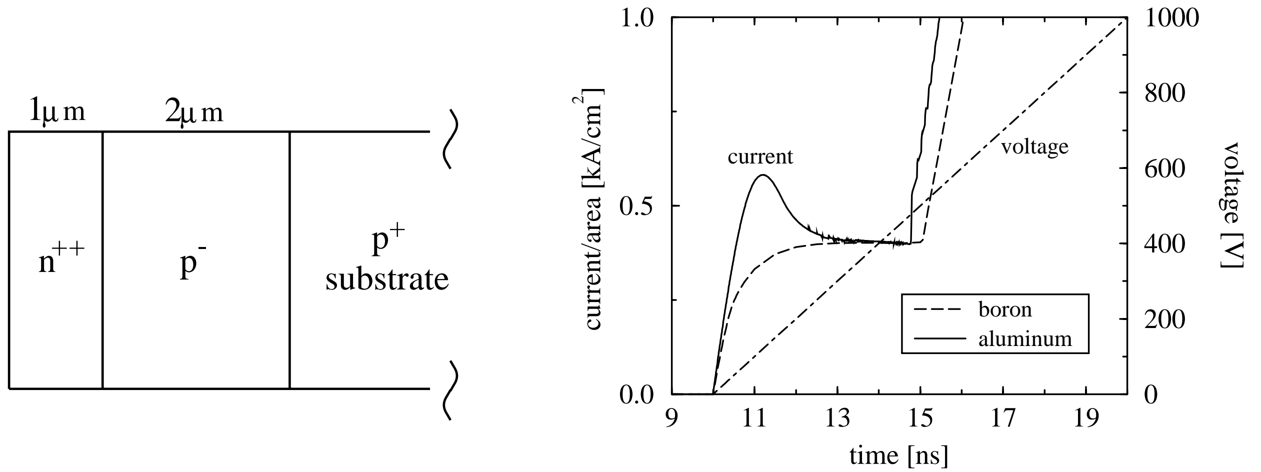


Figure 5.56: Schematic of an $n^+$p-diode in PT design (left) and corresponding transient current (right) during a 1000 V/10 ns reverse bias pulse at 300 K.

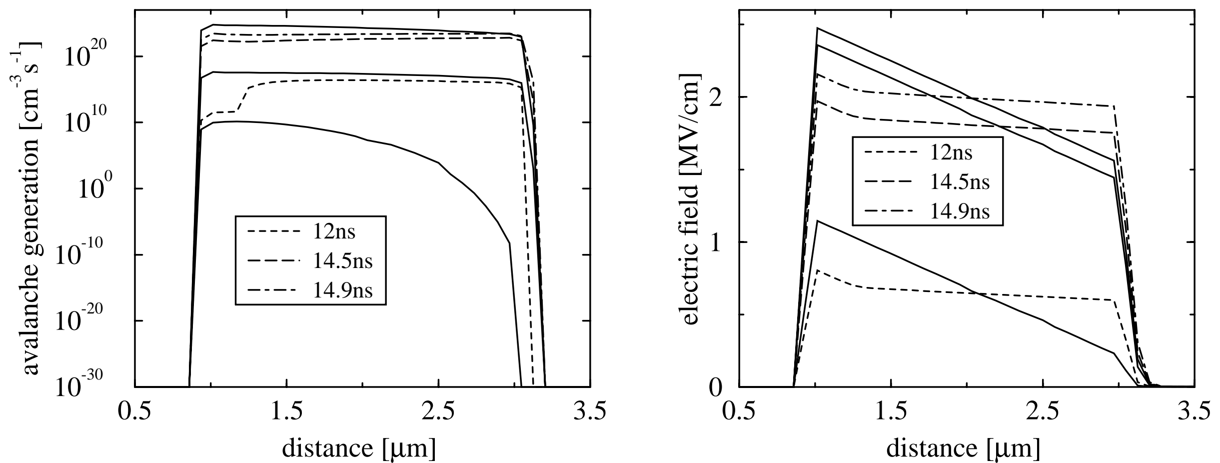


Figure 5.57: Distribution of avalanche generation rate (left) and electric field (right) within the depletion region of a B-doped (dotted lines) and an Al-doped (full lines) $n^+$p-diode in PT design during a 1000 V/10 ns reverse bias pulse at 300 K.

These results suggest that a dynamic reduction of the breakdown voltage can not simply be explained by the emission of free carriers from homogeneously distributed centers within the depletion region. Any “source” of dynamic ionization will simultaneously reduce the maximum electric field which compensates the influence of an additional drift current within the depletion region. The considered configurations can be regarded as a ”worst-case” study with respect to observing any influence of dynamic ionization as the background doping centers themselves act as dynamic ionization centers and the PT design minimizes the dynamic reduction of the maximum electric field.

The influence of any hole trap acting below a shallow acceptor can be treated similarly. In electrothermal equilibrium, a fraction of the free holes within the neutral region will be captured by the hole traps depending on the temperature and center concentration. As the voltage rises, these traps can not emit there holes sufficiently fast and the corresponding fixed positive charge will temporarily compensate

the charge of the ionized shallow acceptors also leading to a dynamic extension of the depletion region. This is shown in Fig. 5.58 by performing the same simulation and assuming an Al-doped epi-layer together with a hole trap. Any coupling of impurities will not principally change the situation, as any transitions occurring only in-between impurities do not change the background charge. Similar results are obtained by deep donors and electron traps acting below shallow donor states.

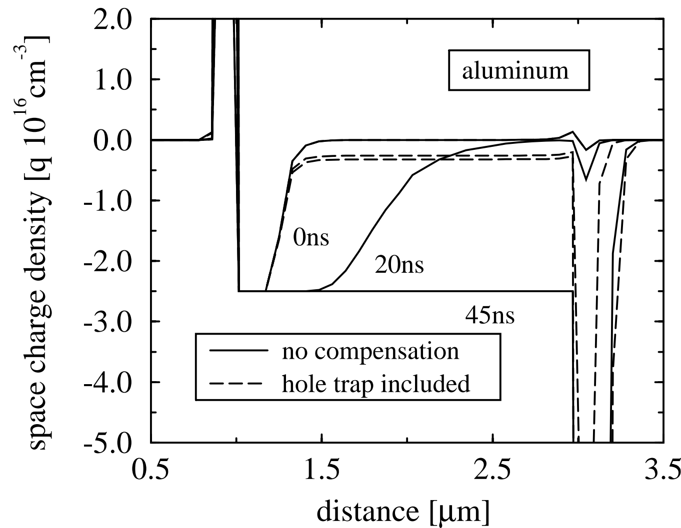


Figure 5.58: Distribution of the space charge density of an Al-doped $n^+$p-diode in PT design including (dotted lines) and excluding (full lines) the influence of traps during a 1000 V/10 ns reverse bias pulse at 300 K.

#### 5.4.3.3 Inhomogeneous compensation profile

More complex two-dimensional effects are therefore required in order to explaining a dynamic reduction of the breakdown voltage by dynamic ionization. A possible mechanism should be demonstrated by an artificial structure as sketched in Fig. 5.59 consisting of an Al-doped $n^+$p-diode with PT design including a region in the middle of the p-layer which is compensated by an additional hole trap. This structure should not reflect any real device structure but be only the basis for investigating the basic impact of inhomogeneous compensation profiles on device characteristics.

The basic mechanisms governing the dynamic reverse bias characteristics of this structure as shown in Fig. 5.59 can be explained by considering the two-dimensional plots of the distribution of the hole current density, the avalanche generation rate, and the hole density within the depletion region at different time instants (Fig. 5.61). The corresponding electric field distributions along different cutlines within the depletion region as shown in Fig. 5.61 are given in Fig. 5.60. A dynamically extended depletion region can only occur within the compensated region whereas the electric field remains approximately undistorted in the outer regions.

The emission of free carriers from yet occupied hole traps in the compensated region of this structure leads to a higher hole density observed 3 ns after the beginning of the bias pulse (left part of Fig. 5.61). These excess holes also drift in a lateral direction due to the lateral gradient of the electric field (Fig. 5.60). Therefore, the corresponding drift current in the vertical direction also extends into the region

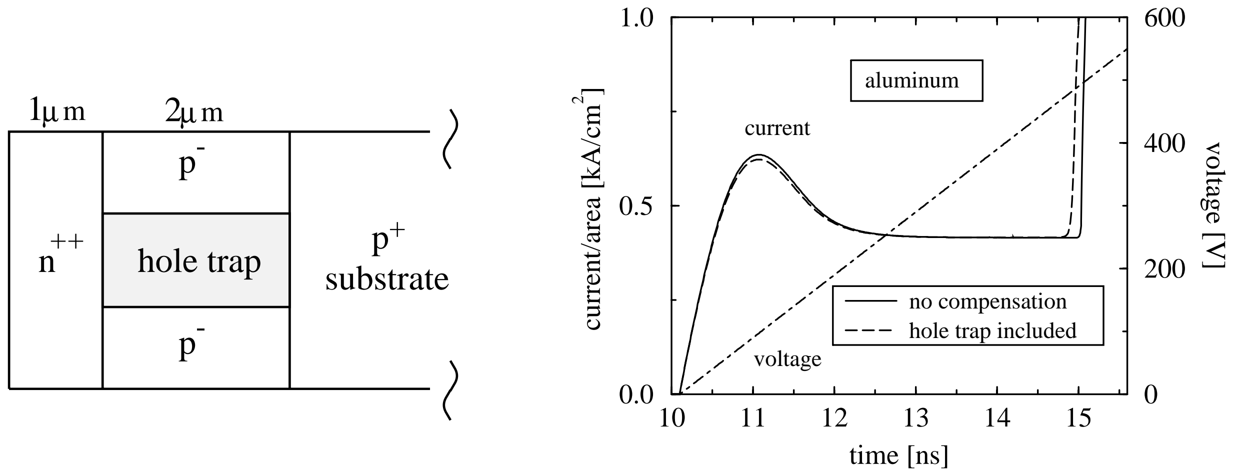


Figure 5.59: Schematic of an n$^+$p-diode in PT design including two-dimensional trap distributions (left) and corresponding transient current (right) during a 1000 V/10 ns reverse bias pulse at 300 K.

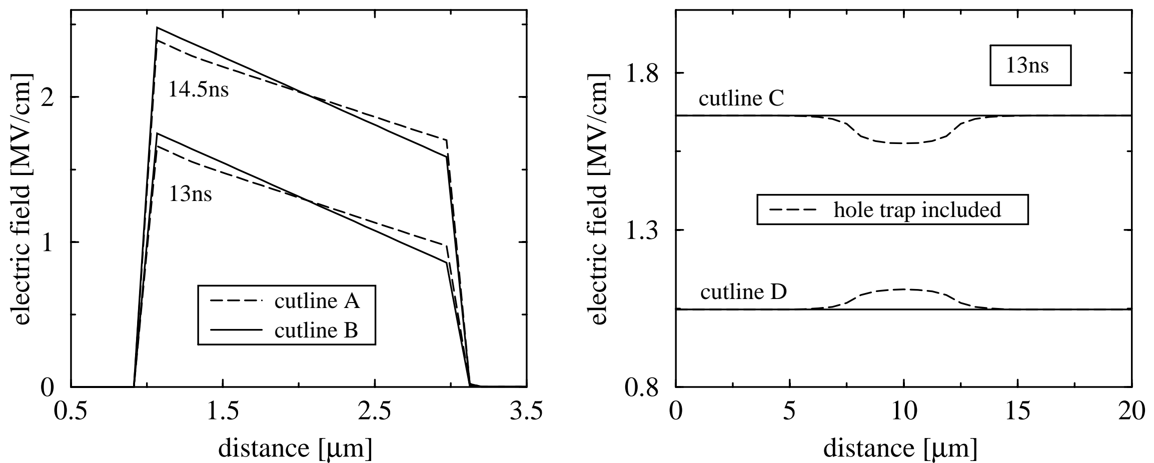


Figure 5.60: Electric field distribution within the p$^-$-region of an Al-doped n$^+$p-diode in PT design including two-dimensional trap distributions along several cutlines (see Fig. 5.61).

with mainly undistorted electric field distribution, thus significantly increasing the avalanche generation rate. As shown in the right part of Fig. 5.61, this mechanism finally results in the formation of current filamentations along the border of the compensated region. A dynamically reduced breakdown voltage of $U_b = 483$ V is obtained compared to $U_b = 495$ V in the quasi-static case (Fig. 5.59).

#### 5.4.3.4 Summary

This study proves that numerical simulation including self-consistently all relevant physical effects is required to obtain a reliable picture of the physical mechanisms suspected to dynamically destroy pn-diode test structures as reported in [52, 53]. It is shown that a dynamically reduced breakdown voltage due to dynamic ionization can only be obtained when assuming two-dimensional inhomogeneous structures.

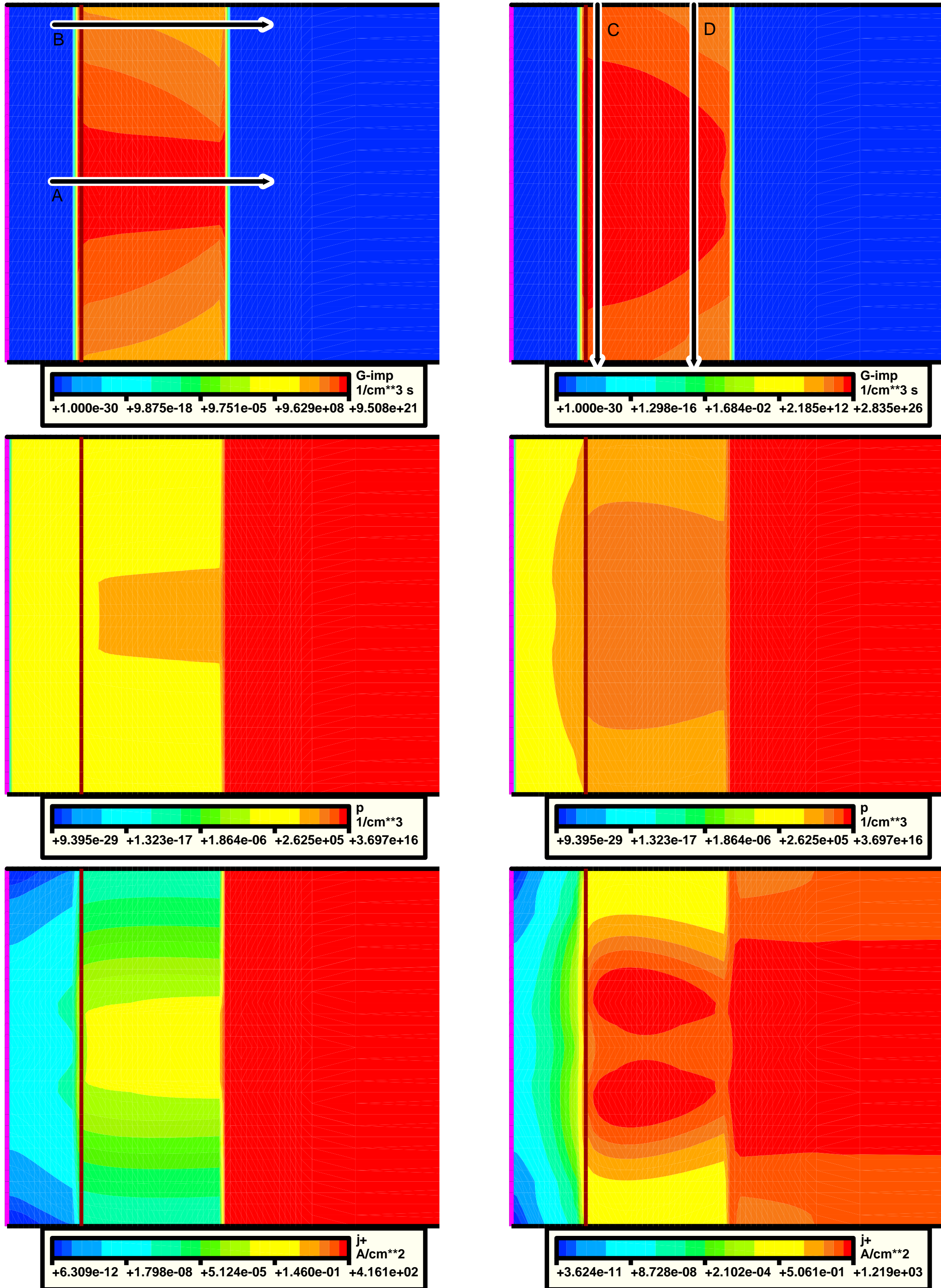


Figure 5.61: Impact ionization rate (first row), hole density (second row), and hole current density (third row) of an $n^+$p-diode in PT design including two-dimensional trap distributions during a 1000 V/10 ns reverse bias pulse at 13 ns (left) and 14.5 ns (right).

As the impact ionization coefficients of holes are larger than those of electrons in $\alpha$-SiC (Tab. 3.7), the avalanche breakdown sets on if the breakdown condition given by the ionization integral

$$\int_0^W \alpha_p \exp\left[-\int_x^W (\alpha_n - \alpha_p)\, dx'\right] dx = 1 \tag{5.17}$$

is fulfilled. The impact ionization coefficients $\alpha_\nu$ given by Eq. (3.28) only depend on the electric field. As shown in Fig. 5.60 and previously demonstrated for diodes with NPT and PT design, the maximum electric field is always lowered by the dynamic ionization effect. Hence, the influence of dynamic ionization generally dynamically enlarges the breakdown voltage.

However, considering the rather extreme compensation configuration shown in Fig. 5.59, the presence of the current filament near the breakdown voltage dynamically reduces the breakdown voltage by 2%. Here, it becomes evident that the reported reduction by as large as 35 % [52, 53] is caused by different physical mechanisms such as, e.g., surface related influences. In [53] it is mentioned that although the reported effects are reproducible with all investigated samples of a certain device type and for both, 4H- and 6H-SiC, there have also been other devices characterized which do not show any dynamically reduced breakdown characteristics.

# Chapter 6

# Conclusions

The enormous progress in SiC research has been mainly fueled by technological enhancements in recent years. The corresponding availability of sufficient material quality facilitates the verification of basic SiC semiconductor theory, accurate measurements of critical material parameters, as well as developing and improving enhanced SiC device concepts and technology. Numerical device simulation has first only been used for evaluating theoretical expectations based on extrapolating Si device physics by substituting SiC parameters into the corresponding physical models of Si devices. The scope of this work has been to evaluate and extend this approach in order to accurately model "real" state-of-the-art SiC devices.

All results are based on an extended electrothermal drift-diffusion model derived within a framework of phenomenological transport theory and implemented in a general-purpose multidimensional device simulation tool [47], experimental characterization of state-of-the-art 4H- and 6H-SiC devices in cooperation with Daimler-Benz AG, Research & Technology, Frankfurt, and the latest published literature.

## 6.1 Incomplete ionization of dopants

The dopants used for 4H- and 6H-SiC have generally to be conceived as "deep" impurity states because of their energetic position within the bandgap. They are modeled by introducing an additional independent state variable together with corresponding rate equations for each relevant impurity state in the complete set of governing differential equations. The additional kinetic equations or some of them can be eliminated and the corresponding state variables can be expressed by the remaining state variables if the time constants governing the corresponding physical processes of carrier emission and capture are negligible compared to the time constant of an external excitation ("quasi-static approximation").

The basic effect occuring beyond the limit for the applicability of the quasi-static approximation has been shown to be a dynamically extended depletion region in response to a reverse bias pulse due to dynamic incomplete ionization (Figs. 5.43 and 5.44). It is governed by the inverse of the corresponding emission coefficient ("ionization time constant") and the ionization energy of the impurity state. The maximum dynamic extension of the depletion region depends on the ratio of this time constant to the

characteristic time constant of the external excitation and is limited by the ionization degree in electrothermal equilibrium. The “key” quantities for evaluating the dynamic impact of a “deep” impurity state on device characteristics is thus given by its ionization time constant and its ionization degree in electrothermal equilibrium. Using analytically calculated figures for the ionization degree dependent on doping concentration and temperature (Fig. 4.1 and 4.3) as well as the calculated maximum dynamically extended depletion region width as function of the ratio of time constants (Fig. 5.45), the impact of dynamic ionization on a given device can be quantitatively estimated.

A major impact of dynamic incomplete ionization arises in the case of devices with back-to-back junction configurations such as thyristors and certain MOSFET structures. If the dynamically extended depletion regions come into contact, an exponential rise of current will appear across the reduced barrier. Detailed numerical simulations of such operation conditions give insight in the transient internal physical mechanisms proving that the corresponding high currents are able to destroy power devices.

Dynamic ionization also impacts the transient blocking characteristics of SiC devices due to a dynamic redistribution of the electric field and the emission of free carriers within the high-field region of depleted regions. It is shown that within homogeneous (“quasi-onedimensional”) structures the influence of a dynamically reduced maximum electric field is dominating, thus leading to dynamically more robust blocking capabilities. The existence of current filaments caused by the emission of free carriers subsequently drifting to regions with electric field distributions approaching the breakdown field within highly-compensated inhomogeneous structures only insignificantly reduces the blocking capability of a device.

## 6.2 Ionization time constants measured by DLTS and thermal admittance spectroscopy

In order to measure the ionization time constants of the currently most relevant dopants in 4H- and 6H-SiC (nitrogen, aluminum, and boron), deep level transient spectroscopy (DLTS) and thermal admittance spectroscopy (TAS) have been applied to pn- and Schottky-diodes. The measured quantities obtained by both methods are directly related to the kinetic properties of the investigated impurity state. By measuring within a wide range of temperature, we obtain a reliable extrapolation of the ionization time constants towards temperatures which are relevant for device applications but not directly accessible by any electrical measurement method (Fig. 4.32).

Being the energetically shallowest impurity of a layer, a basic problem for measuring the electronic properties of Al with these methods is the influence of the serial resistance resulting from the freeze-out of free carriers with decreasing temperatures. Using numerical simulation of the capacitive and conductive spectrum obtained by TAS, it has been shown that a direct measurement of the ionization time of aluminum is only possible by measuring at the highly-doped layers of $p^+$n-junctions due to the much smaller serial resistance of the n-doped substrate and epi-layer.

The applicability of the conventional analytically derived theory of these measurement methods within those conditions has been confirmed by corresponding simulations of both measurement methods. It has been shown that the relation between the spectrum and the kinetic properties remains unchanged

for both methods, while the relation between peak height and center concentration is changed in case of TAS leading to a larger signal with decreasing center concentration.

It has been found that the ionization time constants of nitrogen and aluminum are shorter than 1 ns for temperatures above 250 K and their dynamic behavior can not influence the device operation not even in view of the shortest switching times encountered in today's power device applications, and thus the quasi-static approximation is justified. As a consequence, the effect of incomplete ionization is reflected in the well-known quasi-static increase of the bulk resistance relevant even at higher temperatures. The dynamics of boron, on the other hand, significantly influence transient device behavior up to temperatures as high as 400 K due to its rather large ionization energy and the corresponding long ionization time constant (Fig. 5.42).

## 6.3 Anisotropic material properties

Exploiting crystal symmetry and neglecting magnetic fields, the bulk properties of most anisotropic wide bandgap materials can be formulated as a generic model reducing the number of independent elements of $\tilde{\mu}_\nu$, $\tilde{P}_\nu$, $\tilde{\varepsilon}$, and $\tilde{\kappa}$. Along the crystallographic axes of the semiconductor lattice, these tensors are diagonal with only two independent components modeling the physical properties parallel and perpendicular to the $\hat{c}$-axis, respectively. A tensorial formulation of Poisson's equation and the current equations has been implemented applying the same discretization scheme as in the case of galvanomagnetic current transport.

Several passive and active device structures have been simulated with a view to analyzing the basic effects arising from anisotropic transport properties and estimating their impact on device characteristics. The inhomogeneous redistribution of the electrical potential can lead to unexpected device characteristics even in mainly one-dimensional structures, particularly at very high current ratings. This leads to qualitatively and quantitatively differing characteristics when comparing anisotropic simulation results with those of rescaled isotropic simulations.

The simulation results yield a basis for estimating the impact of anisotropic material properties on the characteristics of typical PN- or Schottky diode, JFET, UMOS, and DIMOS device structures identifying those which can be approximated by rescaling of isotropic simulation results. Furthermore, the difference between the anisotropic properties of both investigated SiC polytypes, 4H- and 6H-SiC, is pointed out emphasizing the superior properties of 4H-SiC. An accurate modeling of the anisotropic material properties is particularly indispensable for devices exhibiting mainly multi-dimensional current flow or very high current ratings.

## 6.4 Investigations on PN-diode and JFET characteristics

Bipolar device operation has been investigated by considering in detail static forward and reverse pn-junction characteristics. It has been shown that the application of thermostatistical methods is justified within today's usual measurement limits. Numerical instabilities such as unreliably simulated ideality

factors of forward pn-junction characteristics or impact ionization artefacts have been investigated and resolved.

The individual characteristic properties of generation-recombination depend strongly on technology and, therefore, they are usually lumped together in quantities like effective electron and hole lifetimes which are easily accessible to measurements. Recombination current plays a dominating role due to the generally much smaller minority carrier lifetimes compared to Si. At forward bias conditions with prevailing recombination (low injection as well as high injection), the relaxation time constant $\tau_{tp}$ of the recombination process is always short because of the large concentration of at least one free carrier species. Hence, the quasi-static approximation is valid and shows that the forward characteristics of pin-diodes can be excellently modeled by applying Shockley-Read-Hall (SRH) statistics. It is shown that additional effects such as field-enhanced capture processes (Poole-Frenkel effect, Franz-Keldysh effect) are not relevant for the investigated devices in forward direction. The temperature-dependence of the forward-characteristics of pin-diodes is correctly reproduced if we assume that the temperature-induced change of the SRH-lifetimes follows a power law (Fig. 5.7).

In the case of prevailing carrier generation, however, $\tau_{tp}$ becomes very large in wide bandgap materials due to the low intrinsic density. Therefore it is very questionable whether the SRH-model can be applied. This doubt is corroborated by the observation that all measured reverse characteristics show thermal activation energies less than half of the bandgap. This finding can not be explained by the assumption of single level SRH-generation processes even if sophisticated high-field effects are included. It is shown that those activation energies may be explained by coupled defect levels with a rate limiting internal coupling. However, further experimental data is required together with a thorough theoretical analysis to clarify the underlying physical mechanisms of excess leakage currents.

Generally, the simulation of unipolar devices is less critical because any generation-recombination and minority carrier diffusion current can be neglected. It has been shown that excellent agreement is obtained between measured and simulated transfer and output JFET characteristics within various bias conditions and temperatures. The electron mobility parameters have been consistently extracted from several samples confirming the values of the evaluated parameter set. Combining the simulation results of several bias conditions and CV characteristics, details about structural parameters are accessible which have been partly confirmed by REM measurements.

## 6.5 Summary and outlook

Revisiting the basic concepts of phenomenological transport theory, an electrothermal drift-diffusion model has been extended by several models particularly relevant for wide bandgap semiconductors. Based on a systematic review of material parameters, a template material parameter set for 4H- and 6H-SiC device simulation is developed (appendix A) and qualified by applying it to a large variety of "real" state-of-the-art unipolar and bipolar devices. It has been shown that the concept of inverse modeling is applicable for JFET devices obtaining quantitative agreement between measured and simulated data for all investigated devices under various operation conditions and temperatures.

The general impact of those extended transport models on device characteristics has been investigated. From these results, the influence of anisotropic material properties on device structures can be esti-

mated. Furthermore, various effects arising from dynamic incomplete ionization have been analyzed in detail giving answer to some general discussions in literature and yielding the basis for a quantitative estimation of such effects for a given device structure.

Additionally, the transient limits arising from the mostly used dopants in 4H- and 6H-SiC have been experimentally determined by consistent DLTS and thermal admittance spectroscopy measurements and corresponding temperature extrapolations of the kinetic coefficients. The experimental results are confirmed by detailed numerical investigations on both measurement methods revealing various details about the influence of serial resistances. In particular, the characteristics of signals obtained from the highly-doped region of a pn-junction are presented which partly differ from the standard theory of these measurement methods.

Further experimental and theoretical work is required for finally developing the simulation of SiC wide bandgap devices as far as state-of-the-art Si device simulation. Particularly, no experimental data about the carrier-carrier scattering at high current ratings is available so far. Apart from understanding the still far too large experimentally observed leakage currents and the detailed physics of the SiC Schottky junction, a major challenge will be the modeling of the SiC-$SiO_2$-interface currently limiting the commercial application of SiC MOS devices. Here, the implemented model for impurity kinetics may be helpful by extending it to coupled defect centers and continuous defect level energy distributions in order to analyzing SiC-$SiO_2$-interface CV characteristics.

There is no doubt that, with the continuing progress in SiC device technology, the availability of predictive simulation of SiC devices will become increasingly important for the success of research in modern power electronics.

# Appendix A

# Material parameters for 4H- and 6H-SiC

| symbol | unit | 6H-SiC | 4H-SiC | symbol | unit | 6H-SiC | 4H-SiC |
|---|---|---|---|---|---|---|---|
| $m_e^*$ | 1 | 0.71 | 0.39 | $m_p^*$ | 1 | 0.80 | 0.82 |
| $M_C$ | 1 | 6 | 3 | $M_V$ | 1 | 1 | 1 |
| $E_g^{T_0}$ [c],[e] | eV | 3.1 | 3.342 | $E_g^{T_0}$ [d],[e] | eV | 3.023 | 3.265 |
| $\alpha^{E_g}$ [c] | eV/K | $3.3 \cdot 10^{-4}$ | [b] | $\alpha^{E_g}$ [d] | eV/K | $3.3 \cdot 10^{-2}$ | [b] |
| $\beta^{E_g}$ [c] | K | 0 | [b] | $\beta^{E_g}$ [d] | K | $1.00 \cdot 10^{5}$ | [b] |
| $C_n^{BGN}$ | eV | $9.0 \cdot 10^{-3}$ | $2.0 \cdot 10^{-2}$ | $C_p^{BGN}$ | eV | $9.0 \cdot 10^{-3}$ | $9.0 \cdot 10^{-3}$ |
| $N_n^{BGN}$ | $cm^{-3}$ | $1.0 \cdot 10^{17}$ | $1.0 \cdot 10^{17}$ | $N_p^{BGN}$ | $cm^{-3}$ | $1.0 \cdot 10^{17}$ | $1.0 \cdot 10^{17}$ |
| $\mu_{n_\perp}/\mu_{n_\parallel}$ | 1 | 5 | 0.8 | $\mu_{p_\perp}/\mu_{p_\parallel}$ | 1 | 1 | 1 |
| $\mu_{n_\perp}^{T_0}$ [e] | $cm^2/Vs$ | 415 | 947 | $\mu_p^{T_0}$ [e] | $cm^2/Vs$ | 99 | 124 |
| $\mu_n^{min}$ | $cm^2/Vs$ | 0 | 0 | $\mu_p^{min}$ | $cm^2/Vs$ | 6.8 | 15.9 |
| $N_n^{mob}$ | $cm^{-3}$ | $1.11 \cdot 10^{18}$ | $1.94 \cdot 10^{17}$ | $N_p^{mob}$ | $cm^{-3}$ | $2.10 \cdot 10^{19}$ | $1.76 \cdot 10^{19}$ |
| $\gamma_n^{mob}$ | 1 | 0.59 | 0.61 | $\gamma_p^{mob}$ | 1 | 0.31 | 0.34 |
| $\alpha_n^{mob}$ | 1 | -1.8 | -1.8 | $\alpha_p^{mob}$ | 1 | -1.8 | -1.8 |
| $v_{n_0}^{sat}$ | cm/s | $1.9 \cdot 10^{7}$ | $2.2 \cdot 10^{7}$ | $\alpha_{n_0}^{sat}$ | 1 | 1.7 | 1.2 |
| $\delta_n^{sat}$ | 1 | -1 | -0.44 | $\beta_n^{sat}$ | 1 | 1.25 | 1 |
| $\varepsilon_\perp/\varepsilon_\parallel$ | 1 | 9.66/10.03 | [b] | $\kappa_\perp/\kappa_\parallel$ | 1 | 0.7 | - |
| $A_c$ | $Jkg^{-1}K^{-1}$ | 1026 | [b] | $B_c$ | $Jkg^{-1}K^{-2}$ | 0.201 | [b] |
| $C_c$ | $Jkg^{-1}K^{-3}$ | 0 | [b] | $D_c$ | $Jkg^{-1}K$ | $-3.66 \cdot 10^{7}$ | [b] |
| $A_\kappa$ | $cmKW^{-1}$ | $2.5 \cdot 10^{-3}$ | [b] | $B_\kappa$ | $cmW^{-1}$ | $2.75 \cdot 10^{-4}$ | [b] |
| $C_\kappa$ | cm/(WK) | $1.3 \cdot 10^{-6}$ | [b] | | | | |
| $N^{SRH}$ | $cm^{-3}$ | $3 \cdot 10^{17}$ [a] | [a] | $\gamma_\nu^{SRH}$ | 1 | 0.3 [a] | 0.3 [a] |
| $C_n$ | $cm^6/s$ | $3.0 \cdot 10^{-29}$ | [b] | $C_p$ | $cm^6/s$ | $3.0 \cdot 10^{-29}$ | [b] |
| $a_n$ | $cm^{-1}$ | $1.66 \cdot 10^{6}$ | $3.44 \cdot 10^{6}$ | $a_p$ | $cm^{-1}$ | $5.18 \cdot 10^{6}$ | $3.24 \cdot 10^{7}$ |
| $b_n$ | V/cm | $1.27 \cdot 10^{7}$ | $2.58 \cdot 10^{6}$ | $b_p$ | V/cm | $1.4 \cdot 10^{7}$ | $1.9 \cdot 10^{7}$ |
| $N_{N_{hex}}$ | meV | $80 \pm 10$ | $50 \pm 5$ | $N_{N_{cub}}$ | meV | $140 \pm 10$ | $90 \pm 10$ |
| $N_{Al}$ | meV | $210 \pm 20$ | $210 \pm 20$ | $N_B$ | meV | $320 \pm 20$ | $320 \pm 20$ |
| $g_D$ | 1 | 2 | 2 | $g_A$ | 1 | 4 | 4 |

Table I: Material parameters of 4H- and 6H-SiC ( [a] values taken from Si, [b] values taken from 6H-SiC, [c] $T > 300\,K$, [d] $T < 300\,K$, [e] $T_0 = 300\,K$ )

# Appendix B

# Numerical methods

The solution of the basic set of nonlinear equations, Eqs. (2.78) - (2.87), is obtained by applying the scheme developed by Bank and Rose [202]. This scheme tries to solve the nonlinear system $\vec{g}(\vec{z}) = 0$ by a Newton method:

$$J\{\vec{g}(\vec{z})\}\vec{x} = -\vec{g}(\vec{z}) \tag{B.1}$$

$$\vec{z}^{j+1} = \vec{z}^{j} + \lambda\vec{x} \tag{B.2}$$

where $J\{\vec{g}(\vec{z})\}$ denotes the corresponding Jacobian matrix and $\lambda$ is a damping factor for updating the solution vector $\vec{z}$

$$\vec{z} = \begin{pmatrix} \vec{\Psi} \\ \vec{n} \\ \vec{p} \\ \vdots \end{pmatrix} \tag{B.3}$$

which has as dimension the number of grid points multiplied by the number of independent state variables. The transient solution is based on a trapezoidal rule/backward-differentiation-formula (TR-BDF2) composite method [203].

## B.1 Discretization

We apply the well known "box discretization" [204, 205, 206] to discretize the partial differential equations (PDE). This method integrates the PDE over a test volume such as shown in Fig. B.1, applies the theorem of Gauss, and discretizes the resulting terms in a first order approximation. In general, it discretizes each PDE of the form

$$\vec{g}(\vec{z}) = \nabla \cdot \tilde{\mathbf{A}} + \vec{B} = 0 \tag{B.4}$$

into

$$\sum_{j \neq i} \kappa_{ij} \cdot a_{ij} + \mu(\Omega_i) \cdot b_i = 0\,. \tag{B.5}$$

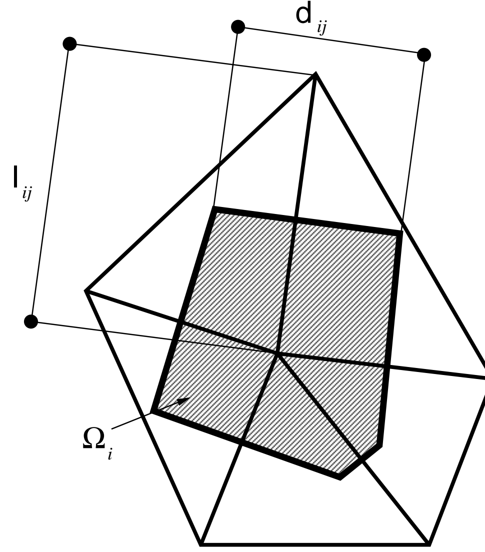


Figure B.1: Single box for a triangular mesh in 2D.

| dimension | $\kappa_{ij}$ | $\mu(\Omega_i)$ |
|---|---|---|
| 1D | $1/l_{ij}$ | box length |
| 2D | $d_{ij}/l_{ij}$ | box area |
| 3D | $D_{ij}/l_{ij}$ | box volume |

Table B.1: Discretization parameters for the "box method".

| equation | $a_{ij}$ | $b_i$ |
|---|---|---|
| poisson | $\varepsilon(\Psi_i - \Psi_j)$ | $-\rho_i$ |
| electron continuity | $\mu_n(n_i B(\Psi_i - \Psi_j) - n_j B(\Psi_j - \Psi_i))$ | $R_i - G_i + \frac{d}{dt} n_i$ |
| hole continuity | $\mu_p(p_j B(\Psi_j - \Psi_i) - p_i B(\Psi_i - \Psi_j))$ | $R_i - G_i + \frac{d}{dt} p_i$ |
| temperature | $\kappa(T_i - T_j)$ | $H_i - \frac{d}{dt} T_i c_i$ |
| trap | 0 | $\frac{\partial N_{tp}^{occ}}{\partial t} + \Pi_{tp}$ |

Table B.2: Physical parameters mapped to the "box method".

The discretization parameters $\kappa_{ij}$ and $\Omega_i$ as well as the physical parameters $a_{ij}$ and $b_i$ are given in Tabs. B.1 and B.2, respectively.

The parameter $a_{ij}$ for the continuity equations is the current contribution along one grid edge. In Tab. B.2, the numerically stable discretization method by Scharfetter and Gummel [207, 208] is given.

## B.2 Calculation of junction admittance

The junction admittance can be calculated by applying a small signal analysis at a given operation point [209] or alternatively from the simulated transient response of a device [210].

## (a) Numerical AC analysis

The most convenient way to obtain the admittance of a junction as function of frequency is the application of a numerical AC analysis [209]. Here, a small signal excitation

$$\vec{z} = \vec{z}_0 + \vec{z}_a \exp(i\omega t) \tag{B.6}$$

is applied to the PDE:

$$\vec{g}(\vec{z}) = \vec{g}_a(t,\vec{z}) + \frac{d\vec{g}_b(t,\vec{z})}{dt} = 0\,. \tag{B.7}$$

The quantities $\vec{g}_a(\vec{z})$ and $\vec{g}_b(\vec{z})$ can be approximated in the vicinity of an operation point $\vec{z}_0$ by

$$\vec{g}_a(\vec{z}) \approx \vec{g}_a(\vec{z}_0) + J\{\vec{g}_a(\vec{z}_0)\}(\vec{z}-\vec{z}_0) \tag{B.8}$$

$$\vec{g}_b(\vec{z}) \approx \vec{g}_b(\vec{z}_0) + J\{\vec{g}_b(\vec{z}_0)\}(\vec{z}-\vec{z}_0) \tag{B.9}$$

with $J$ denoting the Jacobian matrix. From Eqs. (B.8) and (B.9), we obtain

$$(J\{\vec{g}_a(\vec{z}_0)\} + i\omega J\{\vec{g}_b(\vec{z}_0)\})\vec{z}_a = 0 \tag{B.10}$$

for a stationary solution $\vec{z}_0$ with $\vec{g}_a(\vec{z}_0) = 0$. By calculating the matrix

$$Y(\omega) = J\{\vec{g}_a(\vec{z}_0)\} + i\omega J\{\vec{g}_b(\vec{z}_0)\} = \frac{1}{R} + i\omega C \tag{B.11}$$

for a given operation point, we obtain the resistance $R(\omega)$ and the capacitance $C(\omega)$ for all frequencies without any transient solution of the PDE.

## (b) Calculation from the transient device characteristics

The aforementioned method requires a stationary solution at a given operation point which is not available when evaluating a transient capacitive measurement signal $C(t)$ as for instance in case of DLTS. Therefore, this quantity has to be calculated directly from the transient device characteristics.

Basically, the admittance of a junction is obtained by the phase and amplitude of a small signal sinusoidal bias additionally applied to the device. However, the phase modulation is generally very small and an appropriate evaluation method for extracting the admittance from the simulated device characteristics has to be applied. Multiplying the simulated output signal

$$u(t) = u_m(t) + \hat{u}_1 \sin\omega t \tag{B.12}$$

with a small signal reference bias

$$u(t) = \hat{u}_r \cos\omega t\,, \tag{B.13}$$

yield the transient power

$$p(t) = \left(C\frac{du_m(t)}{dt} + \frac{u_m(t)}{R}\right)\hat{u}_r\cos\omega t + \frac{1}{2}C\hat{u}_r\hat{u}_1\omega + \frac{1}{2}\left(C\hat{u}_r\hat{u}_1\omega\cos 2\omega t + \frac{\hat{u}_r\hat{u}_1}{R}\sin 2\omega t\right) \tag{B.14}$$

from which the capacitance is obtained by

$$\bar{p} = \frac{1}{T}\int_0^T p(t)dt = \frac{1}{2}C\hat{u}_r\hat{u}_1\omega \tag{B.15}$$

provided that $u_m(t)$ only slowly varies with time. Similarly, by using

$$u(t) = \hat{u}_r \sin\omega t\,, \tag{B.16}$$

we obtain

$$\begin{aligned} p(t) \quad = \quad & \left(C\frac{du_m(t)}{dt} + \frac{u_m(t)}{R}\right)\hat{u}_r \sin\omega t + \\ & \frac{1}{2}\frac{\hat{u}_r\hat{u}_1}{R} + \frac{1}{2}\left(C\hat{u}_r\hat{u}_1\omega \sin 2\omega t + \frac{\hat{u}_r\hat{u}_1}{R}\cos 2\omega t\right) \end{aligned} \tag{B.17}$$

from which the resistance is obtained by

$$\bar{p} = \frac{1}{T}\int_0^T p(t)dt = \frac{1}{2}\frac{\hat{u}_r\hat{u}_1}{R}\,. \tag{B.18}$$

# Appendix C

# Generation-Recombination models

**(a) Franz-Keldysh effect:** An analytical model for the field and temperature dependence of the SRH lifetimes originating from the Franz-Keldysh effect [98] has been derived by Schenk [99] in a form which is suitable for the implementation into simulation packages [47]. This effect is taken into account by corresponding field-enhancement factors which read in the case of electrons

$$\begin{aligned} g_n(F) &= \frac{1}{3}\sum_{i=x,y,z}\left(1+\frac{\left(\hbar\Theta_{i,\|}\right)^{3/2}\sqrt{E_{tp}-E_0}}{E_0\hbar\omega_0}\right)^{-\frac{1}{2}}\frac{\left(\hbar\Theta_{i,\|}\right)^{3/4}\left(E_{tp}-E_0\right)^{1/4}}{2\sqrt{E_{tp}E_0}}\left(\frac{\hbar\Theta_{i,\|}}{kT}\right)^{\frac{3}{2}} \\ & \text{x}\exp\left\{-\frac{E_{tp}-E_0}{\hbar\omega_0}+\frac{\hbar\omega_0-kT}{2\hbar\omega_0}+\frac{E_{tp}+kT/2}{\hbar\omega_0}\ln\left(E_{tp}/\varepsilon_R\right)-\frac{E_0}{\hbar\omega_0}\ln\left(E_0/\varepsilon_R\right)\right\} \\ & \text{x}\exp\left(\frac{E_{tp}-E_0}{kT}\right)\exp\left[-\frac{4}{3}\left(\frac{E_{tp}-E_0}{\hbar\Theta_{i,\|}}\right)^{3/2}\right]. \end{aligned} \tag{C.1}$$

Here, $E_0$ denotes the energy of an optimum horizontal transition path, which depends on the electric field strength and temperature in the following way:

$$E_0 = 2\sqrt{\varepsilon_F}\left[\sqrt{\varepsilon_F+E_{tp}+\varepsilon_R}-\sqrt{\varepsilon_F}\right]-\varepsilon_R\,, \quad \varepsilon_F = \frac{\left(2\varepsilon_R kT\right)^2}{\left(\hbar\Theta_{i,\|}\right)^3} \tag{C.2}$$

($\varepsilon_R = S\hbar\omega_0$ – lattice relaxation energy, $S$ – Huang-Rhys factor, $\hbar\omega_0$ – effective phonon energy, $E_{tp}$ – energy level of the recombination center (thermal depth), $\Theta_\nu = (e^2F^2/2\hbar m_\nu)^{1/3}$ – electro-optical frequency). The mass $m_{i,\|}$ is the electron tunneling mass in field direction, which differs for the three pairs of equivalent valleys $(i = x,y,z)$

$$m_{i,\|} = \frac{m_t}{1-\left(1-\frac{m_t}{m_l}\right)\frac{F_i^2}{F^2}}\,. \tag{C.3}$$

$F_i$ is the $i$th field component in a coordinate system with axes parallel to the $[100]$-directions. An isotropic approximation has been made by assuming the field orientation to be $< 111 >$:

$$m_{x,\|} = m_{y,\|} = m_{z,\|} = \frac{3\,m_t\,m_l}{2\,m_l+m_t}\,. \tag{C.4}$$

The expression for holes follows from Eq. (C.1) by replacing $m_{i,\|} \to m_{lh}$ (light hole mass) and $E_{tp} \to E_g - E_{tp}$.

**(b) Poole-Frenkel effect:** In a similar way the corresponding expressions for the Poole-Frenkel effect can be derived, where the field effect is caused by lowering the Coulomb barrier in the vicinity of donor- or acceptor-like recombination centers [101]. The lifetimes are reduced by a factor

$$g(F) = \left(\frac{E_t(0)+\varepsilon_R}{E_t(F)+\varepsilon_R}\right)^{3/2} \exp\left(\frac{\Delta E_{PF}\left[E_t(0)+\varepsilon_R\right]}{2\varepsilon_R kT}\right), \tag{C.5}$$

where $\Delta E_{PF} := E_t(0) - E_t(F)$ denotes the reduction of the "thermal depth" of the recombination center and $\varepsilon_R$ is the lattice relaxation energy. Evaluating $\Delta E_{PF}$ according to the one-dimensional Poole-Frenkel model [101] yields the expression

$$\Delta E_{PF} = q(qF/\pi\varepsilon_s)^{1/2}. \tag{C.6}$$

**(c) Coupled defect-level generation-recombination:** Referring to Fig. 5.15, the steady-state recombination-rate for two coupled defect levels calculated by generalizing the single-level SRH formula (see section 2.2.3) is given by [100]:

$$\begin{aligned} R_{CDL} &= R_1 + R_2 + \left(\sqrt{R_{12}^2 - S_{12}} - R_{12}\right) \cdot \\ &\quad \frac{\tau_{n1}\tau_{p2}(n+n_2)(p+p_1) - \tau_{n2}\tau_{p1}(n+n_1)(p+p_2)}{r_1 r_2} \end{aligned} \tag{C.7}$$

$$\begin{aligned} R_{12} &= \frac{r_1 r_2}{2 r_{12}\tau_{n1}\tau_{n2}\tau_{p1}\tau_{p2}(1-\varepsilon)} + \frac{1}{2\tau_{n1}\tau_{p2}(1-\varepsilon)} \\ &\quad \left[\tau_{n1}(p+p_1) + \tau_{p2}(n+n_2)\right] + \\ &\quad \frac{\varepsilon}{2\tau_{n2}\tau_{p1}(1-\varepsilon)}\left[\tau_{n2}(p+p_2) + \tau_{p1}(n+n_1)\right] \end{aligned} \tag{C.8}$$

$$S_{12} = \frac{1}{\tau_{n1}\tau_{p2}(1-\varepsilon)}\left(1 - \frac{\tau_{n1}\tau_{p2}}{\tau_{n2}\tau_{p1}}\varepsilon\right)\left(np - n_i^2\right) \tag{C.9}$$

Here, $\tau_{\nu 1,2}$ are the lifetimes of electrons and holes of the involved defect levels, respectively, and $r_{12} = N_{t1}N_{t2}c_{12}$ is the internal rate between both defects. The quantities $\nu_{1,2}$ are defined in analogy to Eqs. (2.53) and (2.54),

$$n_\nu = N_C\, g_{tp_\nu} \exp\left(-\frac{E_{t_\nu}}{kT}\right) \tag{C.10}$$

$$p_\nu = N_V\, g_{tp_\nu}^{-1} \exp\left(-\frac{E_g - E_{t_\nu}}{kT}\right), \tag{C.11}$$

and $r_{1,2}$ abbreviates the dominator of the single level SRH formula, Eq. (2.62), of the corresponding defect, respectively.

$$\varepsilon = \frac{g_{tp_2}}{g_{tp_1}} \exp\left(-\frac{E_{t_1} - E_{t_2}}{kT}\right) \tag{C.12}$$

models the influence of the energetic position of the defects within the bandgap.

# Appendix D

# Analytical model of dual-gate JFET characteristics

With a view to obtaining insight in the basic physical mechanisms determining the IV characteristics of a dual-gate JFET, an analytical model will be briefly outlined [154]. It is based on the following assumptions:

- Abrupt junction approximation
- Homogeneous doping of substrate, channel, and gate area
- Mobility of free carriers independent of the electric field
- No depletion of the channel if the same electric potential is applied to all contacts of the device ("normally-on")
- Gradual channel approximation: The longitudinal component of the electric field $E_x$ in the channel can be neglected compared with the transversal component $E_y$. This requires a long and narrow channel.

In Fig. D.1, a schematic of the channel area of a dual-gate JFET as shown in Fig. 5.16 together with the principal extensions of the depletion widths at both junctions is given. Because of the different doping concentrations of gate and base, the channel is unsymmetrically controlled by the depletion regions of both junctions with

$$w_G(x) = \sqrt{\frac{2\varepsilon_r\varepsilon_0(U(x) - U_{GS} + U_{bi,G})}{q \cdot N_{ch}}} \tag{D.1}$$

and

$$w_B(x) = \sqrt{\frac{2\varepsilon_r\varepsilon_0(U(x) - U_{BS} + U_{bi,B})}{q \cdot N_{ch}}}. \tag{D.2}$$

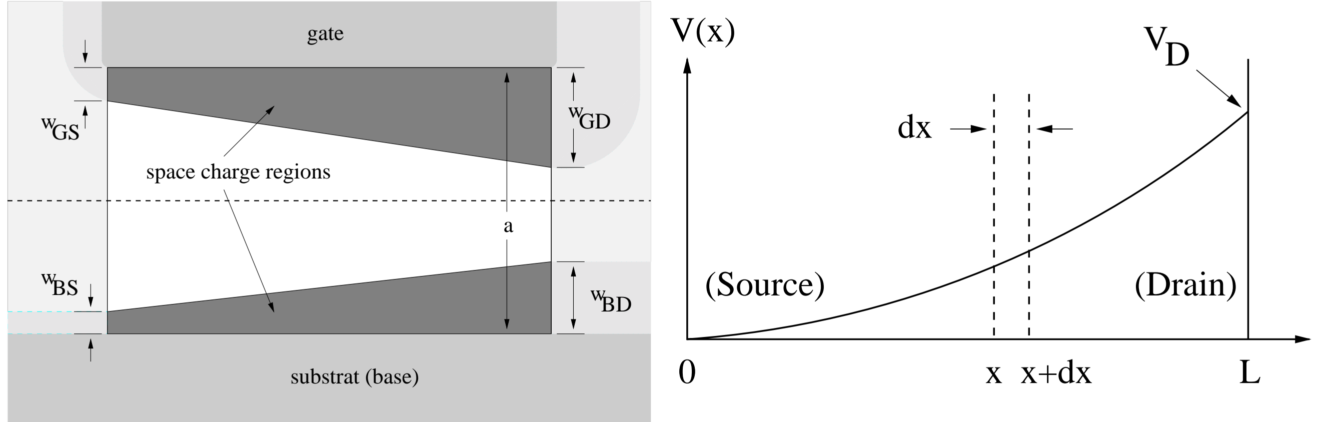


Figure D.1: Schematic of dual-gate channel control (left) and corresponding potential distribution along the channel (right).

Here, $U(x)$ denotes the electric potential of the channel which is qualitatively sketched in Fig. D.1. The corresponding built-in potentials are given by

$$U_{bi,G} = \frac{k \cdot T}{q} \cdot ln\left(\frac{N_D^+ \cdot N_{A,G}^-}{n_i^2}\right) \qquad U_{bi,B} = \frac{k \cdot T}{q} \cdot ln\left(\frac{N_D^+ \cdot N_{A,B}^-}{n_i^2}\right). \tag{D.3}$$

Using Ohm's law,

$$\vec{j} = \sigma \cdot \vec{E}\,, \tag{D.4}$$

we obtain for the current flowing along an infinitesimal distance $dx$ with the potential difference $dU(x)$:

$$I \cdot dx = q \cdot \mu_n \cdot N_{ch}^+ \cdot Z \cdot [a - w_G(x) - w_B(x)] \cdot dU(x)\,. \tag{D.5}$$

Here, the active area is defined by the channel width $Z$ in z-direction and the effective channel thickness $d = a - w_{GD} - w_{BD}$ in y-direction with $a$ being the channel thickness defined by the gate and base pn-junctions of the device. Differentiating Eq. (D.1) with respect to $U(x)$ yield:

$$\frac{dw_G(x)}{dU(x)} = \frac{\varepsilon_r\varepsilon_0}{w_G(x) \cdot q \cdot N_{ch}}\,. \tag{D.6}$$

Inserting Eq. (D.6) in Eq. (D.5), we obtain:

$$I \cdot dx = \frac{q^2 \cdot \mu_n \cdot N_{ch}^+ \cdot N_{ch} \cdot Z}{\varepsilon_r\varepsilon_0} \cdot [a - w_G(x) - w_B(x)] \cdot w_G(x) \cdot dw_G(x)\,. \tag{D.7}$$

Combining Eqs. (D.1) and (D.2) to

$$w_B(x) = \sqrt{w_G^2(x) + b^2} \qquad with \qquad b^2 = \frac{2 \cdot \varepsilon_r\varepsilon_0}{q \cdot N_{ch}} \cdot \left(U_{GS} - U_{BS} - U_{bi,G} + U_{bi,B}\right), \tag{D.8}$$

inserting it in Eq. (D.7) and integrating along the channel length $L$,

$$\int_{Source}^{Drain} I(x)\,dx = K \int_{Source}^{Drain} \left( a\,w_G(x) - w_G^2(x) - w_G(x)\sqrt{w_G^2(x) + b^2} \right) d\,w_G(x) \tag{D.9}$$

finally yield an explicit relation between $I_{DS}$ and $U_{DS}$:

$$I_{DS} = \frac{K}{L}\left[ \frac{a}{2}(w_{GD}^2 - w_{GS}^2) - \frac{1}{3}(w_{GD}^3 - w_{GS}^3) - \frac{1}{3}(w_{GD}^2 + b^2)^{\frac{3}{2}} + \frac{1}{3}(w_{GS}^2 + b^2)^{\frac{3}{2}} \right] \tag{D.10}$$

with

$$K = \frac{q^2 \mu_n N_{ch}^+ N_{ch} Z}{\varepsilon_r \varepsilon_0}. \tag{D.11}$$

The width of the depletion regions of the pn-junction of the gate at source and drain is given by

$$w_{GD} = \sqrt{\frac{2\varepsilon_r \varepsilon_0 \cdot (U_{DS} - U_{GS} + U_{bi,G})}{q \cdot N_{ch}}} \tag{D.12}$$

$$w_{GS} = \sqrt{\frac{2\varepsilon_r \varepsilon_0 \cdot (-U_{GS} + U_{bi,G})}{q \cdot N_{ch}}}. \tag{D.13}$$

In analogy, the width of the depletion regions of the base pn-junction at source and drain is given by

$$w_{BD} = \sqrt{\frac{2\varepsilon_r \varepsilon_0 \cdot (U_{DS} - U_{BS} + U_{bi,B})}{q \cdot N_{ch}}} \tag{D.14}$$

$$w_{BS} = \sqrt{\frac{2\varepsilon_r \varepsilon_0 \cdot (-U_{BS} + U_{bi,B})}{q \cdot N_{ch}}}. \tag{D.15}$$

$I_{DS}$ saturates if above the pinch-off potential defined by

$$a - w_{GD} - w_{BD} = 0 \tag{D.16}$$

which yield together with Eq. (D.8)

$$c = w_{G,sat} = \frac{a^2 - b^2}{2a}. \tag{D.17}$$

The resulting saturation current $I_{DSS}$ is then given by

$$I_{DSS} = \frac{q^2 \mu_n N_{ch}^+ N_{ch} Z}{\varepsilon_r \varepsilon_0 L}\left[ \frac{a}{2}(c^2 - w_{GS}^2) - \frac{1}{3}(c^3 - w_{GS}^3) - \frac{1}{3}(c^2 + b^2)^{\frac{3}{2}} + \frac{1}{3}(w_{GS}^2 + b^2)^{\frac{3}{2}} \right]. \tag{D.18}$$

The on-resistance $R_{on}$ of the JFET defined at small $U_{DS}$ can be derived from Eq. (D.10) to

$$R_{on} = \left[ \frac{d\,I_{DS}}{d\,U_{DS}} \right]^{-1} = \frac{L}{2\,q\mu_n N_{ch}^+ Z\,(a - w_{GD} - w_{BD})} \tag{D.19}$$

and the transconductance to

$$g_m = \frac{d\,I_{DS}}{d\,U_{GS}} = \frac{2\,q\mu_n N_{ch}^+ Z}{L}(w_{GD} - w_{GS}). \tag{D.20}$$

# Appendix E

# Analytical model for the maximum dynamic depletion region width

In the following, an analytical model for estimating the dynamic extension of the depletion region due to dynamic ionization of dopants derived in [195] will be briefly outlined. For simplification, the following assumptions have been made: 1st) one space dimension, 2nd) the pn-junction is abrupt and one-sided, 3rd) the lowly-doped region has a uniform doping and is semi-infinite, and 4th) the free carriers have an arbitrary high mobility. Furthermore, it was assumed that the voltage ramp has a constant slope. The rise time of the ramp is divided into $M$ equidistant time steps $\Delta t = t_{ramp}/M$.

At every time step it is calculated which fraction of doping centers in the depletion region has been ionized during the last time step and how far the depletion region has to extend in order to be able to sustain the bias of the next time step. Finally, $w_{max}$ is obtained as the result of the last time step.

To illustrate the calculation, the profile of the electric field after the m-th time step is sketched in Fig. E.1. Here, $w_{m-1}$ is the width of the previous time step. Hence, the non-shaded area represents the voltage $U'_{m-1}$ which is sustained by the 'old' depletion region having taken into account that further ionization had occurred. The total area is obtained by summing up the areas of all the dashed triangles and rectangles as given in Eq. (E.1). Each triangle, in turn, represents a field strength contribution of the additional depletion region width $\Delta w_i$ of a previous time step and a certain charge density $s_i^m$ (being under depletion condition for $m-i$ time steps) within $\Delta w_i$. The area of the rectangles corresponds to the voltage portions which originate from the depletion region $w_{i-1}$ and are generated by the charge associated with the interval $\Delta w_i$ ("parallel plate capacitor approximation"):

$$U'_{m-1} = U_{bi} + \sum_{i=1}^{m-1} \left( \frac{s_i^m}{\varepsilon} w_{i-1} + \frac{s_i^m}{\varepsilon} \frac{\Delta w_i}{2} \right), \tag{E.1}$$

where $s_i^m$ is given by

$$s_i^m = q N_B \Delta w_i \left[ 1 - (1 - \xi) \exp\left( -\frac{(m-i)\,\Delta t}{\tau_{tp}} \right) \right]. \tag{E.2}$$

Here, $U_{bi}$ denotes the built-in potential of the junction and $N_B$ the background doping concentration. The shaded part of the field distribution in Fig. E.1 represents the additional voltage $\Delta U_m$ which is

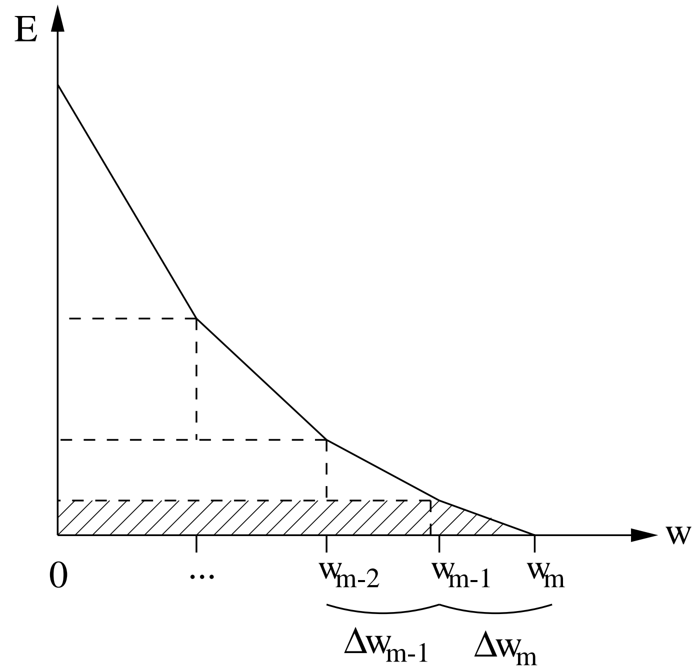


Figure E.1: Distribution of the electric field at the m-th time step.

necessary to sustain the actual voltage $U_m = \Delta U_m + U'_{m-1}$ of the new time step. The value $\Delta U_m$ is obtained in the same way as in Eq. (E.1), except that the charge of the additional region $\Delta w_m$ equals the ionized part $N_B \cdot \xi$ of the dopants under thermal equilibrium:

$$\Delta U_m = \frac{q N_B \xi}{\varepsilon} \Delta w_m \left( w_{m-1} + \frac{\Delta w_m}{2} \right) . \tag{E.3}$$

To obtain the unknown additional depletion region width $\Delta w_m$, this quadratic equation has to be solved. Finally, these steps have to be repeated until the final extension $w_{max}$ of the depletion region is obtained as the sum of all $\Delta w_1 \ldots \Delta w_M$.

# Appendix F

# List of symbols

| symbol | description | unit |
|---|---|---|
| $C$ | capacitance | F |
| $c$ | heat capacity | J kg K |
| $c_{\nu}^{tp}$ | capture coefficient | $cm^3 s^{-1}$ |
| $E$ | electric field | $V cm^{-1}$ |
| $E_g$ | indirect bandgap | eV |
| $E_{gx}$ | exciton bandgap | eV |
| $E_C$ | conduction band energy | eV |
| $E_F$ | Fermi energy | eV |
| $E_{F_{\nu,tp}}$ | electron, hole, trap quasi-Fermi energy | eV |
| $E_i$ | intrinsic Fermi energy | eV |
| $E_{tp}$ | energy of impurity state | eV |
| $E_V$ | valence band energy | eV |
| $E_x$ | exciton binding energy | eV |
| $\Delta E_{V,A}$ | donor, acceptor ionization energy | eV |
| $e_{\nu}^{tp}$ | emission coefficient | $s^{-1}$ |
| $f$ | frequency | Hz |
| $f_c$ | cut-off frequency | Hz |
| $f_{tp}$ | occupation probability of traps | 1 |
| $\gamma_{n,p}$ | emission efficiency of electrons and holes | $(s\,cm^2 K^2)^{-1}$ |
| $\varepsilon$ | relative dielectric constant | 1 |
| $G$ | generation rate | $cm^{-3} s^{-1}$ |
| $G_m$ | measured conductance | $A\,V^{-1}$ |
| $g_{tp,A,D}$ | degereracy factor | 1 |
| $h$ | Planck constant | J s |
| $k$ | Boltzmann factor | $J\,K^{-1}$ |

| symbol | description | unit |
|---|---|---|
| $k_{C,G}^{\omega}$ | TAS constant frequency prop. factor | 1 |
| $k_{C,G}^{T}$ | TAS constant temperature prop. factor | 1 |
| $J$ | electric current density | $\mathrm{Acm^{-2}}$ |
| $j$ | particle current density | $\mathrm{cm^{-2}}$ |
| $\kappa$ | thermal conductivity | $\mathrm{W\,cm^{-1}K^{-1}}$ |
| $m_{\nu}^{*}$ | electron, hole effective mass | kg |
| $\mu$ | carrier mobility | $\mathrm{cm^{2}\,V^{-1}s^{-1}}$ |
| $\mu^{(c)}$ | chemical potential | eV |
| $\mu_{tp_{occ}}^{(c)}$ | chemical potential of occupied trap | eV |
| $\mu_{tp_{emp}}^{(c)}$ | chemical potential of empty trap | eV |
| $\mu^{(ec)}$ | electrochemical potential | eV |
| $M_{C,V}$ | number of equivalent minima in the conduction and valence band | 1 |
| $n$ | electron density | $\mathrm{cm^{-3}}$ |
| $n_i$ | intrinsic density | $\mathrm{cm^{-3}}$ |
| $n_1$ | Shockley-Read-Hall parameter | $\mathrm{cm^{-3}}$ |
| $N_{C,V}$ | effective density of states | $\mathrm{cm^{-3}}$ |
| $N_{tp}$ | trap density | $\mathrm{cm^{-3}}$ |
| $N_{tp}^{occ}$ | density of occupied traps | $\mathrm{cm^{-3}}$ |
| $N_{tp}^{emp}$ | density of empty traps | $\mathrm{cm^{-3}}$ |
| $\nu$ | substitute for electron or hole density | $\mathrm{cm^{-3}}$ |
| $\omega$ | angular frequency | Hz |
| $\omega_c$ | cut-off angular frequency | Hz |
| $p$ | hole density | $\mathrm{cm^{-3}}$ |
| $p_1$ | Shockley-Read-Hall parameter | $\mathrm{cm^{-3}}$ |
| $P_{\nu}$ | electron, hole thermoelectric power | $\mathrm{V\,K^{-1}}$ |
| $\Psi$ | electric potential | V |
| $\Phi_{\nu}$ | electron, hole quasi-Fermi level | V |
| $\phi_{\nu}$ | electron, hole quasi-Fermi potential (imref) | V |

| symbol | description | unit |
|---|---|---|
| $q$ | elementary electric charge | As |
| $R$ | recombination rate | $cm^{-3}s^{-1}$ |
| $R_s$ | serial resistance | $\Omega$ |
| $\sigma$ | electrical conductivity | $A\,V^{-1}\,cm^{-1}$ |
| $\sigma_\nu^{tp}$ | electron and hole capture cross section | $cm^2$ |
| $\rho$ | charge density | $As\,cm^{-3}$ |
| $s$ | entropy density | $eV\,K^{-1}cm^{-3}$ |
| $T$ | temperature | K |
| $T_{\nu,tp,L}$ | electron, hole, trap, and lattice temperature | K |
| $T_0$ | reference temperature (300 K) | K |
| $\tau_{R-G}$ | effective lifetime of recombination or generation process | s |
| $\tau_\nu$ | effective electron, hole minority carrier lifetime | s |
| $\tau_\nu^{tp}$ | electron, hole minority carrier lifetime of impurity $tp$ | s |
| $\tau_{tp,A,D}$ | time constant of trap, acceptor, donor, acceptor, donor | s |
| $u$ | total energy density | $eV\,cm^{-3}$ |
| $U$ | voltage | V |
| $U_{bi}$ | built-in voltage | V |
| $z^{occ}$ | charge number of occupied energy state | 1 |
| $z^{emp}$ | charge number of empty energy state | 1 |
| $W$ | depletion region width | cm |

# Bibliography


[1] W. Shockley, *Proc. of the first int. conf. of Silicon Carbide*, Boston, Ma, 1959.

[2] L. Lorenz, G. Deboy, A. Knapp, M. März, "COOLMOS$^{TM}$ - a new milestone in high voltage Power MOS", *Proceedings of the Int. Symp. of Power Semiconductor Devices and IC's (ISPSD'99)*, Toronto, Ontario, Canada, May 1999, pp. 3-10.

[3] M.N. Yoder, "Wide Bandgap Semiconductor Materials and Devices", *IEEE Trans. Elec. Dev.*, vol. 43, no. 10, 1996, pp. 1633-1636.

[4] J.B. Casady, and R.W. Johnson, "Status of silicon carbide (SiC) as a wide-bandgap semiconductor for high-temperature applications: A review", *Solid State Electronics*, vol. 39, no. 10, 1996, pp. 1409-1422.

[5] Mohit Bhatnagar, B.J. Baliga, "Comparison of 6H-SiC, 3C-SiC, and Si for Power Devices", *IEEE Trans. Elec. Dev.*, vol. 40, no. 3, 1993, pp. 645-655.

[6] E.O. Johnson, "Physical Limitations on Frequency and Power Parameters of Transistors", *RCA Review*, June 1965, pp. 163-177.

[7] R.W. Keyes, "Figure of Merit for Semiconductors for High-Speed Switches", *Proceedings of the IEEE*, Feb. 1972, p. 225.

[8] B.J. Baliga, "Semiconductors for high-voltage, vertical channel field effect transistors", *J. Appl. Phys.*, vol. 53, no. 3, 1982, pp. 1759-1764.

[9] K. Shenai, R.S. Scott, B.J. Baliga, "Optimum Semiconductors for High-Power Electronics", *IEEE Trans. Elec. Dev.*, vol. 36, 1989, pp. 1811-1822.

[10] T.P. Chow, N. Ramungul, M. Ghezzo, "Wide Bandgap Semiconductor Power Devices", *Mat. Res. Soc. Proc.*, vol. 483, 1998, pp. 89-102.

[11] T.P. Chow, V. Khemka, J. Fedison, N. Ramungul, K. Matocha, Y. Tang, R.J. Gutmann, "SiC and GaN bipolar power devices", *Solid-State Electronics*, vol. 44, no. 2, 2000, pp. 277-301.

[12] "Properties and Growth of Diamond and GaN bipolar power devices", *IEE Inspec*, edited by Gordon Davies, 1994.

[13] W. Ebert, A. Vescan, P. Gluche, T. Borst, E. Kohn, "High-voltage Schottky diode on epitaxial diamond layer", *Diamond and Related Materials*, no. 6, 1997, pp. 329-332.

[14] A. Vescan, I. Daumiller, P. Gluche, W. Ebert, E. Kohn, “Very High Temperature Operation of Diamond Schottky Diode”, *IEEE Electron Device Letters*, vol. 18, no. 11, 1997, pp. 556-558.

[15] W. Tsai, M. Delfino, D. Hodul, M Riazat, L.Y. Ching, G. Reynolds, C.B. Cooper, *IEEE Electron Device Letters*, no. 12, 1991, p. 157.

[16] A. J. Tessmer, L.S. Plano, D.L.Dreifus, *IEEE Electron Device Letters*, vol. 14, 1993, p. 66.

[17] T.H. Borst, S. Strobel, O. Weis, “High-temperature diamond p-n junction: B-doped homoepitaxial layer on N-doped substrate” *Appl. Phys. Lett.*, vol. 67, no. 18, 1995, pp. 2651-2653.

[18] H. Morkoç, S. Strite, G.B. Gao, M.E. Lin, B. Sverdlov, M. Burns, “Large-band-gap SiC, III-V nitride, and II-VI ZnSe-based semiconductor device technologies”, *J. Appl. Phys.*, vol. 76, no. 3, 1994, pp. 1363-1398.

[19] W. Asche, “Vom Schleifstein zum Hochtemperatur-Transistor”, *Bild der Wissenschaft*, no. 2, 1993, p. 96.

[20] G. Ziegler, P. Lang, Dietmar Theis, C. Weyrich, “Single Crystal Growth of SiC Substrate Material for Blue Light Emitting Diodes”, *IEEE Trans. Elec. Dev.*, vol. 30, no. 4, 1983, pp. 277-281.

[21] D. Stephani, “Siliziumcarbid, ein Material für Elektronik hoher Leistung”, *Koll. Angewandte Materialwissenschaften*, Munich University of Technology, Nov. 1998.

[22] A. Nilarp, “Silicon Carbide power devices - an industrial perspective”, *Int Conf. on Silicon Carbide III-nitrides and Related Materials (ICSIII-N’97)*, Stockholm, Sweden, Sept. 1997.

[23] K. Rottner, “SiC power devices for high voltage applications”, *Proc. of the 2nd. Europ. Conf. on Silicon Carbide and Related Materials (ECSCRM’98)*, Montpellier, France, Sept. 1998, pp. 61-62.

[24] D. Stephani, “Prospects of SiC Devices from Industry”, *Int Conf. on Silicon Carbide III-nitrides and Related Materials (ICSIII-N’99)*, Durham (NC), USA, Oct. 1999.

[25] V. Härle, “Industrial aspects of GaN/SiC blue LEDs in Europe”, *Proc. of the 2nd. Europ. Conf. on Silicon Carbide and Related Materials (ECSCRM’98)*, Montpellier, France, Sept. 1998, pp. 57-58.

[26] J.W. Palmour, R. Singh, R.C. Glass, O. Kordina, C.H. Carter, Jr., “Silicon Carbide for Power Devices”, *Proc. IEEE Int. Symp. on Power Semiconductor Devices and ICs (ISPSD’97)*, vol. 25, 1997.

[27] C.E. Weitzel, “Comparison of SiC, GaAs, and Si RF MESFET Power Densities”, *IEEE Electron Device Letters*, vol. 16, no. 10, 1995, pp. 451-453.

[28] A. Aleksov, A. Denisenko, E. Kohn, “Prospects of bipolar diamond devices”, *Solid-State Electronics*, vol. 44, no. 2, 2000, pp. 369-375.

[29] C.E. Nebel, J. Münz, M. Stutzmann, R. Zachai, H. Güttler, "Electronic properties of CVD and synthetic diamond", *Phys. Rev. B*, vol. 55, no. 15, 1997, pp. 1-6.

[30] L.Y.S. Pang, S.S.M. Chan, C. Johnston, P.R. Chalker, R.B. Jackman, "High temperature polychristalline diamond metal-insulator-semiconductor field-effect-transistor", *Diamond and Related Materials*, no. 6, 1997, pp. 333-338.

[31] D. Defives, O. Noblanc, C. Dua, C. Brylinski, M. Barthula, F. Meyer, "Electrical Characterization of Inhomogeneous Ti/4H-SiC Schottky Contacts", *Proc. of the 2nd. Europ. Conf. on Silicon Carbide and Related Materials (ECSCRM'98)*, Montpellier, France, Sept. 1998, pp. MTL61-62.

[32] L. Zheng, R.P. Joshi, C. Fazi, "Effects of barrier height fluctuations and electron tunneling on the reverse characteristics of 6H-SiC Schottky contacts", *J. Appl. Phys.*, vol. 85, no. 7, 1999, pp 3701-3707.

[33] R. Held, N. Kaminski, E. Niemann, "SiC Merged p-n/Schottky Rectifiers for High Voltage Applications", *Proc. of Silicon Carbide, III-nitrides and Related Materials (ICSCIII-N'97) - Materials Science Forum*, vol. 264-268, Stockholm, Sweden, 1998, pp. 1057-1060.

[34] R. Rupp, M. Treu, A. Mauder, E. Griebl, W. Werner, W. Bartsch, D. Stephani, "Performance and Reliability Issues of SIC-Schottky Diodes", *Int. Conf. on Silicon Carbide III-nitrides and Related Materials (ICSIII-N'99)*, Durham (NC), USA, Oct. 1999.

[35] P. Friedrichs, H. Mitlehner, W. Bartsch, K.O. Dohnke, R. Kaltschmidt, U. Weinert, B. Weis, D. Stephani, "Static and Dynamic Characteristics of 4H-SiC JFET's Designed for Different Blocking Categories", *Int. Conf. on Silicon Carbide III-nitrides and Related Materials (ICSIII-N'99)*, Durham (NC), USA, Oct. 1999.

[36] R. Schörner, P. Friedrichs, D. Peters, H. Mitlehner, B. Weis, D. Stephani, "Rugged Power MOSFETs in 6H-SiC with Blocking Capability up to 1800V", *Int. Conf. on Silicon Carbide III-nitrides and Related Materials (ICSIII-N'99)*, Durham (NC), USA, Oct. 1999.

[37] S. Sriram, G. Augustine, A.A. Burk Jr., R.C. Class, H.M. Hobgood, P.A. Orphanos, L.B. Rowland, T.J. Smith, C.D. Brandt, M.C. Driver, R.H. Hopkins, "4H-SiC MESFET's with 42 GHz $f_{max}$", *IEEE Electron Device Letters*, vol. 17, no. 9, 1996, pp. 369-371.

[38] K.E. Moore, C.E. Weitzel, K.J. Nordquist, L.L. Pond, J.W. Palmour, S. Allen, C.H. Carter Jr., "4H-SiC MESFETs with 65.7% Power Added Efficiency at 850 MHz", *IEEE Electron Device Letters*, vol. 18, no. 2, 1997, pp. 69-70.

[39] S.T. Allen, R.A. Sadler, T.S. Alcorn, J. Sumakeris, R.C. Glass, C.H. Carter Jr., J.W. Palmour, "Silicon Carbide MESFET's for High-Power S-Band Applications", *Proc. of Silicon Carbide, III-nitrides and Related Materials (ICSCIII-N'97) - Materials Science Forum*, vol. 264-268, Stockholm, Sweden, 1998, pp. 953-956.

[40] J.B. Fedison, T.P. Chow, M. Ghezzo, J.W. Kretchmer, M.C. Nielsen, "Factors Influencing the Design and Performance of 4H-SiC GTO Thyristors", *Int. Conf. on Silicon Carbide III-nitrides and Related Materials (ICSIII-N'99)*, Durham (NC), USA, Oct. 1999.

[41] Y. Sugawara, K. Asano, R. Singh, J.W. Palmour, "6.2 kV 4H-SiC Pin Diode with Low Forward Voltage Drop", *Int. Conf. on Silicon Carbide III-nitrides and Related Materials (ICSIII-N'99)*, Durham (NC), USA, Oct. 1999.

[42] H. Lendemann, N. Johannsson, D. Mou, M. Frischholz, B. Astrand, P. Isberg, C. Ovren, "Operation of a 2500 V 150 A Si-IGBT/SiC Diode Module", *Int. Conf. on Silicon Carbide III-nitrides and Related Materials (ICSIII-N'99)*, Durham (NC), USA, Oct. 1999.

[43] M. True, R. Schörner, P. Friedrichs, D. Stephani, H. Ryssel, "Reliability and Degradation of Metal-Oxide-Semiconductor Capacitors on 4H- and 6H-Silicon Carbide", *Int. Conf. on Silicon Carbide III-nitrides and Related Materials (ICSIII-N'99)*, Durham (NC), USA, Oct. 1999.

[44] R. Schörner, P. Friedrichs, D. Peters, "Detailed Investigation of N-Channel Enhancement 6H-SiC MOSFET", *IEEE Trans. Elec. Dev.*, vol 46, no. 3, 1999, pp. 533-541.

[45] C.J. Scozzie, A. J. Lelis, J.M. McGarrity, F.B. McLean, "Mobility Degradation in 6H-SiC n-Channel MOSFETs", *Int. Conf. on Silicon Carbide III-nitrides and Related Materials (ICSIII-N'99)*, Durham (NC), USA, Oct. 1999.

[46] V.V. Afanas'ev, A. Stesmans, M. Bassler, G. Pensl, M.J. Schulz, "Shalow electron traps at the 4H-SiC/$SiO_2$ interface," *Appl. Phys. Lett.*, vol. 76, no. 3, 2000, pp. 336-338.

[47] ISE Integrated Systems Engineering AG, "DESSIS 5.0 user manual", 1997.

[48] W. Greiner, L. Neise, H. Stöcker, "Thermodynamik und Statistische Mechanik", *Verlag Harri Deutsch*, Theoretische Physik edited by W. Greiner, vol. 9, 1993.

[49] M. Ruff, H. Mitlehner, and R. Helbig "SiC Devices: Physics and Numerical Simulation", *IEEE Trans. Elec. Dev.*, vol. 41, no. 6, 1994, pp. 1040-1054.

[50] M. Ruff, "Elektronische Bauelemente aus Siliziumkarbid (SiC): Physikalische Grundlagen und numerische Simulation", Ph.D. thesis, Naturwissenschaftliche Fakultät der Universität Erlangen-Nürnberg, 1993.

[51] J. Mottok, "Numerische Simulation und Analyse bipolarer 4H-SiC Leistungsbauelemente", Ph.D. thesis, Naturwissenschaftliche Fakultät der Universität Erlangen-Nürnberg, 1996.

[52] P.G. Neudeck, C. Fazi, "High-field fast rise time pulse failures in 4H- and 6H-SiC pn-junction diodes", *J. Appl. Phys.*, vol. 80, no. 2, 1996, pp. 1219-1225.

[53] P.G. Neudeck, C. Fazi, "Study of Bulk and Elementary Screw Dislocations Assisted Reverse Breakdown in Low-Voltage ($< 250$ V) 4H-SiC $p^+n$ Junction Diodes - Part II: Dynamic Breakdown Properties", *IEEE Trans. Elec. Dev.*, vol. 46, no. 3, 1999, pp. 485-492.

[54] R.P. Joshi, and C. Fazi, "Computer Model Simulation of SiC Diode Reverse-Bias Instabilities due to Deep Energy Impurity Levels", *Materials Science Forum*, vol. 264-268, 1998, pp. 1033-1036.

[55] L. Boltzmann, "Vorlesungen über Gastheorie Teil I. und II.", *Ambrosius Barth, Leipzig*, 1896.

[56] A. Schenk, “Advanced Physical Models for Silicon Device Simulation”, *Computational Microelectronics*, ed. Siegfried Selberherr, Springer-Verlag, 1998.

[57] M. Rudan, F. Odeh, “Multi-Dimensional Discretization Scheme for the Hydrodynamic Model of Semiconductor devices”, *COMPEL*, vol. 5 (3), 1986, pp. 149-183.

[58] L. Onsager, “Reciprocal Relations in Irreversible Processes I”, *Phys, Rev.*, vol. 37, 1931, pp. 405-426.

[59] L. Onsager, “Reciprocal Relations in Irreversible Processes II”, *Phys, Rev.*, vol. 38, 1931, pp. 2265-2279.

[60] M. Lax, “Cascade Capture of Electrons in Solids”, *Physical Review*, vol. 199, no. 5, 1960, pp. 1502-1523.

[61] P.T. Landsberg, “Non-Radiative Transitions in Semiconductors”, *phys. stat. sol.*, vol. 41, 1970, p. 457.

[62] G.K. Wachutka, “Rigorous Thermodynamic Treatment of Heat Generation and Conduction in Semiconductor Device Modeling”, *IEEE Trans. on Computer-Aided Design of Integrated Circuits and Systems*, vol. 9, no. 11, 1990, pp. 1141-1149.

[63] G. Wachutka, “Tailored Modeling of Miniaturized Electrothermomechanical Systems using Thermodynamic Methods”, *Micromechanical Systems*, DSC, vol. 40, 1992, pp. 183-198.

[64] G. Wachutka, “Unified Framework for Thermal, Electrical, Magnetic, and Optical Semiconductor Device Modeling”, *COMPEL*, vol. 10, no. 4, 1991, pp 311-321.

[65] H.B. Callen, “Thermodynamics”, *Wiley, New York*, 1960.

[66] A.C Smith, J.F. Janak, R.H. Hopkins, “Electronic Conduction in Solids”, *McGraw-Hill, New York*, 1967.

[67] U. Lindefelt, “Equations for electrical and electrothermal simulation of anisotropic semiconductors”, *J. Appl. Phys.*, vol. 76, no. 7, 1994, pp. 4164-4167.

[68] H. Gajewski, and K. Gärtner, “On the discretization of van Roosbroeck’s equations with magnetic field,” *Proc. of Simulation of Semiconductor Devices and Processes (SISDEP’95)*, Erlangen, Germany, vol. 6, 1995, 234-237.

[69] Concetta Riccobene, “Multidimensional Analysis of Galvanomagnetic Effects in Magnetotransistors”, *Dissertation*, no. 11077, Physical Electronics Laboratory, Swiss Federal Institut of Technology, 1995.

[70] C. Riccobene, G. Wachutka, H. Baltes, “Numerical Study of Structural Variants of Bipolar Magnetotransistors”, *Sensors and Actuators A*, vol. 41, 1994, pp. 279-283.

[71] M. Lades, J. Frank, J. Funk, G. Wachutka, ”Analysis of Piezoresistive Effects in Silicon Structures Using Multidimensional Process and Device Simulation”, *Proc. of Simulation of Semiconductor Devices and Processes (SISDEP’95)*, Erlangen, Germany, vol. 6, 1995, pp. 22-25.

[72] H. Yano, T. Hirao, T. Kimoto, H. Matsunami, K. Asano, Y. Sugawara, "Anisotropy of Inversion Channel Mobility in 4H- and 6H-SiC MOSFETs on (1120) Face", *Int Conf. on Silicon Carbide III-nitrides and Related Materials (ICSIII-N'99)*, Durham (NC), USA, Oct. 1999.

[73] G. Wachutka, "Consistent treatment of carrier emmission and capture kinetics in electrothermal and energy transport models", *Microelectronics Journal*, vol. 26, 1995, pp. 307-315.

[74] J. Hendl, H.P. Strunk, V.D. Heydemann, G. Pensl, "Micropipes: Hollow Tubes in Silicon Carbide", *phys. stat. sol.*, (a) vol. 162, 1997, pp. 251-262.

[75] R. Rupp, A. Wiedenhofer, D. Stephani, "Epitaxial Growth of a Single and a Multi Wafer Vertical CVD System: A Comparison", *Proc. of the 2nd. Europ. Conf. on Silicon Carbide and Related Materials (ECSCRM'98)*, Montpellier, France, Sept. 1998, pp. 29-30.

[76] T. Dalibor, G. Pensl, H. Matsunami, T. Kimoto, W.J. Choyke, A. Schöner, N Nordell, "Deep Defect Centers in Silicon Carbide Monitored with Deep Level Transient Spectroscopy", *phys. stat. sol.*, (a) vol. 162, 1997, pp. 199-225.

[77] J. Crofton, L.M. Porer, J.R. Willians, "The Physics of Ohmic Contacts to SiC", *phys. stat. sol.*, (a) vol. 202, 1997, pp. 581-603.

[78] J.A. Cooper, "Advances in SiC MOS Technology", *phys. stat. sol.*, (a) vol. 162, 1997, pp. 305-320.

[79] V.V. Afanasev, M Bassler, G. Pensl, M. Schulz, "Intrinsic $SiC/SiO_2$ Interface States", *phys. stat. sol.*, (a) vol. 162, 1997, pp. 321-337.

[80] T. Ouisse, "Electron Transport at the $SiC/SiO_2$ Interface", *phys. stat. sol.*, (a) vol. 162, 1997, pp. 339-368.

[81] W. van Haeringen, P.A. Bobbert, W.H. Backes, "On the Band Gap Variations in SiC Polytypes", *phys. stat. sol.*, (b) vol. 202, 1997, pp. 63-79.

[82] W.J. Choyke, L. Patrick, "Absorption of Light in Alpha SiC near the Band Edge", *Phys. Rev.*, vol. 105, 1957, pp. 1721-1723.

[83] L. Patrick, W.J. Choyke, D.R. Hamilton, *Phys. Rev.*, vol. 137, 1965, p. 1515.

[84] W.J. Choyke, L. Patrick, "Exciton Recombination Radiation and Phonon Spectrum of 6H SiC", *Phys. Rev.*, vol. 127, 1962, pp. 1868-1877.

[85] R.P. Devaty, W.J. Choyke, "Optical Characterization of Silicon Carbide Polytypes", *phys. stat. sol.*, (a) vol. 162, 1997, pp. 5-38.

[86] N.T. Son, O. Kordina, A.O. Konstantinov, W. Chen, E. Soerman, B. Monemar, E. Janzen, "Electron effective masses and mobilities in high-purity 6H-SiC chemical vapor deposition layers", *Appl. Phys. Lett.*, vol. 65, no. 25, 1996, pp. 15409-15412.

[87] D. Volm, B.K. Meyer, D.M.Hofman, "Determination of the electron effective-mass tensor in 4H-SiC", *Phys. Rev. B*, vol. 53, no. 23, 1996, pp. 15409-15412.

[88] N.T. Son, P.N. Hai, W.M. Chen, C. Hallin, B. Monemar, E. Janzén, "Hole effective masses in 4H-SiC determined by optically detected cyclotron resonance", *Int Conf. on Silicon Carbide III-nitrides and Related Materials (ICSIII-N'99)*, Durham (NC), USA, Oct. 1999.

[89] C. Persson, U. Lindefelt, "Relativistic band struture calculation of cubic and hexagonal SiC polytypes", *J. Appl. Phys.*, vol.82, 1997, p. 5496.

[90] G. Wellenhofer, U. Rs̈sler, "Global Band Structure and Near-Band-Edge States", *phys. stat. sol*, (b) vol. 202, 1997, pp. 107-123.

[91] J.W. Slotboom, H.C. DeGraff, "Measurements of Bandgap Narrowing in Silicon Bipolar Transistors", *Solid-State Electronics*, vol. 19, 1976, pp. 857-862.

[92] D.B.M. Klaassen, J.W. Slotboom, H.C. DeGraff, "Unified apparent bandgap narrowing in n- and p-type Silicon", *Solid-State Electronics*, vol. 35, no. 2, 1992, pp. 125-129.

[93] U. Lindefelt, "Doping-induced band edge displacements and band gap narrowing in 3C, 4H, 6H-SiC, and Si", *J. Appl. Phys.*, vol. 84, no. 5, 1998, pp. 2628-2637.

[94] C. Persson, U. Lindefelt, "Calculated density of states and carrier concentration in 4H- and 6H-SiC", *Proc. of Silicon Carbide, III-nitrides and Related Materials (ICSCIII-N'97) - Materials Science Forum*, vol. 264-268, Stockholm, Sweden, 1998, pp. 275-278.

[95] D. Kendall, *Conf. Physics and Application of Lithium Diffused Silicon*, NASA, Goddard Space Flight Center, 1969.

[96] J.G. Fossum, D.S. Lee, "A physical model for the dependence of carrier lifetime on doping density in nondegenerate Silicon", *Solid-State Electronics*, vol. 25, no. 8, 1982, pp. 741-747.

[97] J.G. Fossum, R.P. Mertens, D.S. Lee, J.F. Nijs, "Carrier recombination and lifetime in highly doped Silicon", *Solid-State Electronics*, vol. 26, no. 6, 1983, pp. 569-576.

[98] A. Schenk "Rigorous Theory and Simplified Model of the Band-to-Band Tunneling in Silicon", *Solid-State Electronics*, vol. 36, no. 1, 1993, pp. 19-34.

[99] A. Schenk "A Model for the Field and Temperature Dependence of the Shockley-Read-Hall Lifetimes in Silicon", *Solid-State Electronics*, vol. 35, no. 11, 1992, pp. 1585-1596.

[100] A. Schenk, U. Krumbein, "Coupled defect-level recombination: Theory and application to anomalous diode characteristics", *J. Appl. Phys.*, vol. 78, no. 5, 1995, pp. 3185-3192.

[101] J. Frenkel, *Phys. Rev.*, vol. 54, 1938, p. 647.

[102] L. Huldt, N.G. Nilsson, K.G. Svantesson, "The temperature dependence of band-to-band Auger recombination in silicon", *Appl. Phys. Lett.*, vol. 35, no. 10, 1979, p. 776.

[103] W. Lochmann, A. Haug, "Phonon-assisted Auger recombination in Si with direct calculation of the overlap integrals", *Solid State Communications*, vol. 35, 1980, pp. 553-556.

[104] N. Ramungul, V. Khemka, T.P. Chow, M. Ghezzo, J. Kretchmer, "Carrier Lifetime Extraction from a 6H-SiC High-Voltage P-i-N Rectifier Reverse Recovery Waveform", *Proc. of Silicon Carbide, III-nitrides and Related Materials (ICSCIII-N'97) - Materials Science Forum*, vol. 264-268, Stockholm, Sweden, 1998, pp. 1065-1068.

[105] A.G. Chynoweth,.O. Konstantinov, Q. Wahab, N. Nordell, U. Lindefelt, "Study of Avalanche Breakdown nad Impact Ionization in 4H Silicon Carbide", *Journal Eletronic Materials*, vol. 27, no. 4, 1998, pp. 335-339.

[106] R. Raghunathan, B.J. Baliga, "Measurement of Electron and Hole Impact Ionization Coefficients for SiC" *Proc. IEEE Int. Symp. on Power Semiconductor Devices and ICs (ISPSD'97)*, 1997, pp. 173-176.

[107] A.G. Chynoweth, "Ionization rates for electrons and holes in Silicon", *Phys. Rev.*, vol. 109, 1958, pp. 1537-1540.

[108] P.G. Neudeck, C. Fazi, "Study of Bulk and Elementary Screw Dislocations Assisted Reverse Breakdown in Low-Voltage ($< 250\,V$) 4H-SiC $p^+n$ Junction Diodes - Part I: DC Properties", *IEEE Trans. Elec. Dev.*, vol. 46, no. 3, 1999, pp. 478-484.

[109] P.G. Neudeck, W. Huang, M. Dudley, "Breakdown Degradation Associated with Elementary Screw Dislocations in 4H-SiC $p^+n$ Junction Rectifiers", *Mat. Res. Soc. Proc.*, vol. 483, 1998, pp. 285-294.

[110] L. Patrick, W.J. Choyke, "Static Dielectric Constant of SiC", *Phys. Rev. B*, vol. 2, no. 6, 1970, pp. 2255-2256.

[111] S. Ninoyima, S.Adachi, *Japan J. Appl. Phys*, vol. 33, 1994, pp. 2479.

[112] S. Selberherr, *"Analysis and Simulation of Semiconductor Devices"*, Springer, 1984

[113] M. Bakowski, U. Gustafsson, U. Lindefelt, "Simulation of SiC High Power Devices", *phys. stat. sol.*, (a) vol. 162, 1997, pp. 421-440.

[114] W.J. Schaffer, G.H. Negley, K.G. Irvine, and J.W. Palmour, "Conductivity anisotropy in epitaxial 6H and 4H-SiC," *Mat. Res. Soc. Sym.*, vol. 339, 1994, pp. 595-600.

[115] M. Schadt, G. Pensl, R.P. Devatny, W.J. Choyke, R. Stein, D. Stephani, "Anisotropy of the electron Hall mobility in 4H, 6H, and 15R silicon carbide," *Appl. Phys. Lett.*, vol. 65, 1994, pp. 3120-3122.

[116] T. Kinoshita, K.M. Itoh, J. Muto, M. Schadt, G. Pensl, K. Takeda, "Calculation of the Anisotropy of the Hall Mobility in n-type 4H- and 6H-SiC", *Proc. of Silicon Carbide, III-nitrides and Related Materials (ICSCIII-N'97) - Materials Science Forum*, vol. 264-268, Stockholm, Sweden, 1998, pp. 295-298.

[117] D.M. Caughey, R.E. Thomas, "Carrier mobilities in Silicon empirically related to doping and field", *Proc. IEEE*, 1967, pp. 2192.

[118] H.J. van Daal, “Mobility of Charge Carriers in Silicon Carbide”, *Dissertation*, University of Amsterdam, 1994.

[119] H.J. van Daal, W.F. Knippenberg, J.D. Wasscher, “On the Electronic Conduction of α-SiC Crystals between 300 and 1500 K”, *J. Phys. Solids*, vol. 24, 1963, pp. 109-127.

[120] G. Rutsch, R.P. Devaty, D.W. Langer, L.B. Rowland, W.J. Choyke, “Measurement of the Hall Scattering Factors in 4H-SiC Epilayers from 40 K to 290 K and up to Magnetic Fields of Nine Tesla”, *Proc. of Silicon Carbide, III-nitrides and Related Materials (ICSCIII-N'97) - Materials Science Forum*, vol. 264-268, Stockholm, Sweden, 1998, pp. 517-520.

[121] S.C. Choo, “Theory of a Forward-Biased Diffused-Junction P-I-N Rectifier. Part I: Exact Numerical Solutions”, *IEEE Trans. Elec. Dev.*, vol. 19, no. 8, 1972, pp. 954-966.

[122] C. Lombardi, S. Manzini, “A Physically Based Mobility Model for Numerical Simulation of Nonplanar Devices”, *IEEE Trans. on CAD*, vol. 7, no. 11, 1988, pp. 1164-1171.

[123] W.v. Muench, E. Pettenpaul, “Saturated electron drift velocity in 6H silicon carbide”, *J. Appl. Phys.*, vol. 48, 1977, pp. 4823.

[124] I.A. Khan, J.A. Cooper, Jr., “Measurement of High Field Electron Transport in Silicon Carbide”, *Proc. of Silicon Carbide, III-nitrides and Related Materials (ICSCIII-N'97) - Materials Science Forum*, vol. 264-268 Stockholm, Sweden, 1998, pp. 509-512.

[125] C. Canali, G. Majni, R. Minder, G. Ottaviani, “Electron and hole drift velocity measurements in Silicon and their empirical relation to electric field and temperature”, *IEEE Trans. Elec. Dev.*, vol. 22, 1975, pp. 1045-47.

[126] H.E. Nilsson, U. Sannemo, C.S. Petersson, “Monte Carlo simulation of electron transport in 4H-SiC using a two-band model with multiple minima”, *J. Appl. Phys.*, vol. 80, no. 6, 1996, pp. 3365-69.

[127] R.P. Joshi, “Monte Carlo calculations of temperature- and field-dependent electron transport parameters for α-SiC”, *J. Appl. Phys.*, vol. 78, no.9, 1995, pp. 5518-21.

[128] R.P. Joshi, D.K. Ferry “Calculations of the temperature and field dependent electronic mobility in β-SiC”, *Solid-State Electronics*, vol. 38, no. 11, 1995, pp. 1911-16.

[129] A.G. Sabnis, J.T. Clemens, “Characterization of the Electron Mobility in the Inverted (100) Si-Surface”, *Proc. Int. Electron Devices Meeting (IEDM)*, 1979, pp. 18-21.

[130] T.H. Geballe, G.W. Hull, “Seebeck effect in silicon”, *Phys. Rev.*, vol. 98, 1955, pp. 941-947.

[131] W. Fulkerson, J.P. Moore, R.K. Williams, R.S. Graves, D.L. McElroy, “Thermal conductivity, electrical resistivity, and seebeck coefficient of Silicon from 100 to 1300 K”, *Phys. Rev.*, vol. 167, no. 3, 1968, pp. 765-782.

[132] Y.S. Touloukian, E.H. Buyco, “Specific Heat (Nonmetallic Solids) in Thermophysical Properties of Matter”, *IF/Plenum*, New York, vol. 5, 1970.

[133] Y.S. Touloukian, E.H. Buyco, "Specific Conductivity (Nonmetallic Solids) in Thermophysical Properties of Matter", *IF/Plenum*, New York, vol. 4, 1970.

[134] E.A. Burgemeister, W. von Muench, E. Pettenpaul, "Thermal conductivity and electrical properties of 6H silicon carbide", *J. Appl. Phys.*, vol. 50, no. 9, 1979, pp. 5790-5794.

[135] D.T. Morelli, J.P. Heremans, "Phonon-electron scattering in single crystal silicon carbide", *Appl. Phys. Lett.*, vol. 63, no. 23, 1993, pp. 3143-3145.

[136] H.P. Felsl, "private communication", Chair for Physics of Electrotechnology, Munich Technical University, Munich, 1999.

[137] "Properties of Silicon Carbide", *INSPEC*, edited by G.L. Harris, London, 1995.

[138] A. Chen, P. Srichaikul, "Shallow Donor Levels and the Conduction Band Edges Structures in Polytypes of SiC", *phys. stat. sol*, (b) vol. 202, 1997, pp. 81-106.

[139] T. Troffer, M. Schadt, T. Frank, H. Ito, G. Pensl, J. Heindl, H.P. Strunk, M. Maier, "Doping of SiC by Implantation of Boron and Aluminum", *phys. stat. sol.*, vol. 162 (a), 1997, pp. 277-298.

[140] W. Götz, A. Schöner, G. Pensl, W. Suttrop, W.J. Choyke, R. Stein, S. Leibenzeder, *J. Appl. Phys*, vol. 73, 1993, p. 3332.

[141] S.R. Smith, A.O. Eevwaraye, W.C. Mitchel, M.A. Capano, "Shallow Acceptor Levels in 4H- and 6H-SiC", *J. of Electronic Materials*, vol. 28, no. 3, 1999, pp. 190-195.

[142] A.O. Evwaraye, S.R. Smith, W.C. Mitchel, H.McD. Hobgood, "Boron acceptor levels in 6H-SiC bulk samples", *Appl. Phys. Lett.*, vol. 71, no. 9, 1997, p. 1186.

[143] A.O. Evwaraye, S.R. Smith, W.C. Mitchel, "Shallow and deep levels in n-type 4H-SiC", *J. Appl. Phys.*, vol. 79, no. 10, 1996, pp. 7726-7730.

[144] C. Raynaud, F. Ducroquet, G. Guillot, "Determination of ionization energies of the nitrogen donors in 6H-SiC by admittance spectroscopy", *Appl. Phys. Lett.*, vol. 76, no. 3, 1994, pp. 1956-1958.

[145] C. Raynaud, C. Richier, P.N. Brounkov, F. Ducroquet, G. Guillot, L.M. Porter, R.F. Davis, C.Jaussaud, T. Billon, "Determination of donor and acceptor level energies by admittance spectroscopy in 6H-SiC", *Mat. Science Eng.*, vol. B29, 1995, pp. 122-125.

[146] W. Suttrop, G. Pensl, P. Lanig, "Boron-Related Deep Centers in 6H-SiC", *Appl. Phys. A*, vol. 51, 1990, pp. 231-237.

[147] V. Mulpuri, P. Griffiths, "Al and B ion-implantations of 6H- and 3C-SiC," *J. Appl. Phys.*, vol. 77, no.6, 1995, pp. 2479-2485.

[148] H. Sonntag, S. Kalbitzer, "Ion-implantation doping of crystalline 6H-SiC," *Appl. Phys. A*, vol. 61, 1995, pp. 363-367.

[149] T. Kimoto, A. Itoh, H. Matsunami, "Nitrogen donors and deep level in high-quality 4H-SiC epilayers grown by chemical vapor deposition," *Appl. Phys. Lett.*, vol. 67, no. 19, 1995, pp. 2833-35.

[150] V.L. Bonc-Bruevic, S.G. Kalasnikov, "Halbleiterphysik", *Deutscher Verlag der Wissenschaften, Berlin*, 1982.

[151] A. Pellegrini, L. Colalongo, M. Valdinoci, M Rudan, "AC Analysis of Amorphous Silicon Devices", *IEEE Trans. on Computer-Aided Design of Integrated Circuits and Systems*, vol. 15, no. 11, 1996, pp. 1324-1331.

[152] M. Valdinoci, L. Colalongo, G. Baccarani, A Pecora, I. Policicchio, G. Fortunato, P. Legagneux, C. Reita, D. Pribat, "Analysis of Electrical Characteristics of Polycrystalline Silicon Thin-Film Transistors under Static and Dynamic Conditions", *Solid-State Electronics*, vol. 41, no. 9, 1997, pp. 1363-1369.

[153] L. Colalongo, M. Valdinoci, A. Pellegrini, M Rudan, "Dynamic Modeling of Amorphous- and Polycrystalline-Silicon Devices", *IEEE Trans. Elec. Dev.*, vol. 45, no. 1, 1998, pp. 826-833.

[154] S.M. Sze, "Physics of Semiconductor Devices", *John Wiley & Sons*, New York, 1981.

[155] E. Spenke "PN-Übergänge", *Springer Verlag*, Berlin, 1979.

[156] W. Shockley, W.T. Read Jr., *Phys. Rev.*, vol. 87, 1952, pp. 835

[157] R.N. Hall, *Phys. Rev.*, vol. 87, 1952, pp. 387

[158] J. A. Edmond, D. G. Waltz, S. Brueckner, H.S. Kong, J. W. Palmour, H. Carter Jr., "High Temperature Rectifiers in 6H-Silicon Carbide", Proc. 1$^{th}$ Int. High Temperature Electronics Conf., Albuquerque, New Mexico, 1991, pp. 207-212.

[159] P.G. Neudeck, D.J. Larkin, J.E. Starr, J.A. Owell, C.S. Salupo, L.G. Matus, "Electrical Properties of Epitaxial 3C- and 6H-SiC p-n Junction Diodes Produced Side-by-Side on 6H-SiC Substrates", *IEEE Trans. Elec. Dev.*, vol. 41, no. 5, 1994, pp. 826-835.

[160] P.M .Shenoy, B.J. Baliga, "Planar, Ion Implanted, High Voltage 6H-SiC P-N Junction Diodes", *IEEE Electron Device Letters*, vol. 16, no. 10, 1995, pp. 454-456.

[161] O. Kordina, J.P. Bergman, A. Henry, E. Janzén, S. Savage, J. André, L.P. Ramberg, U. Lindefelt, W. Hermansson, K. Bergman, "A 4.5 kV 6H silicon carbide rectifier", *Appl. Phys. Lett.*, vol. 67, no. 11, 1995, pp. 1561-1563.

[162] H. Mitlehner, W. Bartsch, M. Bruckmann, K.O. Dohnke, U. Weinert, "The Potential of Fast High Voltage, SiC Diodes", *Proc. IEEE Int. Symp. on Power Semiconductor Devices and ICs (ISPSD'97)*, 1997, pp. 165-168.

[163] M. Frischholz, J. Seidel, A. Schöner, U. Gustafsson, M. Bakowski, K. Nordgren, K. Rottner, "JTE concept evaluation and failure analysis: OBIC measurements on 4H SiC $p^+ - n$ diodes", *Proc. IEEE Int. Symp. on Power Semiconductor Devices and ICs (ISPSD'98)*, Kyoto, 1998, pp. 391-394.

[164] H. Mitlehner, P. Friedrichs, D. Peters, R. Schörner, U. Weinert, B. Weis, D. Stephani, "Switching behaviour of fast high voltage SiC pn - diodes", *Proc. IEEE Int. Symp. on Power Semiconductor Devices and ICs (ISPSD'98)*, Kyoto, 1998, pp. 127-130.

[165] R. Patel, V. Khemka, N. Ramungul, T.P. Chow, M. Ghezzo, J. Kretchmer, "Phosphorus-Implanted High-Voltage $n^+ - p$ 4H-SiC Junction Rectifiers", *Proc. IEEE Int. Symp. on Power Semiconductor Devices and ICs (ISPSD'98)*, Kyoto, 1998, pp. 387-390.

[166] T. Kimoto, N. Miyamoto, H. Matsunami, "Effects of Surface Defects on the Performance of 4H- and 6H-SiC PN Junction Diodes", *Proc. ECSCRM*, Montpellier, 1998, pp. 67-68.

[167] T. Kimoto, N. Miyamoto, H. Matsunami, "Performance Limiting Surface Defects in SiC Epitaxial p-n Junction Diodes", *IEEE Trans. Elec. Dev.*, vol. 46, no. 3, 1999, pp. 471-477.

[168] N. Ramungul, Y. Zheng, R. Patel, V. Khemka, T.P. Chow, "Beryllium-Implanted 6H-SiC $P^+N$ Junctions", *Proc. of Silicon Carbide, III-nitrides and Related Materials (ICSCIII-N'97) - Materials Science Forum*, vol. 264-268, Stockholm, Sweden, 1998, pp. 1049-1052.

[169] N. Ramungul, Y. Zheng, R. Patel, V. Khemka, T.P. Chow, "6H-SiC $P^+N$ Junctions Fabricated by Beryllium Implantation", *IEEE Trans. Elec. Dev.*, vol. 46, no. 3, 1999, pp. 465-470.

[170] Y. Wang, J.A. Cooper Jr., M.R. Melloch, S.T. Sheppard, "Experimental characterization of Electron-Hole Generation in Silicon Carbide", *J. of Electronic Materials*, vol. 25, no. 5, 1996, pp. 899-907.

[171] P.G. Neudeck, "Perimeter Governed Minority Carrier Lifetimes in 4H-SiC $p^+ - n$ Diodes Measured by Reverse Recovery Switching Transient Analysis", *J. of Electronic Materials*, vol. 27, no. 4, 1998, pp. 317-323.

[172] J.P. Bergman, O. Kordina, E. Janzén, "Time Resolved Spectroscopy of Defects in SiC", *phys. stat. sol.*, (a) vol. 162, 1997, pp. 65-77.

[173] A. Czerwinski, J Ratajczak, J. Katcki, A. Bakowski, M. Bakowski, "Electrical and Transmission Electron Microscopy Characterisation of 4H-SiC Homoepitaxial Mesa Diodes", *Proc. of Silicon Carbide, III-nitrides and Related Materials (ICSCIII-N'97) - Materials Science Forum*, vol. 264-268, Stockholm, Sweden, 1998, pp. 573-576.

[174] O. Takemura, T. Kimoto, H. Matsunami, T. Nakata, M Watanabe, M. Inoue, "Implantation of Al and B Acceptors into Alpha-SiC and pn Junction Diodes", *Proc. of Silicon Carbide, III-nitrides and Related Materials (ICSCIII-N'97) - Materials Science Forum*, vol. 264-268, Stockholm, Sweden, 1998, pp. 701-704.

[175] M.V. Rao, J. Gardner, A. Edwards, N.A. Papanicolaou, G. Kelner, O.W. Holland, M. Ghezzo, J. Kretchmer, "Ion Implantation Doping in SiC and its Device Applivations", *Proc. of Silicon Carbide, III-nitrides and Related Materials (ICSCIII-N'97) - Materials Science Forum*, vol. 264-268, Stockholm, Sweden, 1998, pp. 717-720.

[176] L. Pelaz, J.L. Orantes, J. Vincente, L.A. Bailón, J. Barbolla, “The Poole-Frenkel Effect in 6H-SiC Diode Characteristics”, *IEEE Trans. Elec. Dev.*, vol. 41, 1994, pp. 587-591.

[177] Manufacturer’s address: Cree Research Inc., 2810 Meridian Parkway, Suite 176, Duram, NC 27713

[178] P.D. Yoder, K. Gärtner, W. Fichtner. *J. Appl. Phys.*, vol. 79, no. 4, 1996, p. 1951.

[179] J.N. Shenoy, J.A. Cooper, and M.R. Melloch, “High-voltage double-implanted power MOSFET’s in 6H-SiC”, *IEEE Electron Device Letters*, vol. 18, 1997, pp. 93.

[180] D. Peters, R. Schörner, P. Friedrichs, J. Völkl, H. Mitlehner, D. Stephani, “An 1800V Triple Implanted Vertical 6H-SiC MOSFET”, *IEEE Trans. Elec. Dev.*, vol 46, no. 3, 1999, pp. 542-545.

[181] W. Kaindl, M. Lades, “Numerische Simulation von 6H-SiC Bauelementen”, *Tech. Report*, Chair for Physics of Electrotechnology, Munich Technical University, Munich, 1998.

[182] J. Barbolla, S. Dueñas, and L. Bailón: “Admittance Spectroscopy in Junctions”, *Solid-State Electronics*, vol. 35, no. 3, 1992, pp. 285-297.

[183] D.L. Losee, “Admittance spectroscopy of impurity levels in Schottky barriers”, *J. Appl. Phys.*, vol. 46, no. 5, 1975, pp. 2204-2214.

[184] G. Vincent, D. Bois, and P. Pinard, “Conductance and cpacitance studies in GaP Schottky barriers”, *J. Appl. Phys.*, vol. 46, no. 12, 1975, pp. 5173-5178.

[185] L. Quintanilla, S. Dueñas, E. Castán, R. Pinacho, L.Pelaz, L. Bailón, and J. Barbolla, “Dopant level freeze-out and nonideal effects in 6H-SiC epilayer junctions”, *J. Appl. Phys.*, vol. 79, no. 1, 1996.

[186] J.L. Pautrat, B. Katircioglu, N. Magnea, D. Bensahel, J.C. Pfister, and L. Revoil, “Admittance Spectroscopy: A Powerful Characterization Technique For Semiconductor Crystals”, *Solid-State Electronics*, vol. 23, 1980, pp.1159.

[187] D.K. Schroder, *“Semiconductor Material and Device Characterization”*, *John Wiley & Sons*, New York, 1990.

[188] M.M. Anikin, N.I. Kuznetsov, A.A. Lebedev, N.S. Savkina, A.L. Syrkin, V.E. Chelnokov, *Semiconductors*, vol. 28, no. 3, 1994, pp. 278.

[189] P.van Halen, “A Physical Spice-Compatible Dual-Gate JFET Model”, *Proc. IEEE*, 1991, pp. 715-718.

[190] S.T. Sheppard, V. Lauer, W. Wondrak, and E Niemann, “High Temperature Performance of Implanted-Gate n-Channel JFETs in 6H-SiC”, *Proc. of Silicon Carbide, III-nitrides and Related Materials (ICSCIII-N’97) - Materials Science Forum*, vol. 264-268, Stockholm, Sweden, 1998, pp. 1077-1080.

[191] N. Kaninski, “private communication”, ABB semiconductors, Swtzerland.

[192] R. Rupp, “private communication”, Infineaon Technologies, Munich.

[193] E. Valcheva, T. Paskova, I.S. Ivanov, R. Yakimova, Q. Wahab, S. Savage, N. Nordell, C.I. Harris “Electrical Activation of B Implant in 6H-SiC”, *Proc. of Silicon Carbide, III-nitrides and Related Materials (ICSCIII-N'97) - Materials Science Forum*, vol. 264-268, Stockholm, Sweden, 1998, pp. 705-708.

[194] U. Schmid, “Charakterisierung von lateralen Feldeffekttransistoren aus 6H-SiC”, *Diplomarbeit*, Daimler-Benz AG, Research & Technology, Frankfurt, 1998.

[195] N. Kaminski, “6H-SiC power devices”, *Dissertation*, University of Bremen, 2000.

[196] N. Kaminski, S.T. Sheppard, E. Niemann, “Punch-Through Behaviour of Wide Bandgap Materials (with Example in 6H-SiC and its Benefit to JFETs)”, *Proc. of Silicon Carbide, III-nitrides and Related Materials (ICSCIII-N'97) - Materials Science Forum*, vol. 264-268, Stockholm, Sweden, 1998, pp. 1073-1076.

[197] J.L. Chu, G. Persky, and S.M. Sze, “Thermionic injection and space-charge-limited current in reach-through $p^+np^+$ structures”, *J. Appl. Phys.*, vol. 43, no. 8, 1972, pp. 3510-3515.

[198] P.S. Raderecht, “The development of a gate assisted turn-off thyristor for use in high frequency applications”, *Int. J. Electronics*, vol. 36, no. 3, pp 399-416, 1974.

[199] M.E. Levinshtein, J.W. Palmour, S.L. Rumyanetsev, and R. Singh, “Turn-on Process in 4H-SiC Thyristors”, *IEEE Trans. Elec. Dev.*, vol. 44, no.7, July 1997, pp. 1177-1179.

[200] A.K. Agarwal, J.B. Casady, L.B. Rowland, S. Seshadri, R.R. Siergiej, W.F. Valek, C.D. Brandt, “700-V Asymmetrical 4H-SiC Gate Turn-Off Thyristors (GTO's)”, *IEEE Electron Device Letters*, vol. 18, no. 11, 1997.

[201] G.K. Wachutka, “Analytical Model for the Destruction Mechanism of GTO-Like Devices by Avalanche Injection”, *IEEE Trans. Elec. Dev.*, vol. 38, no. 6, 1991, pp. 1516-1523.

[202] R.E. Bank, D.J. Rose, “Global Approximate Newton Methods”, *Numer. Math.*, vol. 37, 1981, pp. 279-295.

[203] R.E. Bank, W.M Coughran, Jr., W. Fichtner, E.H. Grosse, D.J. Rose, R.K. Smith, “Transient simulation of silicon devices and circuits”, *IEEE Trans.*, vol. CAD-4, 1985, pp. 436-451.

[204] R.S. Varga, “Matrix Iterative Analysis”, *Prentice-Hall*, Series in Automatic Computation, 1962.

[205] E.M. Buturla, P.E. Cottrell, B.M. Grossmann, K.A. Salsburg, “Finite-Element analysis of semiconductor devices”, *IBM J. Res. Develop.*, vol. 25, 1981, pp. 218-239.

[206] R.E. Bank, , D.J. Rose, W. Fichtner, “Numerical Methods for Semiconductor Device Simulation”, *IEEE Trans. Elec. Dev.*, vol. ED-30, 1983, pp. 1031-1041.

[207] D. Scharfetter, H.K. Gummel, “Large-signal analysis of a silicon Read diode oscillator”, *IEEE Trans. Elec. Dev.*, vol. ED-16, 1969, pp. 64-77.

[208] J. Bürgler, "Discretization and Grid Adaption in Semiconductor Device Modeling", *Dissertation*, Integrated Systems Laboratory, Swiss Federal Institut of Technology, 1990, published by: Hartung Gorre Verlag, Konstanz, Germany.

[209] J. Litsios, S. Müller, W. Fichtner, "Mixed -Mode Multi-Dimensional Device and Circuit Simulation", *Techncal Report*, no. 93/28, Integrated Systems Laboratory, Swiss Federal Institut of Technology, Zurich, 1993.

[210] A. Frohnmeyer, "private communication", Chair for Physics of Electrotechnology, Munich Technical University, Munich, 1999.

[211] A. Schöner, "Elektrische Charakterisierung von flachen und tiefen Störstellen in 4H-, 6H- und 15-R Siliziumkarbid", *Dissertation*, Friedrich-Alexander-Universität Erlangen-Nürnberg, 1994.